



**HAL**  
open science

# Laser-pyrolysed ZnFe<sub>2</sub>O<sub>4</sub> anode for lithium-ion batteries: understanding of the lithium storage mechanisms

Samantha Bourrioux

## ► To cite this version:

Samantha Bourrioux. Laser-pyrolysed ZnFe<sub>2</sub>O<sub>4</sub> anode for lithium-ion batteries: understanding of the lithium storage mechanisms. Material chemistry. Communauté Université Grenoble Alpes, 2018. English. ⟨NNT : ⟩. ⟨tel-01870943⟩

**HAL Id: tel-01870943**

**<https://theses.hal.science/tel-01870943v1>**

Submitted on 10 Sep 2018

HAL is a multi-disciplinary open access archive for the deposit and dissemination of scientific research documents, whether they are published or not. The documents may come from teaching and research institutions in France or abroad, or from public or private research centers.

L'archive ouverte pluridisciplinaire HAL, est destinée au dépôt et à la diffusion de documents scientifiques de niveau recherche, publiés ou non, émanant des établissements d'enseignement et de recherche français ou étrangers, des laboratoires publics ou privés.



HAL Authorization



## THÈSE

Pour obtenir le grade de

**DOCTEUR DE LA COMMUNAUTE UNIVERSITE GRENOBLE ALPES**

**Préparée dans le cadre d'une cotutelle entre la Communauté Université Grenoble Alpes et Nanyang Technological University, Singapour**

Spécialité : **Matériaux**

Arrêté ministériel : le 6 janvier 2005 - 7 août 2006

Présentée par

« **Samantha / BOURRIOUX** »

Thèse dirigée par « **Alain / PASTUREL** »

Codirigée par « **Madhavi / SRINIVASAN** »

Préparée au sein des **Laboratoires LEDNA (CEA Saclay) et Energy Research Institute @ NTU (ERIAN)**

Dans les **Écoles Doctorales I-MEP2 et Interdisciplinary Graduate School (IGS)**

# **Laser-pyrolysed ZnFe<sub>2</sub>O<sub>4</sub> anode for lithium-ion batteries: understanding of the lithium storage mechanisms**

Thèse soutenue publiquement le « **2 février 2018** »,

Devant le jury composé de :

**Madame, Christel, LABERTY-ROBERT**

Professeur, Université Pierre et Marie Curie, rôle (Président)

**Monsieur, Frédéric, BERNARD**

Professeur des Universités, Université de Bourgogne, rôle (Rapporteur)

**Monsieur, François, TRAN VAN**

Professeur des Universités, Université François Rabelais, rôle (Rapporteur)

**Monsieur, Claude, GUET**

Professeur, Nanyang Technological University, rôle (Examineur)

**Madame, Fannie, ALLOIN**

Directeur de Recherche, Université Grenoble-Alpes, rôle (Examineur)

**Monsieur, Yann, LECONTE**

Chercheur, CEA, rôle (Co-encadrant)

**Madame, Laure, MONCONDUIT**

Directeur de Recherche, Université de Montpellier, rôle (Membre)





---

## Acknowledgements

---

This PhD has been conducted in cotutelle between the University of Grenoble-Alpes and the Nanyang Technological University of Singapore.

This work has been realized in the laboratory of Nanometric Structures (LEDNA) in the French Alternative Energies and Atomic Energy Commission (CEA) and in the Energy Research Institute @NTU (ERI@N) in Singapore. Financial support came from the Advanced Materials Cross-Cutting Program (PTMA) of the CEA.

I would like to acknowledge first the different persons who made this PhD possible:

Thank you to Cécile Reynaud and Martine Mayne who allowed me to conduct my PhD in their laboratory. Special thanks to Martine who helped me as far as possible especially during the last months of my PhD and during my stay in Singapore. I would also like to acknowledge Professor Claude Guet who partly supervised this cotutelle project and Frédéric Schuster, head of the Cross-Cutting Program.

My thanks also go to Professor Alain Pasturel who accepted to be my PhD supervisor in France. I would like to thank him for his precious help during these three years of studies, especially concerning the corrections of my manuscript and in resolving many administrative issues. My appreciation is also due to Professor Madhavi Srinivasan who welcomed me in her laboratory in NTU for one year. Thank you for the corrections of my manuscript, especially for the electrochemistry part.

I would also want to express my thanks to the different members of the jury who accepted to evaluate my work and for their attendance in my oral defense. More particularly, thank you to Frédéric Bernard and François Tran-Van who accepted to read my manuscript and who were interested in my thesis.

The electrochemistry part of this work has been conducted in collaboration with the Charles Gerhardt Institute of Montpellier. I would like to express my gratitude to Laure Monconduit, head of the AIME laboratory for accepting this collaboration. She helped me a lot during my thesis to answer many questions about electrochemistry for conversion materials. Laure also took time to give me advice and make corrections on my manuscript. Thank you for letting me working few weeks in your laboratory. Thank you to Moulay Sougrati and Lorenzo Stievano too, who were really helpful when I was in Montpellier, especially to conduct some operando measurements.

I would like now to express my thanks to many of my French colleagues so I will continue in French.

Je vais commencer par remercier les différentes personnes que j'ai côtoyées durant ma thèse au CEA, en commençant par l'une des plus importantes, l'expert en pyrolyse laser, appelé parfois Hulk ou Géant Vert en raison de sa force prodigieuse pour refermer les bouteilles de gaz (que je n'arrivais plus à ouvrir après) et de la couleur de son manteau ..., celui qui a encadré ma thèse pendant ces trois années, j'ai nommé : Yann Leconte. Je ne te remercierai sans doute jamais assez pour m'avoir permis de réaliser cette thèse malgré tous les obstacles qu'il y a eu à franchir pour arriver jusqu'au bout. Tu as vraiment été un encadrant en or du début à la fin, tu m'as appris les joies (et les malheurs ... !) de la pyrolyse laser, tu as toujours été présent pour répondre à mes questions, pour me conseiller tout en me laissant toujours de l'autonomie et la possibilité de faire mes choix dans mon projet de recherche. Tu m'as motivée à faire de mon mieux et d'ailleurs, au-delà du boulot, tu as réussi à faire quelque chose que je n'aurais jamais cru possible il y a quelques années : me lancer dans la course à pied ! Maintenant, au lieu de me retrouver en PLS après avoir couru 500 m, je suis capable de tenir 10 km, parce que je ne suis pas une « dégonflée » ! Tu as toujours été là pour me remonter le moral ou me remotiver dans les moments les plus difficiles en fin de thèse et je sais à quel point tu as bataillé pour que tout se passe du mieux possible, en France comme à Singapour. Je me souviendrai toujours de mon entretien, lorsque j'ai vu ta batte de base-ball posée bien en évidence sur ton bureau et où je me suis demandée où je venais d'atterrir et si c'était une bonne idée que j'accepte cette thèse ! Et bien au final, même si cette thèse ne s'est pas déroulée dans les meilleures conditions possibles, tu fais partie des personnes qui m'auront permis d'en garder un très bon souvenir et ça, en partie grâce à ton infaillible sens de l'humour ! Je sais que je t'ai souvent dit que tes blagues étaient nulles mais en fait, pas tant que ça (ou alors je m'y suis habituée ?). Bon, tes remerciements prennent déjà une demi-page alors je vais m'arrêter là sinon les suivants vont être jaloux et puis, il ne faudrait pas que tu aies les chevilles qui enflent ;).

Je souhaite ensuite remercier sincèrement une collègue devenue au fil des mois une grande amie : Axelle Quinsac. Avant que tu ne reviennes au CEA, Yann m'avait dit qu'on allait bien s'entendre toutes les deux et il avait raison ! On se ressemble sur pas mal de points et je suis vraiment contente d'avoir trouvé quelqu'un qui aime au moins autant que moi les chips, les bonbons qui piquent, la chaleur des radiateurs plutôt que le froid glacial de nos bureaux, qui a les mêmes problèmes de chaussettes, qui déteste ses cheveux autant que je déteste les miens et qui est aussi pipelette que moi. Merci pour tous les bons moments passés ensemble, que ça soit au labo ou à l'extérieur, tu as aidé à rendre moins monotone la contemplation de flammes de pyrolyse laser quand on manipait ensemble ! Plus sérieusement, merci à toi d'avoir été un soutien sans faille et d'avoir toujours essayé de me montrer le

côté positif des choses. Je sais que tu pars loin et que je ne te reverrai pas aussi facilement pendant quelques années, mais compte sur moi pour aller faire un tour en Guyane et puis, je te rappelle que l'on a prévu de faire une course ensemble un jour !

Je vais continuer avec notre experte MEB, BET, ATG ... et j'en passe, Miss Aurélie Habert ou tout simplement Lili, notre technicienne multitâches, qui m'a aidé à réaliser tout plein de caracs physico-chimiques depuis le début de ma thèse. On en aura passé des journées devant le MEB, à chercher ces particules d'oxydes zinc-fer, à faire de l'EDX où on ne voyait finalement rien du tout, ou à essayer d'imaginer des formes dans nos images (des têtes de Mickey par exemple !). Comme tout doctorant qui se respecte, je sais que je t'ai demandé beaucoup de caractérisations de dernière minute pour terminer de remplir mon manuscrit ou pour ma soutenance de thèse, alors merci beaucoup d'avoir toujours été disponible et motivée pour m'aider malgré le fait que tu sois sollicitée de partout. Merci aussi pour ta bonne humeur au labo, pour nos petites séances de papotages à l'ATG et pour nos pauses café/chocolat chaud au soleil bien sympas. Et je n'oublie pas notre soirée raclette + PS4 !

Je souhaite également remercier Olivier Sublemontier, grand mentor de Youri pendant quelques années, qui lui a tout enseigné sur comment être un bon « anti-Microsoft » ... oups pardon, comment réaliser de superbes couches minces par co-dépôt PVD/pyrolyse avec *ALICE* bien sûr. Je retiendrai d'Olivier son calme olympien en toutes circonstances ... sauf quand on lui file un ordinateur avec « Windaube » entre les mains ! Je retiendrai aussi ses performances hors normes en course à pied, qui font que j'avais un point de côté en moins de 5 minutes en courant avec lui ! En tout cas Olivier, merci pour ta bonne humeur, pour ton soutien durant cette thèse et pour tes conseils en course à pied !

Je continue avec les permanents en prenant le temps de remercier Henri, THE électrochimiste, le maître des jeux de mots (qui forme un duo d'humoristes « subtil » avec Yann, n'est-ce pas ?) et le musicien du LEDNA (je pense notamment à tes joyeux sifflements que l'on pouvait entendre dans les labos) ! J'ai été et je suis toujours aussi très impressionnée par ta passion pour ton travail, par ta rigueur et ton acharnement sur les manip de pyrolyse laser. Merci de m'avoir soutenue, en particulier pendant la fin de ma thèse, dans cette période un peu tumultueuse entre le manuscrit, les rapports et la préparation de ma soutenance. Je te souhaite le meilleur pour la suite (et de réussir à percer les mystères de la pyrolyse laser ;)).

Je vais continuer avec tous les anciens doctorants, maintenant docteurs, qui ont dû supporter ma présence plus ou moins longtemps pendant ces trois années de thèse. Je commence par mes collègues de bureau qui ont eu à supporter ma compétence + 1000 en bavardage, mon rire assez peu discret que l'on pouvait entendre à l'autre bout du couloir ainsi qu'une température tropicale après allumage du radiateur à fond quand il faisait moins de 25°C dehors.

Collègue pyrolyste/électrochimiste(/loliste ?), je remercie ce très cher Julien Sourice pour nos conversations ô combien intéressantes sur les stratégies à adopter dans la faille de l'Invocateur ... et aussi pour les éclaircissements que tu as pu m'apporter sur SYLVANA et en électrochimie ! Merci aussi d'avoir répondu à mon trèèèèè long mail de 50 questions avant même que je sois acceptée en thèse, j'ai cru comprendre que ça t'avait marqué ! On n'a pas vraiment eu l'occasion de manipuler ensemble et au final, tu as assez rapidement quitté le bureau pour aller t'isoler/t'exiler, seul, dans le « frigo » pour rédiger ton manuscrit. Peut-être avais-tu déjà prédit qu'il te serait impossible de finir ta rédaction dans le temps imparti en restant dans le même bureau que Sarah et moi ! En tout cas, maintenant qu'on est tous les deux diplômés et bien lancés dans le monde de l'électrochimie et du stockage d'énergie, on va peut-être avoir l'occasion de travailler ensemble. Quand est-ce qu'on retourne à la plage ... euh ... à la conférence à Arcachon ?

Mes remerciements vont ensuite à Mlle Bouhadoun, plus connue sous le nom de « Princesse Sarah » ! Pendant près d'un an, tu auras été une voisine de bureau au top, dans lequel tu as su mettre de l'ambiance avec tes régulières sautes d'humeur à cause des manips de pyrolyse laser que tu adorais tant ! Tu m'as aussi beaucoup impressionnée par ta « positive attitude » pendant ta période de rédaction où on a passé pas mal de temps à chercher des synonymes de « en effet », « cependant », « malgré », etc. Je me rappelle aussi du temps qu'on a passé à décorer notre mini sapin de Noël dans le bureau (d'ailleurs, il y est resté plusieurs années !) avec une unique boule de Noël et plein de bouts de papier découpés. Ça devait être le sapin le plus moche qu'on ait jamais vu de notre vie ! Je me rappellerai aussi un bon moment de notre période « Maybe » où on avait toutes les deux totalement craqué quand on lui avait demandé son âge et qu'il nous avait répondu « ça dépend ». En tout cas, merci pour ton soutien pendant ma rédaction et pour les ondes positives que tu m'as envoyées pour ma soutenance alors que tu n'étais même plus ma coloc de bureau. Je te souhaite bon courage pour la suite, tout se passera bien pour toi !

I will switch in English for this paragraph to send many thanks to my former Singaporean colleague Paul Wang, who worked for one year in the lab in France and who helped me a lot then when I came to Singapore. Without your help, I think it would have been really difficult for me to stay and work at NTU. Your assistance was more than a bonus during my PhD. I think I will remember for a long time this evening when you started to taste *limoncello* using a fruit juice glass and I will also remember for a while your unconditional love for cheese. If you came back to France one day, I will be very happy to invite you for a raclette party!

Dans la famille des anciens doctorants qui sont devenus des amis, je demande aussi M. Youri Rousseau ! On peut aussi l'appeler M. Apple ou M. Lexus, ou comme on s'appelle affectueusement,

« bouboule » et « saucisse » ! Youri, co-thésard dont j'ai fait la connaissance dès mon entretien et qui a eu l'amabilité de me faire visiter le sous-sol de la bibliothèque (un lieu incontournable ... ou pas), a été un soutien pendant toute ma thèse, même quand j'étais à 10000 km de là. Si mon séjour à Singapour s'est déroulé un peu mieux, c'est en grande partie grâce à toi Youri. Je me remémore encore nos journées passées au MET, dans le noir et dans le froid, à la recherche des nanoparticules et des coatings de carbone, tout en chantant du Shakira et en tentant vainement d'imiter son déhanché ! Je te remercie aussi d'avoir tenté de partager avec moi une superbe terrine à la Ferme de Dédé à Grenoble... je dis bien « tenté » puisque tu m'as lâchement laissé terminer cette énorme terrine pour pouvoir manger plus de raclette... 200 grammes seulement qu'elle a dit la serveuse c'est ça ? ;) J'en profite par la même occasion pour remercier ta femme, Anaïs Rousseau (je souligne car je sais que c'est un détail important !). Merci à toi Anaïs d'avoir été présente durant ma thèse mais aussi en tant que super amie et cosplayeuse qui a accepté et accepte encore de me suivre dans mes projets tous plus fous les uns que les autres.

Après les anciens doctorants et anciens voisins de bureau, je remercie les nouveaux doctorants qui ont été mes nouveaux voisins pendant mes derniers mois de thèse : Antoine Desrues et Raphaëlle Belchi. Au final, je ne vous ai pas côtoyés très longtemps mais je vous remercie tous deux de votre soutien pendant ma troisième année. Je vous souhaite bon courage pour la suite de votre doctorat, vous en aurez bien besoin pour arriver à dompter SYLVANA ! J'aimerais aussi en profiter pour remercier Florent, un collègue très discret mais avec qui on finit par avoir des discussions très sympas quand on prend le temps de le connaître.

Merci aussi à Nathalie, Dominique, Amandine et tous les collègues du LEDNA que je n'ai pas cités au-dessus, les permanents et non-permanents, les anciens et nouveaux doctorants, post-doctorants, apprentis et stagiaires que j'ai pu côtoyer plus ou moins longtemps durant ma thèse.

Après les anciens collègues et amis, passons aux nouveaux ! Merci à tous mes collègues de Zinium qui m'ont donné le courage d'affronter cette soutenance de thèse et les derniers déboires administratifs en m'envoyant leurs ondes positives. Merci aussi à eux d'instaurer une ambiance géniale dans ce nouveau travail, ce qui a grandement contribué à me permettre de terminer plus sereinement ma thèse. Alors à Antoine, Lorna, Adrien, Fabien, Rémi, Julien, Louis, je vous dis merci et j'espère vraiment qu'on restera une équipe aussi soudée un bon moment encore !

Mes remerciements vont aussi à mes amis qui sont venus me faire coucou à Singapour pendant quelques jours ou quelques semaines : Mehdi, Mégane, Céline, Eve et Denis. Je tiens aussi à remercier Lauren, Amira, Alice et Guillaume, d'autres étudiants Français rencontrés à Singapour et qui ont permis de rendre ce séjour un peu plus sympathique.

Je termine en remerciant ma famille, plus particulièrement mes parents et ma sœur qui ont été des soutiens durant toute la période de ma thèse, bien avant, et même encore maintenant. De même, je souhaite remercier Steven, qui m'a accompagnée et soutenue dans mes choix durant toutes mes années d'études depuis le lycée.

---

## Table of contents

---

Table of contents.....	3
List of figures .....	5
List of tables .....	11
List of abbreviations.....	13
Introduction.....	15
References .....	19
<b>Chapter 1.    Literature review .....</b>	<b>21</b>
I.    Presentation of the lithium-ion technology .....	22
1.    History and basic principles of the lithium-ion battery .....	22
2.    Categories of anode materials depending on the lithium storage mechanism.....	27
II.    Transition metal oxides as anode materials for Li-ion batteries .....	33
1.    Examples of $M_xO_n$ oxides .....	33
2.    Interest of mixed-transition metal oxides (MTMO) .....	37
3.    Optimization of the material performances .....	44
III.    Experimental methods for the synthesis of nanostructured mixed-transition metal oxides .....	53
1.    Solid-state syntheses .....	53
2.    Liquid phase syntheses .....	54
3.    Vapor phase syntheses .....	56
IV.    Laser pyrolysis for the synthesis of nanopowders .....	61
V.    Intermediate conclusion .....	64
References .....	65
<b>Chapter 2.    Experimental protocols.....</b>	<b>71</b>
I.    Description of a synthesis by laser pyrolysis .....	72
1.    Experimental set-up.....	72
2.    Influence of the experimental parameters .....	76
3.    Typical conduct of a synthesis.....	78
II.    Characterization of laser-pyrolysed samples: structural properties .....	81
1.    X-ray powder diffraction (XRD) .....	81
2.    Scanning electron microscopy (SEM) and energy dispersive x-ray spectrometry (EDS).....	81

3.	Transmission electron microscopy (TEM) and high-resolution transmission electron microscopy (HRTEM) .....	81
4.	Thermo-gravimetric analysis (TGA).....	82
5.	Brunauer-emmett-teller (BET).....	82
6.	Mössbauer <sup>57</sup> Fe.....	82
III.	Characterization of laser-pyrolysed samples: electrochemical properties .....	84
1.	Coin cells preparation .....	84
2.	Galvanostatic cycling.....	85
3.	Cyclic voltammetry .....	88
4.	Operando measurements.....	89
<b>Chapter 3.</b>	<b>Syntheses by laser pyrolysis of zinc iron oxides.....</b>	<b>91</b>
I.	Synthesis of zinc iron oxide nanopowders .....	92
1.	Nitrates precursors .....	93
2.	Chlorides precursors .....	107
II.	Synthesis of iron oxide nanopowders .....	113
III.	Synthesis of zinc oxide nanopowders .....	118
IV.	General discussion on nitrate precursors and laser assisted flame synthesis.....	122
V.	Thermal treatment of the samples before electrochemical tests.....	125
VI.	Intermediate conclusion .....	127
	References .....	128
<b>Chapter 4.</b>	<b>Evaluation of the electrochemical performances of ZnFe<sub>2</sub>O<sub>4</sub>, ZnO and Fe<sub>2</sub>O<sub>3</sub>.....</b>	<b>129</b>
I.	Choice of the electrode formulation and of the electrolyte .....	130
II.	Electrochemical performances of ZnFe <sub>2</sub> O <sub>4</sub> nanopowders .....	134
1.	Influence of the morphology of ZnFe <sub>2</sub> O <sub>4</sub> nanoparticles.....	134
2.	Investigation of the lithium storage mechanism.....	149
III.	Electrochemical performances of ZnO and Fe <sub>2</sub> O <sub>3</sub> .....	164
1.	Electrochemical performances of ZnO, Fe <sub>2</sub> O <sub>3</sub> and ZnO/Fe <sub>2</sub> O <sub>3</sub> mixture.....	164
2.	Understanding of the lithium storage mechanism .....	171
IV.	Intermediate conclusion .....	175
	References .....	176
	Conclusions and recommendations for future works.....	179
	Appendix.....	185

---

## List of figures

---

Figure 1. Evolution of greenhouse gases emissions from 1970 to 2010 <sup>3</sup> .....	15
Figure 2. CO <sub>2</sub> emissions from fossil fuel combustion by sector and fuel type (2006) <sup>5</sup> .....	16
Figure 3. Hourly supply and demand in energy <sup>6</sup> .....	17
Figure 1.1. Schematic diagram of (a) a redox reaction, (b) a primary (non-rechargeable) battery upon discharging and (c) a secondary (rechargeable) battery upon charging <sup>3</sup> .....	23
Figure 1.2. Comparison of the energy and power densities for different energy storage technologies <sup>4</sup> .....	24
Figure 1.3. Different technologies of batteries with their gravimetric and volumetric energy density <sup>6</sup> .....	24
Figure 1.4. Rechargeable Li-metal battery (the picture of the dendrite growth at the Li surface was obtained directly from in-situ scanning electron microscopy measurements) <sup>5</sup> .....	25
Figure 1.5. Charge/discharge process for a commercial lithium-ion battery <sup>14</sup> .....	26
Figure 1.6. Insertion of lithium ions between graphite layers <sup>19</sup> .....	28
Figure 1.7. Examples of alloying materials and their theoretical capacity <sup>12</sup> .....	29
Figure 1.8. SEI formation on silicon surface during lithiation and delithiation process <sup>27</sup> .....	30
Figure 1.9. In-situ HREM of lithiation of Co <sub>3</sub> O <sub>4</sub> showing the insertion, amorphization and reduction processes <sup>35</sup> .....	31
Figure 1.10. Different categories of positive and negative electrode materials with their theoretical working voltage vs. Li/Li <sup>+</sup> and their specific capacities <sup>62</sup> .....	36
Figure 1.11. Spinel structure AB <sub>2</sub> O <sub>4</sub> <sup>72</sup> .....	38
Figure 1.12. Cyclic voltamograms of the ZnFe <sub>2</sub> O <sub>4</sub> electrode at a scan rate of 0.1 mV/s in the voltage range of 0.01V-3.0V vs. Li/Li <sup>+81</sup> .....	41
Figure 1.13. First charge and discharge profiles for ZnFe <sub>2</sub> O <sub>4</sub> in the voltage range of 0.01-3.0V <sup>79</sup> .....	42
Figure 1.14. Ex-situ XRD at different steps of the first discharge for ZnFe <sub>2</sub> O <sub>4</sub> <sup>80</sup> .....	43
Figure 1.15. Ex-situ HRTEM after a full discharge and its corresponding SAED <sup>81</sup> .....	43
Figure 1.16. Strategies to enhance electrode performances <sup>18</sup> .....	45
Figure 1.17. Nanostructuring of the active material to sustain the volumetric expansion during cycling <sup>85</sup> .....	46
Figure 1.18. Morphology of the yolk-shell structure observed by TEM (a,b) and electrochemical performances of yolk-shell and spherical ZnFe <sub>2</sub> O <sub>4</sub> nanoparticles at 500 mA.g <sup>-1</sup> (c).....	47
Figure 1.19. Morphology of the nanorods (a) and nanofibers (b) observed by SEM and comparison of performances during cyclings at 60 mA.g <sup>-1</sup> (c).....	48

Figure 1.20. TEM image of ZnFe <sub>2</sub> O <sub>4</sub> /C nanocomposite (a) and comparison of the electrochemical performance with pure ZnFe <sub>2</sub> O <sub>4</sub> at C/10 current rate (b).....	49
Figure 1.21. SEM images of ZnFe <sub>2</sub> O <sub>4</sub> particles (a) and ZnFe <sub>2</sub> O <sub>4</sub> /graphite (b). Comparison of electrochemical performances of ZnFe <sub>2</sub> O <sub>4</sub> and ZnFe <sub>2</sub> O <sub>4</sub> /graphite at 100 mA.g <sup>-1</sup> (c) .....	50
Figure 1.22. TEM images of pure ZnFe <sub>2</sub> O <sub>4</sub> nanoparticles (a) and ZnFe <sub>2</sub> O <sub>4</sub> /graphene (b). Comparison of performances between pure ZnFe <sub>2</sub> O <sub>4</sub> and ZnFe <sub>2</sub> O <sub>4</sub> /graphene composite at 100 mA.g <sup>-1</sup> .....	51
Figure 1.23. Morphology of ZnFe <sub>2</sub> O <sub>4</sub> /C nanodiscs observed by TEM (a) and HRTEM (b) and comparison of performances with ZnFe <sub>2</sub> O <sub>4</sub> (c).....	52
Figure 1.24 Different mechanical routes for the syntheses of nanocrystalline ferrites <sup>92</sup> .....	53
Figure 1.25. (a) ZnFe <sub>2</sub> O <sub>4</sub> nano-octahedrons obtained by hydrothermal synthesis (T: 180° for 14h) <sup>81</sup> , (b) MnCo <sub>2</sub> O <sub>4</sub> spherical nanoparticles obtained by hydrothermal synthesis (T: 180°C, 8h) <sup>94</sup> .....	54
Figure 1.26. Synthesis of nanomaterials by the sol-gel method <sup>95</sup> .....	55
Figure 1.27. SEM images of ZnFe <sub>2</sub> O <sub>4</sub> and NiFe <sub>2</sub> O <sub>4</sub> nanoparticles obtained by the sol-gel method.....	55
Figure 1.28. Schema of the spray pyrolysis process <sup>101</sup> .....	56
Figure 1.29. Different steps of grains formation in spray pyrolysis: solvent vaporization, precipitation, solid state precursors reaction, sintering <sup>102</sup> .....	57
Figure 1.30. Formation mechanism of ZnCo <sub>2</sub> O <sub>4</sub> nanostructures <sup>78</sup> .....	58
Figure 1.31. Different types of aerosol flame synthesis processes <sup>103</sup> .....	59
Figure 1.32. Laser pyrolysis experimental setup .....	61
Figure 1.33. Pyrolysis flame of silicon nanoparticles using silane precursor.....	62
Figure 1.34. a) TEM image of TiO <sub>2</sub> nanoparticles <sup>122</sup> , b) SEM image of SiC nanoparticles <sup>121</sup> .....	62
Figure 2.1 Scheme of the laser pyrolysis experimental set-up .....	72
Figure 2.2. Focusing of the laser beam with a cylindrical lens (f = 50 cm) .....	73
Figure 2.3. Schemes of the two aerosol generators used for the synthesis of zinc iron oxide .....	74
Figure 2.4. Porous filter for the collection of nanopowders in a glass collector .....	76
Figure 2.5. Examples of pyrolysis flames; a: before sending the aerosol, the flame is not very intense; b: with the aerosol, a long and brilliant flame can be observed .....	80
Figure 2.6. Half-cell assembly vs. metallic lithium .....	85
Figure 2.7. Current vs. time curves for galvanostatic cyclings measurements .....	86
Figure 2.8. Charge and discharge profiles. V <sub>1</sub> : discharge cut-off potential, V <sub>2</sub> : charge cut-off potential. ....	86
Figure 2.9. Voltage vs. time curves for cyclic voltammetry measurements.....	88
Figure 2.10. Cyclic voltammetry curves to identify the oxidation and reduction peaks: intensity vs. voltage .....	88
Figure 2.11. Composition of the electrode for each characterization technique .....	89

Figure 2.12. Diagram of the in-situ cell (left), photography of an assembled in-situ cell (right).....	90
Figure 3.1. Laser pyrolysis flame of ethylene, argon and nitrates precursors without air .....	93
Figure 3.2. TGA measurements for ZFO-1 and ZFO-2 from 20°C to 500°C, ramp: 20°C/min and isothermal step of 1h at 500°C .....	94
Figure 3.3. XRD patterns for ZFO-1 and ZFO-2. ZFO-1: pure ZnFe <sub>2</sub> O <sub>4</sub> phase. ZFO-2 presents ZnFe <sub>2</sub> O <sub>4</sub> phase with traces of non-stoichiometric zinc iron oxides phase .....	96
Figure 3.4. SEM (a) and TEM images (b,c) of ZFO-1: presence of both small nanoparticles (< 10 nm) with larger particles (> 50 nm to hundreds of nm) .....	97
Figure 3.5. <sup>57</sup> Fe Mössbauer spectrum of the pristine ZFO-1 sample measured at room temperature. Three phases are observed: ZnFe <sub>2</sub> O <sub>4</sub> (45% at.), γ-Fe <sub>2</sub> O <sub>3</sub> (52% at.) and a minor iron phase (3% at.). .....	98
Figure 3.6. (a) Flame of air and ethylene and (b) flame of air, ethylene and precursors.....	100
Figure 3.7. TGA measurements for ZFO-3 from 40°C to 400°C, ramp: 10°C/min and isothermal of 50 min at 400°C .....	100
Figure 3.8. XRD pattern for ZFO-3: presence of ZnFe <sub>2</sub> O <sub>4</sub> and iron oxide phase.....	101
Figure 3.9. <sup>57</sup> Fe Mössbauer spectrum for ZFO-3 measured at room temperature. Presence of two phases: 65% at. of ZnFe <sub>2</sub> O <sub>4</sub> and 35% at. of γ-Fe <sub>2</sub> O <sub>3</sub> .....	102
Figure 3.10. Morphology of ZFO-3 sample observed by TEM (a,b).....	103
Figure 3.11. HRTEM images of ZFO-3. Interplanar distances corresponding to Fe <sub>2</sub> O <sub>3</sub> maghemite phase (left) and to ZnFe <sub>2</sub> O <sub>4</sub> phase (right) .....	103
Figure 3.12. XRD pattern for ZFO-4: presence of ZnFe <sub>2</sub> O <sub>4</sub> and Fe <sub>0.94</sub> C <sub>0.06</sub> phases .....	105
Figure 3.13. TGA measurements for ZFO-4 from 20°C to 500°C, ramp: 10°C/min, isothermal of 1h at 500°C .....	106
Figure 3.14. TEM images of ZFO-4 (a,b).....	106
Figure 3.15. XRD pattern for ZFO-5 and ZFO-6: presence of ZnFe <sub>2</sub> O <sub>4</sub> in both samples, additional Fe phase for ZFO-6 .....	108
Figure 3.16. Images of ZFO-5 observed by TEM: presence of only small nanoparticles (< 10 nm) embedded in an amorphous matrix .....	109
Figure 3.17. TGA measurements for ZFO-5 from 20°C to 400°C, ramp at 20°C/min with an isothermal at 400°C for 40 min.....	110
Figure 3.18. Morphology of ZFO-6 observed by TEM (left) and highlighting of graphite around the nanoparticles .....	110
Figure 3.19. TGA measurements for ZFO-6 from 20°C to 500°C with an isothermal at 300°C and at 500°C .....	111
Figure 3.20. XRD patterns for FeOx-1 and FeOx-2 .....	114

Figure 3.21. TEM images of FeOx-1 and FeOx-2 showing a bimodal size population due to iron nitrate precursor .....	115
Figure 3.22. XRD patterns of FeOx-3 and FeOx-4.....	116
Figure 3.23. Mössbauer spectroscopy realized at room temperature confirms the presence of the maghemite phase only in FeOx-4 .....	116
Figure 3.24. Observation of FeOx-3 (a) and FeOx-4 (b) morphologies by TEM.....	117
Figure 3.25. XRD patterns for ZnOx-1 and ZnOx-2 revealing a ZnO crystalline phase for both samples .....	119
Figure 3.26. SEM and TEM images of ZnOx-1 (a,b) and ZnOx-2 (c,d).....	120
Figure 3.27. TGA measurements on ZnOx-2 from 50°C to 500°C, ramp of 20°C/min and isotherm at 500°C during 40 min .....	121
Figure 3.28. Possible growth processes during laser pyrolysis conducting to a bimodal particle size distribution .....	123
Figure 3.29. TEM images of ZFO-5, ZnOx-2 and FeOx-4 before (a,b,c, respectively) and after annealing under air at 350 °C (d,e,f, respectively) .....	125
Figure 4.1. Galvanostatic cyclings at 100 mA.g <sup>-1</sup> for ZFO-2 using four different combinations of electrolyte and electrode formulation.....	131
Figure 4.2. Reversible capacity retention and cumulative irreversible capacity for C1, C2, C3 and C4 samples.....	132
Figure 4.3. Galvanostatic cyclings at 100 mA.g <sup>-1</sup> for ZFO-1 and ZFO-5: charge/discharge capacity plots (a, c) and cumulative irreversible capacity plots (b, d).....	134
Figure 4.4. Charge/discharge profiles (a, c) and dQ/dV curves (b, d) for ZFO-1 and ZFO-5 galvanostatic cyclings at 100 mA.g <sup>-1</sup> between 0.01 V and 3.0 V .....	135
Figure 4.5. Discharge capacity contribution from each region (a, c) and evolution of the polarization (b, d) for ZFO-1 and ZFO-5 cyclings at 100 mA.g <sup>-1</sup> between 0.01 V and 3.0 V.....	137
Figure 4.6. Galvanostatic cyclings at 1000 mA.g <sup>-1</sup> for ZFO-1 and ZFO-5: charge/discharge capacity plots (a, c) and cumulative irreversible capacity plots (b, d).....	138
Figure 4.7. Charge/discharge profiles (a, c) and dQ/dV curves (b, d) for ZFO-1 and ZFO-5 galvanostatic cyclings at 100 mA.g <sup>-1</sup> between 0.01 V and 3.0 V .....	139
Figure 4.8. Discharge capacity contribution from each region (a, c) and evolution of the polarization (b, d) for ZFO-1 and ZFO-5 cyclings at 1000 mA.g <sup>-1</sup> between 0.01 V and 3.0 V.....	140
Figure 4.9. Formation of the SEI around iron oxides depending on different particles morphologies <sup>18</sup> .....	141
Figure 4.10. Galvanostatic cyclings at 500, 2000 and 4000 mA.g <sup>-1</sup> for ZFO-1 and ZFO-5: charge/discharge capacity plots (a, c, e) and cumulative irreversible capacity plots (b, d, f) .....	143

Figure 4.11. Charge/discharge profiles (a, c, e) and dQ/dV curves (b, d, f) for ZFO-1 galvanostatic cyclings at 500, 2000 and 4000 mA.g <sup>-1</sup> between 0.01 V and 3.0 V .....	145
Figure 4.12. Discharge capacity contribution from each region (a, c, e) and evolution of the polarization (b, d, f) for ZFO-1 cyclings at 500, 2000 and 4000 mA.g <sup>-1</sup> between 0.01 V and 3.0 V .....	146
Figure 4.13. Evolution of the polarization and of the resistance at the 100 <sup>th</sup> cycle depending on the current rate for ZFO-1.....	147
Figure 4.14. Rate capability between 0.01 V and 3.0 V from C/5 to 4C.....	148
Figure 4.15. Cyclic voltammetry of ZFO-1 for the five first cycles, between 0.01 V and 3.0 V at 0.1 mV.s <sup>-1</sup> scan rate .....	149
Figure 4.16. Operando X-ray diffraction for the first lithiation of ZFO-1 between 0.01 V and 3.0 V at 5.6 mA.g <sup>-1</sup> .....	150
Figure 4.17. Operando <sup>57</sup> Fe Mössbauer spectra measured during the first one and a half cycle (discharge/charge/discharge). The horizontal dotted lines represent the end of the different processes. The step between spectra 13 and 14 corresponds to the reduction of the velocity range from -14 – +14 to -4 – +4 mm/s.....	151
Figure 4.18. Electrochemical signature of the operando cell and corresponding Mössbauer spectra. The red line corresponds to a region where no spectra could be measured due to technical issues (between spectra #42 and #43). The velocity range was reduced starting from spectrum #14..	152
Figure 4.19. Variance plot (top left), principal components (top right) and evolution of the scores (bottom) during the first 13 Mössbauer spectra of the first discharge measured in the velocity range -14 – +14.....	153
Figure 4.20. MCR-ALS components (left) and their evolution (right) during the first 13 Mössbauer spectra of the first discharge measured in the velocity range -14 – +14 mm/s.....	154
Figure 4.21. Variance plot (top left), principal components (top right) and evolution of the scores (bottom) during the 101 Mössbauer spectra of the operando experiment measured in the velocity range -4 – +4 mm/s. ....	155
Figure 4.22. MCR-ALS components (left) and their evolution (right) during the collection of the 101 Mössbauer spectra of the operando experiment measured in the velocity range -4 – +4 mm/s.	156
Figure 4.23. MCR-ALS components (left) and their evolution (right) during the whole operando Mössbauer experiment.....	156
Figure 4.24. Fitting of the first component obtained by the MCR-ALS analysis of the first 13 Mössbauer spectra of the first discharge measured in the velocity range -14 – +14 mm/s.....	157
Figure 4.25. Fitting of the second (left) and the third (right) component obtained by the MCR-ALS analysis of the Mössbauer spectra measured in the velocity range -14 – +14 mm/s (top), and of	

the first (left) and third (right) component obtained by the MCR-ALS analysis of the spectra measured in the velocity range -4 – +4 mm/s (bottom) .....	158
Figure 4.26. Fitting of the second component obtained by the MCR-ALS analysis of the Mössbauer spectra measured in the velocity range -4 – +4 mm/s.....	160
Figure 4.27. Average oxidation state of the iron during cycling obtained from the weighted relative resonance areas of the MCR-ALS components. ....	161
Figure 4.28. Galvanostatic cyclings at 100 mA.g <sup>-1</sup> for ZnO, Fe <sub>2</sub> O <sub>3</sub> and ZnO/Fe <sub>2</sub> O <sub>3</sub> mixture: charge/discharge capacity plots (a, c, e) and cumulative irreversible capacity plots (b, d, f) .....	164
Figure 4.29. Charge/discharge profiles (a), dQ/dV curves (b, c) and polarization (d) for ZnO cycled at 100 mA.g <sup>-1</sup> .....	166
Figure 4.30. Charge/discharge profiles (a), dQ/dV curves (b) and polarization (c) for Fe <sub>2</sub> O <sub>3</sub> cycled at 100 mA.g <sup>-1</sup> .....	167
Figure 4.31. Charge/discharge profiles (a), dQ/dV curves (b, c) and polarization (d) for ZnO/Fe <sub>2</sub> O <sub>3</sub> cycled at 100 mA.g <sup>-1</sup> .....	168
Figure 4.32. Cyclic voltamograms for ZnO, Fe <sub>2</sub> O <sub>3</sub> , ZnO/Fe <sub>2</sub> O <sub>3</sub> and ZnFe <sub>2</sub> O <sub>4</sub> (ZFO-1) at a scan rate of 0.01 mV.s <sup>-1</sup> .....	170
Figure 4.33. Operando XRD during the first lithiation of ZnO/Fe <sub>2</sub> O <sub>3</sub> between 0.01 V and 3.0 V.....	172
Figure 5.1. Cycling of ZnFe <sub>2</sub> O <sub>4</sub> /C with different carbon ratios at 100 and 1000 mA.g <sup>-1</sup> .....	182

---

## List of tables

---

Table 1.1. Electrochemical performances of some CoO anode for lithium-ion batteries .....	34
Table 1.2. Electrochemical performances of some Co <sub>3</sub> O <sub>4</sub> anode for lithium-ion batteries .....	34
Table 1.3. Electrochemical performances of some Fe <sub>2</sub> O <sub>3</sub> anode for lithium-ion batteries .....	35
Table 1.4. Electrochemical performances of some Fe <sub>3</sub> O <sub>4</sub> anodes for lithium-ion batteries .....	36
Table 1.5. Theoretical capacity of several TMO and MTMO .....	37
Table 1.6. Experimental working voltages vs. Li/Li <sup>+</sup> depending on the MTMO .....	38
Table 1.7. Electrochemical performances of various mixed-transition metal oxides .....	39
Table 1.8. Examples of ZnFe <sub>2</sub> O <sub>4</sub> electrochemical performances as anode for lithium-ion batteries .....	43
Table 3.1. List of precursors solutions used for the synthesis of zinc iron oxide nanopowders .....	92
Table 3.2. Experimental conditions for the syntheses of ZFO-1 and ZFO-2 using nitrates solutions and the PALAS generator .....	93
Table 3.3. Experimental conditions for the syntheses of ZFO-3 and ZFO-4 under air using nitrates solutions .....	99
Table 3.4. Fitted parameters for Mössbauer measurements .....	102
Table 3.5. Experimental conditions for the syntheses of ZFO-5 and ZFO-6 under air using chlorides solutions .....	108
Table 3.6. Solutions of precursors used for the synthesis of iron oxide nanopowders .....	113
Table 3.7. Experimental conditions for the synthesis of FeOx-1 and FeOx-2 using a nitrate precursor solution .....	113
Table 3.8. Synthesis conditions for the production of FeOx-3 (chloride precursor) and FeOx-4 (acetylacetonate precursor) .....	115
Table 3.9. Solutions of precursors used for the synthesis of ZnO nanoparticles .....	118
Table 3.10. Experimental conditions for the synthesis of ZnOx-1 and ZnOx-2 .....	118
Table 3.11. Summary of the different samples used for electrochemical tests .....	126
Table 4.1. Electrode formulations and electrolytes for coin cells preparation .....	130
Table 4.2. Performances of some ZnFe <sub>2</sub> O <sub>4</sub> powders in the literature .....	143
Table 4.3. Hyperfine parameters obtained by the fitting of the second and third component obtained by the MCR-ALS analysis of the Mössbauer spectra measured in the velocity range -14 – +14 mm/s, and of the first and third component obtained by the MCR-ALS analysis of the spectra measured in the velocity range -4 – +4 mm/s .....	160



---

## List of abbreviations

---

AFS	Aerosol Flame Synthesis
BET	Brunauer-Emmett-Teller
CB	Carbon black
CMC	Carboxymethylcellulose
DMC	Dimethyl carbonate
EC	Ethylene carbonate
EDS	Energy Dispersive X-ray Spectrometry
FASP	Flame-Assisted Spray Pyrolysis
FSP	Flame Spray Pyrolysis
GHG	Greenhouse Gas
LIB	Lithium-Ion Battery
MTMO	Mixed-Transition Metal Oxide
Ni-Cd	Nickel-Cadmium
NiMH	Nickel-Metal Hydride
PC	Polycarbonate
SEI	Solid Electrolyte Interphase
SEM	Scanning Electron Microscopy
(HR)TEM	(High-Resolution) Transmission Electron Microscopy
TGA	Thermo-Gravimetric Analysis
TMO	Transition Metal Oxide
VFAFS	Vapor-Fed Aerosol Flame Synthesis
VGCF	Vapor-Grown Carbon Fiber
XRD	X-Ray Diffraction



---

## Introduction

---

Many scientific and technological progress have been realized since the industrial revolution in the 19<sup>th</sup> century. This progress has globally led to an increase in the energy demand with a massive growth from the middle of the 20<sup>th</sup> century. Since this period, the world energy consumption has never stopped its fast increase and with the continuous growth of the world population, ensuring everyone's needs in energy becomes a real challenge<sup>1</sup>.

For several decades, more than 80% of the world produced energy has come from the combustion of fossil fuels as coal, oil and gas, the other 20% corresponding to alternative energies as nuclear power and renewable energies (only 1% attributed to wind and solar energy in 2012)<sup>2</sup>. Unfortunately, the massive exploitation of fossil fuels tends to be problematic in the near future.

Indeed, the known and accessible reserves of fossil fuels are predicted to be completely depleted in less than a century assuming that the global energy consumption stays stable in the next decades. Even if other non-exploited areas exist, their exploitation is generally more difficult and expensive and they are still limited. Moreover, the over exploitation of fossil fuels does not only have economic implications. The amount of greenhouse gases (GHG) in the atmosphere, and in particular CO<sub>2</sub>, has increased since the 1950's, primarily because of the combustion of fossil fuels (Figure 1). According to the Intergovernmental Panel on Climate Change (IPCC), the increase of GHG in the atmosphere is very probably the main cause of the global warming observed since 1880 (+0.8°C on average according to NASA scientists)<sup>3</sup>.

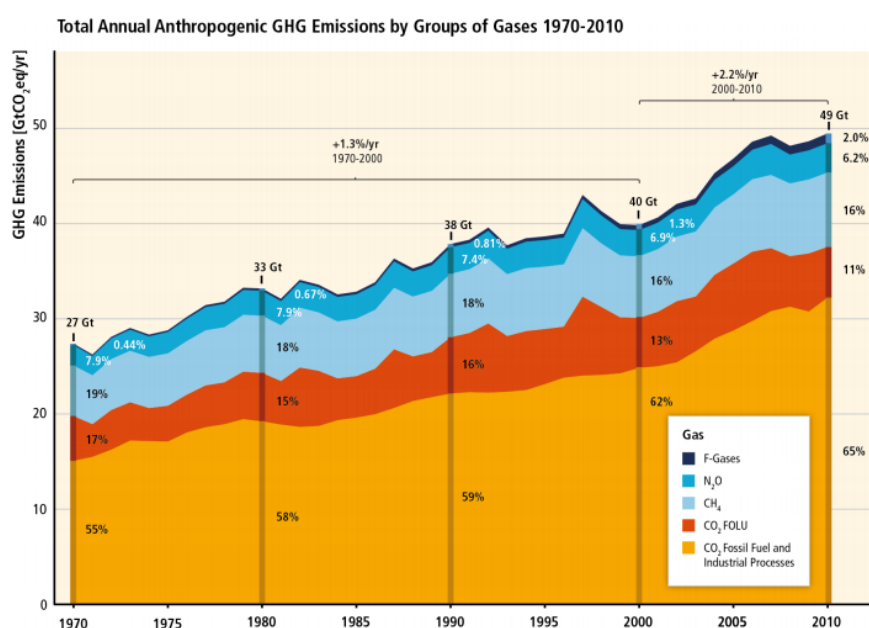


Figure 1. Evolution of greenhouse gases emissions from 1970 to 2010<sup>3</sup>

Since the awareness of these issues by the international community, the Kyoto protocol was adopted in 1997 with the main objective to reduce by 5% the GHG emissions between 2008 and 2012, compared to the level in 1990<sup>4</sup>. However, several scenarios have been predicted by scientists concerning the global warming, starting from an increase of the global temperature of 0.9°C for the most optimistic scenario and of 5.4°C for the most pessimistic one at the end of the 21<sup>st</sup> century. If the GHG emissions follow the same trend as today, an increase of the Earth surface temperature around 4°C is expected<sup>3</sup>. This climate change is already starting to disrupt the ecosystem: melting ice, rising of seas, vanishing of species, air pollution. Such consequences may have a large impact on populations in the near future with health problems as well as migrations due to the change of the environment.

In 2015, the Paris agreement was adopted by 195 countries with the main objective to limit the increase of the average Earth temperature up to 2°C. The United States Environmental Protection Agency data gives an idea of the contribution of each sector in GHG emissions coming from fossil fuel combustions for industrial countries (Figure 2). A large part of the fossil fuels consumption goes to electricity generation and transportation, making the quest of alternative energy sources in these two domains a major challenge to tackle<sup>5</sup>.

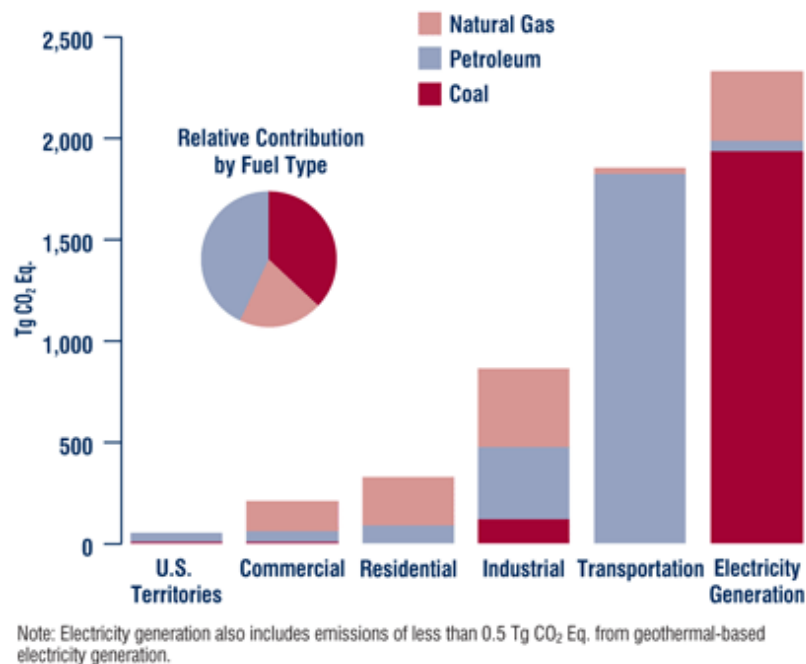


Figure 2. CO<sub>2</sub> emissions from fossil fuel combustion by sector and fuel type (2006)<sup>5</sup>

In this context, the development of new systems for energy production based on the exploitation of solar or wind energy as well as the democratization of electric vehicles in place of combustion engines would limit our dependency on fossil fuels. However, solar and wind are

intermittent energy sources, thus the development of energy storage technologies is necessary<sup>6</sup> (Figure 3). As well, efficient energy storage devices are needed for the development of electric transports.

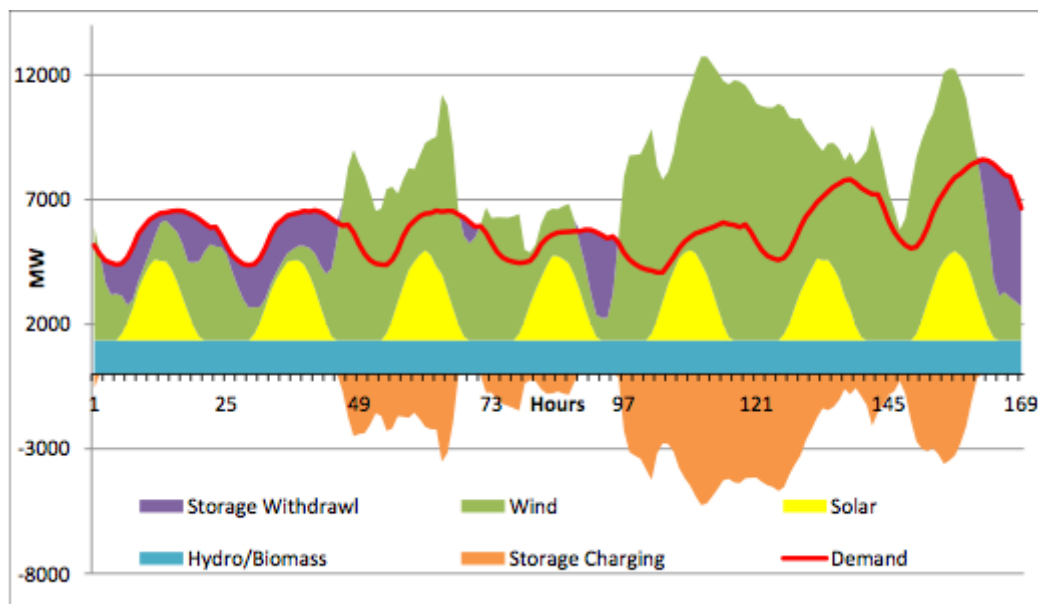


Figure 3. Hourly supply and demand in energy<sup>6</sup>

One of the most common energy storage technologies used nowadays is the lithium-ion battery (LIB). This technology is well implemented for portable electronic devices but suffers from low energy density, safety, cost, cycle life and power density for next-generation large scale applications in electric vehicles and renewable energy storage applications. Advanced electrodes (anode/cathode) and electrolyte materials are necessary to address these challenges of LIB for next generation applications. Research worldwide is focussing on several aspects of improving the energy density of the cathode materials by moving towards higher voltages or newer modified materials. In this thesis we focus on the anode part of the LIB.

Presently, graphite is widely used anode for commercial LIB with a moderate specific capacity ( $372 \text{ mAh.g}^{-1}$ ). The use of graphite induces safety issues due to its very low working voltage vs.  $\text{Li/Li}^+$  (0.15-0.25 V) that favours lithium plating at fast charging<sup>7</sup>. In addition, recent studies on high voltage cathode based on spinel  $\text{LiNi}_{0.5}\text{Mn}_{1.5}\text{O}_4$  and graphite have shown that the electrochemical behaviour of graphite when coupled with high voltage cathodes are not optimal<sup>8</sup>. Hence there is a need for alternative anode material that can in future replace graphite to address these challenges not only in terms of higher specific capacity (note: presently in terms of the specific capacity the cathode is the limiting factor in the cell) but also in terms of safety and moving towards newer high voltage cathodes.

Among various candidates, conversion-based materials, especially binary oxides ( $A_3O_4$  and  $A_2O_3$ ,  $A$  = transition metal), like  $Fe_2O_3$  or  $Co_3O_4$  have been the object of intense research for several years owing to their high theoretical capacity (between 800 and 1100  $\text{mAh}\cdot\text{g}^{-1}$ ). This high capacity is counterbalanced by a high working voltage vs.  $\text{Li}/\text{Li}^+$ , interesting from a safety point of view to avoid lithium plating but that limits the energy density<sup>9</sup> and requires the development of dedicated electrolytes and cathode materials to replace the ones used with graphite. This high capacity is also combined to a volumetric expansion of the material during lithiation leading to the pulverization of the electrode during long-term cycling<sup>10</sup>. Nevertheless, recent works about two ternary oxides like  $\text{ZnFe}_2\text{O}_4$  or  $\text{ZnCo}_2\text{O}_4$  show advantages compared to binary oxides. Indeed, these mixed-transition metal oxides offer the possibility to tune their working voltage<sup>11</sup> by choosing their chemical composition while keeping high specific capacities.

Particularly,  $\text{ZnFe}_2\text{O}_4$  delivers a high theoretical capacity of 1001  $\text{mAh}\cdot\text{g}^{-1}$  at a relatively low working voltage compared to other oxides (1.5 V vs.  $\text{Li}/\text{Li}^+$ ). Moreover, as a cheap, abundant, non-toxic and environment-friendly material, it is more interesting than other metal oxides Co-based ones for instance. To enhance the performances of the material and hinder the drawbacks of volumetric expansion in terms of electrode durability, it is interesting to address nanostructured electrodes using  $\text{ZnFe}_2\text{O}_4$  nanoparticles. Indeed, a higher surface area and a smaller grain size provide more contact between the electrode material and the electrolyte and could also enable faster kinetics for lithium, while ensuring a better mechanical stability, as it will be detailed later. On the contrary, such increase of specific surface could also show deleterious effects by enhancing electrolyte degradation at the electrode surface. Thus the behaviour of nanostructured  $\text{ZnFe}_2\text{O}_4$  electrodes appears worth studying in order to appreciate which of the beneficial or deleterious effects are predominant. Moreover, as  $\text{ZnFe}_2\text{O}_4$  is known to be decomposed into  $\text{ZnO}$  and  $\text{Fe}_2\text{O}_3$  after the first cycle<sup>12</sup>, a comparison between  $\text{ZnFe}_2\text{O}_4$  and a mixture of  $\text{ZnO}$  and  $\text{Fe}_2\text{O}_3$  remains to be achieved in order to highlight a potential advantage of the ternary phase.

To lead such a study,  $\text{ZnFe}_2\text{O}_4$  nanoparticles, as well as  $\text{ZnO}$  and  $\text{Fe}_2\text{O}_3$  ones, have to be synthesized. Laser pyrolysis is a versatile and up-scalable gas phase process that allows the one step, continuous production of crystalline nanoparticles with controlled chemical composition, size and morphologies. This process was used for the first time for the development of the materials reported in this document, and the synthesis part invests a large amount of the experimental work.

As a conclusion, this thesis is divided into two main parts. The first one deals with the development of the different required oxides nanomaterials by laser pyrolysis, while the second one is dedicated to the study of their performances for Li storage and to the related mechanisms. Beyond

the investigation of  $\text{ZnFe}_2\text{O}_4$  by itself, the aim is to provide information about the interest of nanomaterials for battery application. As a consequence, the manuscript is presented with the following 4 chapters.

The first chapter is dedicated to the literature study and reviews first the state-of-art for lithium-ion batteries. It details the different categories of anode materials and more particularly the storage mechanisms and the performances of transition metal oxides (conventional or nanostructured) as well as their limitations. Different nanoparticles synthesis methods with their advantages and drawbacks are then presented in order to highlight the interest of laser pyrolysis.

The experimental details and protocols are presented in chapter 2. More specifically, the laser pyrolysis process is explained in details. The different techniques, samples preparation and analysis protocols for the structural characterizations of the produced nanopowders as well as for the evaluation of their electrochemical properties and performances are then described.

The different ternary and binary oxide nanopowders samples obtained by laser pyrolysis are presented in chapter 3. The influence of the experimental parameters (nature of the carrier gas, solvent, precursors) on the produced powders in terms of crystallinity and morphology are discussed in this part. The main structural characteristics are given for each sample in order to enable the selection of the most interesting ones for the electrochemical study to be reported in chapter 4.

The fourth and last chapter is dedicated to the electrochemical performances of the chapter 3 selected samples in half cells vs. metallic lithium and to the investigation of the lithium storage mechanisms. In particular, the influence of the morphology on the electrochemical performances of  $\text{ZnFe}_2\text{O}_4$  is studied. These performances are also compared to a mixture of  $\text{ZnO}$  and  $\text{Fe}_2\text{O}_3$  nanopowders and the reactions involved during the lithiation and delithiation processes are investigated thanks to operando measurements as X-ray diffraction and  $^{57}\text{Fe}$  Mössbauer spectroscopy.

The obtained results are then summarized in the conclusion in order to highlight the main information gained in this work on nanostructured ternary oxides, and to give the perspectives for further studies on these compounds.

## References

- 1 [Http://www.netl.doe.gov/research](http://www.netl.doe.gov/research), <http://www.netl.doe.gov/research>.

- 2 <https://www.giss.nasa.gov/research/news/20130115/>, .
- 3 R. K. Pachauri and L. A. Meyer, *IPCC, 2014: Climate Change 2014 Synthesis Report*, IPCC, Geneva, Switzerland, 2014.
- 4 <http://unfccc.int/resource/docs/convkp/kpeng.pdf>.
- 5 O. Edenhofer, R. Pichs-Madruga and Y. Sokona, *IPCC, 2014: Climate Change 2014: Mitigation of Climate Change.*, Cambridge University Press, Cambridge, United Kingdom and New York, NY, USA, 2014.
- 6 [Http://ieer.org/wp/wp-content/uploads/2012/03/MN-factsheet.pdf](http://ieer.org/wp/wp-content/uploads/2012/03/MN-factsheet.pdf), <http://ieer.org/wp/wp-content/uploads/2012/03/MN-factsheet.pdf>.
- 7 A. B. Yaroslavtsev, T. L. Kulova and A. M. Skundin, *Russ. Chem. Rev.*, 2015, **84**, 826–852.
- 8 L. Boulet-Roblin, P. Borel, D. Sheptyakov, C. Tessier, P. Novák and C. Villevieille, *J. Phys. Chem. C*, 2016, **120**, 17268–17273.
- 9 C. Yuan, H. Bin Wu, Y. Xie and X. W. D. Lou, *Angew. Chem. Int. Ed. Engl.*, 2014, **53**, 1488–1504.
- 10 H. Bin Wu, J. S. Chen, H. H. Hng and X. W. D. Lou, *Nanoscale*, 2012, **4**, 2526–2542.
- 11 J. Cabana, L. Monconduit, D. Larcher and M. R. Palacín, *Adv. Mater.*, 2010, **22**, E170–92.
- 12 P. F. Teh, S. S. Pramana, C. Kim, C.-M. Chen, C.-H. Chuang, Y. Sharma, J. Cabana and S. Madhavi, *J. Phys. Chem. C*, 2013, **117**, 24213–24223.

---

## Chapter 1. Literature review

---

The first chapter is dedicated to the introduction of the study context and provides information to understand the interest of this work. Presentation of the lithium-ion battery technology is addressed in the first part underlining its advantages and challenges that need to be addressed; the next part details the characteristics of transition metal oxides and explains why these materials were chosen as the subject of interest in this work. Various synthesis methods for transition metal oxides elaboration are then presented in the third part with eventual focus on CO<sub>2</sub> laser pyrolysis technique that was used in this work in the last part.

### I. Presentation of the lithium-ion technology

#### 1. History and basic principles of the lithium-ion battery

While primary batteries (or non-rechargeable batteries) are based on an irreversible redox reaction that allows a one and only use of the device, rechargeable (or secondary) batteries work thanks to a reversible redox reaction that allows several charge/discharge cycles. The first rechargeable battery (the lead-acid technology) was invented in 1859 by the French physicist Gaston Planté. Different types of rechargeable batteries were then developed during the 20<sup>th</sup> century. The most significant ones are the nickel-cadmium batteries (Ni-Cd)<sup>1</sup>, the nickel-metal hydride (NiMH)<sup>2</sup> batteries, and most particularly the lithium-ion technologies (LIB) that will be addressed in this work and will be presented in the following part.

A battery consists of two electrochemically active couples. The positive electrode corresponds to the redox couple with the higher potential and the negative electrode to the one with the lower potential. A separator impregnated with electrolyte is placed between the two electrodes; the electrolyte is electronically insulating but allows ions circulation during the redox reactions. Generally, for lithium-ion batteries, the electrolyte consists in an organic liquid solvent (most of the time, carbonates) in which a lithium salt (often LiPF<sub>6</sub>) is dissolved to ensure the ionic conductivity. Discharge occurs with ions transferred from the negative electrode to the positive one through the electrolyte. Electroneutrality is kept with electrons transported in the same direction through the external circuit. To ensure a fast transportation of the electrons into the electrode material, this latter has to be electronically conductive. For rechargeable batteries, the reverse reaction occurs by applying an external current thus leading to the charge of the battery, with ions and electrons being transferred from the positive to the negative electrode (Figure 1.1).

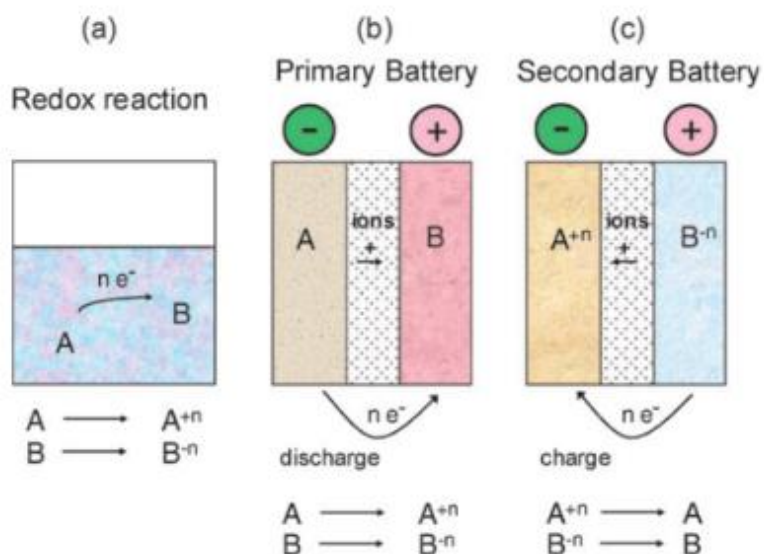


Figure 1.1. Schematic diagram of (a) a redox reaction, (b) a primary (non-rechargeable) battery upon discharging and (c) a secondary (rechargeable) battery upon charging<sup>3</sup>

The voltage of a battery corresponds to the difference between the positive and negative electrode potentials. The battery voltage is maximized by having a low working voltage vs.  $Li/Li^+$  for the negative electrode and a high working voltage vs.  $Li/Li^+$  for the positive electrode. Each electrode material has its own specific capacity (in  $mAh.g^{-1}$ ) corresponding to the number of charge the material can store. For a specific application, the energy density and the power are the two main criteria to be taken into account when choosing the proper battery. The energy density (in  $Wh.kg^{-1}$ ) that can be delivered by a battery directly depends on the battery voltage and on the specific capacities of both electrodes (Energy density = Specific capacity \* voltage): the higher they are, the higher the energy density is. The power density (in  $W.kg^{-1}$ ) corresponds to how fast this energy can be extracted from the battery. This power depends on the diffusion of the conductive species (ions and electrons) into the anode and cathode materials as well as in the electrolyte. The faster the diffusion of these species is, the higher the battery power is. Lithium-ion batteries are generally considered as a good compromise in terms of energy and power densities compared to fuel cells (higher energy density but lower power density) and supercapacitors (lower energy density but higher power density) (Figure 1.2).

## Presentation of the lithium-ion technology

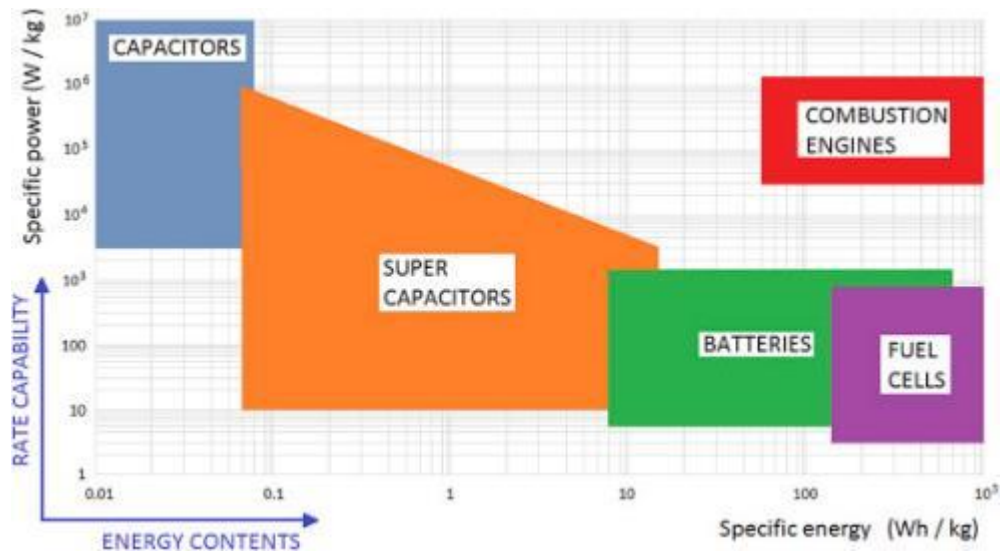


Figure 1.2. Comparison of the energy and power densities for different energy storage technologies<sup>4</sup>

Each new generation of batteries is associated to an improvement in terms of energy density to obtain a lighter and smaller battery delivering the same energy (Figure 1.3). Although lead-acid batteries are the oldest type of rechargeable devices, they are still commonly used in combustion vehicles whereas Ni-Cd and NiMH batteries remain the most suitable technologies for high-power applications<sup>5</sup>.

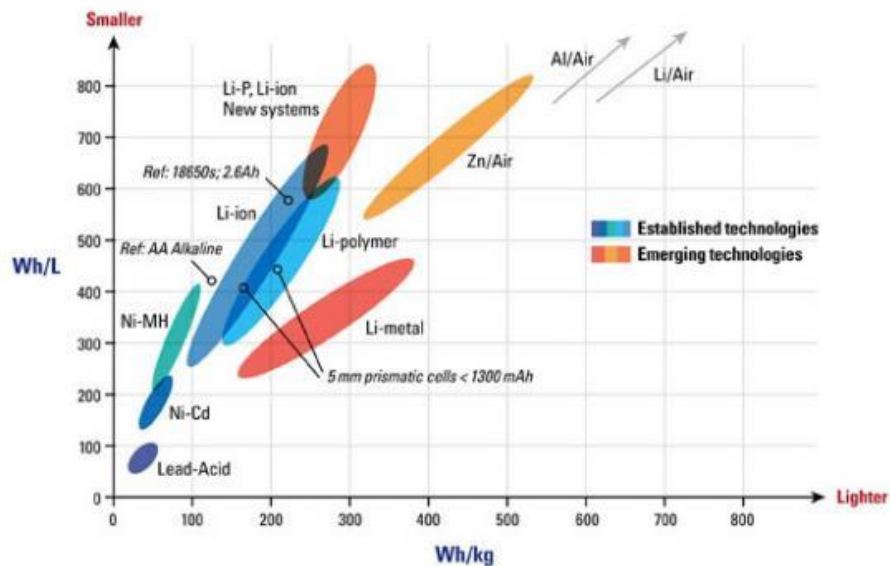


Figure 1.3. Different technologies of batteries with their gravimetric and volumetric energy density<sup>6</sup>

Lithium started to generate interest in the 1970's when its reversible intercalation in materials like TiS<sub>2</sub><sup>7</sup> and MoS<sub>2</sub><sup>8</sup> was discovered by Whittingham. Lithium metal batteries were then used in the 1980's for mobile devices due to a higher energy density when compared to lead-acid and Ni-Cd

batteries. However, the development of this technology was abruptly stopped when safety issues occurred. Indeed for first lithium batteries, the anode was made of metallic lithium and the cathode works as a lithium host. During the discharge, lithium ions are inserted into the positive electrode and upon charge, the reverse reaction occurs. Unfortunately, the uneven deposition of the lithium onto the anode surface results in the formation of dendrites<sup>5</sup>(Figure 1.4).

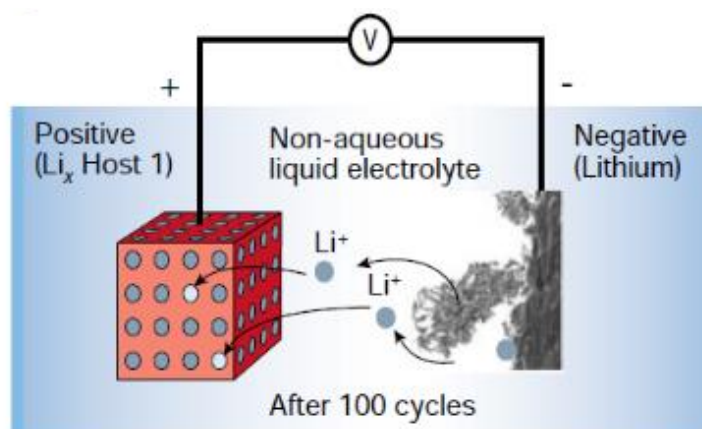


Figure 1.4. Rechargeable Li-metal battery (the picture of the dendrite growth at the Li surface was obtained directly from in-situ scanning electron microscopy measurements)<sup>5</sup>

These dendrites grow continuously during cyclings, eventually penetrating the separator and creating a short circuit between the anode and cathode together<sup>9</sup>. This uncontrolled phenomena can lead to overheating, leakage of electrolyte and Li exposure to air: fires or explosions of the battery were then experienced by users.

To avoid this safety issue, research works were conducted to find alternatives to the use of lithium metal. The substitution of metallic lithium by a second lithium host was proposed and developed by D.W Murphy<sup>10</sup> and B. Scrosati<sup>11</sup> in 1980 and led to the lithium-ion technology or the so-called rocking-chair battery. In this case, during charge, lithium ions are extracted from the cathode and inserted into the anode and during discharge the reverse reaction takes place reversibly. The presence of lithium only in its ionic state rather than its metallic state limits the dendrites growth. Nevertheless, safety of Li-ion batteries remains a challenge to be addressed today.

The first generation of lithium-ion batteries (LIB) were commercialized by Sony in 1990<sup>12</sup> that stored more than twice the energy as compared to nickel and lead-acid batteries of same weight and size. The cathode material in LIB consists of LiCoO<sub>2</sub> coupled with a graphite anode with the battery working through reversible Li-intercalation/deintercalation reactions<sup>13</sup>. During the lithiation of the anode (charge), lithium ions are inserted from the positive to the negative electrode across the electrolyte and intercalated between the graphite layers. During the discharge process (delithiation of the negative electrode), the opposite reaction occurs with lithium ions transferring back to the positive electrode as follows (Figure 1.5).

On the negative electrode:  $C_6 + xe^- + xLi^+ = Li_xC_6$

On the positive electrode:  $LiCoO_2 = xLi^+ + xe^- + Li_{1-x}CoO_2$

To evaluate the reversibility of the storage reaction, the coulombic efficiency is generally calculated. This value corresponds to the ratio between the delithiated capacity and the lithiated capacity. The coulombic efficiency is expected to be as close as possible to 100% meaning that the reaction is totally reversible.

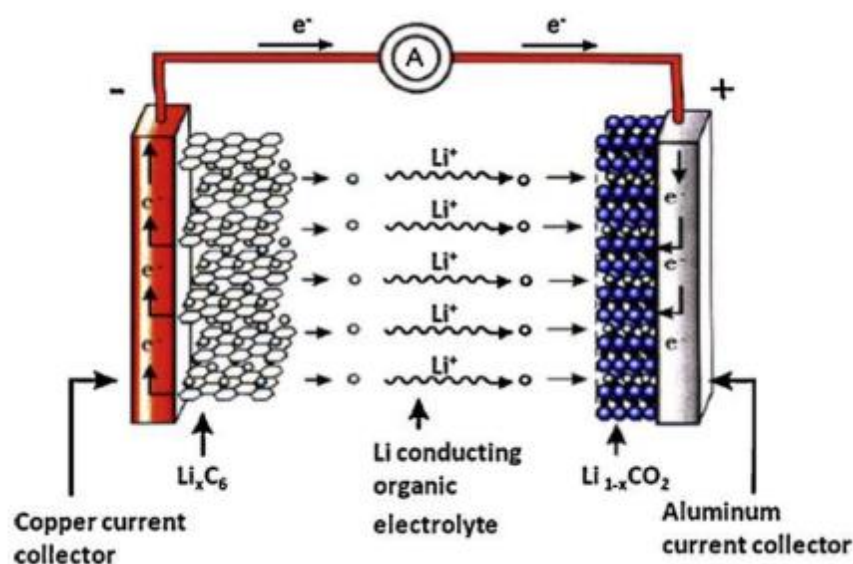


Figure 1.5. Charge/discharge process for a commercial lithium-ion battery<sup>14</sup>

The energy density of a modern LIB is between 150 and 190 Wh.kg<sup>-1</sup>. The LiCoO<sub>2</sub> cathode material has a theoretical capacity of 240 mAh.g<sup>-1</sup> while the graphite anode shows a higher theoretical capacity of 372 mAh.g<sup>-1</sup>. However, in practice, the obtained capacities are lower: 140 mAh.g<sup>-1</sup> for LiCoO<sub>2</sub> (due to the formation of unstable cobalt dioxide during charging) and 320 mAh.g<sup>-1</sup> for graphite. A commercial LIB possesses a voltage from 3.0 V to 4.0 V owing to the high working voltage of lithium cobaltite (3.7 V to 4.0 V vs. Li/Li<sup>+</sup>) and the low working voltage of graphite (0.15-0.25 V vs. Li/Li<sup>+</sup>)<sup>15</sup>. Nevertheless, due to this low working voltage, graphite experiences lithium plating during fast charging that can cause severe safety problems due to lithium dendrites formation. Moreover, this lithium deposition on graphite causes capacity fading due to the loss of active lithium<sup>16</sup>.

Even if these LIB allowed the democratization of portable electronics, this technology is still the object of intense research to enhance performances for next-generation applications such as electric vehicles and renewable energy storage. It is necessary to get batteries with a higher energy density and a longer cycle life while keeping high safety requirements, as well as prices and environmental impact as low as possible. To obtain high performance Li batteries in the future,

intense research and development work has thus to be done on both cathode and anode material to study new charge storage mechanisms and to increase energy/power density and safety.  $\text{LiCoO}_2$ , but also  $\text{Li}(\text{Ni},\text{Mn},\text{Co})\text{O}_2$  and  $\text{Li}(\text{Ni},\text{Co},\text{Al})\text{O}_2$ , the most common cathode materials used in commercial batteries, are today the most limiting issues in terms of capacity ( $140$  to  $180 \text{ mAh.g}^{-1}$ ) compared to graphite anode. Moreover, these materials are partially constituted by cobalt, an expensive and toxic metal. On the other side, the graphite anode shows higher capacity with a good cycling stability. Nevertheless, this capacity is still relatively low when compared to other potential anode materials that will be described later with capacities over  $1000 \text{ mAh.g}^{-1}$ . Moreover, as mentioned before, working potential of graphite vs  $\text{Li}/\text{Li}^+$  tends to favor Li plating and thus enhances safety concerns for commercial Li batteries. In this context, this work focusses on the search of an alternative anode material demonstrating higher capacity and higher working voltage vs  $\text{Li}/\text{Li}^+$  than graphite.

Many research works today are devoted to new anode materials which can be classified in three main categories based on the interaction of lithium: (i) intercalation materials, (ii) alloying materials and (iii) conversion materials. These categories will be described now.

### 2. Categories of anode materials depending on the lithium storage mechanism

Three categories of anode materials have been defined depending on the lithium storage mechanism during charge and discharge processes. Each category of materials has its own advantages and drawbacks.

#### Intercalation (or insertion) materials

For intercalation materials, lithium is inserted into the host without any modification of its crystalline structure. The most common intercalation material is graphite, that can store one lithium ion for six carbon atoms leading to a theoretical capacity of  $372 \text{ mAh.g}^{-1}$  owing to its lamellar structure (Figure 1.6). Moreover, graphite has the combined properties of low cost, abundant availability and high electrical conductivity ( $10^5 \text{ S/m}$ )<sup>17,18</sup>. Although graphite presents a very low working voltage versus  $\text{Li}/\text{Li}^+$ , and higher specific capacity than cathode material ( $\sim 140\text{-}170 \text{ mAh.g}^{-1}$ ), safety issues at fast charging due to Li plating, and the thrust towards future LIB large scale applications like electric vehicles requires higher specific capacity material both on the cathode and anode side.

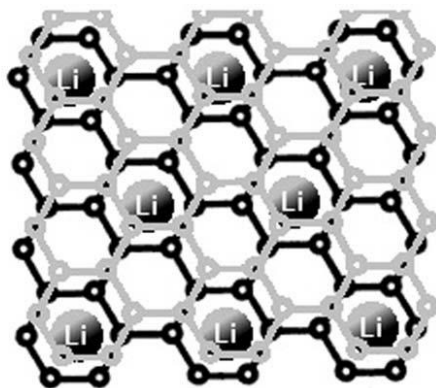
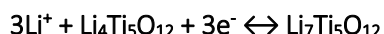


Figure 1.6. Insertion of lithium ions between graphite layers<sup>19</sup>

. Research works on new materials with higher theoretical capacity like graphene<sup>20</sup> (780 to 1100 mAh.g<sup>-1</sup>) or carbon nanotubes<sup>21</sup> (1100 mAh.g<sup>-1</sup>) have been conducted; however, these materials suffer from high production cost as well as high irreversible consumption of Li upon cycling (i.e. low coulombic efficiency) leading to poor cycle life.

In addition to layered sulfides such as TiS<sub>2</sub> and MoS<sub>2</sub> previously mentioned (page 24) , another example of intercalation material is the spinel-structured Li<sub>4</sub>Ti<sub>5</sub>O<sub>12</sub> whose storage mechanism is described below.



This material suffers from a low theoretical specific capacity (175 mAh.g<sup>-1</sup>) and a high working voltage (1.55V vs Li/Li<sup>+</sup>) leading to an energy density much lower than graphite but also has a very good cyclability especially at high currents, making this material useful for power applications<sup>9</sup>.

Due to the non-destruction of the material structure upon Li insertion, intercalation materials are known as very stable anode materials. However, they still show a limited theoretical capacity for next-generation batteries.

### Alloying materials

Another lithium storage mechanism was discovered by Dey *et al.* who demonstrated that some metallic and semi-metallic elements (like Si, Sn, Ge, Mg) are able to reversibly form an alloy with lithium at low potential during the lithiation of the anode<sup>22</sup>. During the delithiation process, the de-alloying reaction occurs leading to the reformation of the metal or semi-metal. A typical alloying/de-alloying reaction is shown below:



Alloying materials generally offer a higher theoretical capacity than intercalation materials as more lithium can be inserted into the material. Several materials have been studied in the literature

(Figure 1.7) like tin, antimony and germanium but the most promising one seems to be silicon thanks to an outstanding theoretical specific capacity allowed by the potential formation of the Li rich  $\text{Li}_{4.4}\text{Si}$  phase ( $4200 \text{ mAh.g}^{-1}$ , more than ten times higher than graphite), and to a relatively low working voltage of  $0.4 \text{ V}$  vs.  $\text{Li/Li}^+$  compared to other alloying materials<sup>23</sup>. Nevertheless, this theoretical capacity has been reported only at high temperature ( $> 100^\circ\text{C}$ ) in experimental works. At ambient temperature, silicon is known to have a capacity around  $3580 \text{ mAh.g}^{-1}$  due to the formation of the  $\text{Li}_{15}\text{Si}_4$  phase<sup>24</sup>.

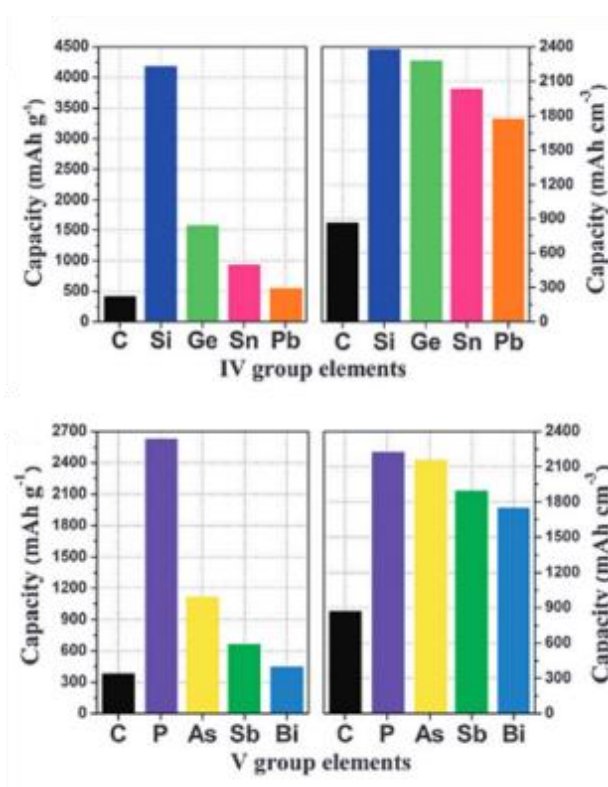


Figure 1.7. Examples of alloying materials and their theoretical capacity<sup>12</sup>

In spite of very high specific capacities, alloying materials are reported to have a very poor capacity retention due to a dramatically high volume expansion during the alloying reaction. For example,  $\text{Li}_{4.4}\text{Si}$  phase leads to a 400% lattice expansion during the alloy formation<sup>25</sup>. This creates mechanical stresses and cracks in the host material leading to the progressive destruction of the negative electrode after few charge-discharge cycles. In addition, silicon is subject to the formation of an unstable solid electrolyte interphase (SEI) on the surface of the electrode. This SEI that is also formed with other anode materials categories comes from degradation reactions of the electrolyte at the electrode/electrolyte interface, at low potential and consumes irreversibly part of the lithium ions during the lithiation process. For a graphite electrode, a stable SEI is formed at the first cycle which acts as a passivation layer, avoiding further reactions on the electrode surface<sup>26</sup>. For silicon, due to the volumetric expansion/reduction of the material during charge/discharge process, the SEI is broken

and reformed continuously, trapping more and more lithium during cycling, explaining the relatively low coulombic efficiency reported for this material (Figure 1.8)<sup>27</sup>.

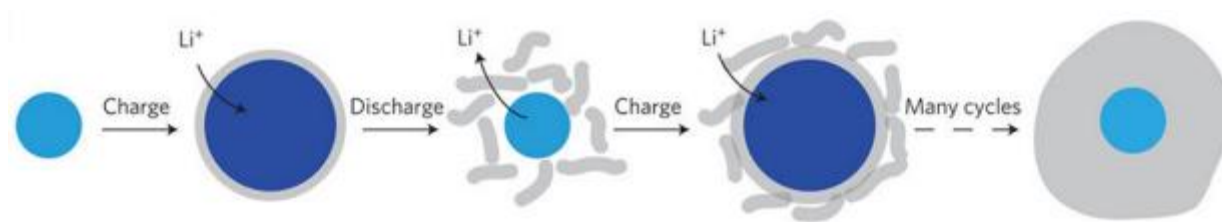


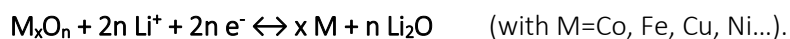
Figure 1.8. SEI formation on silicon surface during lithiation and delithiation process<sup>27</sup>

These drawbacks still hinder alloy/dealloy-based anodes from commercialization, but intensive research work is still going on improving Si-based electrodes stability. In particular, the nanostructuring of silicon is studied by many researchers to limit the volumetric modifications, together with the coating of the Si surface by carbon in order to increase the electrode stability upon cycling<sup>28,29</sup>.

#### Conversion materials

In the past decade, a new lithium storage mechanism has been identified for some transition metal oxides (TMO), named conversion reaction<sup>30</sup>. Even if this reaction mechanism has also been observed for metal nitrides, sulphides, fluorides and phosphides, we will focus on transition metal oxides as they generally show a better reversibility and stability and very good capacities (generally situated between 750 mAh.g<sup>-1</sup> and 1200 mAh.g<sup>-1</sup>)<sup>31</sup>. As this latter category is directly addressed in the experimental part of this document, the mechanisms governing Li insertion in such materials will be more specifically detailed in what follows.

For conversion materials, the storage mechanism is based on a reversible redox reaction between lithium and transition metal cations:



The first lithiation of the TMO starts with the insertion of lithium into the crystalline structure of  $M_xO_n$ , followed by an irreversible amorphization process and the reduction of the metal oxide to form an M/Li<sub>2</sub>O nanocomposite. This nanocomposite consists in metallic nanoparticles of few nanometers in diameter embedded in an amorphous Li<sub>2</sub>O matrix<sup>32,33</sup>. The high surface area of the metallic nanograins fosters the intimate contact with the Li<sub>2</sub>O matrix that enhances the electrochemical reactivity during the following cycles<sup>34</sup>.

Figure 1.9 is an example of a typical lithiation process for  $\text{Co}_3\text{O}_4$  with the different steps of the first discharge<sup>35</sup>. Several intermediate products are identified prior to the formation of  $\text{Li}_2\text{O}$  with Co nanoparticles, as a lithium-inserted  $\text{Co}_3\text{O}_4$  phase and nanosized Co-Li-O clusters.

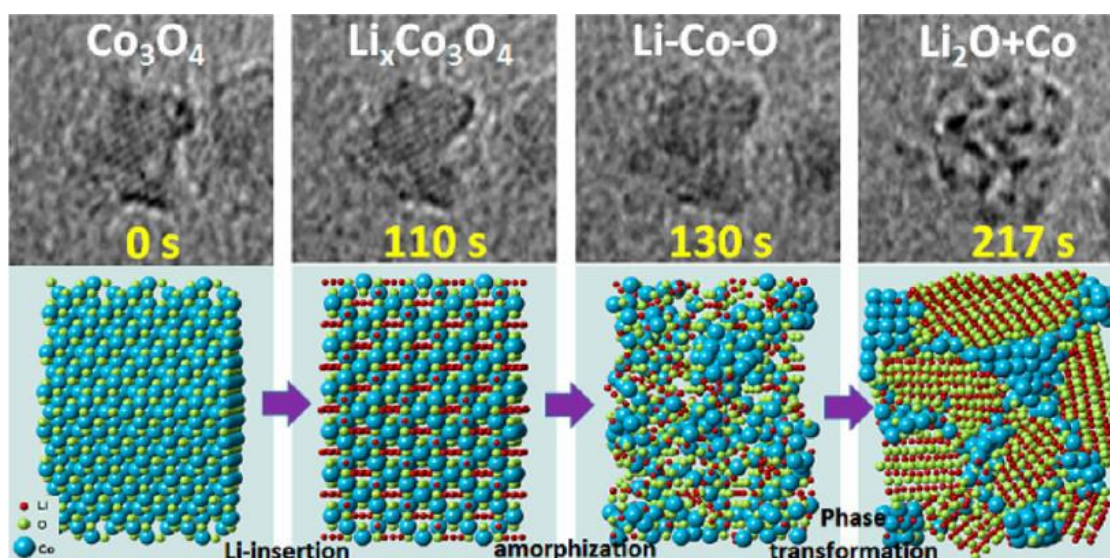


Figure 1.9. In-situ HREM of lithiation of  $\text{Co}_3\text{O}_4$  showing the insertion, amorphization and reduction processes<sup>35</sup>

Moreover, for transition metal oxides, a thin polymeric gel-type layer is formed around the metallic nanoparticles due to the electrolyte decomposition after a deep discharge, serving as an envelope to maintain contact between the metallic nanoparticles<sup>36</sup>. This polymeric layer stores part of the lithium during the lithiation, but on the contrary of SEI, this storage was found to be reversible. Moreover, the formation of this layer seems to be catalyzed by the presence of the nanoparticles<sup>37</sup>. During the following charge, oxidation of the metallic nanoparticles occurs and  $\text{Li}_2\text{O}$  is decomposed, leading to the re-formation of the metal oxide. It should be noted that the initial crystallinity of the transition metal oxide cannot be resumed, this latter being replaced by an amorphous structure.

The capacity of TMO can be calculated thanks to the Faraday's law as follows:

$$Q = 2nFN$$

Q: capacity (Ah)

2n: number of lithium ions transferred

n: number of oxygen in  $\text{M}_x\text{O}_n$

F: Faraday's constant ( $96500 \text{ C}\cdot\text{mol}^{-1}$  or  $26800 \text{ mAh}\cdot\text{mol}^{-1}$ )

N: number of mole of reacting species.

Based on this formula, the theoretical specific capacity (noted C), can be calculated using the following equation<sup>38</sup>:

$$C (\text{mAh}\cdot\text{g}^{-1}) = \frac{Q}{m(\text{oxide})} = \frac{26800 \times n}{M(\text{oxide})}$$

with M: molecular weight of the TMO and m: weight of the oxide.

However, several issues keep these compounds far from industrial applications. In particular, TMO are widely reported to have a very low coulombic efficiency at the first cycle (generally lower than 75%). This phenomena can be attributed to the irreversible formation of a SEI at electrochemically active sites during the first discharge<sup>39,40</sup>. TMO work at high potential compared to graphite which is interesting from a safety point of view to avoid Li plating but it is also actually known that these materials often work outside the stability voltage window of the electrolyte, leading to its degradation and the formation of this organic-type layer<sup>41</sup>. To overcome this issue, several research works are focused on the development of new electrolytes that would be more stable at high voltages<sup>42</sup>. Moreover, the strong structural re-organization taking place during lithiation/delithiation to accommodate the chemical modifications, induces large volume changes (around 100% volume expansion for iron and cobalt oxides<sup>31</sup>) that can eventually lead to the destruction of the electrode and the loss of capacity during cycling. Another drawback comes from the large voltage hysteresis (voltage gap) observed between the charge and discharge processes causing a huge round-trip energy density inefficiency<sup>31</sup>. When the lithiation and delithiation potentials are different, it means that the lithium cannot be inserted in or extracted from the active material easily. However, the origins of this hysteresis are far from being understood for conversion materials yet<sup>13</sup>.

These advantages (higher capacity, higher safety) and drawbacks (cycling stability, SEI issues) motivate research works on these promising TMO materials before introducing them as next-generation anode for lithium-ion batteries<sup>13</sup>. The most common TMO encountered in literature will now be presented, in order to narrow the list to the one chosen for this thesis work.

### II. Transition metal oxides as anode materials for Li-ion batteries

#### 1. Examples of $M_xO_n$ oxides

There is a large variety of compounds among TMO that can reversibly react with lithium and theoretically lead to specific capacities two to five times higher than graphite<sup>12</sup>. This specific capacity as well as the working voltage depend on each oxide. Several studies have been conducted on copper oxides<sup>43</sup>, manganese oxides<sup>44</sup> or nickel oxides<sup>45</sup> but cobalt oxides and iron oxides are those which received the most attention, thanks to high theoretical capacities and good electrochemical performances.

In the following part, performances of Co and Fe-based oxides will thus be reported. Before that, it must be noted that these performances must be compared with caution. Indeed, experimental parameters such as electrode loading or cycling rate play a key role on the obtained performances, which makes hazardous the direct comparison between reported results by different groups.

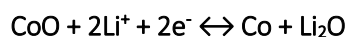
For instance the current is related to the speed, or rate, of the battery cycling: the higher it is, and the faster the battery will cycle. Generally, the current is expressed by a “C-rate”: C/5 means a full lithiation is realized in five hours, C/10 in ten hours, C/20 in twenty hours and so on. This current rate has an impact on the battery performances as seen in Table 1.2. Most of the time, by increasing the current rate, the performances are lower.

The electrode loading (amount of active material in  $\text{mg}/\text{cm}^2$ ) also has an impact on the performances<sup>31</sup>. Generally, a low loading will favor better performances for the electrode during cycling whereas a high loading may show poorer performances but the latter is more representative for commercial batteries. More details about the choice of a current rate and its calculation as well as the choice of a loading will be given in chapter 2.

#### Co-based oxides

For instance, cobalt oxides ( $\text{CoO}$  and  $\text{Co}_3\text{O}_4$ ) present excellent electrochemical performances and relatively high theoretical capacities ( $715 \text{ mAh}\cdot\text{g}^{-1}$  and  $890 \text{ mAh}\cdot\text{g}^{-1}$ , respectively)<sup>12</sup>.

$\text{CoO}$  was first explored by Poizot *et al.* who successfully demonstrated the reduction of nanosized  $\text{CoO}$  to  $\text{Co}/\text{Li}_2\text{O}$  during lithiation through the following reaction<sup>30</sup>.



Several studies were then conducted on this material and very good electrochemical performances were obtained for various particles shapes and different cycling conditions (Table 1.1). The current rate (in  $\text{mA}\cdot\text{g}^{-1}$ ) and electrode loading (when provided) are also indicated in the table. The table also indicates the number of the cycle after which the measurements were stopped.

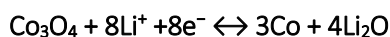
## Transition metal oxides as anode materials for Li-ion batteries

Table 1.1. Electrochemical performances of some CoO anode for lithium-ion batteries

Oxide	Theoretical capacity: 715 mAh.g <sup>-1</sup>			
CoO	Morphology	Reversible capacity/n <sup>th</sup> cycle	Current density (mA.g <sup>-1</sup> )	Electrode loading
	nanoparticles <sup>30</sup>	600 mAh.g <sup>-1</sup> /50 <sup>th</sup> cycle	143 mA.g <sup>-1</sup> (C/5)	2-6 mg.cm <sup>-2</sup>
	nanocages <sup>46</sup>	807 mAh.g <sup>-1</sup> /50 <sup>th</sup> cycle	143 mA.g <sup>-1</sup>	Not reported
	nanoparticles <sup>47</sup>	1050 mAh.g <sup>-1</sup> /20 <sup>th</sup> cycle	71.5 mA.g <sup>-1</sup> (C/10)	5-7 mg per electrode

CoO shows good performances as the reversible capacity obtained after several cycles is very close to the theory or even slightly higher. Getting a reversible capacity higher than the theoretical value is quite common for transition metal oxides<sup>31</sup>. Several assumptions to explain this phenomena will be detailed later.

Despite the initial interest in CoO, Co<sub>3</sub>O<sub>4</sub> has become more attractive because of its higher theoretical capacity coming from the insertion of 8 Li<sup>+</sup> ions in the oxide during lithiation, as follows<sup>32</sup>.



The electrochemical performance of Co<sub>3</sub>O<sub>4</sub> has been evaluated through various research works (Table 1.2).

Table 1.2. Electrochemical performances of some Co<sub>3</sub>O<sub>4</sub> anode for lithium-ion batteries

Oxide	Theoretical capacity: 890 mAh.g <sup>-1</sup>			
Co <sub>3</sub> O <sub>4</sub>	Morphology	Reversible capacity/n <sup>th</sup> cycle	Current density (mA.g <sup>-1</sup> )	Electrode loading (mg.cm <sup>-2</sup> )
	nanotubes <sup>48</sup>	856 mAh.g <sup>-1</sup> /60 <sup>th</sup> cycle	223 mA.g <sup>-1</sup> (C/4)	2.5 mg.cm <sup>-2</sup>
		677 mAh.g <sup>-1</sup> /60 <sup>th</sup> cycle	890 mA.g <sup>-1</sup> (1C)	
	nanowires <sup>48</sup>	805 mAh.g <sup>-1</sup> /60 <sup>th</sup> cycle	223 mA.g <sup>-1</sup>	2.5 mg.cm <sup>-2</sup>
		588 mAh.g <sup>-1</sup> /60 <sup>th</sup> cycle	890 mA.g <sup>-1</sup>	
flower-like <sup>49</sup>	700 mAh.g <sup>-1</sup> /100 <sup>th</sup> cycle	890 mA.g <sup>-1</sup>	X	
nanoflakes <sup>50</sup>	824 mAh.g <sup>-1</sup> /50 <sup>th</sup> cycle	100 mA.g <sup>-1</sup>	X	

Outstanding stable capacities higher than 800 mAh.g<sup>-1</sup> can be obtained for some cobalt oxides anodes. However, they are not the ideal choice for anode materials due to their high cost, high toxicity and high working voltage (2.1 vs. Li/Li<sup>+</sup>)<sup>51</sup>. In this context, Fe-based oxides appear more promising.

Fe-based oxides

First observations of conversion reaction for Fe<sub>2</sub>O<sub>3</sub> date from the 1980's<sup>12</sup>. Most of the investigations were performed on α-Fe<sub>2</sub>O<sub>3</sub> but it was found that γ-Fe<sub>2</sub>O<sub>3</sub> behaves similarly<sup>52</sup>. The conversion reaction of Fe<sub>2</sub>O<sub>3</sub> involves 6 Li<sup>+</sup> inserted during discharge, as follows, corresponding to 1007 mAh.g<sup>-1</sup> of theoretical capacity.



Besides, low cost and low toxicity make iron oxides very attractive candidates as anode materials. As a consequence, many papers deal with Fe<sub>2</sub>O<sub>3</sub> for lithium-ion batteries and evaluate its electrochemical activity. The most representative results are shown in the table below (Table 1.3).

Table 1.3. Electrochemical performances of some Fe<sub>2</sub>O<sub>3</sub> anode for lithium-ion batteries

Oxide	Theoretical capacity: 1007 mAh.g <sup>-1</sup>			
	Morphology	Reversible capacity/n <sup>th</sup> cycle	Current density (mA.g <sup>-1</sup> )	Electrode loading (mg.cm <sup>-2</sup> )
Fe <sub>2</sub> O <sub>3</sub>	nanoflakes <sup>53</sup>	680 mAh.g <sup>-1</sup> /80 <sup>th</sup> cycle	65 mA.g <sup>-1</sup> (C/15)	0.2 mg.cm <sup>-2</sup>
	nanoellipses <sup>54</sup>	1164 mAh.g <sup>-1</sup> /60 <sup>th</sup> cycle	100 mA.g <sup>-1</sup>	1 mg per electrode
	nanowires <sup>55</sup>	456 mAh.g <sup>-1</sup> /100 <sup>th</sup> cycle	100 mA.g <sup>-1</sup>	X
	nanospheres <sup>56</sup>	414 mA.g <sup>-1</sup> /60 <sup>th</sup> cycle	101 mA.g <sup>-1</sup>	X

Fe<sub>3</sub>O<sub>4</sub> can theoretically store 8 Li<sup>+</sup> ions per formula unit:



However, it received less attention than Fe<sub>2</sub>O<sub>3</sub> because of its lower theoretical capacity of 926 mAh.g<sup>-1</sup>. Besides, the reversibility of Fe<sub>3</sub>O<sub>4</sub> is very poor and capacity fades very rapidly during cycling as it can be seen in the table below (Table 1.4). According to the different studies about cobalt oxides and iron oxides summarized here, they show similar performances as anode material for lithium-ion batteries depending on the cycling conditions though. In this case, it is interesting to work with iron oxides to avoid the use of toxic and expensive elements as cobalt.

## Transition metal oxides as anode materials for Li-ion batteries

Table 1.4. Electrochemical performances of some  $\text{Fe}_3\text{O}_4$  anodes for lithium-ion batteries

Oxide	Theoretical capacity: $926 \text{ mAh.g}^{-1}$			
	Morphology	Reversible capacity/ $n^{\text{th}}$ cycle	Current density ( $\text{mA.g}^{-1}$ )	Electrode loading ( $\text{mg.cm}^{-2}$ )
$\text{Fe}_3\text{O}_4$	hollow spheres <sup>57</sup>	700 $\text{mAh.g}^{-1}/50^{\text{th}}$ cycle	100 $\text{mA.g}^{-1}$	6 $\text{mg.cm}^{-2}$
	nanospheres <sup>58</sup>	269 $\text{mAh.g}^{-1}/80^{\text{th}}$ cycle	93 $\text{mA.g}^{-1}$ (C/10)	X
	mesoporous microspheres <sup>59</sup>	450 $\text{mAh.g}^{-1}/110^{\text{th}}$ cycle	185 $\text{mA.g}^{-1}$	X

Even if iron oxides can be very interesting as anode materials, they still suffer a high working voltage around 2.1V vs.  $\text{Li/Li}^+$ , like for cobalt oxides, which limits the energy density of the full battery<sup>60</sup>. A direct replacement of graphite by these materials is thus not possible (Figure 1.10) and a specific cathode material with matching potential has thus to be used to preserve the energy density. In particular, many research works focus on the development of  $\text{LiNi}_{0.5}\text{Mn}_{1.5}\text{O}_4$  and  $\text{LiCoPO}_4$  as high-voltage cathodes<sup>61</sup>.

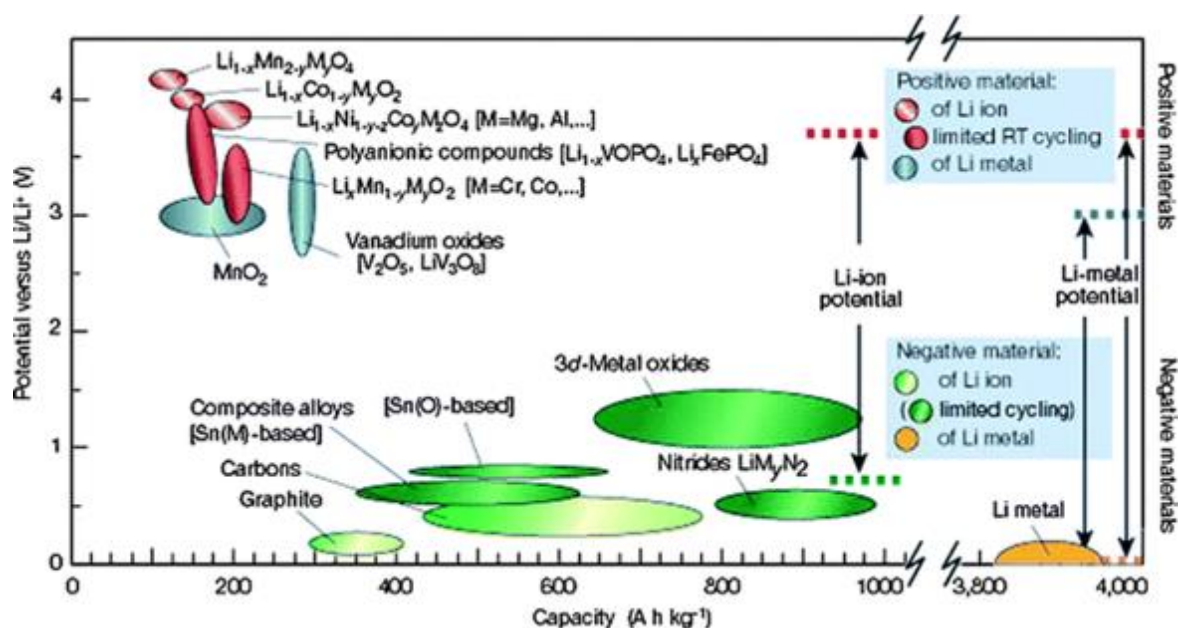


Figure 1.10. Different categories of positive and negative electrode materials with their theoretical working voltage vs.  $\text{Li/Li}^+$  and their specific capacities<sup>62</sup>

To enhance the energy density of the final battery, the working voltage of TMO can also be reduced while keeping a high specific capacity. On this point, mixed-transition metal oxides can be interesting.

## 2. Interest of mixed-transition metal oxides (MTMO)

### Limitation of transition metal oxides

As evocated before, MTMO offer the possibility to tune the working voltage depending on the nature of the chosen transition metals<sup>63</sup>. The substitution of one metal cation in Co<sub>3</sub>O<sub>4</sub>, Fe<sub>3</sub>O<sub>4</sub> or Mn<sub>3</sub>O<sub>4</sub> by another transition metal gives the possibility to form MTMO like ZnCo<sub>2</sub>O<sub>4</sub>, FeCo<sub>2</sub>O<sub>4</sub>, ZnFe<sub>2</sub>O<sub>4</sub> or ZnMn<sub>2</sub>O<sub>4</sub> that show lower working potentials (1.5 V for ZnFe<sub>2</sub>O<sub>4</sub><sup>64</sup>, 1.2 V for ZnMn<sub>2</sub>O<sub>4</sub><sup>65</sup>) while keeping similar theoretical capacities (Table 1.5).

Table 1.5. Theoretical capacity of several TMO and MTMO

TMO	Theoretical capacity	MTMO	Theoretical capacity
Fe <sub>2</sub> O <sub>3</sub>	926 mAh.g <sup>-1</sup>	ZnFe <sub>2</sub> O <sub>4</sub>	1001 mAh.g <sup>-1</sup>
Fe <sub>3</sub> O <sub>4</sub>	1007 mAh.g <sup>-1</sup>	CoFe <sub>2</sub> O <sub>4</sub>	916 mAh.g <sup>-1</sup>
CoO	890 mAh.g <sup>-1</sup>	NiCo <sub>2</sub> O <sub>4</sub>	896 mAh.g <sup>-1</sup>
Co <sub>3</sub> O <sub>4</sub>	715 mAh.g <sup>-1</sup>	ZnCo <sub>2</sub> O <sub>4</sub>	900 mAh.g <sup>-1</sup>

The working voltage (E) can theoretically be calculated for transition metal oxides using the Nernst equation<sup>34</sup>:

$$\Delta G = n\Delta G_0(\text{Li}_2\text{O}) - \Delta G_0(\text{M}_x\text{O}_n) = -2nEF$$

n: number of oxygen in M<sub>x</sub>O<sub>n</sub>

2n: number of electrons involved in the redox reaction

F: Faraday's constant

$\Delta G_0$ : Gibbs free energy of the species involved in the conversion reaction

However, the above formula is valid for bulk and highly crystalline materials. During conversion reaction, amorphization of the active material occurs as well as the formation of nanoparticles. As a consequence, differences between the theoretical voltage value and the experimental one are often observed. It is thus very difficult to estimate the operating working voltage vs. Li/Li<sup>+</sup> for a MTMO.

Several researchers have observed though the influence of the two metals nature on the working voltage for charge and discharge for MTMO. Some values are given in the Table 1.6 where the working voltages during lithiation and delithiation vary depending on the oxide.

Table 1.6. Experimental working voltages vs. Li/Li+ depending on the MTMO

MTMO	Experimental working voltages vs. Li/Li <sup>+</sup> during lithiation and delithiation
ZnCo <sub>2</sub> O <sub>4</sub>	0.85 V – 1.6 V <sup>66</sup>
ZnFe <sub>2</sub> O <sub>4</sub>	0.75 V – 1.5 V <sup>67</sup>
ZnMn <sub>2</sub> O <sub>4</sub>	0.4 V – 1.2 V <sup>68</sup>

Performances of several mixed-transition metal oxides

Several spinel-structured MTMO containing two transition metals (AB<sub>2</sub>O<sub>4</sub> – A, B transition metals) have been studied for lithium-ion batteries but are also of great interest in solid state chemistry for various applications like catalysis, sensors<sup>69</sup> and biomedicine<sup>70</sup>. Spinel metal oxides possess a cubic structure in which A<sup>2+</sup> cations are situated in the tetrahedral sites and B<sup>3+</sup> cations in the octahedral ones (Figure 1.11)<sup>71</sup>.

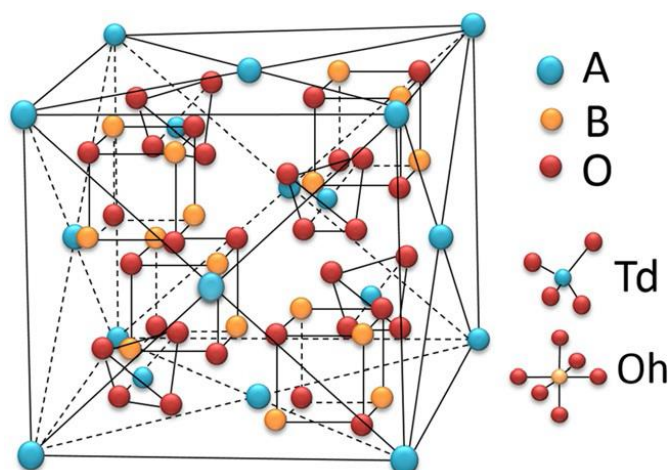


Figure 1.11. Spinel structure AB<sub>2</sub>O<sub>4</sub><sup>72</sup>

The lithium storage mechanism for MTMO depends on the chosen metal cations, although it is often assumed to be very similar to TMO. Indeed, the cycling of MTMO with lithium gives place to the different steps of lithium insertion into the crystalline structure followed by the amorphization of the material and the conversion reaction.

A non-exhaustive list of electrochemical performances for some MTMO is summarized in the table below (Table 1.7).

## Transition metal oxides as anode materials for Li-ion batteries

Table 1.7. Electrochemical performances of various mixed-transition metal oxides

Oxide	Morphology	Theoretical capacity	1 <sup>st</sup> cycle			Reversible capacity/n <sup>th</sup> cycle	Current rate
			Lithiation	Delithiation	Efficiency		
ZnMn <sub>2</sub> O <sub>4</sub> <sup>73</sup>	Faceted nanoparticles	1008 mAh.g <sup>-1</sup>	1192 mAh.g <sup>-1</sup>	<b>632 mAh.g<sup>-1</sup></b>	65%	<b>670 mAh.g<sup>-1</sup></b> 160 <sup>th</sup> cycle	1000 mA.g <sup>-1</sup>
NiCo <sub>2</sub> O <sub>4</sub> <sup>74</sup>	Nanorods	896 mAh.g <sup>-1</sup>	1095 mAh.g <sup>-1</sup>	<b>799 mAh.g<sup>-1</sup></b>	73%	<b>1000 mAh.g<sup>-1</sup></b> 400 <sup>th</sup> cycle	448 mA.g <sup>-1</sup>
CoFe <sub>2</sub> O <sub>4</sub> <sup>75</sup>	Macroporous	916 mAh.g <sup>-1</sup>	1782 mAh.g <sup>-1</sup>	1141 mAh.g <sup>-1</sup>	64%	702 mAh.g <sup>-1</sup> 30 <sup>th</sup> cycle	0.2 mA.cm <sup>-2</sup>
ZnCo <sub>2</sub> O <sub>4</sub> <sup>66</sup>	Nanoparticles	900 mAh.g <sup>-1</sup>	1179 mAh.g <sup>-1</sup>	913 mAh.g <sup>-1</sup>	77%	900 mAh.g <sup>-1</sup> 60 <sup>th</sup> cycle	60 mA.g <sup>-1</sup>
ZnFe <sub>2</sub> O <sub>4</sub> <sup>76</sup>	Octahedral nanoparticles	1001 mAh.g <sup>-1</sup>	1006 mAh.g <sup>-1</sup>	661 mAh.g <sup>-1</sup>	66%	450 mAh.g <sup>-1</sup> 50 <sup>th</sup> cycle	60 mA.g <sup>-1</sup>
ZnFe <sub>2</sub> O <sub>4</sub> <sup>77</sup>	Spicate architecture	1001 mAh.g <sup>-1</sup>	1647 mAh.g <sup>-1</sup>	<b>1221 mAh.g<sup>-1</sup></b>	74%	<b>1398 mAh.g<sup>-1</sup></b> 100 <sup>th</sup> cycle	100 mA.g <sup>-1</sup>
ZnCo <sub>2</sub> O <sub>4</sub> <sup>78</sup>	Hollow spheres	900 mAh.g <sup>-1</sup>	1108 mAh.g <sup>-1</sup>	819 mAh.g <sup>-1</sup>	74%	586 mAh.g <sup>-1</sup> 200 <sup>th</sup> cycle	3000 mA.g <sup>-1</sup>

As it can be observed above, all the different MTMO are able to provide a reversible capacity superior to graphite (theoretical capacity of graphite: 372 mAh.g<sup>-1</sup>), sometimes for more than 100 cycles. Transition metal oxides are widely reported to show a very low coulombic efficiency for the first cycle what is confirmed by the various examples in Table 1.7, with a first efficiency between 60 and 75% regardless of the current rate. The most commonly accepted explanation is that this large irreversible capacity during the first cycle is coming from the formation of the SEI (like for TMO) due to the electrolyte degradation on the electrode surface.

For some of the materials presented above, the reversible capacity after several cycles is higher than the delithiation capacity of the first cycle. These materials generally show a decrease of capacity at the beginning of the cycling for ten to twenty cycles before starting to gradually increase. This behavior is quite common for MTMO and TMO, especially for cobalt oxides<sup>31</sup> and can sometimes lead to a reversible capacity higher than the theoretical value after several cycles (Table 1.7, example 6). Some explanations are proposed to justify the origin of this phenomenon:

- The gradual increase of capacity can be an effect of the material morphology. For instance, for NiCo<sub>2</sub>O<sub>4</sub> nanorods, it is assumed that the increase of capacity is coming from the material porosity whereas for ZnFe<sub>2</sub>O<sub>4</sub> spicate architecture, the phenomenon can be due to a morphological re-configuration, both of them leading to the activation of more additional

particles to react with lithium that were not initially electroactive<sup>65,73</sup>. This assumption only explains the gradual increase of capacity but not the value higher than the theory.

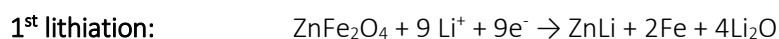
- Another explanation for this particular behavior is that the increase capacity is coming from the formation of a reversible polymeric gel-type layer on the active material. This polymeric layer may reversibly store part of the lithium<sup>65,75,76</sup>. Such films are electrochemically formed by the polymerization of the electrolyte, which depends on the metal species. That is why it is more often observed for cobalt which has a high catalytic activity compared to other metals<sup>75</sup>.
- The SEI can also work as an extra-charge reservoir allowing the reversible reaction of more lithium during cycling. Rezvani *et al.* worked on the study of this electrolyte interface and showed that the SEI formation can be accompanied by the formation of a reversible layer of few nm as the uppermost SEI. They demonstrated by calculation that the reversible storage of lithium into this reversible SEI can be one source of extra-capacity observed for TMO and MTMO<sup>41</sup>.

Even if several assumptions have been proposed to explain the origin of this specific behavior, further studies are still needed to understand the storage mechanism and the enhancement of electrochemical performances.

### Choice of ZnFe<sub>2</sub>O<sub>4</sub>

Among the various MTMO (in particular ACo<sub>2</sub>O<sub>4</sub>, AFe<sub>2</sub>O<sub>4</sub> and AMn<sub>2</sub>O<sub>4</sub>), ZnFe<sub>2</sub>O<sub>4</sub> was chosen to be studied in this thesis. Indeed, even if cobaltites (ACo<sub>2</sub>O<sub>4</sub>) seem to be the MTMO with the greatest storage properties according to literature results, they are however toxic and expensive materials. Manganese-based oxides can also be very attractive as they possessed high theoretical capacities. But practically, it is very difficult to fully use manganese oxides for cycling because of their low electrical conductivity (around 10<sup>-7</sup>-10<sup>-8</sup> S.cm<sup>-1</sup>) that can cause poor capacity retention and low rate capability<sup>31</sup>. Iron-based oxides materials show high theoretical capacities and are abundant, cheap, non-toxic and environment-friendly.

ZnFe<sub>2</sub>O<sub>4</sub> was thus chosen for this work instead of CoFe<sub>2</sub>O<sub>4</sub> as zinc can contribute to additional capacity owing to the ability of Zn to form an alloy with lithium which is not the case of cobalt. Zinc ferrite has a theoretical capacity of 1001 mAh.g<sup>-1</sup> coming from the insertion of 9 Li<sup>+</sup> ions during the lithiation process. Various research works try to explain the lithiation and delithiation storage mechanism in ZnFe<sub>2</sub>O<sub>4</sub>. The most commonly accepted mechanism is presented below:





This mechanism has been partially confirmed and detailed by several research works<sup>79–81</sup>. It has been supposed that during lithiation, the process is divided into three main steps: first, there is the insertion of lithium into the crystalline structure to form a  $\text{Li}_x\text{ZnFe}_2\text{O}_4$  phase; the second part of the mechanism involves the conversion reaction and the destruction of the crystalline structure (amorphization) leading to the formation of a Zn-Fe- $\text{Li}_2\text{O}$  nanocomposite. This nanocomposite consists in metallic Zn and Fe nanoparticles embedded in a  $\text{Li}_2\text{O}$  matrix. A third and last step occurs then, corresponding to the alloying reaction between Zn nanoparticles and Li giving the alloy ZnLi. This first lithiation process is not completely reversible because during the first delithiation, the initial crystalline structure with  $\text{ZnFe}_2\text{O}_4$  cannot be recovered. ZnO and  $\text{Fe}_2\text{O}_3$  amorphous phases are assumed to be formed instead. It is assumed that lithium further cycling is then realized with the two phases ZnO and  $\text{Fe}_2\text{O}_3$ .

To validate the storage mechanism proposed above, cyclic voltammetry (CV) has been conducted by Xing *et al* with a scan rate of  $0.1 \text{ mV}\cdot\text{s}^{-1}$  on a  $\text{ZnFe}_2\text{O}_4$  electrode (with a nano-octahedrons morphology) vs. metallic lithium, in the voltage range of 0.01 V-3.0 V (Figure 1.12)<sup>81</sup>.

This electrochemical technique measures the current when the potential of the working electrode ( $\text{ZnFe}_2\text{O}_4$ ) is varied. This technique allows the observation of the cathodic/reduction (lithiation of  $\text{ZnFe}_2\text{O}_4$ ) and anodic/oxidation (delithiation of  $\text{ZnFe}_2\text{O}_4$ ) peaks. More details about this characterization technique will be given in chapter 2.

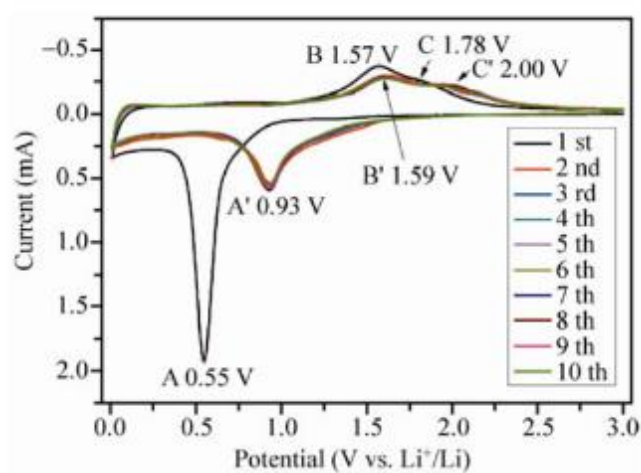


Figure 1.12. Cyclic voltamograms of the  $\text{ZnFe}_2\text{O}_4$  electrode at a scan rate of  $0.1 \text{ mV/s}$  in the voltage range of  $0.01\text{V}-3.0\text{V}$  vs.  $\text{Li}/\text{Li}^+$ <sup>81</sup>

During the first lithiation, a main cathodic peak is observed at 0.55V that can be assigned to the reduction reaction of  $\text{ZnFe}_2\text{O}_4$  with lithium to form Zn and Fe metals and eventually the further lithiation of Zn by the alloying ZnLi reaction. The first delithiation shows two main oxidation peaks at 1.57V and another one at 1.78V which may correspond to the oxidation of Zn to ZnO and Fe to  $\text{Fe}_2\text{O}_3$ .

The shift of both reduction and oxidation peaks after the first cycles can indicate a structural rearrangement of the anode material.

The proposed storage mechanism can also be supported by the charge and discharge curves shown below (Figure 1.13). For the first discharge, areas A, B and C are characterized by three small voltage slopes that can be attributed to the progressive insertion of lithium into the crystalline structure of  $\text{ZnFe}_2\text{O}_4$ . The long voltage plateau at 0.8V is attributed to the conversion reaction with the formation of Zn and Fe nanoparticles. The last slope until the cut-off voltage may represent the alloying reaction between Zn and Li but also the formation of a polymeric gel-type layer at a deep discharge<sup>79</sup>.

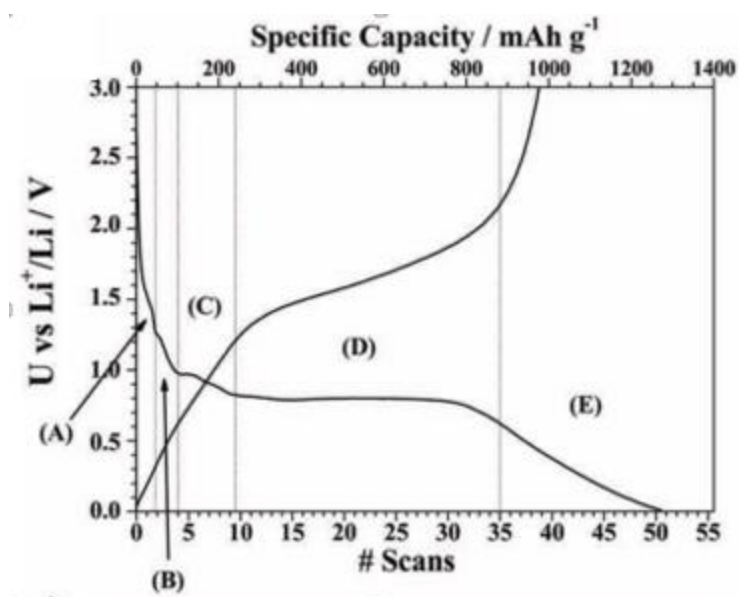


Figure 1.13. First charge and discharge profiles for  $\text{ZnFe}_2\text{O}_4$  in the voltage range of 0.01-3.0V<sup>79</sup>

Some further characterization can help in identifying the different species involved in the lithium storage mechanism. In particular, XRD can show the intermediate steps of the lithiation process for the first cycle. X-ray diffraction (XRD) measurements were done by Teh *et al.* at different potentials during the first discharge (1.3V, 0.9V and 0.005V vs.  $\text{Li}/\text{Li}^+$ ) (Figure 1.14). It can be observed that intermediate  $\text{Li}_x\text{ZnFe}_2\text{O}_4$  phases are formed before 0.9V showing the lithium insertion before the conversion reaction. However, after this lithium insertion, the material seems to become amorphous and no more peak is observable. This loss of crystalline structure is definitive and XRD characterization is no longer efficient to characterize the electrode material after the first lithiation.

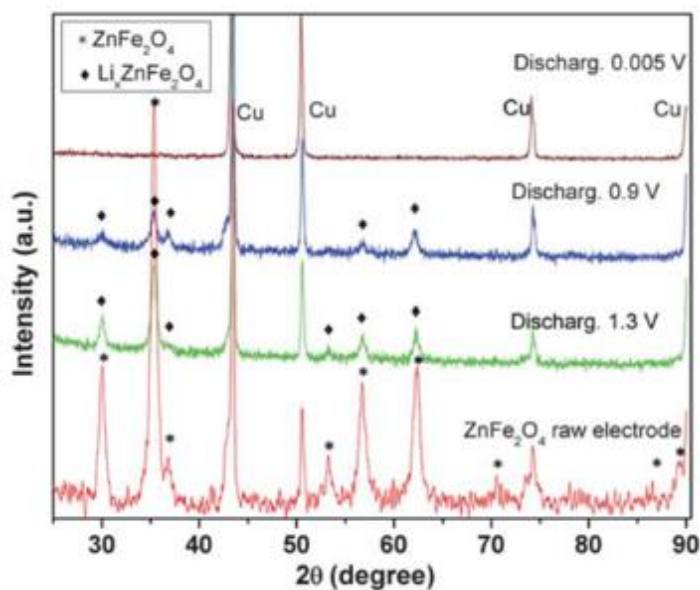


Figure 1.14. Ex-situ XRD at different steps of the first discharge for  $\text{ZnFe}_2\text{O}_4$ <sup>80</sup>

Ex-situ high-resolution transmission electron microscopy (HRTEM) images and selected area electron diffraction (SAED) after a discharge (fully discharged at 0.01V) and a charge (fully charged at 3.0V) demonstrate the presence of the different species involved in the lithiation and delithiation reactions (Figure 1.15). In particular, HRTEM images of the discharged electrode highlight small nanoparticles (3- 6 nm) dispersed into an amorphous matrix corresponding to Fe, Zn and LiZn according to the lattice fringes and the diffraction rings of SAED. When the electrode is fully charged, ZnO and  $\text{Fe}_2\text{O}_3$  are observed instead of  $\text{ZnFe}_2\text{O}_4$ , showing that the initial mixed-transition metal oxide is not resumed after the first cycle but a mixture of ZnO and  $\text{Fe}_2\text{O}_3$ <sup>81</sup>.

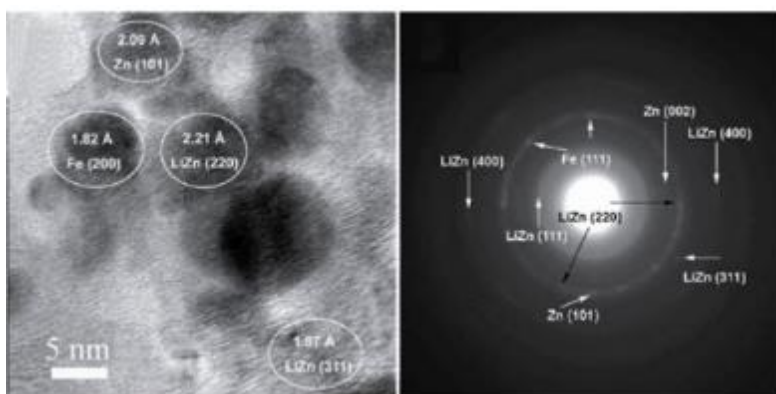


Figure 1.15. Ex-situ HRTEM after a full discharge and its corresponding SAED<sup>81</sup>

Various studies have been conducted by the research community to evaluate  $\text{ZnFe}_2\text{O}_4$  electrochemical performances and some of these results are displayed in Table 1.8.

## Transition metal oxides as anode materials for Li-ion batteries

Table 1.8. Examples of ZnFe<sub>2</sub>O<sub>4</sub> electrochemical performances as anode for lithium-ion batteries

Morphology	1 <sup>st</sup> cycle			Reversible capacity/n <sup>th</sup> cycle	Voltage range	Current rate and loading (when provided)
	Lithiation	Delithiation	Efficiency			
Nanospheres <sup>82</sup>	1215 mAh.g <sup>-1</sup>	851 mAh.g <sup>-1</sup>	70%	500 mAh.g <sup>-1</sup> 50 <sup>th</sup> cycle	0.005-3.0V	50 mA.g <sup>-1</sup> X
Cubic nanoparticles <sup>76</sup>	1151 mAh.g <sup>-1</sup>	801 mAh.g <sup>-1</sup>	70%	367 mAh.g <sup>-1</sup> 50 <sup>th</sup> cycle	0.01-3.0V	60 mA.g <sup>-1</sup> X
Agglomerated nanoparticles <sup>67</sup>	1180 mAh.g <sup>-1</sup>	810 mAh.g <sup>-1</sup>	69%	615 mAh.g <sup>-1</sup> 50 <sup>th</sup> cycle	0.005-3.0V	60 mA.g <sup>-1</sup> 3 mg/electrode
Hollow spheres <sup>83</sup>	1200 mAh.g <sup>-1</sup>	900 mAh.g <sup>-1</sup>	75%	900 mAh.g <sup>-1</sup> 50 <sup>th</sup> cycle	0.005-3.0V	65 mA.g <sup>-1</sup> X
Nanorods <sup>84</sup>	1339 mAh.g <sup>-1</sup>	1112 mAh.g <sup>-1</sup>	83%	625 mAh.g <sup>-1</sup> 300 <sup>th</sup> cycle	0.01-3.0V	150 mA.g <sup>-1</sup> X

The results of the Table 1.8 show very different performances for ZnFe<sub>2</sub>O<sub>4</sub>, some of them giving very low reversible capacity after few cycles at low current rate. Even if electrochemical performances are dependent on the cycling conditions, the electrode formulation as well as the chosen electrolyte, the active material itself also have a large influence on the experimental performance. These considerations make difficult the straightforward comparison between the different materials morphologies reported in Table 1.8. Nevertheless, it is obviously necessary to work on the material optimization to improve the electrochemical activity of ZnFe<sub>2</sub>O<sub>4</sub>.

### 3. Optimization of the material performances

Conversion materials as MTMO suffer volume expansion/contraction during lithiation and delithiation, limiting their performance for long-time cyclings but several ways are under consideration to overcome this issue (Figure 1.16).



Figure 1.16. Strategies to enhance electrode performances<sup>18</sup>

### Nanostructuring

It is initially important to know that the nanoscaling of MTMO is crucial to realize the conversion reaction. Indeed it has been proven that a reversible conversion reaction can only become effective in nanoscale particles as they are able to manifest superior electrochemical activity<sup>85</sup>. The redox reaction between metal oxides and lithium ions is thermodynamically favorable but the reverse reaction seems to be unachievable for bulk materials<sup>86</sup>. It is assumed that the metal nanoparticles formed during the lithiation can facilitate the reversible decomposition of the Li<sub>2</sub>O matrix meaning that working with nanostructured materials with a large surface area and a high surface energy can facilitate the delithiation reaction<sup>85</sup>.

Electrochemical performances can be improved at nanoscale thanks to a better diffusion of lithium into the material. To improve the lithium kinetics, the diffusion time of lithium into the material has to be shortened. For solid-state diffusion of lithium, the diffusion time is dependent on the diffusion coefficient and the diffusion length. By decreasing the diffusion length (i.e. by nanostructuring the electrode materials), lithium kinetics can be substantially improved<sup>52</sup>. In nanoparticles systems, lithium ions can diffuse faster thanks to shortened distances and the material can quickly absorb and store a high number of lithium without causing large degradation of the electrode, resulting in enhanced reversible capacity and capacity retention.

Except the thermodynamic restriction for the conversion reaction, another problem with the lithiation/delithiation of mixed-transition metal oxides is the important volumetric variation upon cycling which has been identified as the main cause of capacity fading. Proper nanostructures can

sustain this structural disintegration and promote lithium storage reactions<sup>85</sup>. For instance, nanowires or nanosheets, with their low-dimensional structure can sustain large lithium insertion as well as hollow or mesoporous particles that can accommodate the volume variation (Figure 1.17). However, by limiting the volume variation, the volumetric capacity becomes lower due to the decrease content of the active material<sup>85</sup>.

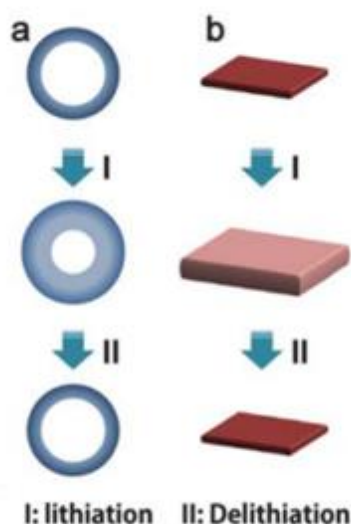


Figure 1.17. Nanostructuring of the active material to sustain the volumetric expansion during cycling<sup>85</sup>

Even if nanoparticles present several advantages (enhanced electrochemical reactions, shorten diffusion lengths for faster ionic and electronic transport, better accommodation of the strain during lithiation and delithiation for longer cycle life, higher electrode and electrolyte contact for higher charge/discharge rates) the use of nanoparticles can sometimes be problematic<sup>33</sup>. Because of the increased surface area of the active material, more undesirable reaction between electrolyte and electrode can occur with the formation of more SEI, which causes high irreversibility, leading to poor cycling and calendar life<sup>52</sup>. Moreover, for MTMO, it is known that the nanoparticles are easy to aggregate during cycling, making the insertion and extraction of lithium ions more and more difficult<sup>87</sup>. Another major drawback with nanoparticles is their synthesis, which can be much more complex to obtain the desired morphology.

### Morphology control

As explained above, nanostructuring may help in improving the electrochemical activity of  $\text{ZnFe}_2\text{O}_4$ . However, beyond the size, the morphology of these nanoparticles can have a non-negligible influence on the obtained performances.

Won *et al.* have worked on yolk-shell nanostructures for  $\text{ZnFe}_2\text{O}_4$ . This morphology consists in a core-void-shell configuration as shown on the TEM image below. The performances of this specific

morphology are compared with those of spherical  $\text{ZnFe}_2\text{O}_4$  nanoparticles with similar size (Figure 1.18).

At the first cycle, the yolk-shell particles have a higher discharge capacity and a higher coulombic efficiency. They show that the yolk-shell structure is able to maintain a large reversible capacity around  $900 \text{ mAh.g}^{-1}$  for 200 cycles whereas the filled structure sees its capacity fading very rapidly to be stabilized around  $350 \text{ mAh.g}^{-1}$  only after 200 cycles. The authors explain this better performance by a more stable structure for yolk-shell particles, able to accommodate the volumes changes which is not the case for the filled particles<sup>88</sup>. However, as the void between the shell and the core does not seem to be very large, this better performance for the yolk-shell particles may also be explained by the formation of a more stable SEI.

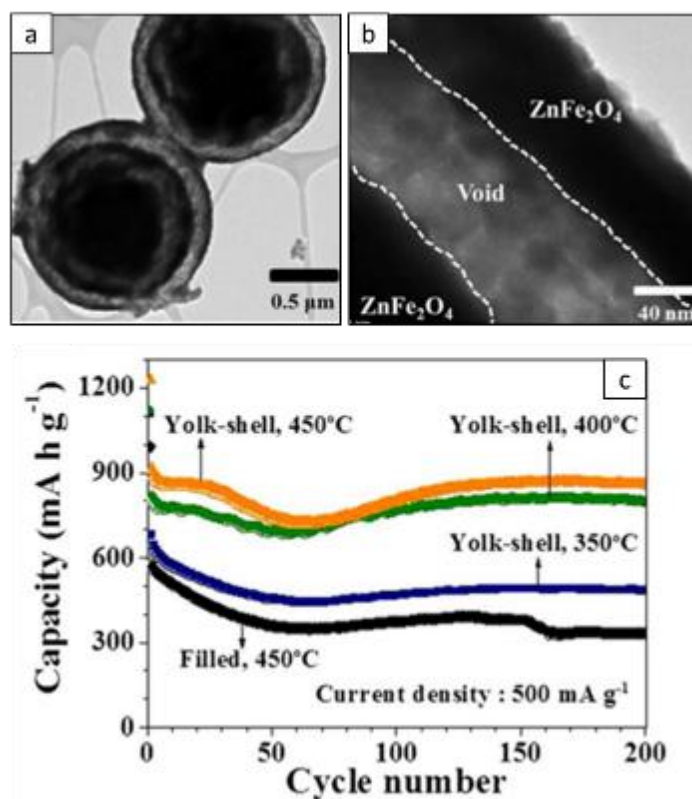


Figure 1.18. Morphology of the yolk-shell structure observed by TEM (a,b) and electrochemical performances of yolk-shell and spherical  $\text{ZnFe}_2\text{O}_4$  nanoparticles at  $500 \text{ mA.g}^{-1}$ (c)

Another study compares the performances of  $\text{ZnFe}_2\text{O}_4$  nanorods and nanofibers prepared by electrospinning (Figure 1.19)<sup>80</sup>. They were both cycled vs. metallic lithium at  $60 \text{ mA.g}^{-1}$ . Zinc ferrite nanofibers are able to maintain a capacity above  $600 \text{ mAh.g}^{-1}$  for 30 cycles with a slow decrease of the capacity. In comparison, nanorods performances are really low with a rapid decrease of the capacity after the first cycle and a stabilization of the reversible capacity below  $300 \text{ mAh.g}^{-1}$  (less than graphite capacity) after 30 cycles. The difference in the electrochemical behavior of these two materials are

related to their morphology. According to the authors, the nanofibers are longer and thinner than the nanorods and form a continuous framework with opened pores which are beneficial for the cycling vs. lithium.

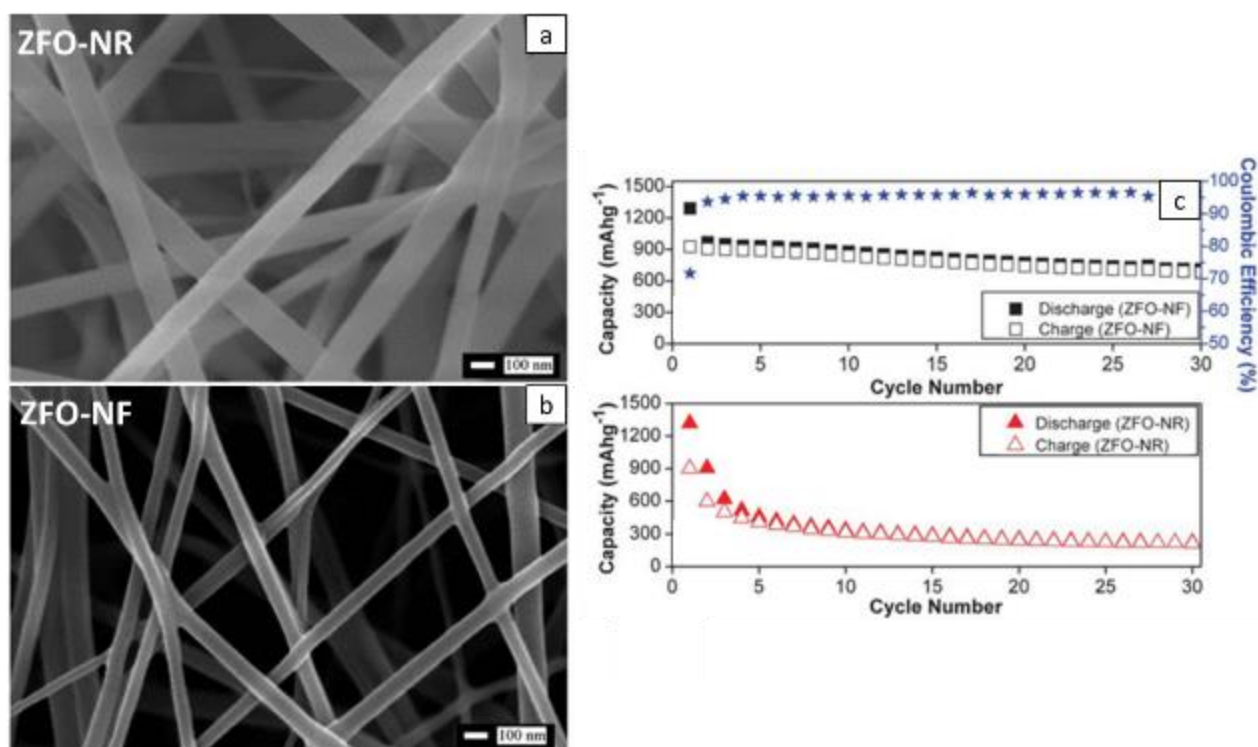


Figure 1.19. Morphology of the nanorods (a) and nanofibers (b) observed by SEM and comparison of performances during cyclings at 60 mA.g<sup>-1</sup>(c)

The optimization of the material morphology seems to be very important to keep the benefits of nanostructuration and enhance the electrochemical performances vs. lithium. Another solution to improve the electrochemical activity of the material is to work on carbon addition or carbon coating as discussed below.

#### Carbon addition

The storage performance of ZnFe<sub>2</sub>O<sub>4</sub> can be enhanced by carbon addition or carbon coating of the nanoparticles. The synthesis of ZnFe<sub>2</sub>O<sub>4</sub>/carbon composite can help in improving the conductivity of the material and so lead to better ions and electrons kinetics during charge/discharge process. Besides, the coating around the nanoparticles can be beneficial to the material by limiting the volume expansion/contraction during lithiation and delithiation and allow a better stability during cycling.

Tankachan *et al.* have investigated the effect of carbon addition on ZnFe<sub>2</sub>O<sub>4</sub> nanopowder (Figure 1.20)<sup>89</sup>. They synthesized a ZnFe<sub>2</sub>O<sub>4</sub>/C nanocomposite and a pure ZnFe<sub>2</sub>O<sub>4</sub> nanopowder. Pure ZnFe<sub>2</sub>O<sub>4</sub> nanopowder was prepared by a sol-gel method to obtain agglomerated nanoparticles. The

composite has been prepared using Super P Li carbon black ball-milled with the previous sol-gel prepared  $\text{ZnFe}_2\text{O}_4$ . This process leads to a  $\text{ZnFe}_2\text{O}_4/\text{C}$  nanocomposite with small particles and a higher surface area with higher pore volume. The obtained nanocomposite shows a morphology consisted in small clusters and nanoparticles homogeneously dispersed in a carbon host.

The two materials were then cycled at C/10 current rate (corresponding to  $100 \text{ mA.g}^{-1}$  for  $\text{ZnFe}_2\text{O}_4$  and  $71 \text{ mA.g}^{-1}$  for the composite, calculated with the amount of carbon). The same electrolyte was used for the two samples but the formulation of the electrode was slightly different: pure  $\text{ZnFe}_2\text{O}_4$  electrode was prepared using 70% of active material, 20% of carbon black and 10% of CMC whereas the proportions were 80:10:10 for  $\text{ZnFe}_2\text{O}_4/\text{C}$  nanocomposite. Comparison of both materials during a galvanostatic cycling shows the better electrochemical performance of the nanocomposite. Except for the first cycle where there is a large capacity loss (certainly due to SEI formation) for both electrodes, the capacity of the  $\text{ZnFe}_2\text{O}_4/\text{C}$  nanocomposite is stabilized after the second cycle until hundred cycles with a capacity of  $681 \text{ mA.h.g}^{-1}$ , which is very close to the theoretical capacity of the composite ( $710 \text{ mA.h.g}^{-1}$ ). On the contrary, pure  $\text{ZnFe}_2\text{O}_4$  sees its reversible capacity continuously decrease with less than  $400 \text{ mA.h.g}^{-1}$  left after 100 cycles. The carbon black serves as a conductive scaffold between the current collector and  $\text{ZnFe}_2\text{O}_4$  particles. Besides, the large specific surface area and the porosity offer a better and larger electrolyte/electrode contact and promote the infiltration of electrolyte and the fast diffusion of lithium ions during cycling in the electrode. These advantages cannot be found with pure  $\text{ZnFe}_2\text{O}_4$  and can explain the important difference in terms of performances.

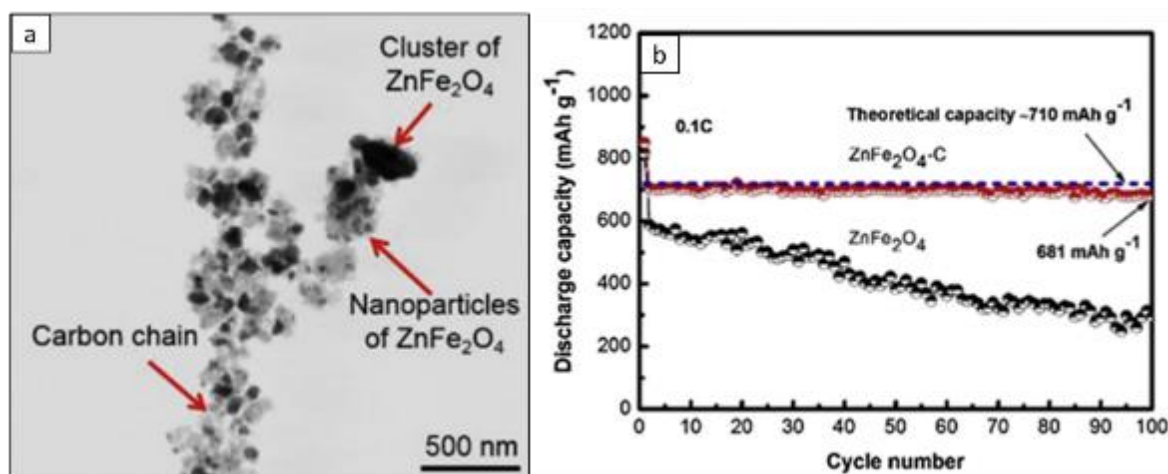


Figure 1.20. TEM image of  $\text{ZnFe}_2\text{O}_4/\text{C}$  nanocomposite (a) and comparison of the electrochemical performance with pure  $\text{ZnFe}_2\text{O}_4$  at C/10 current rate (b)

Other researchers have worked on a  $\text{ZnFe}_2\text{O}_4/\text{graphite}$  nanocomposite with nanoparticles of zinc ferrite (20-30nm) onto the surface of flake graphite (10-20  $\mu\text{m}$ ) prepared by a hydrothermal synthesis followed by a sintering process (Figure 1.21). Pure zinc iron oxide has been cycled as well as

ZnFe<sub>2</sub>O<sub>4</sub>/graphite for comparison at 100 mA.g<sup>-1</sup>. As in the previous examples, the nanocomposite shows better electrochemical performances with a more stable capacity during cycling directly after few cycles whereas the pure ZnFe<sub>2</sub>O<sub>4</sub> sees its capacity decreasing gradually during the charge/discharge process. Once again, according to the authors, this improvement of performance for the nanocomposite can be due to the presence of graphite which is able to work as a buffer and increase the whole material conductivity, enhancing the lithiation/delithiation kinetics<sup>87</sup>.

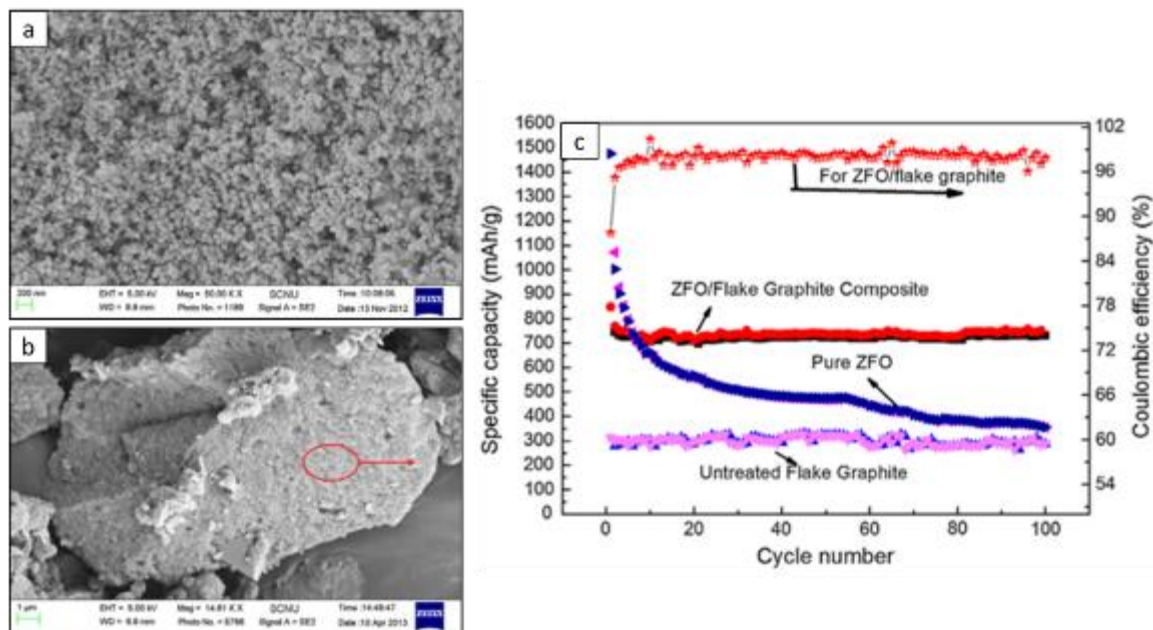


Figure 1.21. SEM images of ZnFe<sub>2</sub>O<sub>4</sub> particles (a) and ZnFe<sub>2</sub>O<sub>4</sub>/graphite (b). Comparison of electrochemical performances of ZnFe<sub>2</sub>O<sub>4</sub> and ZnFe<sub>2</sub>O<sub>4</sub>/graphite at 100 mA.g<sup>-1</sup>(c)

Among the different carbon compounds which are studied, graphene is interesting to improve ZnFe<sub>2</sub>O<sub>4</sub> for lithium-ion batteries. ZnFe<sub>2</sub>O<sub>4</sub> particles were prepared by urea-assisted auto-combustion synthesis using zinc and iron nitrates solution. The ZnFe<sub>2</sub>O<sub>4</sub>/graphene composite was prepared by mixing this precursors solution with graphene nanosheets before the combustion process. The comparison of electrochemical performances between ZnFe<sub>2</sub>O<sub>4</sub>/graphene and pure ZnFe<sub>2</sub>O<sub>4</sub> reveals once again the improvement coming from the graphene addition (cycling at 100 mA.g<sup>-1</sup>) (Figure 1.22). Pure ZnFe<sub>2</sub>O<sub>4</sub> delithiation capacity fades directly after the first cycle during 30 cycles before being stabilized around 200 mAh.g<sup>-1</sup> which is lower than graphite. The nanocomposite however shows greatly enhanced electrochemical activity with 700 mAh.g<sup>-1</sup> of reversible capacity after 75 cycles. The significantly improved performance of the nanocomposite electrode can be attributed to the fact that the ZnFe<sub>2</sub>O<sub>4</sub> nanoparticles were bonded to the graphene nanosheets, which could greatly improve the intrinsic conductivity of ZnFe<sub>2</sub>O<sub>4</sub> and effectively buffer the strain induced by lithiation<sup>90</sup>.

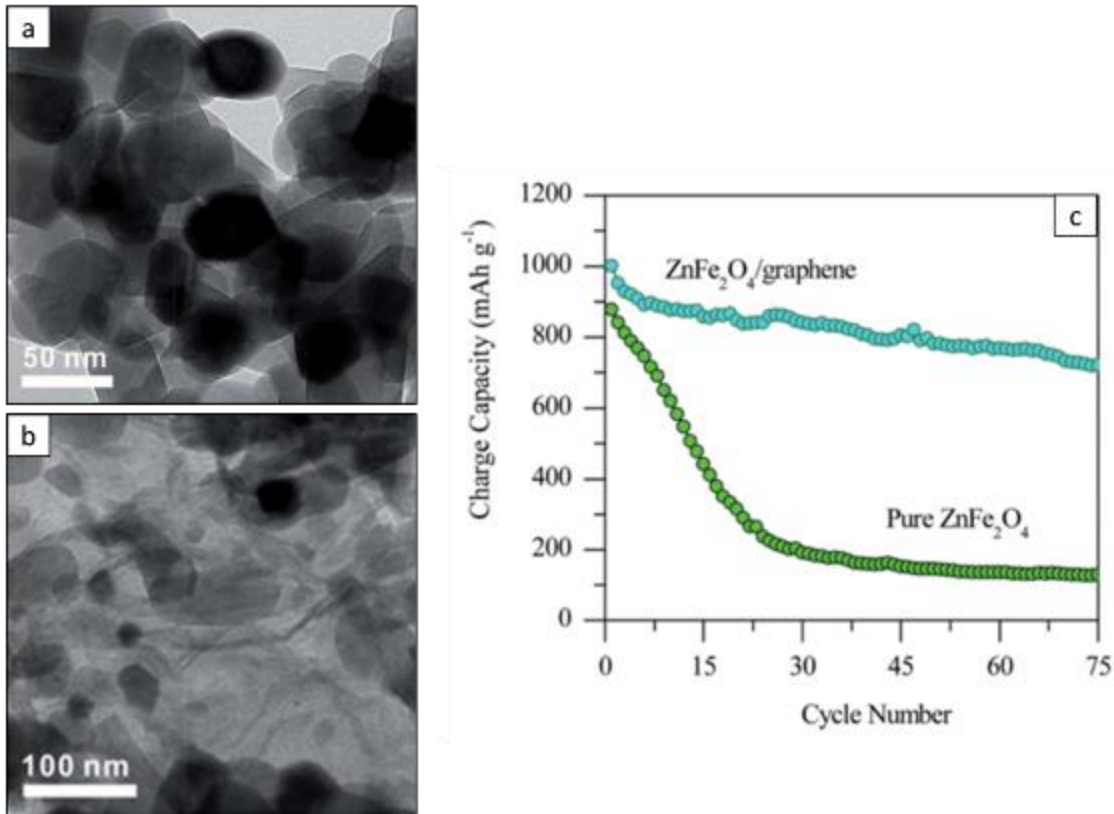


Figure 1.22. TEM images of pure ZnFe<sub>2</sub>O<sub>4</sub> nanoparticles (a) and ZnFe<sub>2</sub>O<sub>4</sub>/graphene (b). Comparison of performances between pure ZnFe<sub>2</sub>O<sub>4</sub> and ZnFe<sub>2</sub>O<sub>4</sub>/graphene composite at 100 mA.g<sup>-1</sup>.

Instead of only carbon addition, it is possible to go further with a carbon coating. A comparison was made between ZnFe<sub>2</sub>O<sub>4</sub>/C nanodiscs and ZnFe<sub>2</sub>O<sub>4</sub> nanodiscs<sup>91</sup> (Figure 1.23). ZnFe<sub>2</sub>O<sub>4</sub>/C nanodiscs are coated with a uniform carbon shell realized by a molten salt route followed by a carbonization process. The galvanostatic cycling of this sample compared to pure ZnFe<sub>2</sub>O<sub>4</sub> highlights a difference in terms of reversible capacity, stability and capacity retention. As it can be seen below, the carbon coated zinc iron oxide shows a stable capacity from the first few cycles until the 100<sup>th</sup> cycle, around 965 mAh.g<sup>-1</sup> at 100 mA.g<sup>-1</sup>. In comparison, the pure phase ZnFe<sub>2</sub>O<sub>4</sub> reveals a gradual capacity fading during the 100 cycles. It seems the carbon coating can accommodate the volume change in the material and avoid the agglomeration of the small nanoparticles during the repeated charge/discharge process, resulting in the good Li-ion storage performance.

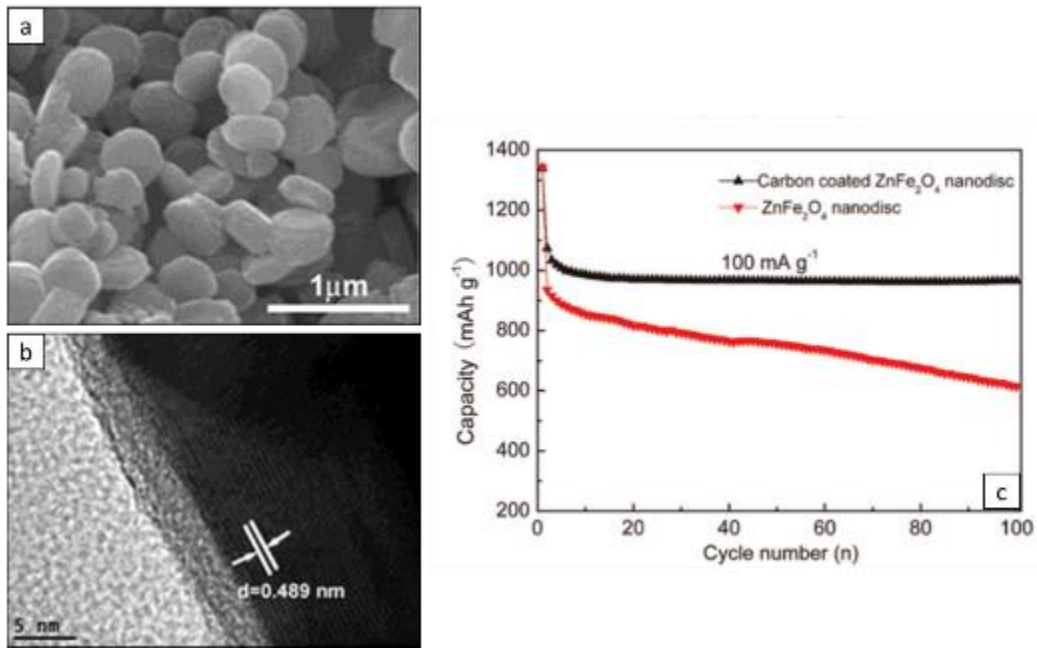


Figure 1.23. Morphology of ZnFe<sub>2</sub>O<sub>4</sub>/C nanodiscs observed by TEM (a) and HRTEM (b) and comparison of performances with ZnFe<sub>2</sub>O<sub>4</sub> (c)

The importance of nanoscaling for electrode materials has been demonstrated in this part, as well as the influence of the morphology and the benefits of carbon addition to enhance ZnFe<sub>2</sub>O<sub>4</sub> performances. In particular, nanostructuration and morphology influence should be studied in this thesis. In this context, a proper synthesis technique has to be chosen to be able to obtain the required ZnFe<sub>2</sub>O<sub>4</sub> nanoparticles with controlled composition and morphology.

**III. Experimental methods for the synthesis of nanostructured mixed-transition metal oxides**

Several processes can be used to synthesize mixed-transition metal oxides nanoparticles. The different methods can be classified in three categories: solid-state syntheses, liquid-phase syntheses and vapor-phase syntheses. This latter category, which includes laser pyrolysis, will be presented in details here.

**1. Solid-state syntheses**

Mechanical routes

MTMO nanomaterials can be prepared by different mechanical routes. These techniques use mechanical energy by ball-milling the reactants to achieve chemical reactions. These processes constitute easy and cheap solid state approaches to prepare nanostructured powders. Different mechanical routes for the syntheses of ferrites nanopowders are presented in the Figure 1.24.

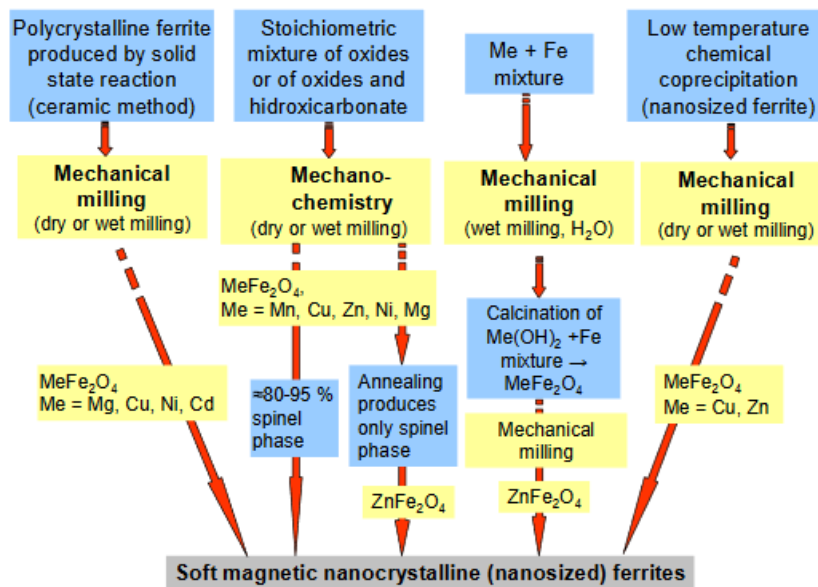


Figure 1.24 Different mechanical routes for the syntheses of nanocrystalline ferrites<sup>92</sup>

During the synthesis, micrometric powders are mechanically crushed. Sometimes, heat energy is applied during annealing to promote the atomic diffusion and form a new nanostructured material. Moreover, high-energy ball-milling presents a drawback that can be turned into an advantage for battery application: it is difficult to obtain isolated nanoparticles by this process and grains generally suffer from severe agglomeration (nanocrystalline large grains) and wide particle size distribution. As a result, the specific surface area is lower, which could help in limiting SEI-related issues in the

## Experimental methods for the synthesis of nanostructured mixed-transition metal oxides

electrode. However, the purity of the obtained nanoparticles is limited by the contact between the reactants and the jars and balls that favours the presence of impurities in the final product.

### 2. Liquid phase syntheses

#### Solvothermal and hydrothermal methods

Solvothermal and hydrothermal methods are among the most common processes used for the synthesis of MTMO nanopowders. These techniques refer to the synthesis by chemical reactions in a sealed autoclave above ambient temperature and pressure making easier the interaction of precursors during synthesis<sup>93</sup>.  $\text{ZnFe}_2\text{O}_4$ <sup>81</sup>,  $\text{MnCo}_2\text{O}_4$ <sup>94</sup> or  $\text{ZnMn}_2\text{O}_4$ <sup>39</sup> nanoparticles have already been obtained by these methods. In this process, precursors like nitrates, chlorides, sulfates, acetates are dissolved in water for hydrothermal synthesis or in non-aqueous solvent for solvothermal synthesis. The solution is then transferred into a stainless steel sealed autoclave and heated for several hours. A precipitate is synthesized during the process and after several washings and drying into vacuum, nanopowders are obtained.

Solvothermal and hydrothermal syntheses offer the possibility to control the shape and morphology of the obtained particles by controlling the experimental conditions as shown below (Figure 1.25). On the counterpart, they suffer multiple process steps and long duration, and also show issues of repeatability of batch production.

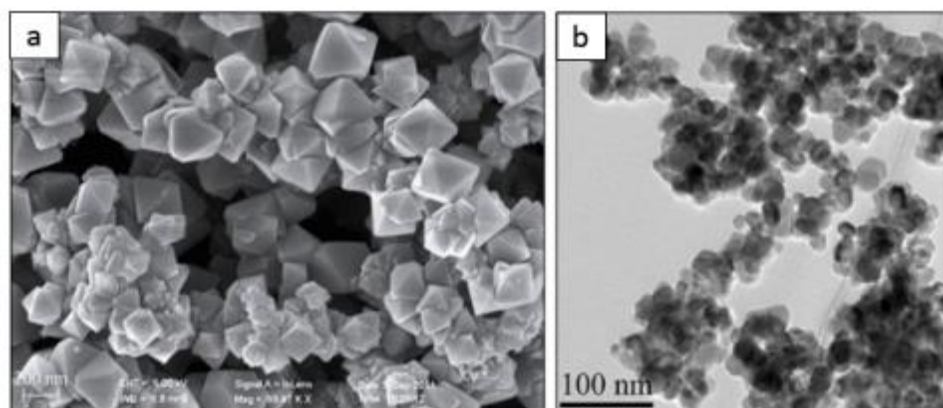


Figure 1.25. (a)  $\text{ZnFe}_2\text{O}_4$  nano-octahedrons obtained by hydrothermal synthesis ( $T: 180^\circ$  for 14h)<sup>81</sup>, (b)  $\text{MnCo}_2\text{O}_4$  spherical nanoparticles obtained by hydrothermal synthesis ( $T: 180^\circ\text{C}$ , 8h)<sup>94</sup>

#### Sol-gel synthesis

The sol-gel synthesis is a flexible way to produce nanomaterials, and in particular metal oxides, of high purity. Depending on how the synthesis is realized, nanopowders as well as coatings or fibers can be obtained (Figure 1.26).

## Experimental methods for the synthesis of nanostructured mixed-transition metal oxides

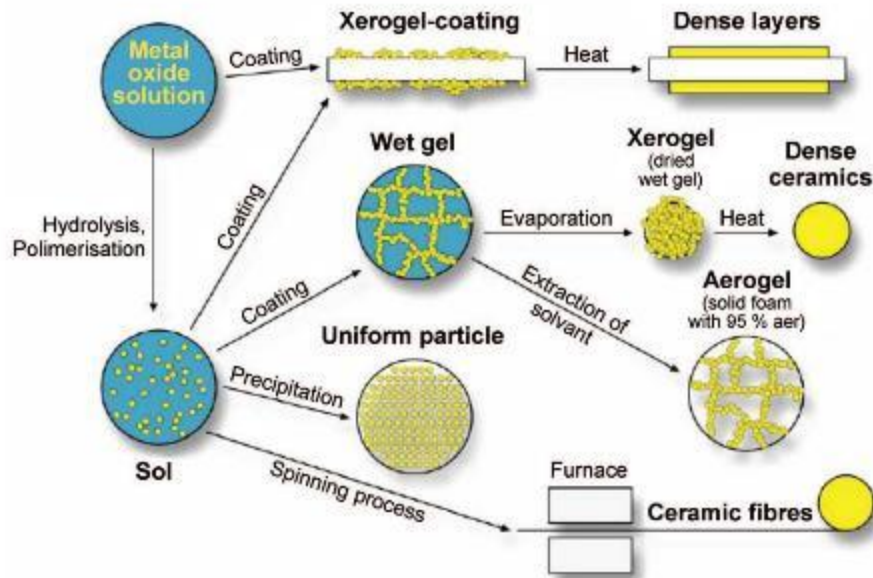


Figure 1.26. Synthesis of nanomaterials by the sol-gel method<sup>95</sup>

To obtain metal oxides powders, the technique consists in the hydrolysis and polymerization of a precursor solution, followed by a condensation. A colloidal suspension is so formed (sol). Further polymerization leads to the formation of a gel. After a thermal treatment, the desired oxide powders can be obtained.

ZnFe<sub>2</sub>O<sub>4</sub> nanopowders were obtained by using nitrate precursors and citrate to form the sol which was then annealed at 600°C<sup>96</sup>. As well, CoFe<sub>2</sub>O<sub>4</sub> nanoparticles were synthesized by mixing nitrate precursors in isopropylalcohol. The mixture was then annealed at 350°C<sup>63</sup> (Figure 1.27).

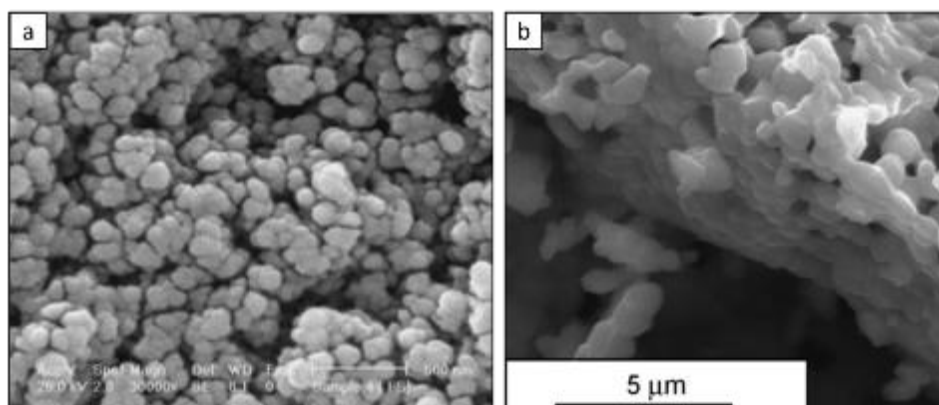


Figure 1.27. SEM images of ZnFe<sub>2</sub>O<sub>4</sub> and NiFe<sub>2</sub>O<sub>4</sub> nanoparticles obtained by the sol-gel method

The sol-gel method presents several advantages as the possibility to synthesize various types of nanomaterials (nanopowders, nanofibers, coatings) and the fact that it is a low temperature

## Experimental methods for the synthesis of nanostructured mixed-transition metal oxides

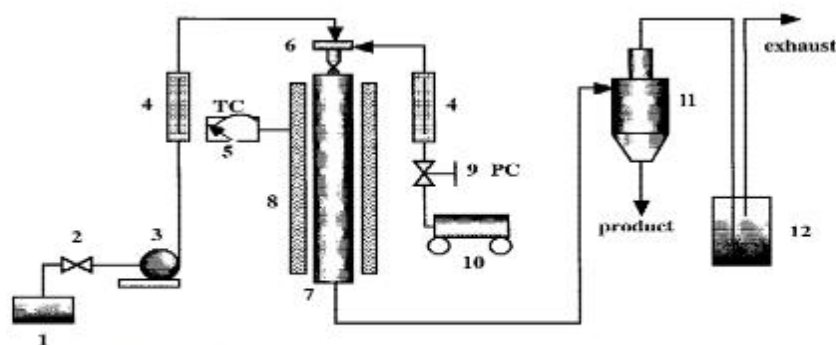
process. Some residual organic compounds are sometimes still present in the produced powder and one more step of thermal post-treatment is necessary to obtain the pure nanopowder.

### 3. Vapor phase syntheses

#### Spray pyrolysis

Many mixed-transition metal oxides are produced by spray pyrolysis that allows the synthesis of nanopowders as well as thin films<sup>97-100</sup>. This process can be easily used for large-scale production as a continuous and cost effective technique.

Basically, a solution of precursors is sprayed with an atomizer into a furnace operating at high temperature under continuous flow. The solution can be a pure liquid precursor, or constituted by a solute dissolved in an aqueous or organic solvent. A typical set up is reported in Figure 1.28 from Zhao et al<sup>101</sup>.



Experimental apparatus of spray pyrolysis process: (1) precursor solution, (2) control valve, (3) metering pump, (4) flow meter, (5) thermal controller, (6) two-fluid atomizer, (7) quartz reaction tube, (8) resistance furnace, (9) pressure controller, (10) air compressor, (11) bag filter, (12) gas purification column.

Figure 1.28. Schema of the spray pyrolysis process<sup>101</sup>

Upon heating, the precursors molecules contained in the aerosol droplets are decomposed, leading to the formation of the powders. In the specific case of metal oxides synthesis, the most commonly used precursors are acetates<sup>100</sup> or nitrates dissolved in water<sup>78</sup>.

Depending on solution characteristics (nature of the pure liquid or of the solvent, nature of dissolved salt, concentration) and operating parameters (precursor flow rate, temperature...), different growth mechanisms can be followed. These different mechanisms, mostly related to solvent evaporation, diffusion of species and precipitation in the drying droplets lead to objects that can share the same chemical composition but exhibit very different morphologies (hollow particles, porous or dense, large or small...). These general mechanisms were well described by Messing *et al*<sup>102</sup>, and lead generally to the formation of one particle per droplet after drying of the solution droplet and thermal

## Experimental methods for the synthesis of nanostructured mixed-transition metal oxides

reaction of the precursors inside the dried particle (Figure 1.29). While the obtained grains can be nanostructured with crystallites about several nm, their outer dimensions are generally of few hundreds of nm.

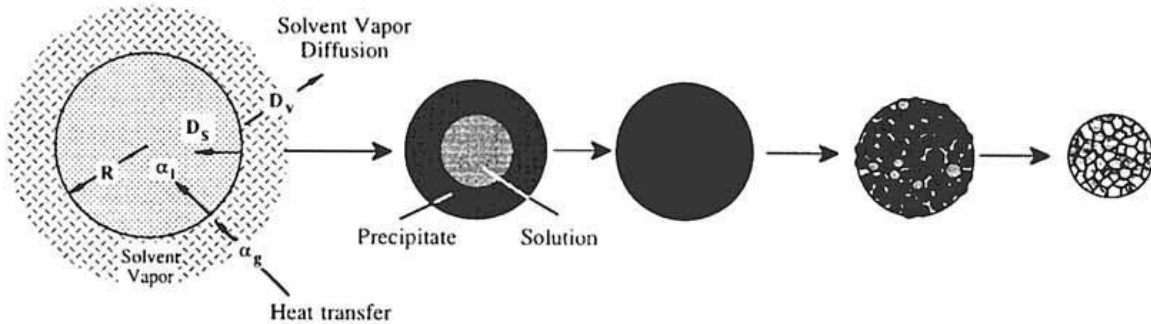


Figure 1.29. Different steps of grains formation in spray pyrolysis: solvent vaporization, precipitation, solid state precursors reaction, sintering<sup>102</sup>

More recently, spray pyrolysis process was detailed in the specific case of  $\text{ZnCo}_2\text{O}_4$  nanoparticles synthesis by Choi *et al*<sup>78</sup>. Thanks to the versatility of this technique, the authors were able to tune the morphology of the obtained grains (Figure 1.30). This study is of peculiar interest because the authors also pointed out the difficulty to produce small free nanoparticles by spray pyrolysis instead of large nanostructured particles. To overcome this limitation, they used a combustion flame to increase the reaction temperature and to decrease the residence time in the hot zone. The authors consider that the precursor is then fully vaporized and that nanoparticles grow from this gas phase through nucleation and growth phenomena as depicted in Figure 1.30. Such process is called aerosol flame synthesis, it enables the efficient production of small nanoparticles. This process is presented in the next part.

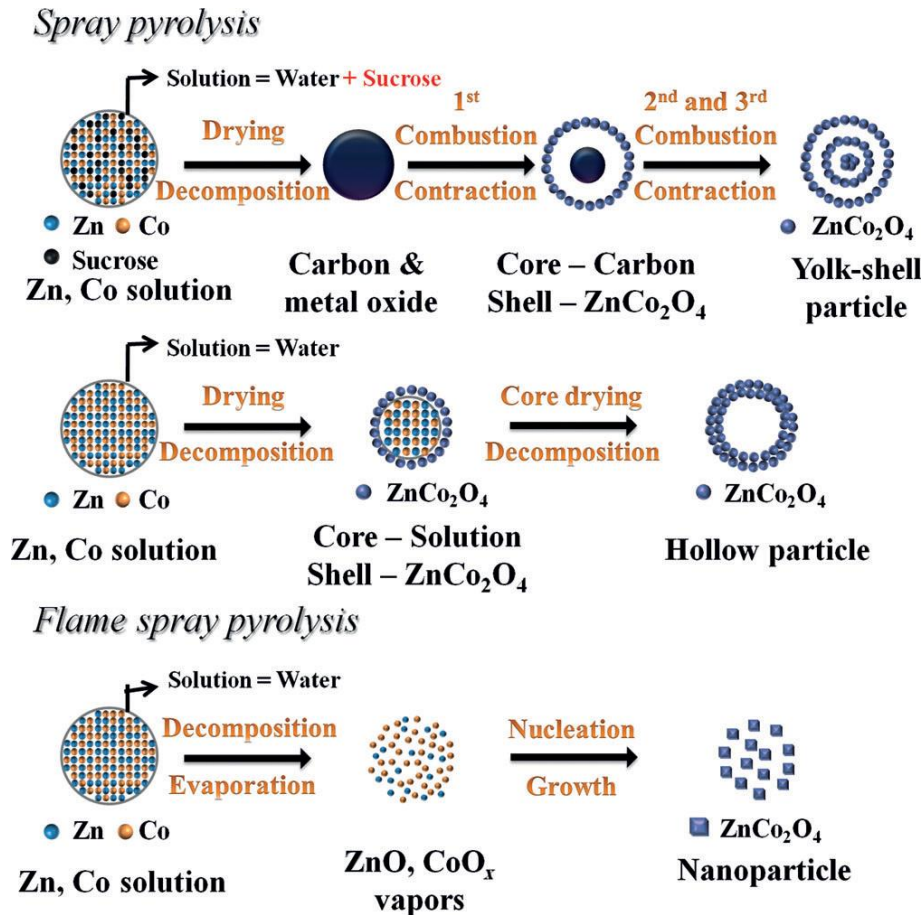


Figure 1.30. Formation mechanism of ZnCo<sub>2</sub>O<sub>4</sub> nanostructures<sup>78</sup>

### Aerosol flame synthesis

Aerosol flame synthesis (AFS) is widely used for the synthesis of oxide nanopowders. In this technique, precursors are thermally decomposed thanks to a combustion reaction between an oxidizer and a fuel, leading to the formation of the nanopowders upon nucleation and growth in the gas phase. This high temperature process is cost effective, able to produce very large amount of powders, and operates in continuous flow with very few steps of process. For these reasons it is already widely employed at the industrial scale for the production of silica, alumina or zirconia nanopowders. This process was actually chosen by DeGussa for the production of its ultrafine grade of TiO<sub>2</sub> (P25).

As reported in a review by Pratsinis *et al*<sup>103</sup>, AFS processes can be classified in three main categories, depending on the state of the precursor being fed to the flame (Figure 1.31). When the precursor is vaporized, the process is called vapor-fed AFS (VFAFS). When it is fed as droplets aerosol, two cases appear: if the precursor is not flammable (aqueous solution for example) it is called flame assisted spray pyrolysis (FASP); if it is flammable then it is called flame spray pyrolysis (FSP). In this

## Experimental methods for the synthesis of nanostructured mixed-transition metal oxides

latter case, the precursor is combusted and the reaction takes place at the highest temperature for this kind of process (3000 K).

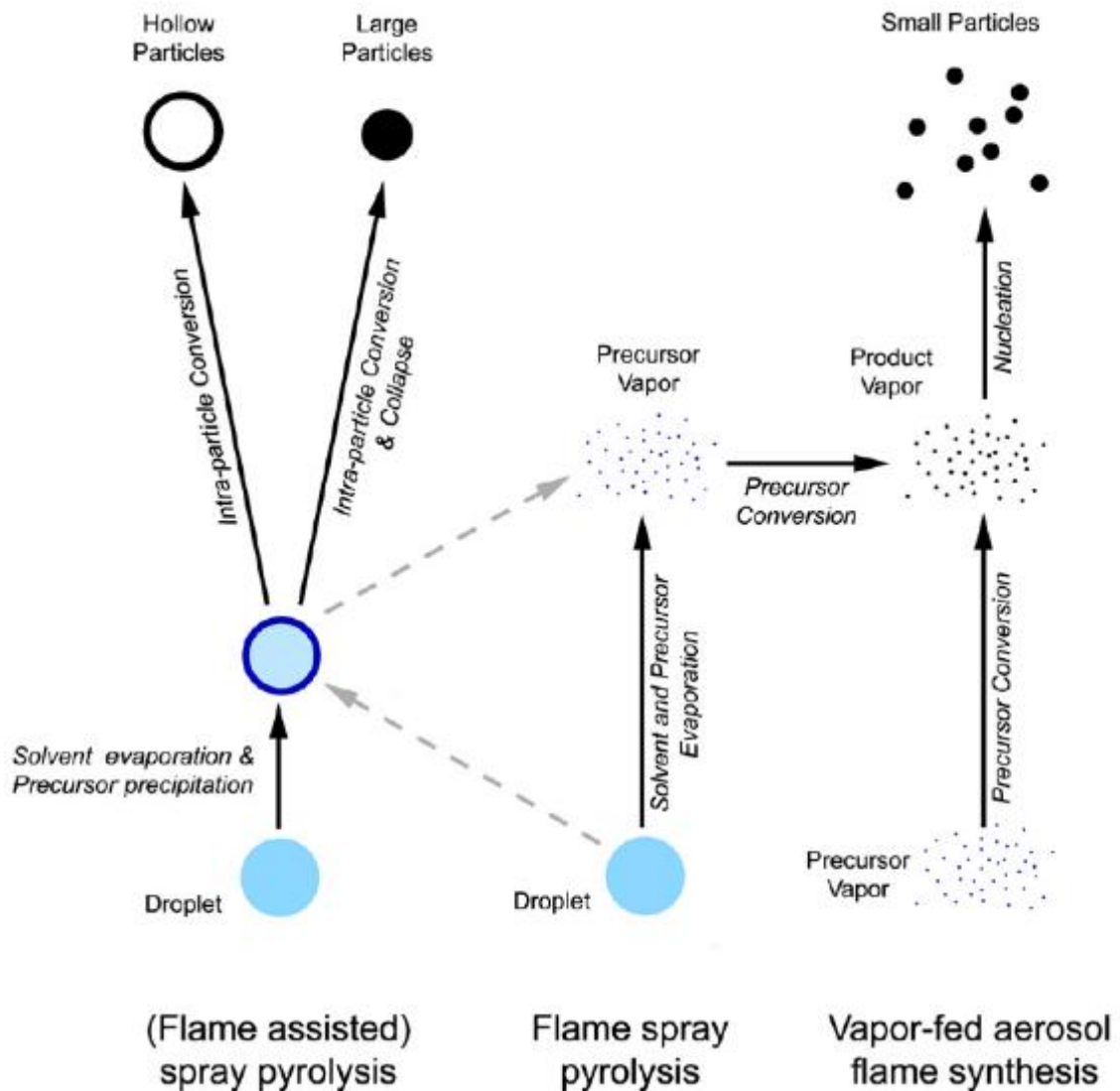


Figure 1.31. Different types of aerosol flame synthesis processes<sup>103</sup>

When compared to spray pyrolysis, all AFS based processes present two main advantages: they show short residence time and operate at high temperature, which make them able to synthesize efficiently small, dense, and crystalline nanoparticles. Instead of obtaining large nanostructured grains, VFAS, FSP and potentially FASP lead to the synthesis of small nanoparticles agglomerated in chain-like type structures. FASP appear to be more versatile, as depending on synthesis conditions nanoparticles can be obtained (when the droplet is vaporized and reaction takes place in the gas phase), as well as hollow or large particles in a similar way to spray pyrolysis when reaction occurs in the droplet. On the

## Experimental methods for the synthesis of nanostructured mixed-transition metal oxides

contrary FSP appears more efficient for nanoparticles production because of the high operating temperature and combustion of the precursors that lead generally to gas phase reactions.

More particularly, for the production of ternary metal oxides, solutions containing metal salts like nitrates, acetates or acetylacetonates dissolved in ethanol or toluene are commonly used<sup>104,105</sup>. The metal salts act as the oxidizer while the organic solvent act as the fuel.

This solution combustion synthesis is based on the principle that the reaction is initiated under heating and that it becomes then self-sustaining, allowing the formation of the nanopowder as final product. However, the product of the combustion reaction sometimes needs a subsequent heat treatment to obtain the desired powder<sup>106</sup>, this can be the case for the synthesis of carbon-coated metal oxides for instance<sup>107</sup>.

### Laser pyrolysis

Laser pyrolysis is part of the spray pyrolysis processes, with the peculiarity of using a laser beam as the precursor decomposition energy source. It can be easily compared to flame based processes (FASP or FSP) in terms of residence time or particles growth mechanisms, sharing the same advantages of these processes versus conventional spray pyrolysis. The obtained nanopowders characteristics in terms of size, shape, crystallinity or agglomeration are quite similar to flame synthesized ones. The main difference comes from the absence of combustion reaction required to heat up the system, as the energy is supplied by the infrared laser.

No oxygen addition is thus necessary in the system, what makes easier the synthesis of non-oxide materials. Moreover, lower reaction temperatures can be addressed in order to obtain amorphous structures<sup>108,109</sup>.

Laser pyrolysis was chosen for the synthesis of  $\text{ZnFe}_2\text{O}_4$  nanoparticles in this work. A more detailed description of this vapor-phase process is presented in the following part.

### IV. Laser pyrolysis for the synthesis of nanopowders

Laser pyrolysis is a vapor-phase process based on the decomposition of precursors thanks to a CO<sub>2</sub> laser, it enables the reproducible synthesis in large scale of various nanopowders.

#### History

The first synthesis by CO<sub>2</sub> laser pyrolysis was introduced by Cannon *et al.* at the beginning of the 1980's for the synthesis of SiC, SiCN and Si<sub>3</sub>N<sub>4</sub> ceramics<sup>110</sup>. In France, this process was developed by Cauchetier *et al.* in 1987 for the synthesis of Si and SiC<sup>111</sup>. Even if this method is particularly efficient for the synthesis of Si-based<sup>112</sup> or carbon-based nanopowders<sup>113</sup>, a large variety of oxide and non-oxide nanopowders were synthesized, as for example (non-exhaustive list) ZrO<sub>2</sub><sup>114</sup>, MoS<sub>2</sub><sup>115</sup>, FeC<sup>116</sup>, TiO<sub>2</sub><sup>117</sup>, or more recently core-shell silicon/carbon structures<sup>118</sup> and SnO<sub>2</sub> nanoparticles<sup>119</sup> for battery applications.

#### Principle

The laser pyrolysis process is a thermal synthesis method, based on the interaction between a liquid or gaseous precursor and an infrared CO<sub>2</sub> laser beam emitting at 10.6 μm. A scheme of the experimental setup is shown below (Figure 1.32)

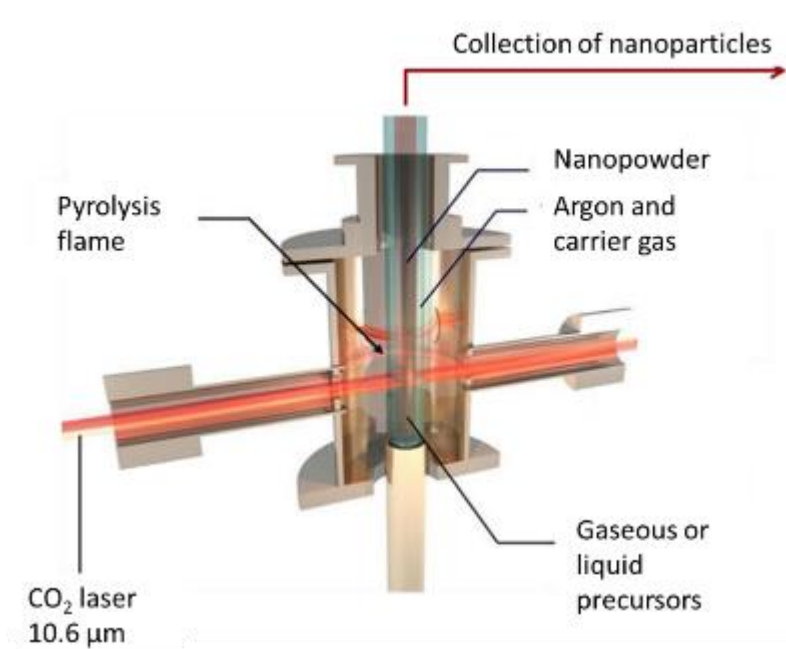


Figure 1.32. Laser pyrolysis experimental setup

The high power CO<sub>2</sub> laser allows the absorption of several photons by the precursor molecules while they cross the beam. In the case where precursor molecules do not absorb at the laser

wavelength, a sensitizer gas is added. The energy is transferred into the whole reaction zone by collisions leading to a rapid increase of the average temperature, allowing the decomposition of the precursor, sometimes accompanied by the appearance of a “flame”<sup>120</sup> when excited radicals are formed. This flame should not be compared to a combustion flame, as no oxygen or fuel is involved in the reaction (excepted when necessary for the targeted material). When gaseous precursors are used, nucleation and growth happen in the vapor phase and enable the formation of nanoparticles whose temperature contributes to the “flame” brightness through thermal radiation (Figure 1.33).



Figure 1.33. Pyrolysis flame of silicon nanoparticles using silane precursor

As these nanoparticles rapidly leave the interaction zone, they generally show a very small size of few nanometers to tens of nanometers because of limited growth duration<sup>121</sup> (Figure 1.34). As they are produced in gaseous stream, the primary nanoparticles undergo many collisions with each other, leading to the collection of large chain-like agglomerates of several micrometers with very low density. With vaporized liquid precursors, same mechanisms occur as with gaseous ones, but when liquids are used as aerosol droplets the process can be directly compared with thermal spray pyrolysis with faster heating rate, possibly higher temperature, and shorter reaction times.

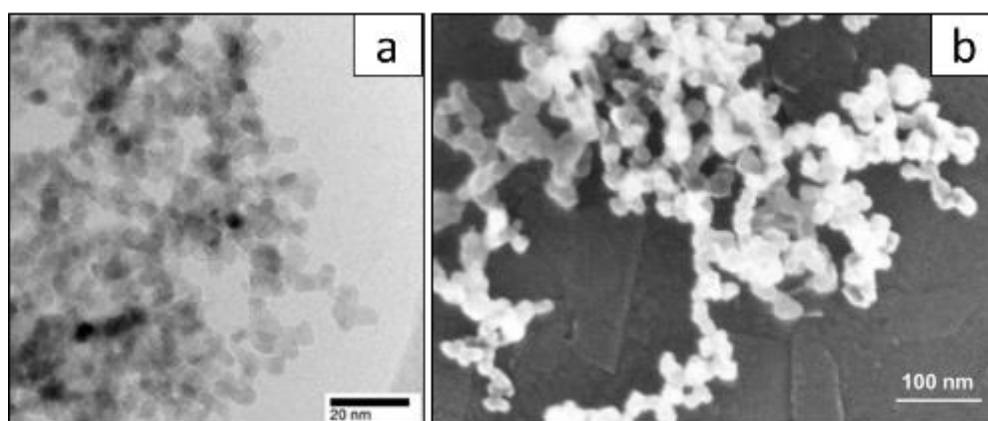


Figure 1.34. a) TEM image of  $\text{TiO}_2$  nanoparticles<sup>122</sup>, b) SEM image of  $\text{SiC}$  nanoparticles<sup>121</sup>

Growth mechanisms are similar to FASP process, where the heat source of combustion flame is replaced by laser absorption. Depending on synthesis parameters, aerosol droplets can be completely vaporized, and lead to a gas phase nucleation and growth mechanism. In other conditions, the reaction can take place inside the droplet before or during the solvent vaporization (precipitation of solute) and lead to large or hollow nanostructured particles. On the contrary of flame based processes where the combustible nature of solvent is important (FASP or FSP reactions), this latter solvent property is generally not a key in laser pyrolysis. Only vaporization characteristics of the solvent influence the cooling of the reaction, and its nature can nevertheless play a role in terms of reaction chemistry.

When a higher reaction temperature or a more oxidizing atmosphere is required for the targeted phase synthesis, oxygen or air can be added in the process. If a combustible precursor or solvent is also used, a combustion reaction can take place. In this latter case, the process shows similarities with FSP, even if the overall temperature remains smaller because of neutral gas dilution.

More details about the experimental setup and the different parameters influencing the size of the nanoparticles will be given in the next chapter.

### Advantages and drawbacks

Compared to other nanoparticles synthesis methods, laser pyrolysis presents several advantages. It is an up-scalable and flexible flow process enabling the production of large amounts of nanoparticles of high purity (no contact with reactor walls). Gaseous as well as liquid precursors can be used, opening a wide range of achievable materials. Moreover, laser pyrolysis allows a very localized and fast heating and cooling of the reaction zone. As a consequence, the obtained nanoparticles can be as small as few nm. The synthesis of many types of nanoparticles in terms of crystallinity, chemical composition and morphology is possible by this gas-phase method, depending on the choice of different experimental parameters (precursors, gas flow rates, laser power, etc).

However, this technique presents one main drawback; as pyrolysis lies on the absorption of the infrared wavelength by the precursor, this latter needs to be able to absorb the 10.6  $\mu\text{m}$  wavelength. Alternatively, an absorbing gas (named sensitizer) can be added to the precursor mixture: ethylene, ammonia and sulphur hexafluoride are the most employed sensitizers due to their relatively high dissociation energy (7.2 eV for  $\text{C}_2\text{H}_4$ , 3.95 eV for  $\text{SF}_6$  and 3.91 eV for  $\text{NH}_3$ )<sup>121</sup>. As the use of  $\text{SF}_6$  can lead to the formation of hazardous compounds with hydrogen during the synthesis,  $\text{C}_2\text{H}_4$  and  $\text{NH}_3$  are often favored but can sometimes be the cause of a carbon or nitrogen pollution into the nanopowder. Moreover, ammonia can generate deleterious reactions with the precursors prior to the interaction with the laser beam (for example formation of  $\text{NH}_4\text{Cl}$  with chlorides), and lead to lack of oxygen in

some oxides phases. Depending on the targeted material, some of these drawbacks can also be turned as advantages (nitrogen doping<sup>119</sup> or suboxides phases<sup>123</sup> synthesis for example).

### V. Intermediate conclusion

For next-generation applications, LIB performance must be improved particularly in terms of energy density and safety. The use of a graphite anode in commercial LIB can be hazardous because of the formation of lithium dendrites at fast charging. This phenomena can be avoided by using anode materials with a higher working voltage vs. Li/Li<sup>+</sup>. However, the use of a high voltage anode will reduce the energy density of the full battery that is why high voltage cathodes must also be the object of intense works. As well, new electrolytes stable at high potential have to be found.

The main target of this thesis is to develop and study ZnFe<sub>2</sub>O<sub>4</sub> nanopowders as high capacity and high voltage anode for future LIB. This work is divided in two parts. The first part concerns the synthesis by laser pyrolysis of zinc iron oxides nanopowders and their characterization. The second part focuses on the electrochemical properties of the obtained powders: evaluation of the electrochemical performances of zinc iron oxides as anode for LIB on one hand and understanding of the lithiation process thanks to operando studies on the other hand.

The following chapter will detailed the experimental protocols used for the synthesis of the nanopowders, for their structural and morphological characterizations and for the evaluation of their electrochemical performances as well as for the operando measurements.

References

- 1 F. Putois, *J. Power Sources*, 1995, **57**, 67–70.
- 2 M. A. Fetcenko, S. R. Ovshinsky, B. Reichman, K. Young, C. Fierro, J. Koch, A. Zallen, W. Mays and T. Ouchi, *J. Power Sources*, 2007, **165**, 544–551.
- 3 M. R. Palacin, *Chem. Soc. Rev.*, 2009, **38**, 2665–2575.
- 4 C. Sandoval, V. M. Alvarado, J.-C. Carmona, G. Lopez Lopez and J. F. Gomez-Aguilar, *Renew. Energy*, 2017, **105**, 407–418.
- 5 J.-M. Tarascon and M. Armand, *Mater. Sustain. Energy*, 2010, **414**, 171–179.
- 6 [www.estquality.com/technology](http://www.estquality.com/technology), .
- 7 M. S. Whittingham and F. R. G. Jr, *Science (80-. )*, 1976, **192**, 1126–1127.
- 8 M. S. Whittingham and F. R. G. Jr, *Mater. Res. Bull.*, 1975, **10**, 363–372.
- 9 N. Loeffler, D. Bresser and S. Passerini, *Johnson Matthey Technol. Rev.*, 2015, **59**, 34–44.
- 10 M. Armand and D. W. Murphy, *Materials for Advanced Batteries*, Plenum Press, New York, 1980.
- 11 B. Lazzari, M. Scrosati, *J. Electrochem. Soc.*, 1980, **127**, 773.
- 12 C.-M. Park, J.-H. Kim, H. Kim and H.-J. Sohn, *Chem. Soc. Rev.*, 2010, **39**, 3115.
- 13 J. Cabana, L. Monconduit, D. Larcher and M. R. Palacín, *Adv. Mater.*, 2010, **22**, E170–92.
- 14 B. Scrosati and J. Garche, *J. Power Sources*, 2010, **195**, 2419–2430.
- 15 A. B. Yaroslavtsev, T. L. Kulova and A. M. Skundin, *Russ. Chem. Rev.*, 2015, **84**, 826–852.
- 16 V. Zinth, C. Von Lüders, M. Hofmann, J. Hattendorff, I. Buchberger, S. Erhard, J. Rebelo-Kornmeier, A. Jossen and R. Gilles, *J. Power Sources*, 2014, **271**, 152–159.
- 17 B. Marinho, M. Ghislandi, E. Tkalya and C. Koning, *Powder Technol.*, 2012, **221**, 351–358.
- 18 N. Nitta, F. Wu, J. T. Lee and G. Yushin, *Mater. Today*, 2015, **18**, 252–264.
- 19 C. De Casas and W. Li, *J. Power Sources*, 2012, **208**, 74–85.
- 20 E. J. Yoo, J. Kim, E. Hosono, H. S. Zhou, T. Kudo and I. Honma, *Nano Lett.*, 2008, **8**, 2277–2282.
- 21 Z. Xiong, Y. Yun and H.-J. Jin, *Materials (Basel)*, 2013, **6**, 1138–1158.
- 22 A. N. Dey, *J. Electrochem. Soc.*, 1971, **118**, 1547–1549.
- 23 W. Zhang, *J. Power Sources*, 2011, **196**, 13–24.
- 24 J. Y. Kwon, J. H. Ryu and S. M. Oh, *Electrochim. Acta*, 2010, **55**, 8051–8055.

- 25 U. Kasavajjula, C. Wang and A. J. Appleby, *J. Power Sources*, 2007, **163**, 1003–1039.
- 26 V. A. Agubra and J. W. Fergus, *J. Power Sources*, 2014, **268**, 153–162.
- 27 H. Wu, G. Chan, J. W. Choi, I. Ryu, Y. Yao, M. T. McDowell, S. W. Lee, A. Jackson, Y. Yang, L. Hu and Y. Cui, *Nat Nano*, 2012, **7**, 310–315.
- 28 L. Leveau, *PhD thesis. Etude de nanofils de silicium comme matériau d'électrode négative de batterie lithium-ion (Ecole Polytechnique)*, 2015.
- 29 J. Sourice, *PhD thesis. Synthèse de nanocomposites cœur-coquille silicium carbone par pyrolyse laser double étage : application à l'anode de batterie lithium-ion (Université Paris-Sud)*, 2016.
- 30 J. Tarascon, P. Poizot, S. Laruelle, S. Grugeon and L. Dupont, *Nature*, 2000, **407**, 496–499.
- 31 S.-H. Yu, S. H. Lee, D. J. Lee, Y.-E. Sung and T. Hyeon, *Small*, 2015, 1–27.
- 32 M. V Reddy, G. V Subba Rao and B. V Chowdari, *Chem Rev*, 2013, **113**, 5364–5457.
- 33 B. P. Arico, A. S. Scrosati, B. Tarascon, J. M. Schalkwijk, W. V, *Nat. Mater.*, 2005, **4**, 366–377.
- 34 H. Li, P. Balaya and J. Maier, *J. Electrochem. Soc.*, 2004, **151**, A1878.
- 35 L. Luo, J. Wu, J. Xu and V. P. Dravid, *ACS Nano*, 2014, 11560–11566.
- 36 Y. Sharma, N. Sharma, G. V. Subba Rao and B. V. R. Chowdari, *Solid State Ionics*, 2008, **179**, 587–597.
- 37 J. Tarascon, S. Grugeon, M. Morcrette and S. Laruelle, *Comptes Rendus Chim.*, 2005, **8**, 9–15.
- 38 R. G. Ehl and A. J. Ihde, *J. Chem. Educ.*, 1954, **31**, 226–232.
- 39 Y. Yang, Y. Zhao, L. Xiao and L. Zhang, *Electrochem. commun.*, 2008, **10**, 1117–1120.
- 40 L. Yao, X. Hou, S. Hu, Q. Ru, X. Tang, L. Zhao and D. Sun, *J. Solid State Electrochem.*, 2013, **17**, 2055–2060.
- 41 S. J. Rezvani, R. Gunnella, A. Witkowska, F. Mueller, M. Pasqualini, F. Nobili, S. Passerini and A. Di Cicco, *ACS Appl. Mater. Interfaces*, 2017, **9**, 4570–4576.
- 42 E. Nanini-maury, *PhD thesis. Formulation d'électrolytes haut potentiel pour la caractérisation d'électrodes positives innovantes : batteries lithium-ion pour le véhicule électrique (Université Pierre et Marie Curie)*, 2014.
- 43 S. Grugeon, S. Laruelle, R. Herrera-Urbina, L. Dupont, P. Poizot and J.-M. Tarascon, *J. Electrochem. Soc.*, 2001, **148**, A285–A292.
- 44 X. Q. Yu, Y. He, J. P. Sun, K. Tang, H. Li, L. Q. Chen and X. J. Huang, *Electrochem. commun.*, 2009, **11**, 791–794.

- 45 Y. F. Yuan, X. H. Xia, J. B. Wu, J. L. Yang, Y. B. Chen and S. Y. Guo, *Electrochem. commun.*, 2010, **12**, 890–893.
- 46 H. Guan, X. Wang, H. Li, C. Zhi and T. Zhai, *Chem Commun*, 2012, 4878–4880.
- 47 J. S. Do and C. H. Weng, *J. Power Sources*, 2005, **146**, 482–486.
- 48 M. Chen, X. Xia, J. Yin and Q. Chen, *Electrochim. Acta*, 2015, **160**, 15–21.
- 49 X. W. Lou, D. Deng, J. Y. Lee, J. Feng and L. A. Archer, *Adv. Mater.*, 2008, **20**, 258–262.
- 50 Y. Yao, J. Zhang, T. Huang, H. Mao and A. Yu, *Int. J. Electrochem. Sci.*, 2013, **c**, 3302–3309.
- 51 P. F. Teh, S. S. Pramana, Y. Sharma, Y. W. Ko and S. Madhavi, *ACS Appl. Mater. Interfaces*, 2013, **5**, 5461–5467.
- 52 E. B. W. K. M. Abraham, D. M. Pasquariello, *J. Electrochem. Soc.*, 1990, **137**, 743–749.
- 53 M. V Reddy, T. Yu, C. H. Sow, Z. X. Shen, C. T. Lim, G. V Subba Rao and B. V. R. Chowdari, *Adv. Funct. Mater.*, 2007, **17**, 2792–2799.
- 54 X. Wang, Y. Xiao, C. Hu and M. Cao, *Mater. Res. Bull.*, 2014, **59**, 162–169.
- 55 L. Zhang, H. Bin Wu and X. W. Lou, *Adv. Energy Mater.*, 2014, **4**, 1–11.
- 56 X. Wu, Y. Guo, L. Wan and C. Hu, *J. Phys. Chem. C*, 2008, **112**, 16824–16829.
- 57 Y. Chen, H. Xia, L. Lu and J. Xue, *J. Mater. Chem.*, 2012, **22**, 5006–5012.
- 58 W. Wei, S. Yang, H. Zhou, I. Lieberwirth, X. Feng and K. Müllen, *Adv. Mater.*, 2013, **25**, 2909–2914.
- 59 J. Xu and Y. Zhu, *ACS Appl. Mater. Interfaces*, 2012, **4**, 4752–4757.
- 60 C. Yuan, H. Bin Wu, Y. Xie and X. W. D. Lou, *Angew. Chem. Int. Ed. Engl.*, 2014, **53**, 1488–1504.
- 61 M. Hu, X. Pang and Z. Zhou, *J. Power Sources*, 2013, **237**, 229–242.
- 62 D. Liu and G. Cao, *Energy Environ. Sci.*, 2010, **3**, 1218–1237.
- 63 P. Lavela and J. L. Tirado, *J. Power Sources*, 2007, **172**, 379–387.
- 64 L. Lian, L. R. Hou, L. Zhou, L. S. Wang and C. Z. Yuan, *Rsc Adv.*, 2014, **4**, 49212–49218.
- 65 Y. Deng, S. Tang, Q. Zhang, Z. Shi, L. Zhang, S. Zhan and G. Chen, *J. Mater. Chem.*, 2011, **21**, 11987.
- 66 Y. Sharma, N. Sharma, G. V. Subba Rao and B. V. R. Chowdari, *Adv. Funct. Mater.*, 2007, **17**, 2855–2861.
- 67 Y. Sharma, N. Sharma, G. V. S. Rao and B. V. R. Chowdari, *Electrochim. Acta*, 2008, **53**, 2380–

- 2385.
- 68 L. Xiao, Y. Yang, J. Yin, Q. Li and L. Zhang, *J. Power Sources*, 2009, **194**, 1089–1093.
- 69 A. Kmita, A. Pribulova, M. Holtzer, P. Futas and A. Rocznik, *Arch. Metall. Mater.*, 2016, **61**, 2141–2146.
- 70 F. Li, H. Wang, L. Wang and J. Wang, *J. Magn. Magn. Mater.*, 2007, **309**, 295–299.
- 71 M. Atif, S. K. Hasanain and M. Nadeem, *Solid State Commun.*, 2006, **138**, 416–421.
- 72 Z. Yan, D. A. Keller, K. J. Rietwyk, H. Barad, K. Majhi, A. Ginsburg, A. Y. Anderson and A. Zaban, *Energy Technol.*, 2016, **4**, 809–815.
- 73 S. H. Choi and Y. C. Kang, *Int. J. Electrochem. Sci.*, 2013, **8**, 6281–6290.
- 74 H. S. Jadhav, R. S. Kalubarme, C.-N. Park, J. Kim and C.-J. Park, *Nanoscale*, 2014, **6**, 10071–10076.
- 75 Z. H. Li, T. P. Zhao, X. Y. Zhan, D. S. Gao, Q. Z. Xiao and G. T. Lei, *Electrochim. Acta*, 2010, **55**, 4594–4598.
- 76 X.-B. Zhong, B. Jin, Z.-Z. Yang, C. Wang and H.-Y. Wang, *RSC Adv.*, 2014, **4**, 55173–55178.
- 77 X. Hou, X. Wang, L. Yao, S. Hu, Y. Wu and X. Liu, *New J. Chem.*, 2015, **39**, 1943–1952.
- 78 S. H. Choi and Y. C. Kang, *ChemSusChem*, 2013, **6**, 2111–2116.
- 79 D. Bresser, E. Paillard, R. Kloepsch, S. Krueger, M. Fiedler, R. Schmitz, D. Baither, M. Winter and S. Passerini, *Adv. Energy Mater.*, 2013, **3**, 513–523.
- 80 P. F. Teh, Y. Sharma, S. S. Pramana and M. Srinivasan, *J. Mater. Chem.*, 2011, **21**, 14999.
- 81 Z. Xing, Z. Ju, J. Yang, H. Xu and Y. Qian, *Nano Res.*, 2012, **5**, 477–485.
- 82 H. Xu, X. Chen, L. Chen, L. Li, L. Xu, J. Yang and Y. Qian, *Int. J. Electrochem. Sci.*, 2012, **7**, 7976–7983.
- 83 X. Guo, X. Lu, X. Fang, Y. Mao, Z. Wang, L. Chen, X. Xu, H. Yang and Y. Liu, *Electrochem. commun.*, 2010, **12**, 847–850.
- 84 L. Yao, X. Hou, S. Hu, J. Wang, M. Li, C. Su, M. O. Tade, Z. Shao and X. Liu, *J. Power Sources*, 2014, **258**, 305–313.
- 85 H. Bin Wu, J. S. Chen, H. H. Hng and X. W. D. Lou, *Nanoscale*, 2012, **4**, 2526–2542.
- 86 Y.-G. Guo, J.-S. J.-S. Hu and L.-J. Wan, *Adv. Mater.*, 2008, **20**, 2287–2878.
- 87 L. Yao, X. Hou, S. Hu, X. Tang, X. Liu and Q. Ru, *J. Alloys Compd.*, 2014, **585**, 398–403.

- 88 J. M. Won, S. H. Choi, Y. J. Hong, Y. N. Ko and Y. C. Kang, *Sci. Rep.*, 2014, **4**, 5857.
- 89 R. M. Thankachan, M. M. Rahman, I. Sultana, A. M. Glushenkov, S. Thomas, N. Kalarikkal and Y. Chen, *J. Power Sources*, 2015, **282**, 462–470.
- 90 A. K. Rai, S. Kim, J. Gim, M. H. Alfaruqi, V. Mathew and J. Kim, *RSC Adv.*, 2014, **4**, 47087–47095.
- 91 R. Jin, H. Liu, Y. Guan, J. Zhou and G. Chen, *Mater. Lett.*, 2015, **158**, 218–221.
- 92 I. Chichinas, *J. Optoelectron. Adv. Mater.*, 2006, **8**, 439–448.
- 93 B. Gersten, *Chemfiles*, **5**.
- 94 H. Liu and J. Wang, *J. Electron. Mater.*, 2012, **41**, 3107–3110.
- 95 [https://www.nanowerk.com/how\\_nanoparticles\\_are\\_made.php](https://www.nanowerk.com/how_nanoparticles_are_made.php), .
- 96 M. H. Habibi and A. H. Habibi, *J. Therm. Anal. Calorim.*, 2012, **113**, 843–847.
- 97 A. Sutka, J. Zavickis, G. Mezinskis, D. Jakovlevs and J. Barloti, *Sensors Actuators, B Chem.*, 2013, **176**, 330–334.
- 98 H. Yu and A. M. Gadalla, *J. Mater. Res.*, 1996, **11**, 663–670.
- 99 J. Kurian, S. P. John, M. M. Jacob, V. R. Reddy, K. E. Abraham and V. S. Prasad, *IOP Conf. Ser. Mater. Sci. Eng.*, 2015, **73**, 12032.
- 100 L. Zhang, S. Zhu, H. Cao, G. Pang, J. Lin, L. Hou and C. Yuan, *RSC Adv.*, 2015, **5**, 13667–13673.
- 101 X. Zhao, B. Zheng, H. Gu, C. Li, S. C. Zhang and P. D. Ownby, *J. Mater. Res.*, 1999, **14**, 3073–3082.
- 102 G. L. Messing, S.-C. Zhang and G. V. Jayanthi, *J. Am. Ceram. Soc.*, 1993, **76**, 2707–2726.
- 103 R. Strobel, A. Baiker and S. E. Pratsinis, *Adv. Powder Technol.*, 2006, **17**, 457–480.
- 104 A. Vital, A. Angermann, R. Dittmann, T. Graule and J. Töpfer, *Acta Mater.*, 2007, **55**, 1955–1964.
- 105 F. M. Hilty, A. Teleki, F. Krumeich, R. Büchel, R. F. Hurrell, S. E. Pratsinis and M. B. Zimmermann, *Nanotechnology*, 2009, **20**, 475101–475111.
- 106 A. Kopp Alves, C. P. Bergmann and F. A. Berutti, *Novel Synthesis and Characterization of Nanostructured Materials*, Springer, 2013.
- 107 H. Yue, Q. Wang, Z. Shi, C. Ma, Y. Ding, N. Huo, J. Zhang and S. Yang, *Electrochim. Acta*, 2015, **180**, 622–628.
- 108 N. Herlin-Boime, J. Vicens, C. Dufour, F. Ténégal, C. Reynaud and R. Rizk, *J. Nanoparticle Res.*, 2004, **6**, 63–70.

- 109 J. Sourice, A. Bordes, A. Boulineau, J. P. Alper, Y. Leconte, E. De Vito and W. Porcher, *J. Power Sources*, 2016, **328**, 527–535.
- 110 W. R. Cannon, S. C. Danforth, J. H. Flint, J. S. Haggerty and R.A. Marra, *Ceram.Soc*, 1982, **65**, 324–330.
- 111 M. Cauchetier, O. Croix, M. Luce, M. Michon, J. Paris and S. Tistchenko, *Ceram. Int.*, 1987, **13**, 13–17.
- 112 O. Sublemontier, H. Kintz, F. Lacour, X. Paquez, V. Maurice, Y. Leconte, D. Porterat, N. Herlin-Boime and C. Reynaud, *KONA Powder Part. J.*, 2011, **29**, 236–250.
- 113 M. Ehbrecht, M. Faerber, F. Rohmund, V. V. Smirnov, O. Stelmakh and F. Huisken, *Chem. Phys. Lett.*, 1993, **214**, 34–38.
- 114 A. Audren, M. Ha-Thi, S. Coste and Y. Leconte, *J. Nanosci. Nanotechnol.*, 2010, **10**, 6216–6221.
- 115 P. Borsella, E.; Botti, S.; Cesile, M.; Martelli, S.; Nesterenko, A.; Zappelli, *J. Mater. Sci. Lett.*, 2001, **20**, 187–191.
- 116 C. Grimes, D. Qian, E. C. Dickey, J. L. Allen and P. C. Eklund, *J. Appl. Phys.*, 2000, **87**, 5642–5644.
- 117 B. Pignon, H. Maskrot, V. Guyot Ferreol, Y. Leconte, S. Coste, M. Gervais, T. Pouget, C. Reynaud, J.-F. Tranchant and N. Herlin-Boime, *Eur. J. Inorg. Chem.*, 2008, 883–889.
- 118 J. Sourice, A. Quinsac, Y. Leconte, O. Sublemontier, W. Porcher, C. Haon, A. Bordes, E. De Vito, A. Boulineau, S. Jouanneau Si Larbi, N. Herlin-Boime and C. Reynaud, *ACS Appl. Mater. Interfaces*, 2015, **7**, 6637–6644.
- 119 L. P. Wang, Y. Leconte, Z. Feng, C. Wei and Y. Zhao, *Adv. Mater.*, 2016.
- 120 E. Borsella, S. Botti, L. Caneve, L. De Dominicis and R. Fantoni, *Phys. Scr.*, 2008, **78**, 58112.
- 121 R. D’Amato, M. Falconieri, S. Gagliardi, E. Popovici, E. Serra, G. Terranova and E. Borsella, *J. Anal. Appl. Pyrolysis*, 2013, **104**, 461–469.
- 122 S. Bouhadoun, C. Guillard, F. Dapozze, S. Singh, D. Amans, J. Bouclé and N. Herlin-boime, *Applied Catal. B, Environ.*, 2015, **174–175**, 367–375.
- 123 P. Simon, B. Pignon, B. Miao, S. Coste-Leconte, Y. Leconte, S. Marguet, P. Jegou, B. Bouchet-Fabre, C. Reynaud and N. Herlin-Boime, *Chem. Mater.*, 2010, **22**, 3704–3711.

---

## Chapter 2. Experimental protocols

---

The second chapter summarizes the different experimental protocols used in this work. The laser pyrolysis setup is first detailed and the influence of the different tunable parameters is explained. The typical conduct of the nanopowders synthesis by this technique is also presented. A second part is dedicated to the structural and morphological characterization techniques for the nanopowders and a last part gives more details on the techniques used for the evaluation of the electrochemical performances of the produced materials.

## I. Description of a synthesis by laser pyrolysis

### 1. Experimental set-up

A scheme of the experimental assembly for the laser pyrolysis synthesis is shown below (Figure 2.1). The presentation of the set-up will be divided in three parts: the first one concerns the optical path of the laser beam, the second one is focused on the injection of precursors and gases into the reaction chamber and the last part details what happens in the interaction zone and how the produced nanopowders are collected.

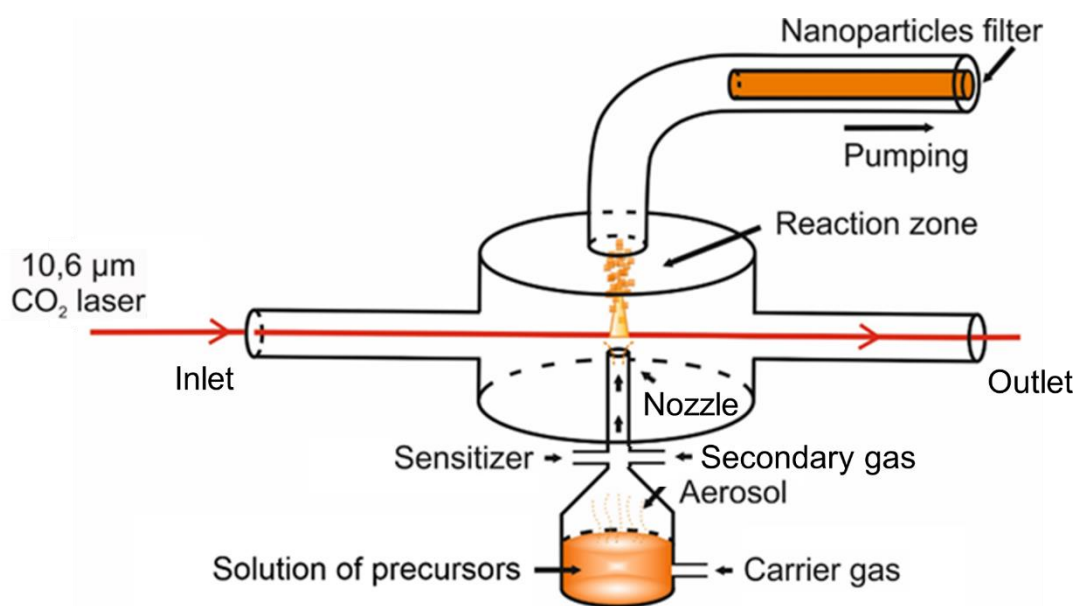


Figure 2.1 Scheme of the laser pyrolysis experimental set-up

#### Optical path of the CO<sub>2</sub> laser beam

A CO<sub>2</sub> laser (model PRC 2200) providing a 10.6 μm beam up to 2200 W is used for the synthesis of nanoparticles. The choice of a CO<sub>2</sub> laser offers several advantages when compared to other lasers: it is possible to use it in a continuous mode or in a pulsed mode, and it can deliver the high mean power required for large scale nanopowders synthesis. In our case, the continuous mode is necessary as the aerosol of precursors is carried into the reaction chamber with a continuous flow: too long off period between the pulses could allow the aerosol droplet to cross the reaction zone with only weak interaction with the beam. Moreover, high power is generally needed to allow the decomposition of liquid precursors when these latter are fed into the reactor as an aerosol. Part of the laser power is indeed consumed in the vaporization of the liquid droplets.

The alignment of the laser with the precursor inlet nozzle is first roughly achieved by using a visible He-Ne laser. When the power density increase of the incident beam is required, the laser is focused in a plan perpendicular to the nozzle axis using a cylindrical lens located at 50 cm (focal

length) from the interaction zone (i.e. centre of the nozzle). Such lens was preferred to a spherical one because it provides a wide spot able to efficiently cover the whole precursor flow out of the nozzle. The focusing allows to obtain a flat laser spot of few hundreds of micrometres in thickness instead of the initial 20 mm in diameter spherical spot (Figure 2.2). The width of the beam is roughly unchanged. Such focusing is also a good mean for shortening the residence time of the precursors in the beam.

After visible beam alignment, more accurate alignment is achieved with the CO<sub>2</sub> beam impacted on a target. This impact, which is larger than the spot size (especially in thickness) because of target burning, enables the setting of the laser-to-nozzle distance (7 mm in this work). This distance should not be too large (loss of precursor flow confinement and excessive mixing with the neutral gas of the reactor) nor too small (heat transfer from the flame to the nozzle and deposition of products on the top).

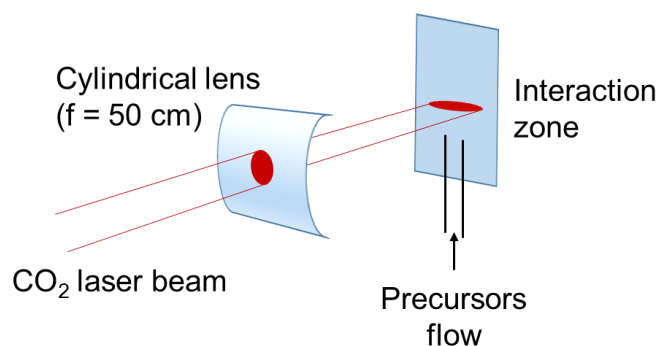


Figure 2.2. Focusing of the laser beam with a cylindrical lens ( $f = 50$  cm)

Inlet and outlet laser windows are flushed by a continuous argon flow to avoid particles deposition. In order to estimate the power absorption in the interaction zone during the synthesis, the laser power has to be measured before feeding the precursors and reactants into the reactor, and then afterwards. To do this, a power meter is positioned at the exit of the reactor. It is also used as a beam stopper. The absorbed power corresponds to the difference between the incident power measured under neutral gas and the one measured during the reaction.

### Injection of precursors and gases

Historically, laser pyrolysis was invented for the synthesis of nanopowders from gaseous precursors. However, the precursors can also be liquid or solid as soon as an aerosol can be formed to be injected into the reaction chamber and interact with the laser beam.

For the synthesis of zinc iron oxide, zinc and iron precursors have to be chosen. As there is no affordable or available gaseous and liquid precursors, solid ones were used. These solid precursors can be dissolved into a solvent and then nebulized to obtain an aerosol that can be fed into the reaction chamber, in a similar way to what is done in spray pyrolysis or flame synthesis. To do this, two

different aerosol generators were tested for the synthesis of  $\text{ZnFe}_2\text{O}_4$ : the pyrosol system from RBI instrumentation and the atomizer AGK 2000 from PALAS (Figure 2.3).

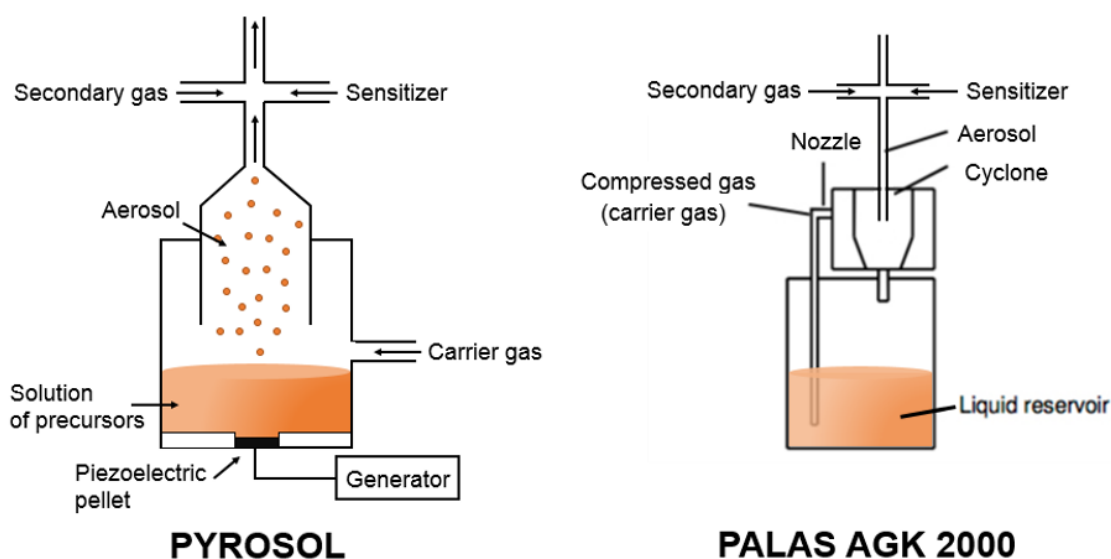


Figure 2.3. Schemes of the two aerosol generators used for the synthesis of zinc iron oxide

The pyrosol is an ultrasonic atomizer. It consists in a glass vessel containing the solution of precursors, and in a piezoelectric pellet located at the base of the container and generating ultrasounds. These latter lead to the formation of a dense aerosol at the surface of the liquid, composed of fine droplets of less than  $10\ \mu\text{m}$  in diameter. To limit the solvent evaporation during the generation of the aerosol and to keep the nebulization as stable as possible in time, a water cooling system is provided to keep a constant solution temperature. For the different experiments reported here this temperature was set to  $20^\circ\text{C}$ , leading to an effective solution temperature of  $35^\circ\text{C}$  during nebulization. A carrier gas is injected into the mist to transport the produced aerosol to the interaction zone. The operating frequency and power of the generator enable the control of the aerosol density, and the carrier gas flow rate can be set accurately to control the feeding rate. However, the pyrosol suffers from a main drawback: the efficiency of the aerosol generation by the piezoelectric pellet is closely depending on the physical properties of the liquid (viscosity, surface tension, vapour pressure). As these parameters strongly vary with the concentration of a salt in its solvent, the use of the pyrosol limits this concentration and as a consequence lowers the powder production rate.

For the AGK 2000 atomizer, a glass bottle is filled with the solution of precursors and is connected to a two-ways nozzle. While the first way is fed with the liquid, the second way of the nozzle is connected to the compressed gas supply (which serves also as the carrier gas). The gas flow generates a depression in the tube connected to the solution tank, pumping the liquid up to the nozzle where it is nebulized by the gas flow. The produced mist of droplets flows tangentially into a

cyclone where the large droplets are separated by centrifugal force and drip back to the bottle whereas the remaining smaller droplets ( $< 20 \mu\text{m}$ ) are carried to the reaction zone. This nebulization system shows several advantages: the pneumatic generation of aerosol is reliable, poorly dependent on liquid properties (at least less than the pyrosol) and highly concentrated solutions can be used. Moreover the use of suspensions is also possible. The pressure of the atomizing gas is controlled by a manometer, however to produce an aerosol, the minimum pressure results in a relatively high carrier gas flow rate (more than 3 l/min). In comparison the pyrosol system, where the aerosol generation and the carrier gas flow rate are independent, can run with flow rates as low as 0.5 L/min. Moreover, as the atomizing pressure is set by means of a simple manometer, the carrier gas flow rate control is less accurate than with the pyrosol where it is controlled by a flowmeter.

In both cases, the produced aerosol has to be flown to the interaction zone thanks to a carrier gas. The carrier gas can be an inert gas like argon as well as a reactive gas like air or oxygen (if an oxygen source is needed in the system for the formation of the desired product for instance). The aerosol is introduced into the reaction chamber using a nozzle of 6 mm in diameter, centred in a concentric confinement chimney under argon flow. The distance between the top of the chimney and the top of the nozzle is set to 1 cm. The chimney purpose is to keep the precursors flowing in a laminar way, avoiding their dissemination in the whole reactor.

To be decomposed, the aerosol of precursors has to absorb the laser wavelength at  $10.6 \mu\text{m}$ . When none of the precursors can absorb the laser beam, a sensitizer gas has to be added. Three main gases are generally employed: ethylene ( $\text{C}_2\text{H}_4$ ), ammonia ( $\text{NH}_3$ ) and sulphur hexafluoride ( $\text{SF}_6$ ).  $\text{SF}_6$  was not chosen due to the toxicity of the products potentially coming from its decomposition in presence of hydrogen ( $\text{HF}$ ,  $\text{H}_2\text{S}$ ).  $\text{NH}_3$  was not used in this work as this gas reacts with some precursors to form side products which can clog the inlet nozzle ( $\text{NH}_4\text{Cl}$  for instance with chloride precursors). While the use of ethylene is a potential source of carbon pollution in the obtained nanopowders, this latter gas is still the best choice for this work as it does not lead to side reactions with the precursors or to hazardous decomposition products. Moreover, this source of carbon can be turned into an advantage if the synthesis of carbon coated particles is needed.

### Nanoparticles production in the interaction zone and their collection

After being evacuated down to few mbar, the reactor is maintained at a constant pressure of 740 torr during the synthesis thanks to a continuous argon flow and regulating valve. The pressure is set just below 1 atm in order to avoid any release of chemical products or nanopowders in case of leaks in the reactor appearing during the synthesis (for example breaking of a laser window). The area where the laser beam and the aerosol flow interact together is defined as the reaction zone. Here, the sensitizer gas absorbs part of the laser beam leading to the appearance of a visible or non-visible

(infrared) flame. The phenomenon is also observed on the power meter with a sudden decrease of the measured power upon absorption. In this flame, the decomposition of the precursors occurs leading to the formation of nanoparticles, generally by a nucleation and growth process. The hot particles take also part to the brightness of the flame through thermal emission process. The produced nanoparticles are pumped in direction of the porous filters to be collected (Figure 2.4).



*Figure 2.4. Porous filter for the collection of nanopowders in a glass collector*

Laser pyrolysis is a very flexible method for the production of nanopowders where various experimental parameters are controllable. Each of them may have an influence on the synthesis process.

## 2. Influence of the experimental parameters

### Laser

Several parameters can be set on the laser in order to optimize the pyrolysis reaction.

The power of the incident laser beam first can be tuned up to 2000 W approximately. The higher is the chosen power, the higher may be the absorbed power by the sensitizer gas fostering the formation of a warmer pyrolysis flame. With a warmer interaction zone, the precursors can be decomposed more efficiently and the particles show well organized crystalline structures.

The laser beam can also be focused or not. The focusing of the beam enables the increase of the power density but also the decrease of the residence time of the precursors in the interaction zone, which has an influence on the produced nanoparticles. The lower the residence time is, the smaller the nanoparticles. High energy density allows the particles to show crystallized structure despite the short interaction time.

### Precursors

The use of solutions involves the choice of the precursors, the choice of the solvent and also the choice of the solution concentration.

Several criteria must be taken into consideration for the choice of these precursors and of the solvent: cost, toxicity, environmental benignity, easy handling and solubility of the precursors into the

solvent, in order to facilitate their dissolution and allow high concentrations. That is why precursors like nitrates, chlorides, acetates and acetylacetonates are prioritized to prepare solutions with deionized water or absolute ethanol. These precursors are similar to the ones used in other gas phase synthesis processes (see chapter 1).

The use of solutions presents several limitations though. Compared to the use of pure gaseous or liquid precursors, solution based syntheses show a lower production yield (ratio between the amount of produced nanopowder and the amount of consumed aerosol) as only one part of the solution is used for the production of the targeted material. Moreover, the solvent tends to cool the reaction zone through its vaporization. As the laser pyrolysis is a thermal process, the use of a solvent may have an influence on the flame temperature compared to pure precursors. Moreover, the reaction can take place inside the liquid droplets through precipitation of the solute and lead to large nanostructured particles as discussed in chapter 1.

To maximize the production rate, the concentration should theoretically be the highest possible.

If the solution concentration is relatively low, during the synthesis a huge amount of solvent will be evaporated fostering the cooling of the flame and leading to a lower temperature for the decomposition of the precursors. On the contrary, when the concentration is too high, the reaction hardly decomposes the totality of the precursors what can lead to the clogging of the filters and production of impurities. Besides, the concentration is sometimes limited by the aerosol generator itself (the pyrosol in particular cannot create any aerosol if the solution is too concentrated).

The influence of the nature of the precursors and of the solvent is studied in this work and the results are reported in the next chapter dedicated to the syntheses of  $\text{ZnFe}_2\text{O}_4$  by laser pyrolysis.

### Gases

The different gases used during laser pyrolysis as well as the chosen flow rates also have an influence on the flame temperature and on the residence time, and thus on the decomposition of the precursors and on the produced nanopowders (crystalline phase and particles size in particular).

The precursors chosen for this work, described in chapter 3, do not absorb the laser wavelength: a sensitizer was thus used for synthesis. As previously mentioned, some precursors show deleterious reactions with  $\text{NH}_3$ , the sensitizer used for zinc iron oxide synthesis was thus  $\text{C}_2\text{H}_4$ . When  $\text{C}_2\text{H}_4$  absorbs the laser energy, it can be decomposed partially or completely depending on synthesis parameters which leads to the formation of different by-products (hydrocarbons, hydrogenated polyaromatics, soots...) found as impurities in powders.

. Depending on the metal affinity for oxygen, additional oxygen source is sometimes needed for the formation of oxide phases. This oxygen may come from the precursors, the solvent or more likely

directly from the addition of oxygen or air. In this latter case, the carrier gas which is generally a neutral one can be directly replaced by air. When there is a combination of an oxygen source with a solvent like ethanol or a flammable sensitizer like  $C_2H_4$ , it can lead to a combustion reaction in the flame that sometimes takes precedence over the pyrolysis reaction itself. If enough oxygen is available in the reactional medium, the combustion of  $C_2H_4$  occurs and leads to an increased reaction temperature. Such combustion reaction, especially when obtained in oxygen rich ratio, produces  $H_2O$  and  $CO_2$  and avoids carbon pollution in the powders.

The flow rate (controllable thanks to mass flow meters) for both carrier gas and sensitizer gas are important parameters. More precisely, the higher is the carrier gas flow rate, the higher will be the amount of precursors solution carried inside the reaction chamber in a given time. This should provide higher production rates. On the other hand, high flow rates decrease the residence time of the precursors in the flame which could limit the decomposition and reaction completeness. As previously indicated, increasing the carrier flow means more aerosol and thus more solvent being fed for a given time. In this way, the flame should be cooler through solvent vaporization. In addition, more carrier gas also means more dilution of the sensitizer gas in the flame again fostering the cooling of the flame. These latter phenomena lead to lower production rates, excepted in the case where the solvent is itself decomposed and takes part to solid phase formation, boosting production rate as particles of interest or as impurities. Moreover, when the residence time is reduced, the time for the nucleation and growth of nanoparticles is shortened and smaller nanoparticles are expected in the produced powder. As a consequence, the increase of carrier gas can be seen as an advantage or as a drawback.

In addition to these residence time issues, the chosen flow rate for the sensitizer gas is important as it is directly linked to the flame temperature. The higher the sensitizer flow rate is, the higher the laser absorption is and thus the interaction zone temperature.

Pressure is an important parameter too, as it directly influences the frequency of collisions between precursors molecules, growing particles and aggregates. The lower the pressure is, the lower the particles size is. This parameter was set to 740 Torr for this work, because the overall gas flowrate makes difficult the regulation to lower values of pressure.

In conclusion, for a given chemistry, the temperature of the flame and the residence time appear as the most important parameters to control the production of the desired nanoparticles.

### 3. Typical conduct of a synthesis

The typical conduct for a synthesis is presented below.

### Experimental setup preparation

- Laser alignment: before each series of syntheses, the alignment of the laser is checked to have a beam passing 7 mm above the center of the inlet nozzle.
- Calibration of the mass flow controllers: gas flow outlet of the flowmeters is checked under argon flow. The measured effective flow rate is converted for other gases using their conversion factor.

$$\text{Gas flow rate} = \text{argon flow rate} \times \frac{\text{factor}(\text{gas})}{\text{factor}(\text{argon})}$$

Gas	Conversion factor
Argon	1.395
C <sub>2</sub> H <sub>4</sub>	0.619
Air	0.998

- The reaction chamber is then closed and connected to three filters for the collection of nanopowders. The aerosol generator is connected below the reaction chamber. Gas lines are connected below the reaction chamber too for the injection of the carrier gas, the sensitizer gas and any other secondary gas if needed.
- A vacuum test is done before starting the experiment to prevent any leak and then the whole experiment is filled with argon and set to a pressure of 740 torr under continuous argon flow.

### Synthesis

- After laser heating for one hour, the experiment can start. Only one filter is opened to collect the products during the parameters setting (garbage collector).
- The whole experiment is under argon flow. The CO<sub>2</sub> laser is set to 10% of its maximum power first and the shutter is opened to send the laser beam into the reactor. The power is then increased 10% by 10% to the desired value.
- When the laser power has been stabilized for few minutes at the chosen working value, the different gases are sent into the reactor. Once conditions are stable, the aerosol is sent using the aerosol generator.
- The aspect of the flame changes as soon as the precursors arrive into the reaction zone (Figure 2.5). When the experiment is stable for few minutes (pressure and aerosol production), a clean filter is opened to collect the produced powder and the garbage one is closed.

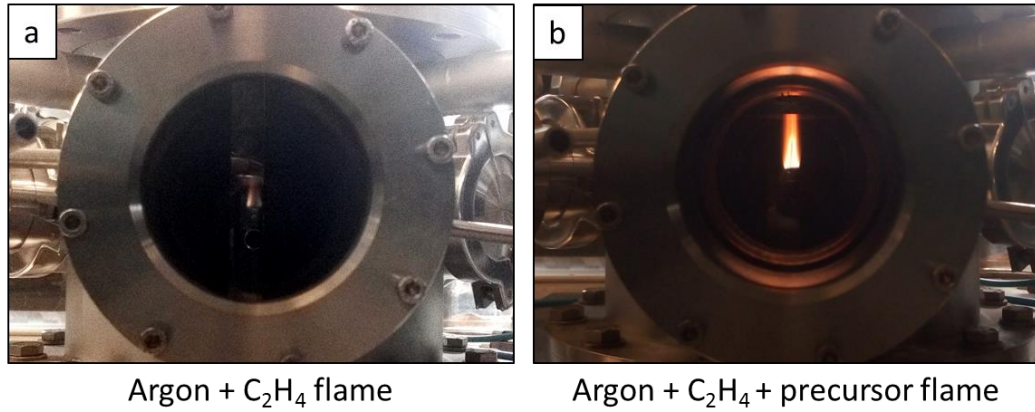


Figure 2.5. Examples of pyrolysis flames; a: before sending the aerosol, the flame is not very intense; b: with the aerosol, a long and brilliant flame can be observed

#### Stop of the experiment

- To stop the production of powder and the whole experiment, the garbage filter is opened (and the previous filter is closed to avoid any pollution). The generation of aerosol and then the different gas flows are stopped to be replaced by argon flows. Then the laser is stopped. After evacuating the reactor and flushing with argon back to 1 atm, the filters are disassembled to collect the produced nanopowders.
- The different gas lines are purged to replace all the gases by argon. The weight of consumed solution of precursors is measured to determine its consumption during the synthesis.

### II. Characterization of laser-pyrolysed samples: structural properties

#### 1. X-Ray Powder Diffraction (XRD)

The first characterization for the produced powders is the X-ray diffraction to obtain structural information. The analysis of the diffraction patterns is generally used to determine the crystalline phase(s) of the sample but can also help to obtain the crystallite sizes and study the defects in the crystal structure. If the sample shows several crystalline phases, their amount can sometimes be determined by quantitative analysis. A Siemens D5000 diffractometer with the Bragg-Brentano geometry is used, it is equipped with a copper anticathode ( $\lambda(K\alpha) = 1.5418 \text{ \AA}$ ). For the measurements, the powders are put in a flat sample holder. The XRD patterns are acquired during approximately 3 hours at ambient temperature with an angular range from  $20^\circ$  to  $80^\circ$ , with a step size of  $0.04^\circ$  and 7 seconds of measuring time. The different phases are determined using ICDD database.

#### 2. Scanning Electron Microscopy (SEM) and Energy Dispersive X-ray Spectrometry (EDS)

The shape and size of the nanoparticles are observed by scanning electron microscopy using an Ultra 55 microscope from Carl Zeiss. The working distance is varied from 4 mm to 8 mm depending on the samples with an accelerating voltage from 3 kV to 20 kV.

Elemental composition of the powders are also analyzed by energy dispersive X-ray spectrometry. The accelerating voltage is set to 20 kV for that purpose.

#### 3. Transmission Electron Microscopy (TEM) and High-Resolution Transmission Electron Microscopy (HRTEM)

For small nanoparticles, transmission electron microscopy and high-resolution transmission electron microscopy are used to exploit the morphological and crystallographic information of the produced nanopowders. TEM images are taken with a Phillips CM12 microscope and with the JEOL 2010 F microscope to observe particles of few nanometers. HRTEM with a resolution almost 100 times higher than TEM is used to measure the thickness of coatings around particles and to determine the interplanar distances of the crystalline phases present in a powder.

The accelerating voltage is set to 80 kV for TEM observations with the Phillips CM12 and to 200 kV for TEM and HRTEM observations with the JEOL 2010 F. The samples are prepared using lacey

carbon grids. A small amount of nanopowders is dispersed in absolute ethanol by sonication, then the TEM grid is dipped into the dispersion and dried before observation.

#### 4. Thermo-Gravimetric Analysis (TGA)

In order to estimate the amount of carbon (pollution or desired coating) in the nanopowders, TGA measurements are conducted. This latter analysis enables the determination of by-products content (water, organics), and allows to determine the kinetics of carbon combustion under air flow in order to set the annealing parameters that will be used for carbon removal. The use of TGA is not as accurate as the use of a chemical analyzer but it enables the comparison of the carbon content with other similar samples. Still additional characterizations were made with a chemical analyzer to measure the carbon content with accuracy and the values given by TGA and by the analyzer are very close to each other. As the chemical analyzer consumes a relatively high amount of powder, TGA is preferentially used in this work.

The analyses are performed using a TA Instrument Q500 or a SETARAM 92-16-18. The samples (10-15 mg in a crucible) are heated from room temperature to target temperature (400°C or 500°C) under air, with an isotherm at the target temperature for at least 30 minutes. The ramp rate is chosen at 10°C or 20°C.min<sup>-1</sup> depending on the equipment.

#### 5. Brunauer-Emmett-Teller (BET)

Nanopowders generally show relatively high specific surface area (in m<sup>2</sup>.g<sup>-1</sup>). The BET surface area is recorded for several samples using a Micromeritics Flowsorb 2300 model under a mixture of nitrogen/helium gases (1:3).

#### 6. Mössbauer <sup>57</sup>Fe

In this work, <sup>57</sup>Fe Mössbauer analyses are used in addition of XRD measurements, especially when there is a doubt between two different iron phases.

Indeed, in XRD, iron oxides and zinc iron oxides phases show diffraction peaks which are very close to each other making sometimes difficult to differentiate them. <sup>57</sup>Fe Mössbauer spectroscopy is a very sensitive technique used to probe the nature and the relative amounts of iron containing phases; moreover, it is also used to characterize amorphous phases not addressed by XRD.

## Characterization of laser-pyrolysed samples: electrochemical properties

This technique uses the absorption and re-emission of  $\gamma$  rays to study the nuclear structure. Mössbauer spectroscopy probes the hyperfine transitions between the excited and the ground states of a nucleus and allows the study of three types of nuclear interactions: the **isomeric shift**, the **quadrupole splitting** and the magnetic splittings.

Transmission  $^{57}\text{Fe}$  Mössbauer spectra are recorded at room temperature with a  $^{57}\text{Co}(\text{Rh})$   $\gamma$ -ray source in the constant acceleration mode. The velocity scale is calibrated using the magnetic six line spectrum of a high-purity iron absorber.

Pellets of 2 cm<sup>2</sup> containing 20 to 30 mg of the material are used for the Mössbauer measurements. These latter are performed and analyzed by M. Sougrati and L. Stievano in AIME laboratory (ICGM, Montpellier).

### III. Characterization of laser-pyrolysed samples: electrochemical properties

#### 1. Coin cells preparation

The electrochemical performances of the different materials obtained by laser pyrolysis are evaluated in 2016 coin cells. They mainly consist in an electrode containing the metal oxide, a separator impregnated with electrolyte and a lithium metal electrode. As metallic lithium is used instead of a real cathode material, the coin cells are considered as half cells. In this case, metallic lithium corresponds to the negative electrode whereas the metal oxide is the positive electrode (Figure 2.6).

The negative electrode consists in a metallic lithium disk of 10 mm diameter with a thickness of 0.8 mm (Aldrich, 99.9%). Whatman® glass microfiber filters are used as separator. This latter is soaked with the electrolyte EC PC 3DMC (ethylene carbonate, polycarbonate and dimethylcarbonate) + 1M LiPF<sub>6</sub>

The positive electrode corresponds to the metal oxide electrode. The metal oxide nanopowder cannot be used directly as an electrode therefore an ink is prepared in order to intimately mix the three main components: the active material, the carbon additives and the binder.

The active material is the metal oxide nanopowder which gives its specific capacity to the electrode. For the electrochemical measurements in half cell, the ink is always composed of 70% wt. of active material.

Carbon additives have to be used in the ink preparation to ensure the electronic percolation of the electrode. If the conductivity in the electrode is too low, charges cannot be easily transferred from one electrode to another what reduces the electrochemical performances. Two types of carbon additives are embedded in the mixture: vapor grown carbon fibers (VGCF) from Showa Denko (150 nm

## Characterization of laser-pyrolysed samples: electrochemical properties

diameter, 10-20  $\mu\text{m}$  length) ensure a good conductivity through large parts of the electrode thanks to their length. Carbon particles from Timcal (Super P, carbon black) of approximately 50 nm diameter also contributes to increase the conductivity between the active material particles. In the ink preparation, 9% wt. of VGCF and 9% wt. of carbon black are used.

The last component of the ink is the binder, necessary to ensure the mechanical strength of the electrode. The binder is generally a polymer which is in contact with the conductive additives of the electrode as well as with the active material. For conversion materials, carboxymethylcellulose (CMC) is often identified as an appropriate binder. 12% wt. of CMC is incorporated into the ink.

The different components are first manually mixed together with a spatula into a jar. Deionized water is added and the mixture is then ball-milled for thirty minutes with a Planetary Micro Mill Pulverisette 7. After this process, the homogeneous ink is coated onto a copper foil thanks to a blade. The thickness of the coating is fixed to 150  $\mu\text{m}$ , it is dried overnight under air. The thickness of the coating after drying is around 20  $\mu\text{m}$ . Electrodes of 12 mm diameter are then cut and dried in a Buchi oven for 12h at 120°C under vacuum.

This preparation enables the production of electrodes with a smooth surface without any peels or cracks at the surface. The tested electrodes have loadings of active material in the range of 1-2  $\text{mg}\cdot\text{cm}^{-2}$ , making possible the comparison of the electrochemical performances between the different electrodes.

The coin cells are assembled in a glovebox under argon atmosphere. The electrodes are weighted in the glovebox before assembling. It is then placed on the bottom cap of the cell. The separator is deposited on it with around 15 droplets of electrolyte. The lithium metal electrode is fitted on a stainless steel collector. The second cap is placed and the whole cell is closed using a crimper to be tightened.

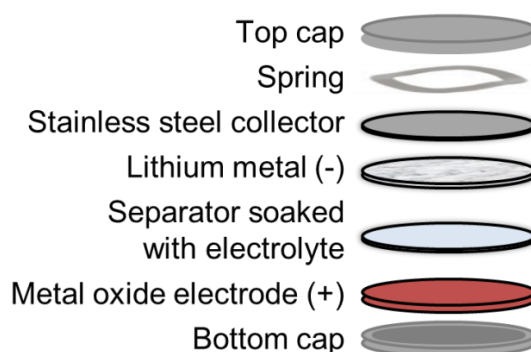


Figure 2.6. Half-cell assembly vs. metallic lithium

## 2. Galvanostatic cycling

## Characterization of laser-pyrolysed samples: electrochemical properties

Galvanostatic cyclings are used to evaluate the battery performance in terms of cycle life and effective capacity. For galvanostatic cycles, the current is set and the battery potential vs.  $\text{Li}/\text{Li}^+$  is measured into a potential window (charge and discharge cut-off potentials). For a discharge (delithiation of the negative electrode, so lithiation of the metal oxide), the current is negative and for a charge (lithiation of the negative electrode so delithiation of the metal oxide), the current is positive. For galvanostatic cyclings in half-cell, the first current is set negatively to lithiate the metal oxide (Figure 2.7).

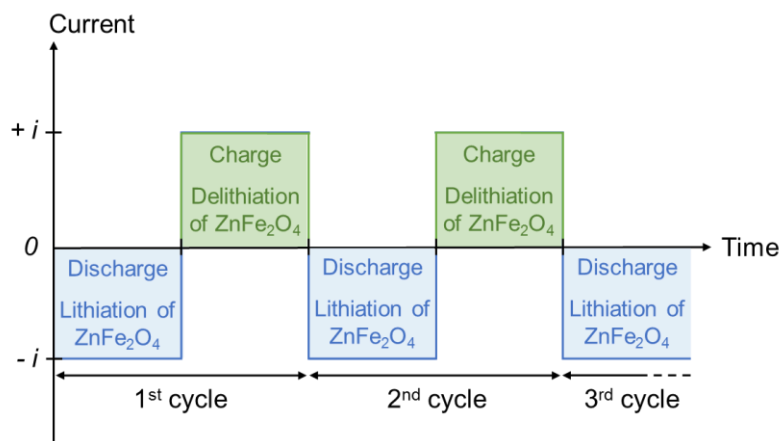
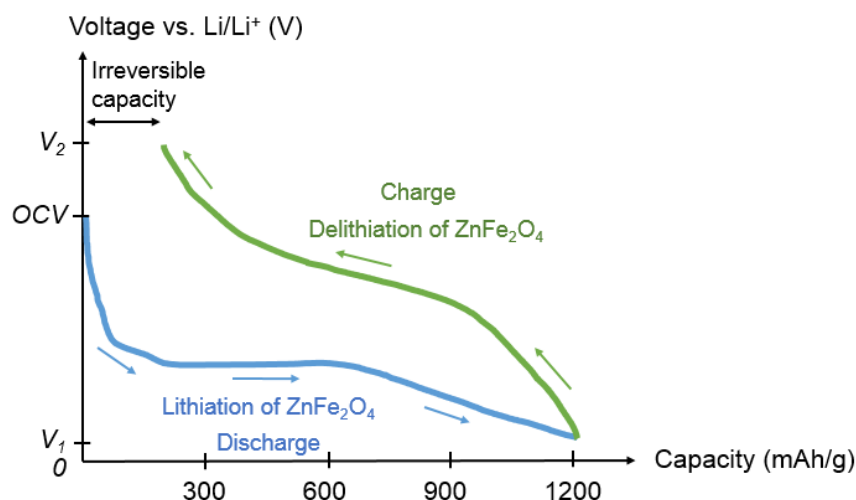


Figure 2.7. Current vs. time curves for galvanostatic cyclings measurements

When the current is negative, the voltage vs.  $\text{Li}/\text{Li}^+$  is decreasing from the open circuit voltage (OCV) to the discharge cut-off potential. When the current is positive, the potential vs.  $\text{Li}/\text{Li}^+$  is increasing from the lowest cut-off potential to the charge cut-off potential (Figure 2.8). In this work, the potential window is set from 0.01V to 3.0V as in many measurements in literature to have elements of comparison.



## Characterization of laser-pyrolysed samples: electrochemical properties

Figure 2.8. Charge and discharge profiles.  $V_1$ : discharge cut-off potential,  $V_2$ : charge cut-off potential.

The current is related to the speed of the battery cycling and is expressed by a “C-rate” value. For instance, when a C/10 current rate is chosen, it means that theoretically, the discharge should take 10 hours as well as the charge, so a full cycle takes 20 hours. C/5 means one cycle in 10 hours and 1C, 2C and 4C correspond to one discharge in 1 hour, 30 minutes and 15 minutes respectively. The set current is calculated thanks to the theoretical capacity of the active material.

For example, for  $\text{ZnFe}_2\text{O}_4$ , the theoretical capacity is  $1000 \text{ mAh.g}^{-1}$  what means one discharge can be realized in one hour with a current of  $1000 \text{ mA.g}^{-1}$ . For a C/10 current rate, the discharge has to be ten times slower so the current has to be ten times lower so  $100 \text{ mA.g}^{-1}$ .

The current to set (in mA) is calculated using the weight of the active material only (so 70% of the electrode mass):

$$\text{Current (mA)} = \text{active material weight (g)} \times \text{theoretical capacity (mAh.g}^{-1}\text{)}$$

The C-rate has to be carefully chosen as it has an impact on the battery performance during cycling. Indeed, the higher the C-rate is, the higher the polarization during cycling will be, which means that the cut-off voltages will be reached quickly in detriment of the stored capacity. A high C-rate is generally leading to a poor cycle life due to kinetic effects as the lithium may not be able to diffuse properly in the entire active material. However, if the chosen C-rate is low, the cycling will take more time and the working of the battery will be less representative of a real applications. But as it is a long experiment, there is less polarization and degradation, generally leading to higher capacity and better cycle life. In this work, galvanostatic cyclings are conducted with different current rates from C/50 to 4C depending on the studied sample.

What is evaluated during galvanostatic cyclings are the specific capacities during charge and discharge which are compared to the theoretical value, but also the coulombic efficiency. This value corresponds to the ratio between the discharge capacity and the charge capacity and is expected to be the closest to 100%. When the coulombic efficiency is not at 100%, it means that part of the lithium is not reversibly stored during the discharge. Generally, this phenomena is due to parasitic reactions between the lithium ions and the electrolyte leading to the formation of a SEI layer that traps part of the lithium.

The electrochemical data are acquired thanks to several multichannel battery testers: VMP, MPG, MPG-2 and Macpile from Biologic and MTI from Neware. EC-lab software is used to analyze the data coming from Biologic instruments and data from MTI are studied with the Neware BTS Data Analysis software.



### 3. Cyclic voltammetry

Cyclic voltammetry is an additional characterization to analyze the oxidation and reduction reactions occurring during the charge and discharge processes in a chosen potential window. For this characterization, the potential of the half cell is varied cyclically and the intensity is measured. Generally, cyclic voltammetry is conducted between 0.01 and 3.0 V (as for the galvanostatic cyclings) and with a scan rate of  $0.1 \text{ mV}\cdot\text{s}^{-1}$  (Figure 2.9).

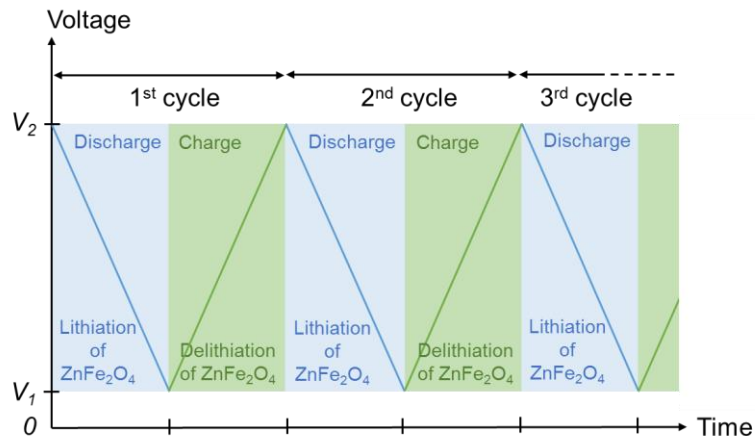


Figure 2.9. Voltage vs. time curves for cyclic voltammetry measurements

During the discharge, the intensity is negative and the reduction/cathodic peaks appear whereas during charge, the intensity is positive and the oxidization/anodic peaks are shown (Figure 2.10).

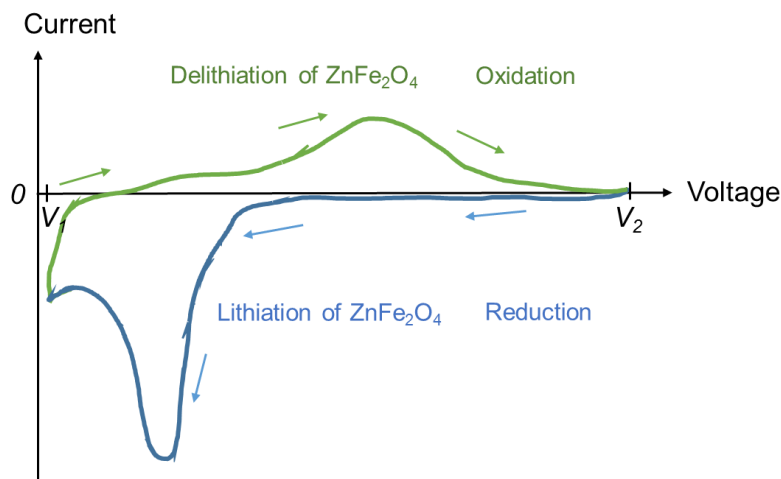


Figure 2.10. Cyclic voltammetry curves to identify the oxidation and reduction peaks: intensity vs. voltage

This electrochemical technique helps to understand the lithium storage mechanism for an active material, coupled with the charge/discharge curves of the galvanostatic cyclings. However, these two techniques do not give enough information to have a deep understanding of the processes

involved for the lithium storage in mixed-transition metal oxides. That is why some techniques like operando measurements are also used to obtain more information.

#### 4. Operando measurements

Operando characterization techniques are useful to observe in real time what is happening during the charge and the discharge processes. This can be interesting to understand the lithiation and delithiation mechanism, in particular for the first cycle. Indeed, as explained in the first chapter, the first cycle of lithiation/delithiation for  $\text{ZnFe}_2\text{O}_4$  leads to the formation of  $\text{ZnO}$  and  $\text{Fe}_2\text{O}_3$  instead of recovering the initial  $\text{ZnFe}_2\text{O}_4$  oxide.

XRD only allows the analysis of the first lithiation as the material becomes amorphous after this step.  $^{57}\text{Fe}$  Mössbauer is performed to confirm what is found in XRD patterns and to give more information on the iron containing phases during both lithiation and delithiation.

To highlight the interest of  $\text{ZnFe}_2\text{O}_4$  compared with a mixture of  $\text{ZnO}$  and  $\text{Fe}_2\text{O}_3$ , operando XRD are conducted on  $\text{ZnFe}_2\text{O}_4$  and  $\text{ZnO/Fe}_2\text{O}_3$  and supplementary information is given with operando  $^{57}\text{Fe}$  Mössbauer on  $\text{ZnFe}_2\text{O}_4$ .

For these two characterization techniques, a specific electrode must be prepared with the proper amount of active material as shown below (Figure 2.11).

	XRD	$^{57}\text{Fe}$ Mössbauer
Electrode composition (%) (oxide/CMC/VGCF/CB)	50/20/20/10	50/20/20/10
Oxide weight	15 mg/cm <sup>2</sup>	20-30 mg/cm <sup>2</sup>

*Figure 2.11. Composition of the electrode for each characterization technique*

For operando acquisitions, the electrode is not used with a coin cell but with a specific in-situ cell. A metallic lithium disk is used as negative electrode, a separator is placed between the lithium and the metal oxide electrode. The separator is soaked with EC DMC + 1M  $\text{LiPF}_6$  electrolyte. This electrolyte is used instead of EC PC 3DMC + 1M  $\text{LiPF}_6$  (used in coin cells) as preliminary tests with the in-situ cell showed more stable cycling with EC DMC + 1M  $\text{LiPF}_6$  than with EC PC 3DMC + 1M  $\text{LiPF}_6$ . Two beryllium windows are located on the top and bottom part of the cell (Figure 2.12). The electrode preparation and the assembly of the cell are realized according to the procedure developed at the ICGM (Montpellier).

## Characterization of laser-pyrolysed samples: electrochemical properties

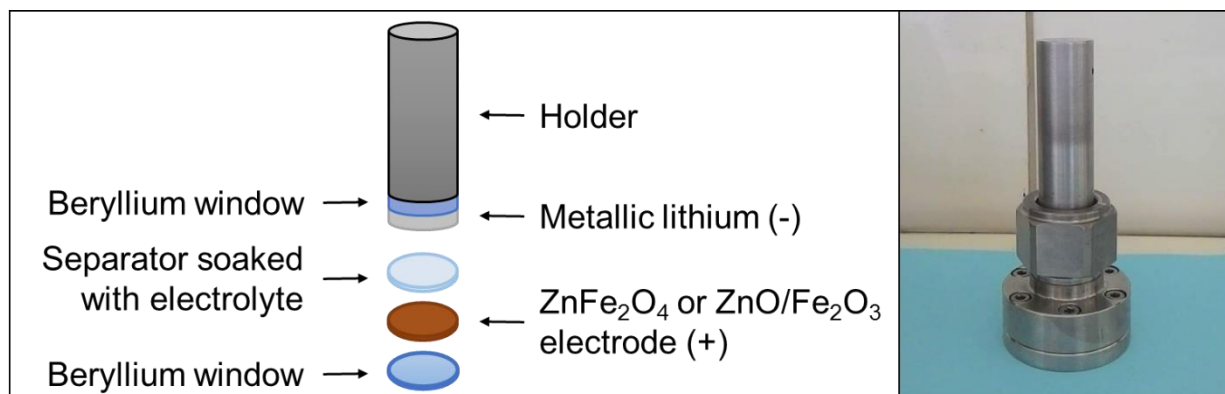


Figure 2.12. Diagram of the in-situ cell (left), photography of an assembled in-situ cell (right)

The Philips X'Pert MPD diffractometer is used for the acquisition of diffraction patterns. A pattern is acquired for thirty minutes every two hours for one lithiation. The current is set to store one lithium per 10 hours; theoretically the acquisition should last 90 hours.

For Mössbauer, one spectra is acquired every four hours during one cycle and a half. The current is set to insert one lithium ion per mole of active material in 13 hours. The complete data acquisition lasts approximately two weeks.

---

## Chapter 3. Syntheses by laser pyrolysis of zinc iron oxides

---

This chapter is focused on the characterization of the nanopowders obtained by laser pyrolysis. The first part presents a selection of different zinc iron oxide samples synthesized under different conditions whereas the second and third parts are dedicated to iron oxide nanopowders and zinc oxide nanopowders respectively. Indeed, as presented in chapter 1,  $\text{ZnFe}_2\text{O}_4$  structure is rapidly lost upon cycling in battery, and the materials after the first cycle is composed of a mixture of the two binary oxides that are submitted to the redox reactions during the following cycles.

For timetable reasons, the usual systematic approach of synthesis parameters could not be achieved in this work, priority being given to the fast obtaining of the required crystalline phase. The influence of some experimental conditions was nevertheless investigated, and more particularly the effect of the chosen precursors on the nanoparticles morphology is shown.

The last part summarizes the thermal treatment realized for some samples before battery tests. Beyond this selection of the most representative samples, more than 100 syntheses were conducted throughout the PhD work to define relevant pyrolysis parameters and precursors solutions.

## I. Synthesis of zinc iron oxide nanopowders

Zinc iron oxide nanoparticles were obtained by laser pyrolysis using different solutions of precursors (Table 3.1). Zinc and iron nitrates and chlorides were identified as cheap and easy to use precursors. Moreover they are highly soluble in deionized water or in absolute ethanol. They offer the possibility to prepare highly concentrated solutions (solutions S1 and S2), which could maximize the production rate. Either PALAS or pyrosol generators were used to form an aerosol. Indeed, chlorides precursors are not compatible with PALAS generator as they degrade some parts of the apparatus. For the pyrosol, only ethanol solutions could be employed as no aerosol could be formed with aqueous solutions (this limitation is no longer true with the newest version of the pyrosol device, which was not available at the beginning of this work). Moreover, with the pyrosol, the concentration needs to be much lower to obtain a dense aerosol with the piezoelectric device (solutions S3 to S5).

Table 3.1. List of precursors solutions used for the synthesis of zinc iron oxide nanopowders

Solution	Precursors	Solvent
<b>S1</b>	$\text{Zn}(\text{NO}_3)_2 \cdot 6\text{H}_2\text{O} + \text{Fe}(\text{NO}_3)_3 \cdot 9\text{H}_2\text{O}$ 50% wt.	DI H <sub>2</sub> O 50% wt.
<b>S2</b>	$\text{Zn}(\text{NO}_3)_2 \cdot 6\text{H}_2\text{O} + \text{Fe}(\text{NO}_3)_3 \cdot 9\text{H}_2\text{O}$ 40% wt.	Absolute EtOH 60% wt.
<b>S3</b>	$\text{Zn}(\text{NO}_3)_2 \cdot 6\text{H}_2\text{O} + \text{Fe}(\text{NO}_3)_3 \cdot 9\text{H}_2\text{O}$ 3% wt.	Absolute EtOH 97% wt.
<b>S4</b>	$\text{ZnCl}_2 + \text{FeCl}_3 \cdot 6\text{H}_2\text{O}$ 3% wt.	Absolute EtOH 97% wt.
<b>S5</b>	$\text{ZnCl}_2 + \text{FeCl}_3 \cdot 6\text{H}_2\text{O}$ 9% wt.	Absolute EtOH 91% wt.

For all syntheses presented in this work, the laser power was set to 90% to deliver approximately 1600 W in the reaction zone above the nozzle. The difference with the theoretical laser power output (approx. 2000 W) lies in the losses along optical chain (mirrors, lens, windows). Other parameters were varied in order to obtain the desired phases, compositions and morphologies.

Two main objectives were pursued: obtaining the pure desired oxide phase, and enabling the coating of the particles by a continuous shell of carbon that could have beneficial effect on battery performances as mentioned in chapter 1. As we did not have enough time to complete the electrochemical study of the carbon coated samples, this latter synthesis of these particles will only be presented in the perspectives part at the end of the manuscript.

## 1. Nitrates precursors

Nitrates solutions S1 (water) and S2 (ethanol) were tested with the PALAS generator for the synthesis of  $\text{ZnFe}_2\text{O}_4$  nanopowders and thus observe the influence of the solvent. Two powders named ZFO-1 and ZFO-2 were obtained by using argon as carrier gas. All the details about the experimental conditions are summarized in Table 3.2. For these two powders, nitrates are the only source of oxygen (no air as additional gas). In comparison with ZFO-1, the  $\text{C}_2\text{H}_4$  and argon flow rates had to be modified for the synthesis of ZFO-2 in order to obtain a stable flame and to avoid the clogging of the filter.

Table 3.2. Experimental conditions for the syntheses of ZFO-1 and ZFO-2 using nitrates solutions and the PALAS generator

	Aerosol generator	Solution	$\text{C}_2\text{H}_4$	Carrier gas	Additional gas	Feeding rate	Production rate
<b>ZFO-1</b>	PALAS	S1	430 sccm	Argon 4800 sccm	X	13.2 g/h	313 mg/h
<b>ZFO-2</b>	PALAS	S2	680 sccm	Argon 3740 sccm	X	28 g/h	885 mg/h

An image of a typical yellow/orange laser pyrolysis flame that appears during syntheses under argon conditions is shown below (Figure 3.1). The brightness of the flame is significantly increased when the aerosol of precursors is carried to the reaction zone because of the thermal radiation of the hot particles and agglomerates.



Figure 3.1. Laser pyrolysis flame of ethylene, argon and nitrates precursors without air

A higher production rate is measured for ZFO-2. The higher feeding rate recorded for this latter sample, partially responsible for higher production here, could be surprising as the carrier gas flow was lower. The easier vaporization of ethanol vs water upon nebulization is known to artificially

increase the aerosol production. Nevertheless, this should not increase the production rate of oxide powders as vaporization of pure solvent would not feed nitrates into the reaction zone. On the contrary, ethanol can be a source of carbon production, this latter pollution being possibly enhanced by the increase in ethylene flow in ZFO-2. Such carbon production could increase the overall production rate. In order to find out, the amount of carbon in the two powders was determined by TGA. The measurements were conducted under air from 20°C to 500°C, with a ramp of 20°C/min and an isothermal step at 500°C during 1h (Figure 3.2).

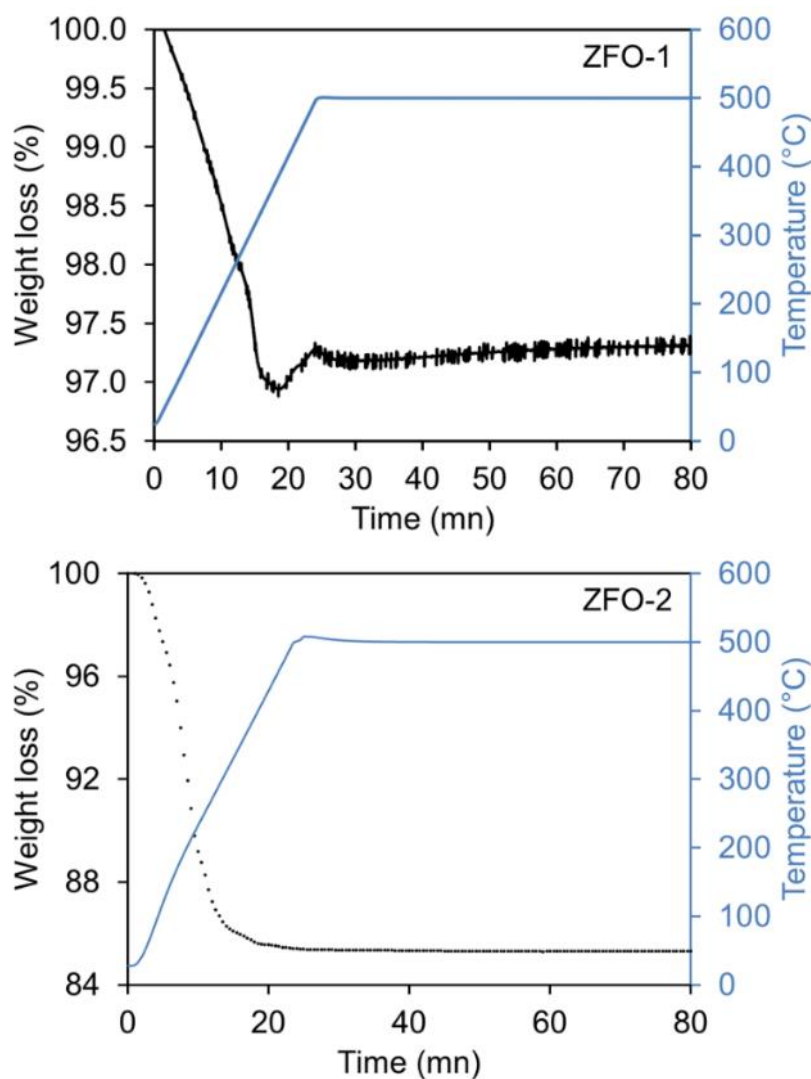


Figure 3.2. TGA measurements for ZFO-1 and ZFO-2 from 20°C to 500°C, ramp: 20°C/min and isothermal step of 1h at 500°C

For ZFO-1, the graph shows a loss smaller than 3% wt., with a majority being lost under 250 °C. Such low temperature loss is ascribed to adsorbed water and organic residuals degassing. The amount of free carbon in ZFO-1 is thus less than 1% wt. what means the  $C_2H_4$  gas was very poorly decomposed during the synthesis. For ZFO-2, the weight loss is about 15% but only 5% is ascribed to

the loss of free carbon above 250°C. The higher content in organics residuals and in free C in ZFO-2 can be ascribed to the increased ethylene flow and to the replacement of water by ethanol.

However, this relatively low carbon-based pollution and the increase in feeding rate by a factor of 2.1 cannot explain by themselves the increase in production rate by a factor of 2.8.

The decomposition yields of Fe and Zn for ZFO-1 and ZFO-2 were estimated by calculating the ratio between the weight of produced zinc and iron (deduced from the amount of produced oxide phase) and the weight of consumed zinc and iron (obtained with the amount of carried solution). Even if this decomposition yield is to take with caution because of the major approximations on the measurements of feeding rate (difference in solution weight in the tank before and after the synthesis), large variations of this parameter between two syntheses remain meaningful. For ZFO-1, this decomposition yield was estimated to 22%, whereas for ZFO-2, it was estimated to 36%. This higher decomposition yield is explained by the higher reaction temperature, which is the consequence of three main facts: i) because of a higher  $C_2H_4$  flow, the laser absorption was 50% higher for ZFO-2 than for ZFO-1, ii) vaporization of water is more efficient to cool the reaction than ethanol one, iii) decrease in argon flow rate in ZFO-2 leads to a longer residence time and lower dilution of the reaction by the neutral gas.

The two produced powders were first characterized by XRD to determine the synthesized crystalline phases (Figure 3.3). ZFO-1 seems to be a pure  $ZnFe_2O_4$  phase (01-079-1499, franklinite) whereas ZFO-2 presents a  $ZnFe_2O_4$  phase but also traces of non-stoichiometric zinc iron oxide phase. As the  $C_2H_4$  flow rate was higher for ZFO-2 than for ZFO-1, the reaction takes place in a carbon rich environment. Part of the available oxygen coming from the nitrates precursors is then likely consumed in reactions with carbon species leading to a lack of this element to achieve complete oxidization of the oxide phase in the case of ZFO-2.

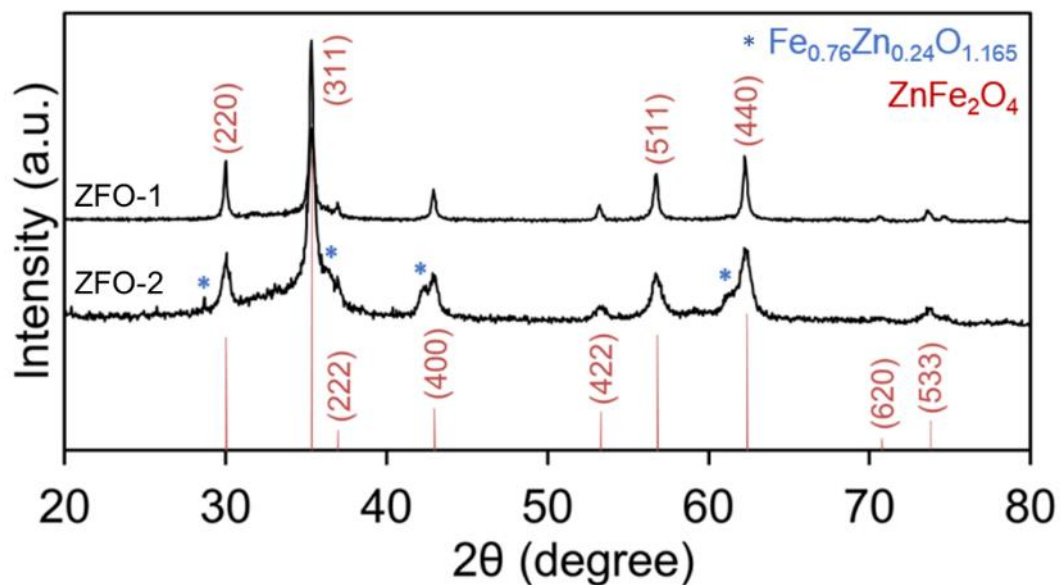


Figure 3.3. XRD patterns for ZFO-1 and ZFO-2. ZFO-1: pure ZnFe<sub>2</sub>O<sub>4</sub> phase. ZFO-2 presents ZnFe<sub>2</sub>O<sub>4</sub> phase with traces of non-stoichiometric zinc iron oxides phase

The morphology of ZFO-1 was observed by SEM and TEM (Figure 3.4). Both images show agglomerated small nanoparticles (< 10 nm) together with large particles (> 50 nm to hundreds of nm).

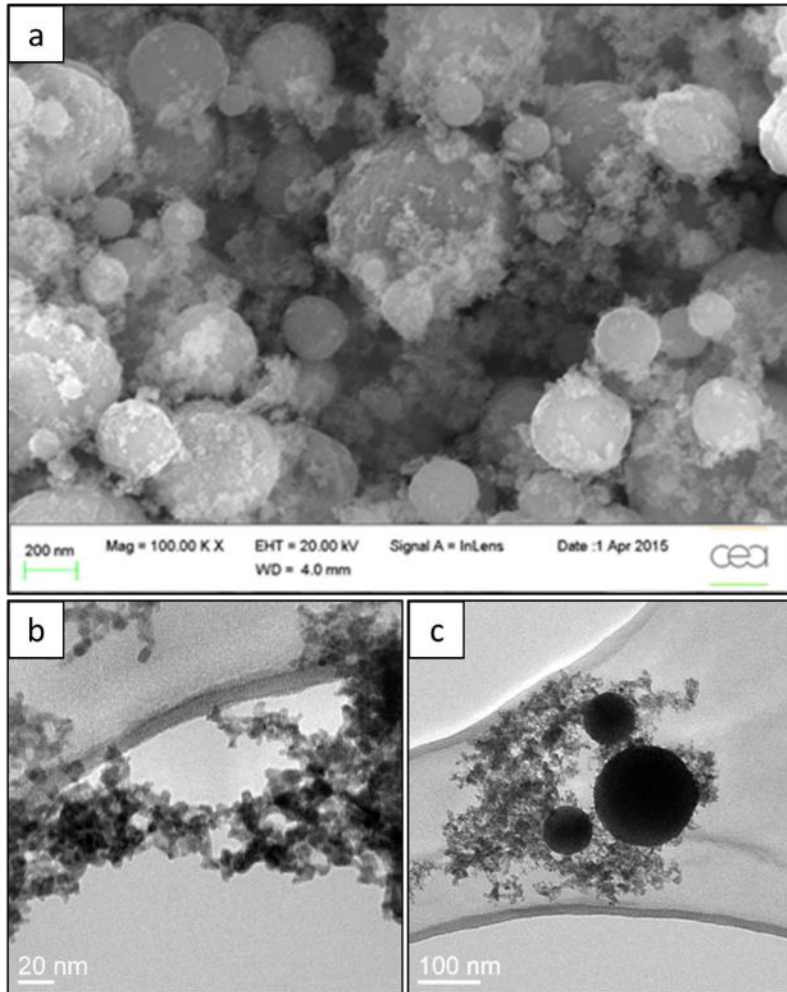


Figure 3.4. SEM (a) and TEM images (b,c) of ZFO-1: presence of both small nanoparticles (< 10 nm) with larger particles (> 50 nm to hundreds of nm)

ZFO-1 is interesting for electrochemical tests as it shows a pure  $\text{ZnFe}_2\text{O}_4$  phase in XRD. In order to prepare operando measurements,  $^{57}\text{Fe}$  Mössbauer analysis was first achieved on the pristine ZFO-1 material, as shown in Figure 3.5.

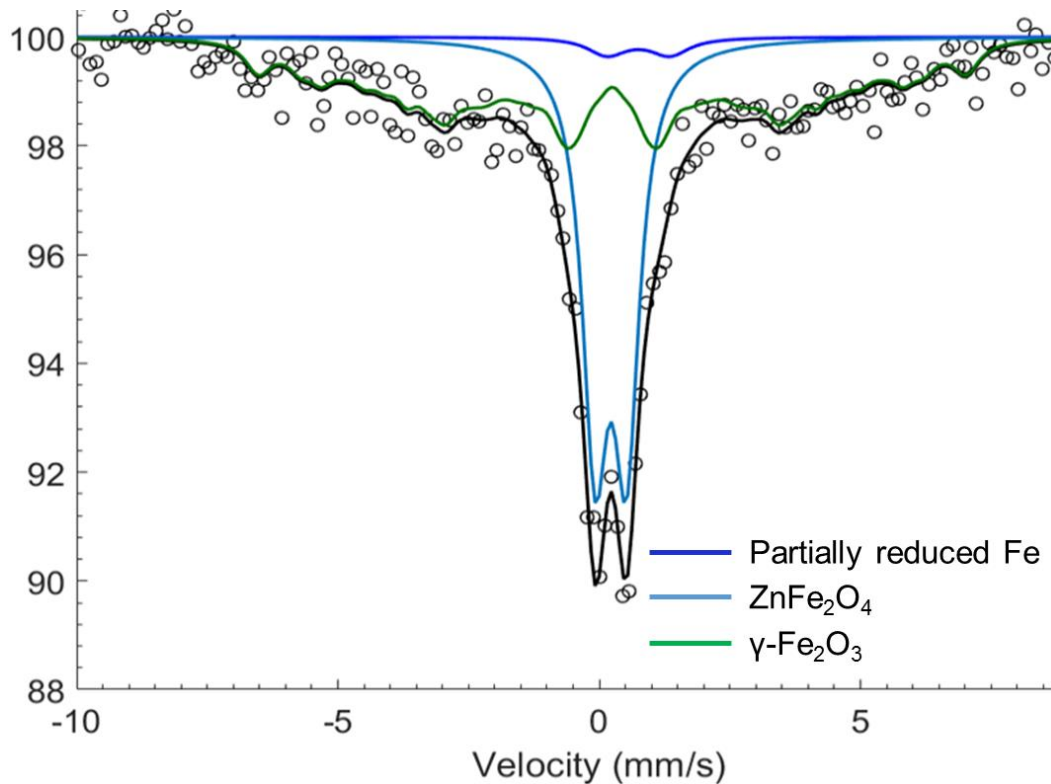


Figure 3.5.  $^{57}\text{Fe}$  Mössbauer spectrum of the pristine ZFO-1 sample measured at room temperature. Three phases are observed:  $\text{ZnFe}_2\text{O}_4$  (45% at.),  $\gamma\text{-Fe}_2\text{O}_3$  (52% at.) and a minor iron phase (3% at.).

The spectrum consists in an intense quadrupole doublet, which is however accompanied by a major fraction of broadly distributed magnetic hyperfine patterns, which were fitted here using a histogram distribution of Lorentzian components extending from 5 to 42 T. The magnetic component has an intensity of 52 % of the total resonance area, is centred at  $\delta = 0.36$  mm/s with no quadrupole splitting, and likely represents disordered or nanosized iron oxides, most probably maghemite ( $\gamma\text{-Fe}_2\text{O}_3$ ). Since this compound only starts to order magnetically at room temperature, it corresponds to grain sizes between 3 and 10 nm<sup>1-3</sup>. The quadrupole doublet, on the other hand, has a quadrupole splitting  $\Delta = 0.60$  mm/s and an isomer shift  $\delta = 0.33$  mm/s, in line with previous spectra of zinc ferrite  $\text{ZnFe}_2\text{O}_4$ <sup>5</sup> and corresponds to 45 % of the total iron in the sample. A minor doublet which corresponds to only partially reduced iron is also present, even though with very low intensity (less than 4 % of the total spectral intensity).

The presence of such an amount of  $\gamma\text{-Fe}_2\text{O}_3$  was not expected as it was not detected by XRD. Moreover, EDX analyses show that the atomic ratio Fe/Zn is very close to 2 in ZFO-1 powder. This means that a zinc-based phase should also be present in ZFO-1, what was not observed with XRD as well. A possibility is that both  $\gamma\text{-Fe}_2\text{O}_3$  and any zinc-based phase are amorphous and thus do not show diffraction peaks. However, the diffraction pattern background shape does not reveal the presence of any amorphous contribution. In addition, laser pyrolysis is conducted under a relatively high

temperature which does not foster the formation of amorphous materials. Complementary XAS studies will be conducted in a very near future to conclude about the presence of any other zinc and iron phases. HRTEM observations should also be performed to confirm whether both parts of the bimodal size distribution consist in the same crystalline phase or correspond to ternary and binary oxide phases suggested by Mössbauer spectroscopy.

The use of a nitrates aqueous solution combined with argon carrier gas seems to be efficient to produce  $\text{ZnFe}_2\text{O}_4$  nanopowders. Nevertheless, the obtained morphology always shows bimodal size distribution. Changing the solvent did not help on that point, as ZFO-2 sample shows the same size distribution. To observe the influence of the atmosphere, syntheses under air (carrier gas) were then conducted (Table 3.3). The idea was to increase the reaction temperature by means of combustion without increasing the carbon content in the reaction in order to avoid free carbon pollution or incomplete oxidization of the ternary phase as depicted for ZFO-2 sample.

Table 3.3. Experimental conditions for the syntheses of ZFO-3 and ZFO-4 under air using nitrates solutions

	Aerosol generator	Solution	$\text{C}_2\text{H}_4$	Carrier gas	Additional gas	Feeding rate	Production rate
<b>ZFO-3</b>	PALAS	S1	220 sccm	Air 5600 sccm	X	10.3 g/h	327 mg/h
<b>ZFO-4</b>	Pyrosol	S3	240 sccm	Argon 1850 sccm	Air 1570 sccm	24.6 g/h	281 mg/h

For the synthesis of ZFO-3, the same solution as ZFO-1 was used and argon was replaced by air as carrier gas in the PALAS generator. The chosen air flow rate was chosen to obtain a blue and stable flame during the synthesis.

For the synthesis of ZFO-4, a solution of nitrates in ethanol was used and for safety reasons, the pyrosol generator was chosen as with the PALAS, the use of air as carrier gas with flammable solvents is hazardous. The air flow rate cannot be as high as with the PALAS for the pyrosol. In addition, S2 solution could not be used because of its too high loading in nitrates that inhibits aerosol formation in pyrosol. A more diluted solution in ethanol had to be prepared (solution S3) and was used for ZFO-4 synthesis.

$\text{C}_2\text{H}_4$  and air flow rates had to be chosen in order to:

- Avoid soot production
- Avoid flame diffusion towards inlet nozzle
- Keep pressure stable in the regulating loop.

Images of typical flames for this series of synthesis are shown in Figure 3.6. The use of air during the synthesis conducts to the appearance of a blue flame before the sending of the aerosol and a blue and orange flame when the precursors are reacting. This blue part reveals the contribution of a combustion reaction in addition to the pyrolysis process.

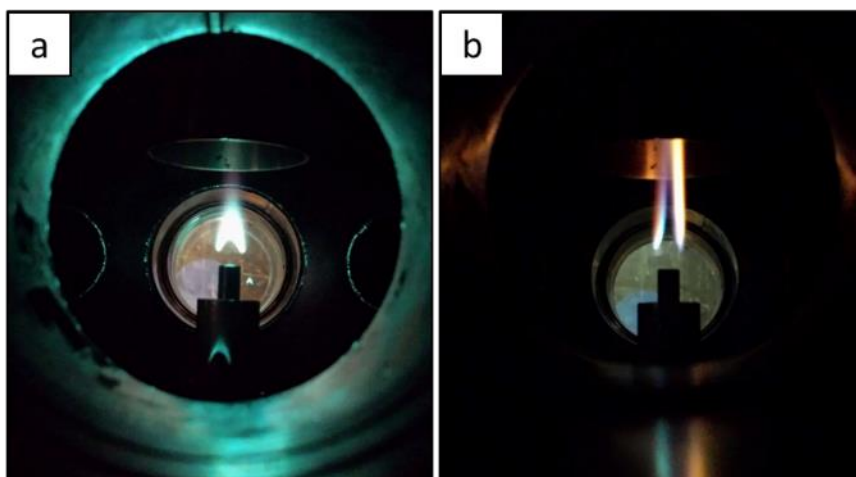


Figure 3.6. (a) Flame of air and ethylene and (b) flame of air, ethylene and precursors

For ZFO-3, the feeding rate was a little lower when compared to ZFO-1, certainly because air was less efficient than argon for the liquid spraying in PALAS generator. Nevertheless, production rate was close to the one for ZFO-1, which seems to indicate a decomposition yield of the precursor a little higher (estimated here at 29%). This can be due to the increase of the flame temperature thanks to the combustion reaction. However the amount of a potential carbon pollution was evaluated by TGA (Figure 3.7).

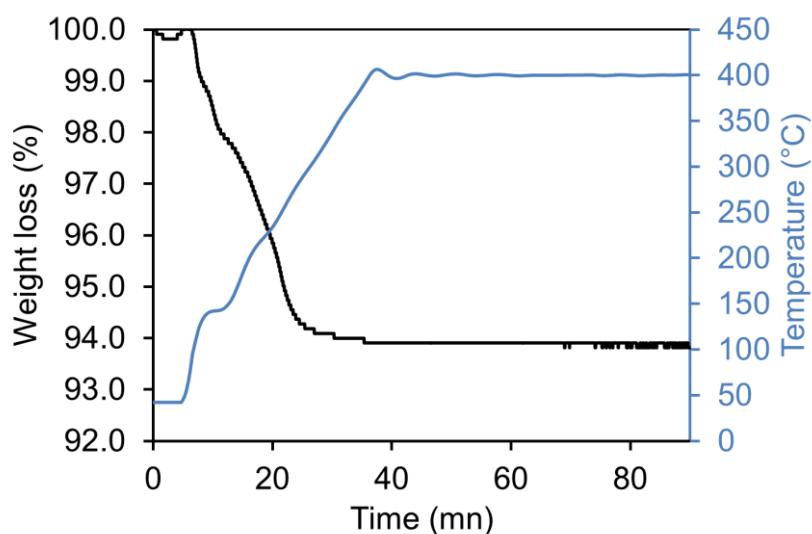


Figure 3.7. TGA measurements for ZFO-3 from 40°C to 400°C, ramp: 10°C/min and isothermal of 50 min at 400°C

This graph shows a total weight loss of 6% occurring before 300°C and which could mainly be attributed to the loss of water and PAH as amorphous free carbon generally disappears around 350°C. The powder does not seem to be carbon polluted meaning that the synthesis conditions were suitable for the complete decomposition of ethylene.

The obtained ZFO-3 powder was then characterized by XRD (Figure 3.8).

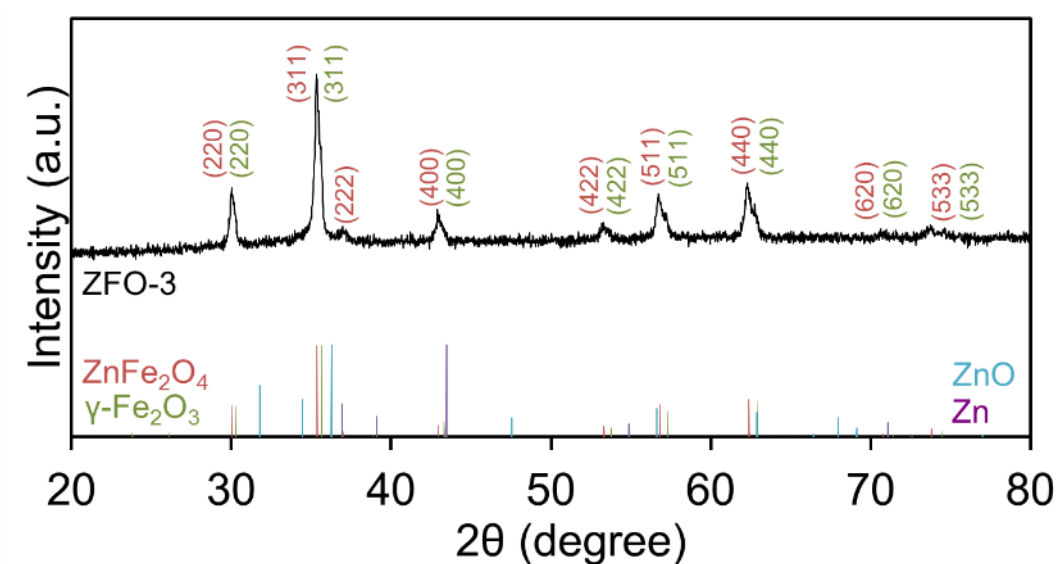


Figure 3.8. XRD pattern for ZFO-3: presence of  $\text{ZnFe}_2\text{O}_4$  and iron oxide phase

The XRD pattern shows two main series of peaks: one can be attributed to the  $\text{ZnFe}_2\text{O}_4$  franklinite phase and the second one to  $\gamma\text{-Fe}_2\text{O}_3$  phase (00-039-1346, maghemite) or  $\text{Fe}_3\text{O}_4$  (00-026-1136, magnetite). Indeed, XRD peaks for  $\gamma\text{-Fe}_2\text{O}_3$  are very close to  $\text{Fe}_3\text{O}_4$  peaks ones, therefore  $^{57}\text{Fe}$  Mössbauer measurements were conducted to determine the nature of the iron oxide (Figure 3.9).

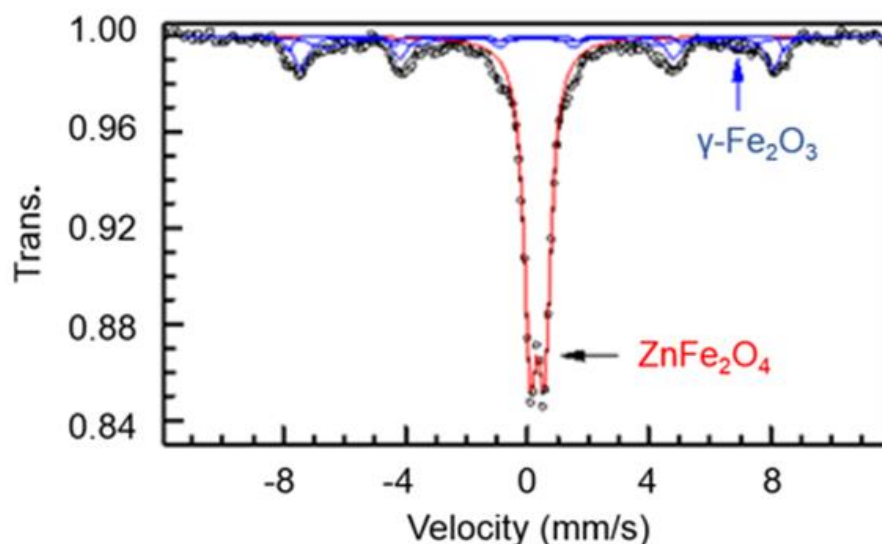


Figure 3.9.  $^{57}\text{Fe}$  Mössbauer spectrum for ZFO-3 measured at room temperature. Presence of two phases: 65% at. of  $\text{ZnFe}_2\text{O}_4$  and 35% at. of  $\gamma\text{-Fe}_2\text{O}_3$

This spectrum confirms the presence of two contributions: the main one, accounting for 65% of the total resonance area, is a quadrupole doublet, while the remainder of the spectrum (35%) undergoes magnetic splitting into a distribution of Zeeman sextets. The doublet has typical parameters of superparamagnetic nanosized  $\text{ZnFe}_2\text{O}_4$  particles<sup>6,7</sup> while the magnetically ordered portion can be fitted with at least three magnetic sextets having virtually the same isomer shift and different hyperfine fields (42, 48 and 50 T). These sextets can be assigned to  $\gamma\text{-Fe}_2\text{O}_3$ <sup>8</sup> particles with different particle sizes. Fitted parameters are shown below (Table 3.4).

Table 3.4. Fitted parameters for Mössbauer measurements

	$\delta$ (mm/s)	$\Delta E_Q$ (mm/s)	$\Gamma$ (mm/s)	$B_{\text{HF}}$ (Tesla)	RA (%)
Doublet	0.34	0.46	0.50	-	65
Sextets	0.30*	-0.03	0.82*	42, 48 and 50.6	35

Mössbauer results enable to ascribe the iron oxide phase observed by XRD to maghemite. The presence of both  $\text{ZnFe}_2\text{O}_4$  and  $\text{Fe}_2\text{O}_3$  was not expected as the solution was prepared with a stoichiometric ratio of precursors. The XRD pattern of ZFO-3 does not clearly reveal the presence of any zinc oxide phase, while a small contribution of Zn phase cannot be excluded. Nevertheless EDX analyses show that the atomic ratio Fe/Zn is close to 2 in the powder. As for ZFO-1, the most probable hypothesis is that an amorphous Zn based phase is formed and not seen in XRD.

ZFO-3 morphology was then observed by TEM to be compared to ZFO-1 (Figure 3.10).

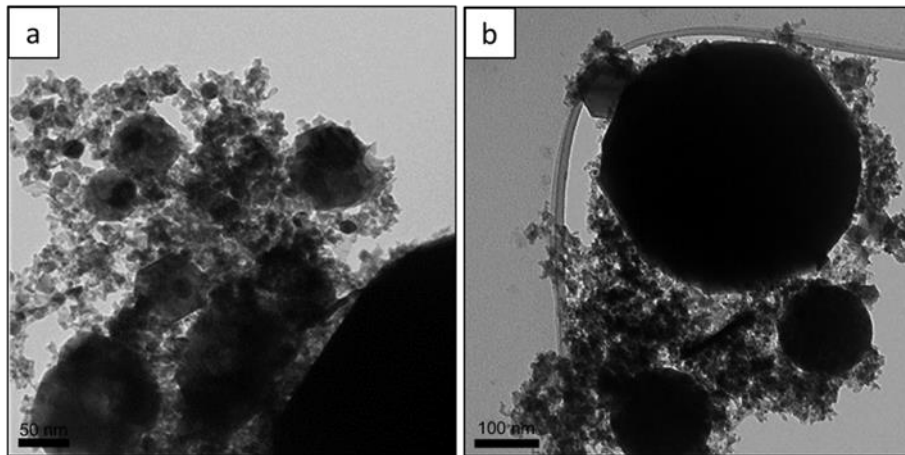


Figure 3.10. Morphology of ZFO-3 sample observed by TEM (a,b).

As for ZFO-1 and ZFO-2 samples, a bimodal size distribution can be observed in ZFO-3 with small nanoparticles of 10-20 nm and larger particles from a hundred nm to a micron. The observed morphology is thus very similar to the one depicted for ZFO-1 with slightly larger particles in both parts of the size distribution. When compared to this latter sample, the main effect of air introduction seems to be the appearance of the binary iron oxide phase. The desired effect on the size distribution was not obtained. HRTEM images were also taken to measure interplanar distances and confirm the nature of existing phases (Figure 3.11).

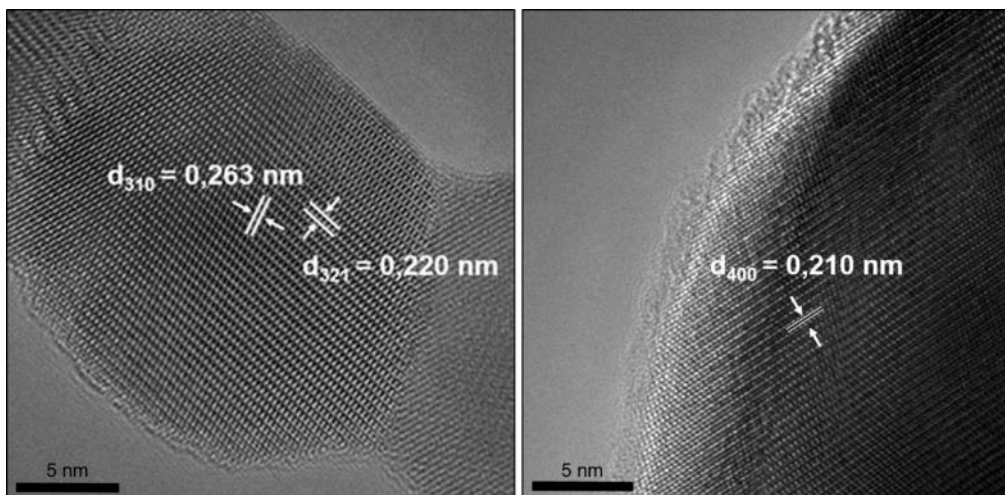


Figure 3.11. HRTEM images of ZFO-3. Interplanar distances corresponding to  $\text{Fe}_2\text{O}_3$  maghemite phase (left) and to  $\text{ZnFe}_2\text{O}_4$  phase (right)

HRTEM confirms the composition of the powder with particles showing either the interplanar distance characteristic of  $\gamma\text{-Fe}_2\text{O}_3$  ( $d = 0.263$  nm for (310) plane,  $d = 0.220$  nm for (321) plane) and the interplanar distance corresponding to  $\text{ZnFe}_2\text{O}_4$  ( $d = 0.210$  nm, (400) plane). It is interesting to note that

both phases can be found in the small and large size parts of the size distribution, which seems to indicate that the mechanisms that leads to the formation of the two crystalline phases occurs independently of the one that leads to the bimodal size distribution.

The appearance of secondary phases during the synthesis of MTMO has already been observed by Choi *et al*<sup>9</sup> for the synthesis of  $\text{ZnCo}_2\text{O}_4$  by a combustion process. According to these authors, the ternary oxide is formed first. As  $\text{ZnCo}_2\text{O}_4$  is not stable above  $800^\circ\text{C}$ <sup>10</sup>, the partial loss of oxygen and the decomposition of the MTMO occurs because of the high temperature encountered in such flames, leading to the formation of separated ZnO and CoO phases. In our case, synthesis of ZFO-3 was realized under combustion conditions and the presence of the iron oxide phase may be related to the temperature of the flame which is assumed to be higher than for conventional laser pyrolysis reactions. A mechanism of ternary oxide decomposition similar to the one reported by Choi is likely to happen, even if in our case the second metal oxide phase (Zn in our case) is not detected by XRD on the contrary of Choi who observed the CoO phase. This could be due to different crystallization conditions for ZnO and CoO, or to flame temperature differences. The observation of intermediate iron phases was also reported by Li *et al.* during the combustion synthesis of  $\text{ZnFe}_2\text{O}_4$ <sup>11</sup>.

Nevertheless, during the high temperature synthesis of Zn-Fe oxide by flame spray pyrolysis, Pratsinis *et al* observed the appearance of an additional  $\text{Fe}_2\text{O}_3$  phase only for high precursors concentrations (metal concentrations above 0.8M)<sup>12</sup>. For ZFO-3, the solution S1 was used with a concentration of 0.9M of Zn and 1.8M of Fe, which places us in the upper range of concentrations used by these authors

ZFO-4 sample was synthesized using pyrosol. This latter generator operates in quite different conditions when compared to PALAS, which makes uneasy any comparison. Indeed, as argon has to be used as carrier gas for ethanol based solutions, the total flow that can be processed by the pressure regulation system does not enable the use of similar air flow rate as for ZFO-3. Even though the feeding rate was much higher because of the better efficiency of the pyrosol device, the production rate was a little lower than for ZFO-3. The main explanation comes from the very low precursor concentration in the solution that could be used with pyrosol.

ZFO-4 sample also synthesized with air addition was characterized by XRD (Figure 3.12).

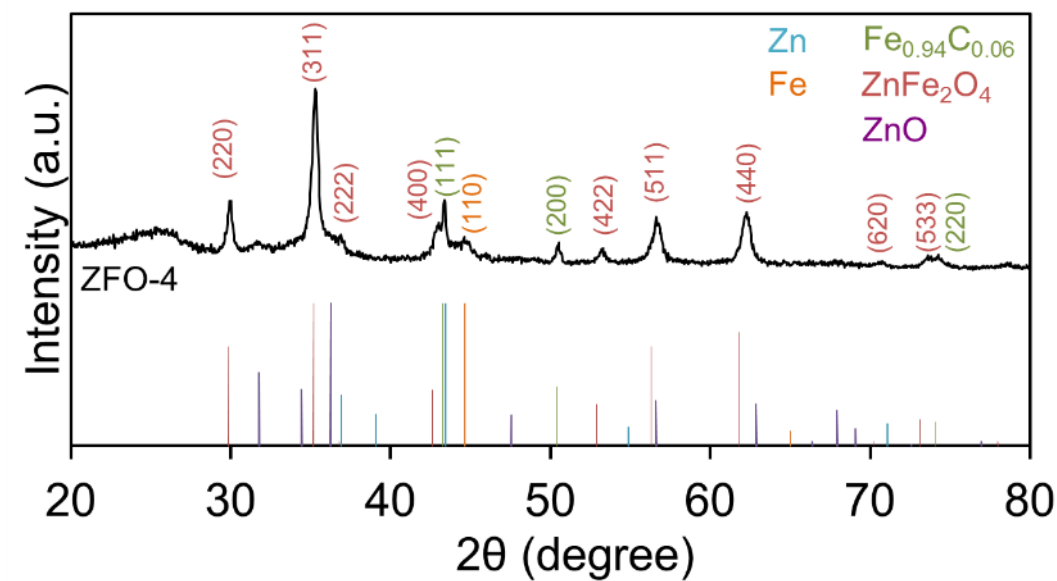


Figure 3.12. XRD pattern for ZFO-4: presence of  $\text{ZnFe}_2\text{O}_4$  and  $\text{Fe}_{0.94}\text{C}_{0.06}$  phases

Once again the  $\text{ZnFe}_2\text{O}_4$  phase was produced, however a  $\text{Fe}_{0.94}\text{C}_{0.06}$  phase (01-074-5520, austenite) and metallic iron were also identified. Zn based phases in small amount cannot be completely excluded. The presence of the non-oxide iron phases can be explained by the amount of carbon in the reactional medium compared to the amount of oxygen. For ZFO-3, the air flow rate was 25 times higher than  $\text{C}_2\text{H}_4$  whereas for ZFO-4, this flow was only 6.5 times higher than  $\text{C}_2\text{H}_4$  flow rate. Moreover ethanol in fuel rich conditions can add more carbon to the system. The incomplete oxidation of iron for ZFO-4 may be due to a lack of oxygen in the reactional medium compared to the amount of available carbon (coming from both ethylene and ethanol), leading to the formation of a secondary phase. Moreover, as ethanol is used as the solvent in the solution, it may act as a fuel and lead to a hotter flame, in a similar way to FSP vs FASP in flame based processes. In this case, as mentioned for ZFO-3, the high temperature can conduct to the loss of oxygen and the decomposition of the ternary oxide to form iron-based phase. The pattern shape before  $30^\circ$  is typical of the presence of an amorphous phase. In order to determine if this amorphous component could be attributed to carbon pollution, ZFO-4 was analyzed by TGA (Figure 3.13). The results are very different from the ones recorded for the previous samples which exhibited low amount of carbon.

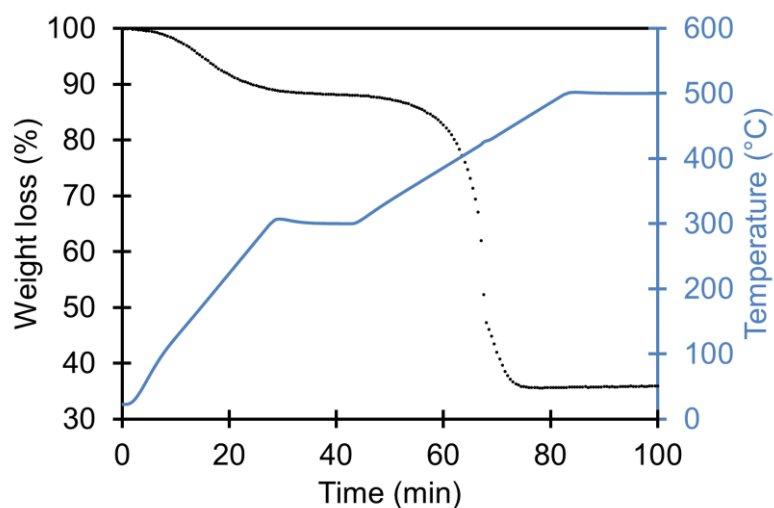


Figure 3.13. TGA measurements for ZFO-4 from 20°C to 500°C, ramp: 10°C/min, isothermal of 1h at 500°C

As it can be seen on the graph above, the amount of free carbon is high. The first weight loss about 12% before 300°C can be attributed to the evaporation of water and PAH. The second weight loss of more than 50% between 350 and 450°C can be attributed to the combustion of free carbon in the powder. This seems to confirm that the amorphous contribution seen on XRD diagrams can be ascribed to this carbon pollution. When compared to ZFO-3, the presence of large amount of carbon is originated by the lack of available oxygen to burn efficiently the sources of carbon.

The morphology of ZFO-4 powder was also observed by TEM (Figure 3.14).

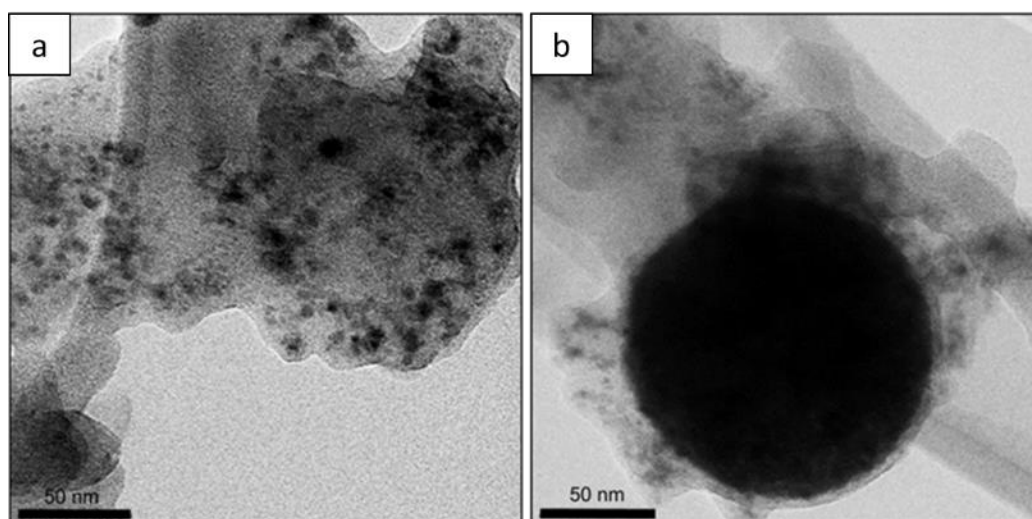


Figure 3.14. TEM images of ZFO-4 (a,b).

ZFO-4 sample shows a similar bimodal size distribution, as previously observed in all samples. Nevertheless, the size of the objects seems lower than the ones observed in the other samples. This

could be a consequence of the higher dilution of the precursor in the solvent, leading to smaller solid precursor particles in the aerosol after solvent vaporization in the hot reaction zone. Moreover, the very small particles population can hardly be distinguished, as it is imbedded in a matrix that can be identified as amorphous carbon. The large particles population appears coated by this amorphous structure too. These TEM images are consistent with the TGA measurements which have shown large carbon content. In comparison, ZFO-3 powder showed small and large particles that could be clearly observed without the presence of any coating or matrix around the particles. The possibility to control this carbon based coating offers interesting perspectives for battery applications, this will be discussed at the end of the manuscript.

For the four investigated samples, the bimodal size populations of particles is characterized by the presence of small nanoparticles of 10-20 nm and larger particles from a hundred nm to a micron. Such size distribution is not commonly observed for laser pyrolysis grown nanoparticles and is more similar to the ones obtained in conventional spray pyrolysis after reaction in droplets. Additional syntheses were then achieved using other types of precursors with the objective of investigating the origin of this unusual size distribution.

## 2. Chlorides precursors

Solutions of chlorides precursors were prepared for the syntheses of zinc iron oxides (solutions S4 and S5).

For the synthesis of  $\text{ZnFe}_2\text{O}_4$  using chlorides precursors, the PALAS generator could not be used (degradation of some parts of the device which are not chemically compatible). As the pyrosol was the only compatible generator, ethanol had to be used instead of water and the concentration of precursors in the solution had to be relatively low.

Two powders were produced using two different chlorides solution. The solution S4 was used to obtain ZFO-5 and the solution S5, more concentrated than S4, was used for the production of ZFO-6. As chlorides precursors do not supply oxygen to the reaction, on the contrary of nitrates, the syntheses were conducted under air atmosphere while keeping argon as carrier gas. Synthesis conditions are detailed in Table 3.5.

	Aerosol generator	Solution	$\text{C}_2\text{H}_4$	Carrier gas	Additional gas	Feeding rate	Production rate
<b>ZFO-5</b>	Pyrosol	S4	240 sccm	Argon 1830 sccm	Air 1630 sccm	34.3 g/h	328 mg/h
<b>ZFO-6</b>	Pyrosol	S5	240 sccm	Argon 920 sccm	Air 1570 sccm	14 g/h	226 mg/h

Table 3.5. Experimental conditions for the syntheses of ZFO-5 and ZFO-6 under air using chlorides solutions

Synthesis conditions for ZFO-5 are very similar to the ones used for ZFO-4. Feeding rate and thus production rates are a little higher, certainly because of the different properties of chloride solution when compared to nitrates ones in terms of aerosol formation. For ZFO-6, carrier gas flow rate was decreased in order to lower the feeding rate and increase residence time, aiming at higher temperature reaction and more available energy for a given mass of precursors. When comparing ZFO-5 and ZFO-6, it is interesting to quote that even if feeding rate is divided by more than 2, production rate is only decreased by one third. This could be attributed to higher precursors decomposition yield and/or production of carbon.

The collected ZFO-5 and ZFO-6 were characterized by XRD (Figure 3.15).

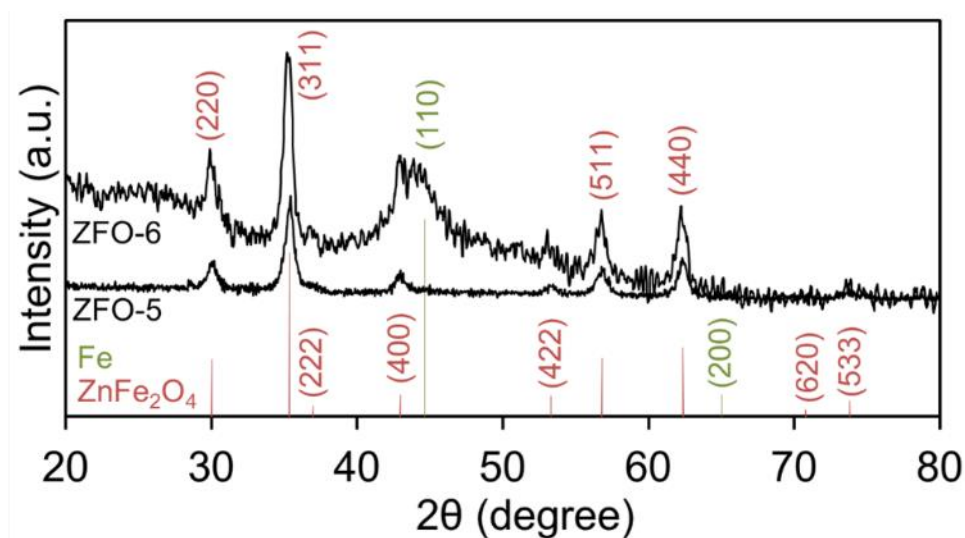


Figure 3.15. XRD pattern for ZFO-5 and ZFO-6: presence of  $\text{ZnFe}_2\text{O}_4$  in both samples, additional Fe phase for ZFO-6

Both ZFO-5 and ZFO-6 patterns reveal the presence of the  $\text{ZnFe}_2\text{O}_4$  crystalline phase. However, ZFO-6 presents a very large peak at  $44^\circ$  which can represent the (400) plane of  $\text{ZnFe}_2\text{O}_4$  besides the (110) plane of crystalline iron. Moreover, ZFO-6 pattern shows a small bump between  $20$  and  $30^\circ$  what may reflect the presence of a large amount of an amorphous phase. This latter pattern is similar to the one recorded for ZFO-4 with different ratios between the phases. The overall peak width for these samples appears broader than the ones obtained with nitrate solutions, which tends to indicate smaller crystallite sizes.

TEM images were taken to observe the morphology of ZFO-5 (Figure 3.16).

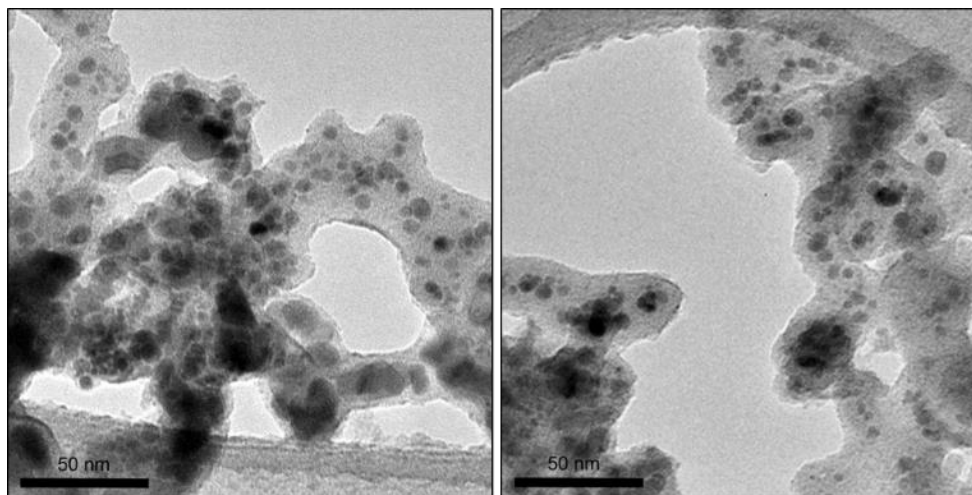


Figure 3.16. Images of ZFO-5 observed by TEM: presence of only small nanoparticles (< 10 nm) embedded in an amorphous matrix

ZFO-5 images highlights a different size distribution of particles from the nanopowders obtained with nitrates precursors. Only very small nanoparticles of about 10 nm embedded in an amorphous matrix can be observed. This amorphous part may be attributed to carbon production coming from the decomposition, at least partial, of ethylene and/or ethanol. Such carbon coating, similar to the one observed for ZFO-4 but in smaller amount, could show advantages for battery applications, as discussed in chapter 1. Nevertheless this amorphous carbon does not provide contribution on XRD diagrams. The main difference with particles obtained from nitrates solutions is thus the absence of bimodal size distribution: indeed, no large particles could be observed in ZFO-5.

TGA measurement conducted between 20°C and 400°C (Figure 3.17) shows a total weight loss of 45% separated in two weight losses. One is before 200°C and probably corresponds to the evaporation of water and PAH. The next weight loss from 300°C to 400°C may correspond to amorphous carbon. The amount of carbon in ZFO-5 powder is evaluated at 25%. This is noticeably lower than the one recorded in ZFO-4 powder obtained in similar synthesis conditions.

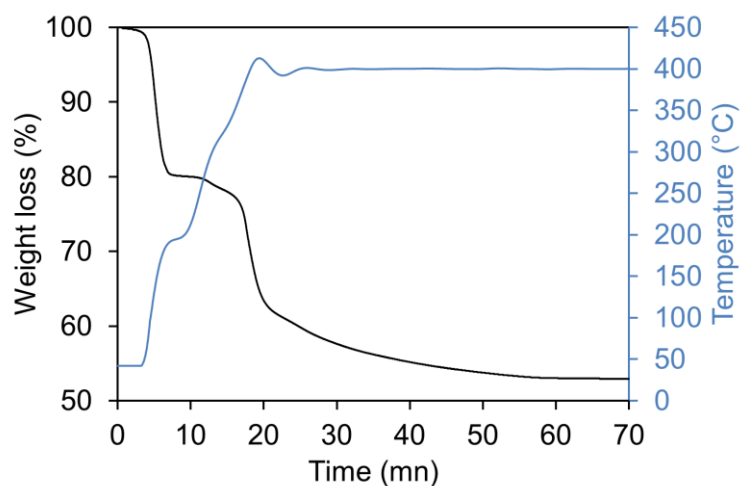


Figure 3.17. TGA measurements for ZFO-5 from 20°C to 400°C, ramp at 20°C/min with an isothermal at 400°C for 40 min

A monomodal size distribution of nanoparticles, slightly larger than for ZFO-5, is observed for ZFO-6 by TEM, with the presence of a matrix around these particles too. However, unlike for ZFO-5, the coating around the nanoparticles seems to be partially more organized as shown on HRTEM images (Figure 3.18). In particular in the vicinity of the nanoparticles surface, the first layers of carbon show graphite-like structure. The interplanar distance measured in this structures can actually be attributed to the (002) plane of graphite. The presence of graphite in this powder in the vicinity of particles surface can be related to the presence of iron based phases as these latter can foster the growth of graphite rather than amorphous carbon<sup>13</sup>.

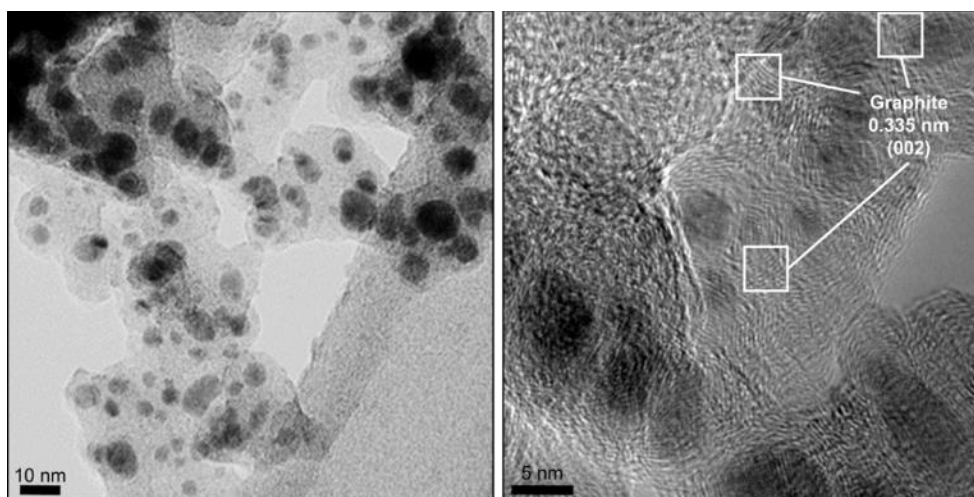


Figure 3.18. Morphology of ZFO-6 observed by TEM (left) and highlighting of graphite around the nanoparticles

ZFO-6 sample was also analyzed by TGA (Figure 3.19). The graph below shows a total loss of 64%, what is higher than for ZFO-5. The mass loss before 200°C may be due to water and PAH while the higher weight loss from 350°C to 500°C can be attributed to carbon loss. The amount of carbon in

ZFO-6 is evaluated at 36% so 10% higher than for ZFO-5. For ZFO-6, the carrier gas flow rate was two times lower than for ZFO-5 meaning the residence time of the particles in the flame was higher. With less neutral gas dilution, the flame temperature was also higher which promotes the carbon precursors decomposition. Consequently, more carbon may be formed around the nanoparticles for ZFO-6 than for ZFO-5. Moreover, this carbon spends more time in a hotter zone and can be partially organized thanks to iron rich surfaces. The higher temperature encountered here is also assumed to be responsible for the formation of the secondary iron phase seen in XRD.

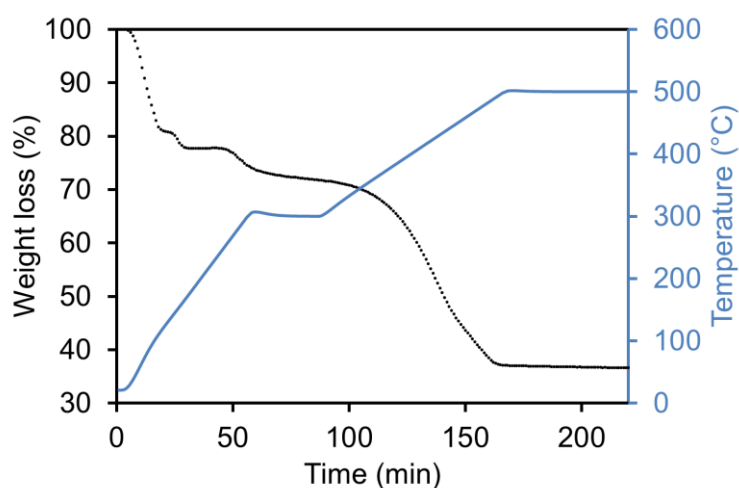


Figure 3.19. TGA measurements for ZFO-6 from 20°C to 500°C with an isothermal at 300°C and at 500°C

The synthesis of ZFO-5 and ZFO-6 based on the use of chlorides precursors also gives the possibility to obtain zinc iron oxide phases. As observed for nitrates based solutions, in presence of air the use of too high temperature conditions seems to favor the appearance of secondary phases. Moreover, the choice of the precursors seems to be important to obtain the desired size distribution of particles: nitrates appear to favor a bimodal size population and chlorides a monomodal one with only small nanoparticles. Discussion on that point will be pursued after the part dealing with binary oxides synthesis.

In this part dedicated to  $\text{ZnFe}_2\text{O}_4$  synthesis, we have seen that the proper choice of the precursors nature, of the gas atmosphere (air and/or argon) and of their flow rates gives the possibility to tailor the size distribution of particles in the obtained ternary oxide nanoparticles: bimodal or monomodal size distribution, with or without carbon coating. This is an advantage to investigate the most appropriate structure for battery performance.

To compare the influence of the size distribution on the electrochemical performances, one sample with the bimodal size distribution and one with the monomodal size distribution were cycled in batteries. ZFO-1 and ZFO-5 were chosen as they show less secondary phases. The corresponding results will be presented in the chapter 4. This chapter will also present the investigation about the interest of the mixed-transition oxide  $\text{ZnFe}_2\text{O}_4$  compared to a mixture of  $\text{ZnO}$  and  $\text{Fe}_2\text{O}_3$ , as upon cycling these two phases replace the starting ternary compound very soon. In this context,  $\text{ZnO}$  and  $\text{Fe}_2\text{O}_3$  nanoparticles were also produced by laser pyrolysis in order to prepare the required binary oxides mixtures.

## II. Synthesis of iron oxide nanopowders

Several solutions of precursors were used for the synthesis of iron oxide nanopowders: iron nitrate, iron chloride and iron acetylacetonate were chosen (Table 3.6).

Solution	Precursors	Solvent
<b>S6</b>	Fe(NO <sub>3</sub> ) <sub>3</sub> · 9H <sub>2</sub> O 50% wt.	DI H <sub>2</sub> O 50% wt.
<b>S7</b>	FeCl <sub>3</sub> · 6H <sub>2</sub> O 3% wt.	Absolute EtOH 97% wt.
<b>S8</b>	Fe(Acac) <sub>3</sub> 3% wt.	Absolute EtOH 97% wt.

Table 3.6. Solutions of precursors used for the synthesis of iron oxide nanopowders

Two powders labeled FeOx-1 and FeOx-2 were obtained using the nitrate solution with air or argon as carrier gas. The details of the experiments are summarized below (Table 3.7). FeOx-2 synthesis parameters are similar to the ones used for ZFO-1, and the obtained absorption and feeding rate are similar too. On the contrary, the production rate is divided by two. The decomposition yield for FeOx-1 and FeOx-2 is estimated around 13%.

	Aerosol generator	Solution	C <sub>2</sub> H <sub>4</sub>	Carrier gas	Additional gas	Feeding rate	Production rate
<b>FeOx-1</b>	PALAS	S6	0.37 slm	Air 5.60 slm	X	12.4 g/h	160 mg/h
<b>FeOx-2</b>	PALAS	S6	0.31 slm	Argon 4.80 slm	X	12.4 g/h	144 mg/h

Table 3.7. Experimental conditions for the synthesis of FeOx-1 and FeOx-2 using a nitrate precursor solution

XRD patterns for the two samples reveal series of peaks corresponding to iron oxides (Figure 3.20).

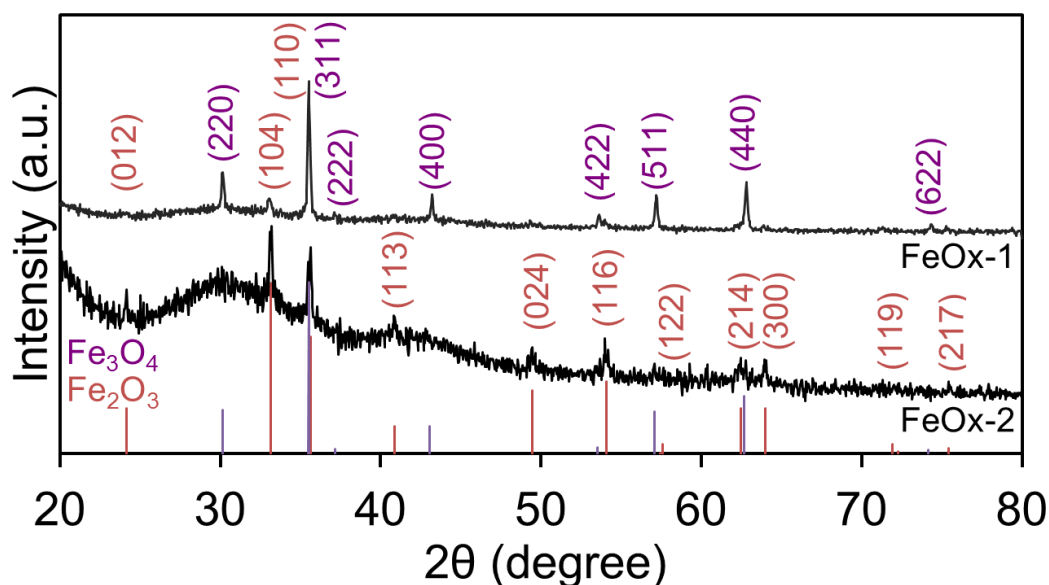


Figure 3.20. XRD patterns for FeOx-1 and FeOx-2

For FeOx-1, the synthesis under air atmosphere leads to the formation of two iron crystalline phases: both  $\text{Fe}_2\text{O}_3$  (01-077-9925, hematite) and  $\text{Fe}_3\text{O}_4$  (19-0629, magnetite) seems to be produced by laser pyrolysis. For FeOx-2, the  $\text{Fe}_2\text{O}_3$  phase can be mainly observed on the XRD pattern even though few peaks may show the presence of a minority  $\text{Fe}_3\text{O}_4$  phase. An amorphous contribution is also observed on the diagram that might come from the sample holder.

The morphology of FeOx-1 and FeOx-2 observed by TEM corresponds to spherical nanoparticles with a bimodal size distribution with small agglomerated nanoparticles of 10-20 nm and large particles with sizes ranging from several hundreds of nm to a micron, like for ZFO-1, ZFO-3 and ZFO-4 (Figure 3.21). This is coherent with the assumption that iron nitrate is the cause of a bimodal size population. As usually obtained with water based solutions, no amorphous carbon coating can be observed over the agglomerates. This latter material is thus not responsible for the amorphous contribution in FeOx-2 XRD diagram.

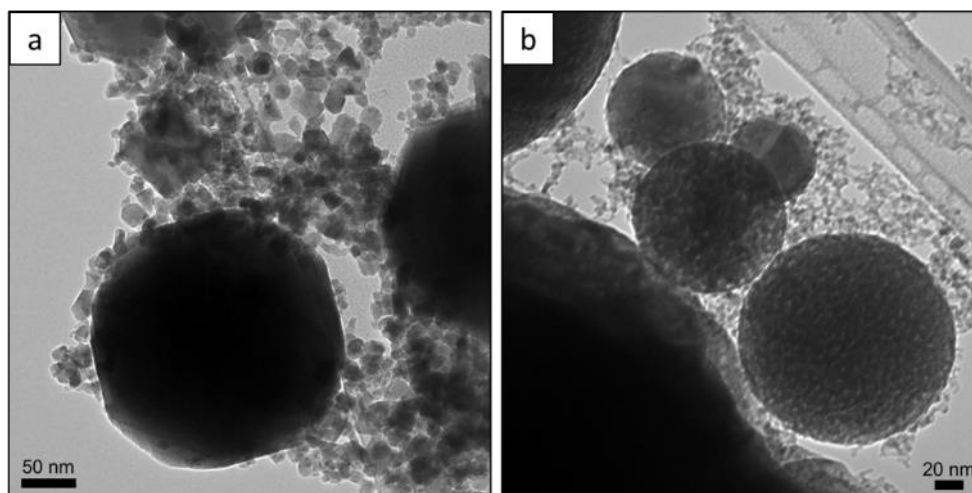


Figure 3.21. TEM images of FeOx-1 and FeOx-2 showing a bimodal size population due to iron nitrate precursor

To obtain a pure Fe<sub>2</sub>O<sub>3</sub> phase with only one size population, syntheses were also conducted using iron chloride and iron acetylacetonate precursors. Two powders were obtained, both using the pyrosol generator (PALAS was not compatible with chlorides) and under air atmosphere (Table 3.8). Solution with acetylacetonate enables an increase of the feeding rate, which is not followed by an increase of production rate. The decomposition yields are estimated at 71% for FeOx-3 and 55% for FeOx-4. It seems that the chloride precursor is decomposed more easily during the synthesis compared to the acetylacetonate one.

	Aerosol generator	Solution	C <sub>2</sub> H <sub>4</sub>	Carrier gas	Additional gas	Feeding rate	Production rate
<b>FeOx-3</b>	Pyrosol	S7	0.24 slm	Argon 1.83 slm	Air 2 slm	34.6 g/h	213 mg/h
<b>FeOx-4</b>	Pyrosol	S8	0.24 slm	Argon 1.83 slm	Air 2.42 slm	50.2 g/h	189 mg/h

Table 3.8. Synthesis conditions for the production of FeOx-3 (chloride precursor) and FeOx-4 (acetylacetonate precursor)

FeOx-3 and FeOx-4 XRD patterns both show a  $\gamma$ -Fe<sub>2</sub>O<sub>3</sub> phase (maghemite) but FeOx-3 also reveals few peaks that belong to  $\alpha$ -Fe<sub>2</sub>O<sub>3</sub> phase (hematite) (Figure 3.22).

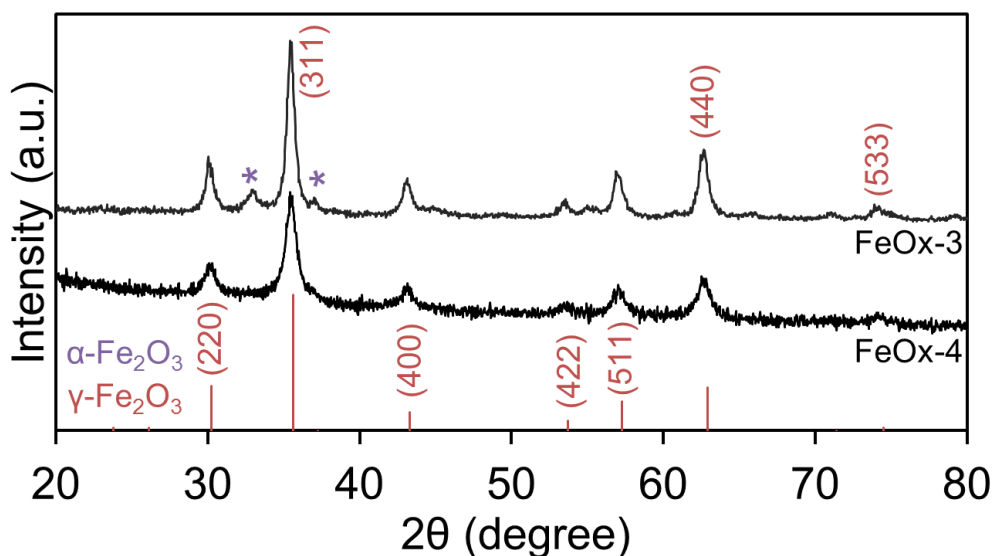


Figure 3.22. XRD patterns of FeOx-3 and FeOx-4

To confirm the presence of the only maghemite phase for FeOx-4, Mössbauer measurements were conducted for this sample (Figure 3.23).

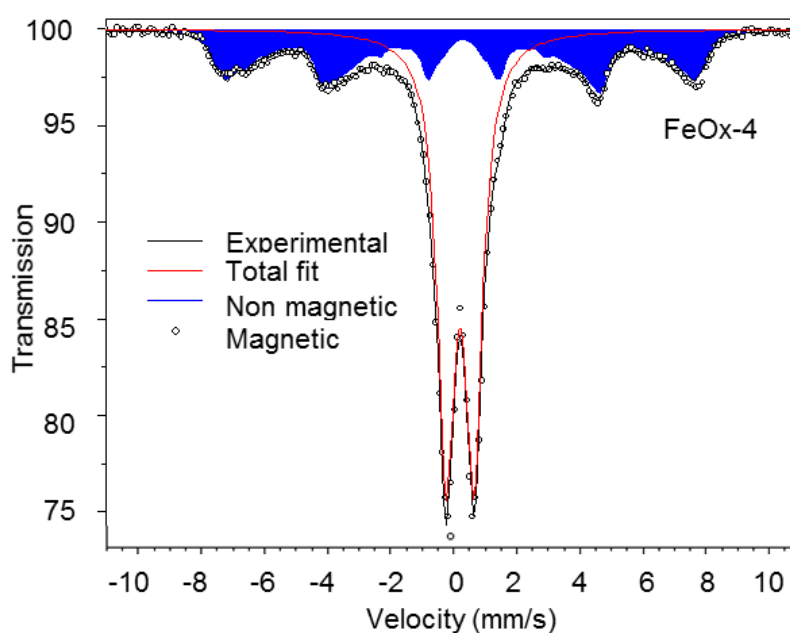


Figure 3.23. Mössbauer spectroscopy realized at room temperature confirms the presence of the maghemite phase only in FeOx-4

According to the  $^{57}\text{Fe}$  Mössbauer spectroscopy, only  $\text{Fe}^{3+}$  exists and no  $\text{Fe}^{2+}$ . The sample shows two contributions: one is a magnetic sextet accounting for 39% of the total resonance area that can be attributed to the maghemite phase. The second contribution is a non-magnetic doublet (61%) that can correspond to very small nanoparticles of maghemite. Indeed maghemite is no more magnetic at

nanoscale<sup>14</sup>. We assume that the FeOx-4 sample corresponds to a maghemite phase with very small nanoparticles that are non-magnetic and perhaps some larger particles that are magnetic.

FeOx-3 and FeOx-4 powders were observed by TEM (Figure 3.24). In both cases, samples seem to mainly consist in very small and agglomerated nanoparticles (less than ten nm) with monomodal distribution. Thus the formation of the second and large size population appears to be encountered only in the case of nitrates precursors. Moreover, no carbon coating can be observed in the samples.

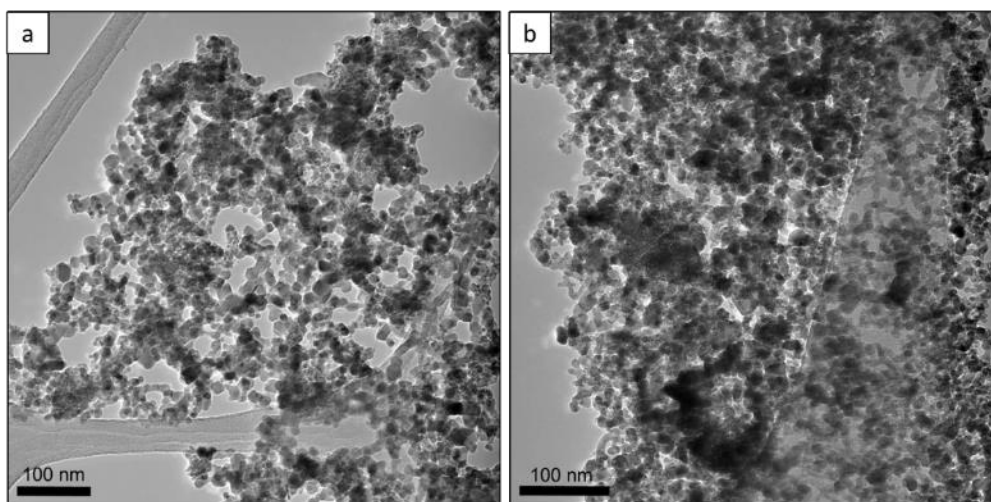


Figure 3.24. Observation of FeOx-3 (a) and FeOx-4 (b) morphologies by TEM

A pure Fe<sub>2</sub>O<sub>3</sub> phase with mainly small nanoparticles was only obtained by using Fe(Acac)<sub>3</sub> precursor (FeOx-4). This powder was thus selected for electrochemical tests. The results will be detailed in the chapter 4.

### III. Synthesis of zinc oxide nanopowders

The syntheses of ZnO were realized using two different solutions of precursors: one was made with zinc nitrate hexahydrate and the other one with anhydrous zinc chloride (Table 3.9).

Solution	Precursors	Solvent
<b>S9</b>	Zn(NO <sub>3</sub> ) <sub>2</sub> · 6H <sub>2</sub> O 50% wt.	DI H <sub>2</sub> O 50% wt.
<b>S10</b>	ZnCl <sub>2</sub> 3% wt.	Absolute EtOH 97% wt.

Table 3.9. Solutions of precursors used for the synthesis of ZnO nanoparticles

The nitrate solution was used with the PALAS generator and the chloride solution with the pyrosol generator to obtain two different powders named ZnOx-1 and ZnOx-2. The experimental conditions are detailed below (Table 3.10).

	Aerosol generator	Solution	C <sub>2</sub> H <sub>4</sub>	Carrier gas	Additional gas	Feeding rate	Production rate
<b>ZnOx-1</b>	PALAS	S9	370 sccm	Air 5600 sccm	X	14.1 g/h	373 mg/h
<b>ZnOx-2</b>	Pyrosol	S10	240 sccm	Argon 1830 sccm	Air 2420 sccm	31.7 g/h	98 mg/h

Table 3.10. Experimental conditions for the synthesis of ZnOx-1 and ZnOx-2

To ensure the oxidation of zinc during the synthesis, air was used as the carrier gas with the PALAS and as additional gas with the pyrosol (carrier gas was argon). Syntheses using only argon gas were tried in previous studies but always lead to the formation of zinc or other non-completely oxidized compounds.

Both ZnOx-1 and ZnOx-2 were characterized by XRD first (Figure 3.25).

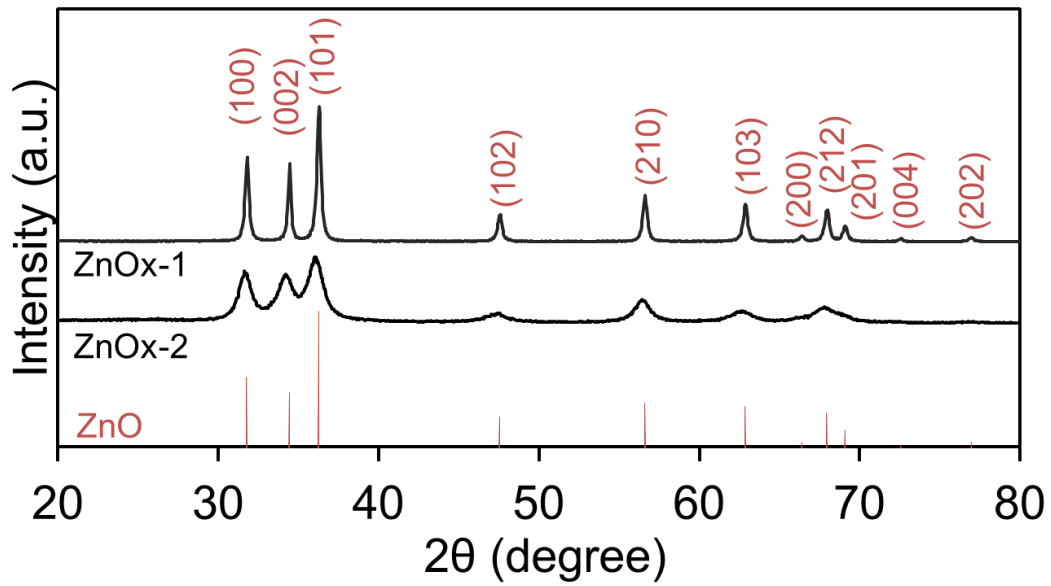


Figure 3.25. XRD patterns for ZnOx-1 and ZnOx-2 revealing a ZnO crystalline phase for both samples

XRD patterns of ZnOx-1 and ZnOx-2 both show the ZnO crystalline phase (01-070-8070, zincite). The XRD peaks for ZnOx-2 are wider than those for ZnOx-1 revealing a difference in the particles size with theoretically smaller particles for ZnOx-2.

SEM and TEM images were acquired for the two samples to observe their morphology (Figure 3.26).

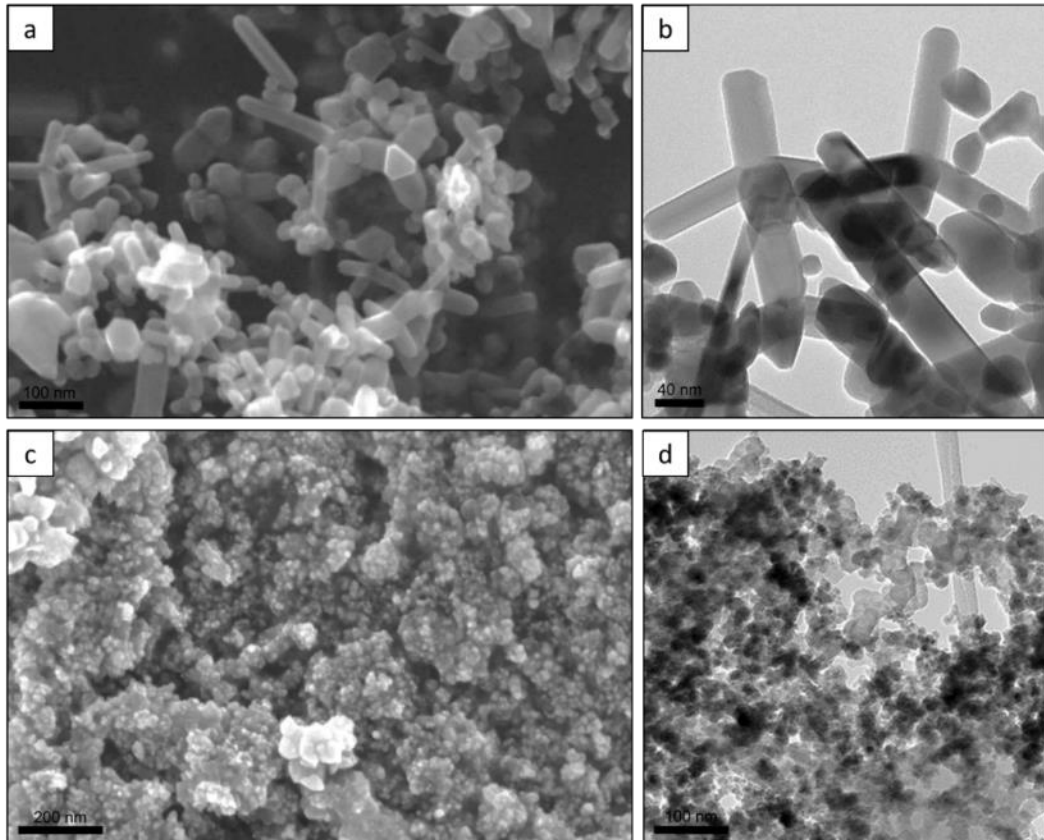


Figure 3.26. SEM and TEM images of ZnOx-1 (a,b) and ZnOx-2 (c,d)

The use of zinc nitrate precursor for the synthesis of ZnO leads to the formation of nanorods (several hundreds of nm length, tens of nm large). This morphology is quite common for ZnO and can be synthesized by various processes<sup>15</sup>. Zinc chloride precursor enables the synthesis of very small spherical nanoparticles of ZnO (10-20 nm). On some parts of the TEM images, a thin film can be seen around the nanoparticles which may be attributed to PAH and amorphous carbon. The difference in size and morphology between ZnOx-1 and ZnOx-2 are consistent with the difference of peaks width on XRD patterns. For battery tests, comparison of electrochemical performances and operando measurements, ZnOx-2 will be used as it presents a morphology similar to the other samples presented before, with only roughly spherical nanoparticles.

TGA measurements were conducted on ZnOx-2 only as this sample shows the desired morphology (Figure 3.27).

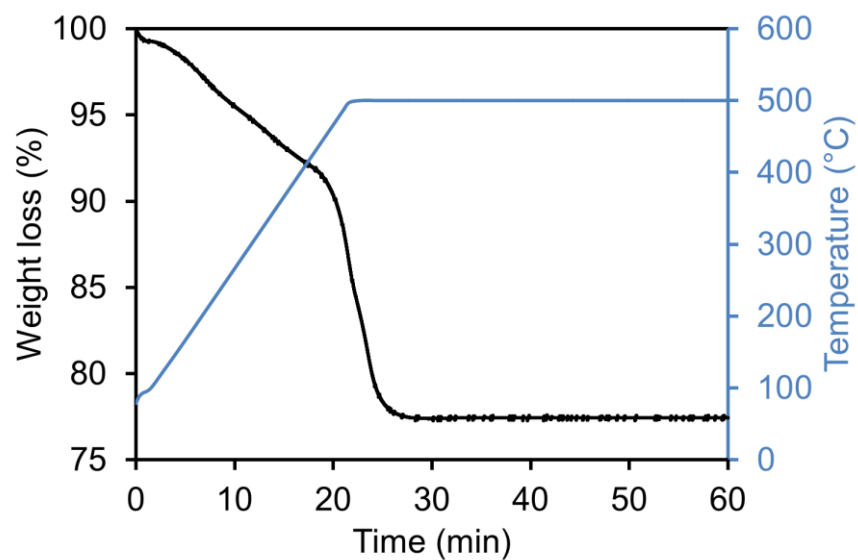


Figure 3.27. TGA measurements on ZnOx-2 from 50°C to 500°C, ramp of 20°C/min and isotherm at 500°C during 40 min

Considering that carbon corresponds to the weight loss after 300°C, the carbon content can be evaluated to 15% for ZnOx-2 and the water and PAH content around 6% (weight loss before 300°C).

#### IV. General discussion on nitrate precursors and laser assisted flame synthesis

All along this part dedicated to the synthesis of oxide nanoparticles, it appears that the synthesis of nanopowders with a bimodal size distribution is correlated with the use of iron nitrate precursor. Chloride or acetylacetonate precursors actually lead to the commonly obtained in laser pyrolysis monomodal size distribution with small nanoparticles, whatever the synthesis conditions. Such peculiar behavior of iron nitrates precursors when compared to other salts was already reported by a Spanish group<sup>16</sup> working on iron oxides synthesis by thermal spray pyrolysis, but no clear explanation was given. Their assumption is that the nitrate precursor keeps the structure of the droplet during the decomposition of the precursor. In their review on spray pyrolysis, Messing *et al.* have also stressed out the peculiar behavior of nitrates precursors because of their low melting point that is not so higher than the boiling point of solvent<sup>17</sup>. In that case, in the same time as the solvent vaporizes, the dissolved salt could melt and form a large spherical drop instead of forming directly a solid precipitate as most of other precursors.

In our case, the formation of the bimodal size distribution of particles with nitrate precursors may involve two simultaneous growth processes (Figure 3.28). When the aerosol droplets enter the reaction zone, the solvent is vaporized and the dissolved salts precipitate to form smaller dry objects, as presented in chapter 1 concerning thermal spray processes. Upon heating, a solid phase reaction can take place within these particles leading to large nanostructured spherical particles. In the specific case of laser pyrolysis, the heating rate is very fast upon interacting with the laser beam and the energy density encountered by the dried particles is very high, especially with a focused beam. In that case, part or totality of the solid salt is vaporized before reacting, leading to a gas phase reaction (nucleation and growth) which would form small nanoparticles agglomerated in chain-like poorly dense structures. This latter vaporization phenomenon could take place at the surface of the dried particles simultaneously to the solid state reaction occurring in the core of the particles, leading to the final formation of two different size distributions of particles.

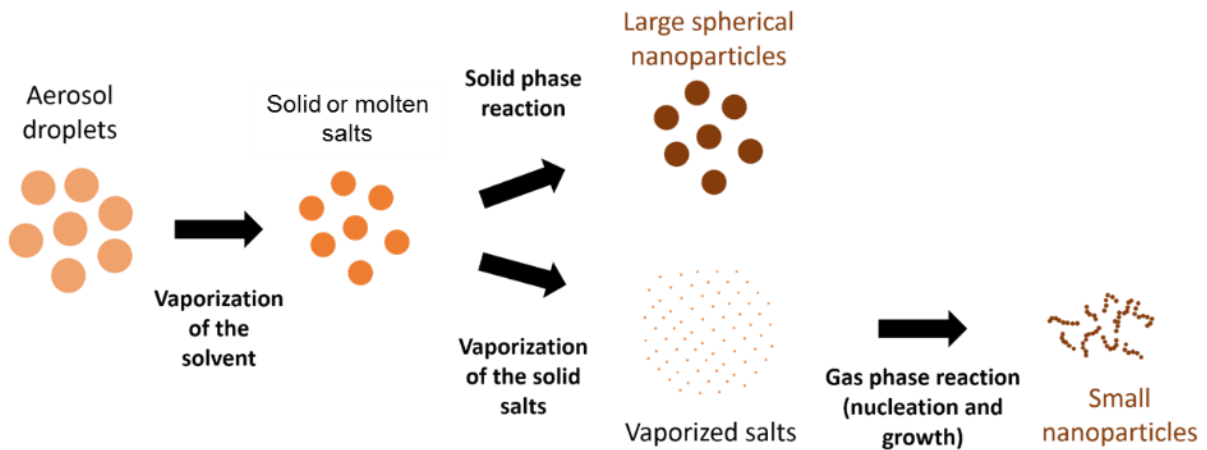


Figure 3.28. Possible growth processes during laser pyrolysis conducting to a bimodal particle size distribution

The specific case of large particles formation that seems to be favored with nitrates precursors can come from the very low melting points of these precursors (110°C for zinc nitrate and 47°C for iron nitrate) compared with those of chloride precursors for instance (290°C for zinc chloride and 306°C for iron chloride). As mentioned before, the melting of the precursors could occur at the same time as the solvent evaporation leading to the formation of large molten nitrates droplets. Surface vaporization of these droplets leads to the formation of the small size part of the bimodal size distribution, while core reactions lead to the large size part. The difference in melting point between Zn nitrate and Fe nitrate could explain why a different behavior is observed for ZnO synthesis from nitrates which leads to a monomodal size distribution.

It is important to note that with FSP synthesis of zinc ferrite nanoparticles, the temperature seems high enough to completely vaporize the solution droplets, avoiding the formation of a bimodal size distribution<sup>18</sup>. Interestingly, even for these very high temperature conditions, the ternary oxide phase is not decomposed to binary ones.

Another general remark can be done concerning synthesis with air in laser pyrolysis, in comparison with reported works by FASP or FSP. The appearance of a blue flame before the introduction of the precursor aerosol demonstrates the combustion nature of the reaction. Nevertheless, even when blue contribution remains visible in the yellow-orange flame produced by the particles thermal emission after a combustible aerosol introduction, the pyrolysis process remains specific to the laser driven reaction. Indeed, in these stable conditions, the reaction stops as soon as the laser beam is turned off. In this particular case, a so-called laser assisted combustion reaction seems to govern the decomposition of the precursors and the growth of the particles. When compared to conventional laser pyrolysis, it offers the advantage of a better oxidization of the desired

## General discussion on nitrate precursors and laser assisted flame synthesis

oxide phases, a potential higher temperature and the possibility, when required, to obtain a longer residence time. The underlying mechanisms in such reactions remain to be carefully understood.

## V. Thermal treatment of the samples before electrochemical tests

The samples presented above show different carbon contents after the synthesis by laser pyrolysis. This carbon can play a role in the cycling behavior of the material. Whether this role is positive or negative, it has to be removed in order to evaluate the intrinsic electrochemical performances of the different oxide phases. In this context, the samples needed to be thermally treated under air. Particularly, the samples ZFO-5, ZnOx-2 and FeOx-4 that show the desired pure oxide phase were annealed at 350°C for three hours before their use for electrode preparation and battery testing. The annealing temperature was chosen to avoid changes in the morphology of the particles during the thermal treatment but also to be high enough to remove both PAH and free carbon or coating in the powder.

The morphology of the annealed powders was observed by TEM (Figure 3.29). The images reveal that after the thermal treatment, the carbon coating is removed with the nanoparticles keeping their primary size roughly unchanged.

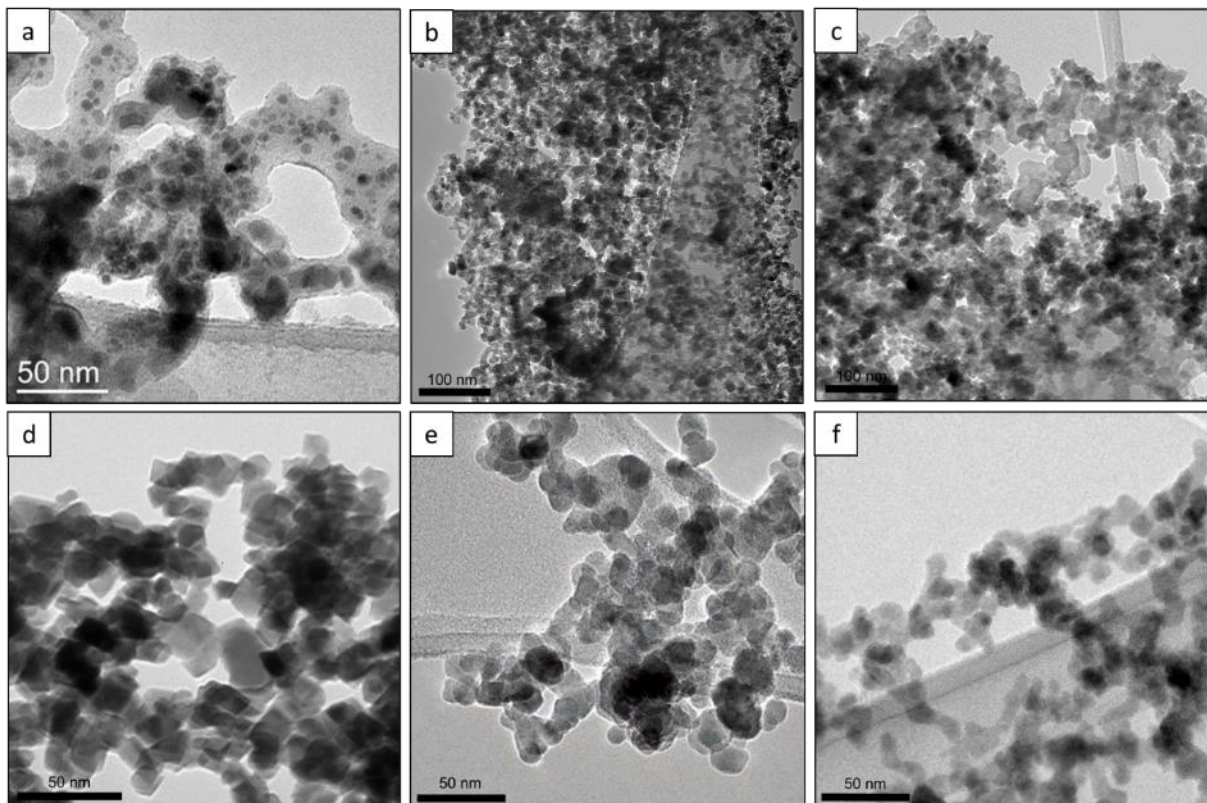


Figure 3.29. TEM images of ZFO-5, ZnOx-2 and FeOx-4 before (a,b,c respectively) and after annealing under air at 350 °C (d,e,f respectively)

## Thermal treatment of the samples before electrochemical tests

The next chapter will be dedicated to the electrochemical performances of the different zinc and iron oxides obtained by laser pyrolysis and to the understanding of the lithium storage mechanisms. The different samples selected among the samples reported in this chapter and furtherly used for battery tests are summarized below (Table 3.11). These samples were chosen as the purest in terms of crystalline phase and for the morphology of their grains (size distribution).

<b>Samples</b>	<b>Phases</b>	<b>Morphology</b>
<b>ZFO-1</b>	$\text{ZnFe}_2\text{O}_4$	Bimodal size population
<b>ZFO-5</b>	$\text{ZnFe}_2\text{O}_4$	Small nanoparticles
<b>ZnOx-2</b>	$\text{ZnO}$	Small nanoparticles
<b>FeOx-4</b>	$\text{Fe}_2\text{O}_3$	Small nanoparticles

Table 3.11. Summary of the different samples used for electrochemical tests

## VI. Intermediate conclusion

In this chapter dedicated to  $\text{ZnFe}_2\text{O}_4$ ,  $\text{ZnO}$  and  $\text{Fe}_2\text{O}_3$  syntheses by laser pyrolysis, the influence of several experimental parameters have been observed: the choice of the precursors gives the possibility to tailor the size distribution of the particles (bimodal or monomodal size population, with nitrates or chlorides respectively) and the gas atmosphere (air or argon) and their flow rates play a role on the formation of a carbon coating.

By choosing the proper synthesis conditions,  $\text{ZnFe}_2\text{O}_4$  nanopowders with a bimodal and a with a monomodal size population were synthesized as well as small  $\text{ZnO}$  and  $\text{Fe}_2\text{O}_3$  nanoparticles. After a thermal treatment to remove the carbon if necessary, these nanopowders were cycled in batteries.

Their electrochemical performances vs. metallic lithium are detailed in the next chapter. The latter will also compare the performances and the lithium storage mechanism between  $\text{ZnFe}_2\text{O}_4$  and a mixture of  $\text{ZnO}$  and  $\text{Fe}_2\text{O}_3$ .

References

- 1 D. K. Kim, Maria Mikhaylova, Yu Zhang and Mamoun Muhammed, *Chem. Mater.*, 2003, **15**, 1617–1627.
- 2 G. M. Da Costa, E. De Grave, P. M. A. De Bakker and R. E. Vandenberghe, *J. Solid State Chem.*, 1994, **113**, 405–412.
- 3 G. Grinbom, D. Duveau, G. Gershinsky, L. Monconduit and D. Zitoun, *Chem. Mater.*, 2015, **27**, 2703–2710.
- 4 G. Grinbom, D. Duveau, G. Gershinsky, L. Monconduit and D. Zitoun, *Chem. Mater.*, 2015, **27**, 2703–2710.
- 5 B. J. Evans, S. S. Hafner and H. P. Weber, *J. Chem. Phys.*, 1971, **55**, 5282–5288.
- 6 Y. Ahn, E. J. Choi, S. Kim, D. H. An, K. U. Kang, B. G. Lee, K. S. Baek and H. N. Oak, *J. Korean Phys. Soc.*, 2002, **41**, 123–128.
- 7 G. F. Goya and H. R. Rechenberg, *J. Magn. Magn. Mater.*, 1999, **196–197**, 191–192.
- 8 P. M. A. de Bakker, E. De Grave, R. E. Vandenberg, L. H. Bowen, R. J. Pollard and P. R.M., *Phys. Chem. Miner.*, 1991, **18**, 131–143.
- 9 S. H. Choi and Y. C. Kang, *ChemSusChem*, 2013, **6**, 2111–2116.
- 10 G. V. Bazuev, O. I. Gyrdasova, I. G. Grigorov and O. V. Koryakova, *Inorg. Mater.*, 2005, **41**, 288–292.
- 11 Y. Li, J. Zhao, J. Jiang and J. Han, *Mater. Res. Bull.*, 2003, **38**, 1393–1399.
- 12 F. H. L. Starsich, G. A. Sotiriou, M. C. Wurnig, C. Eberhardt, A. M. Hirt, A. Boss and S. E. Pratsinis, *Adv. Healthc. Mater.*, 2016, **5**, 2698–2706.
- 13 M. Kumar and Y. Ando, *J. Nanosci. Nanotechnol.*, 2010, **10**, 3739–3758.
- 14 J. Tuček and R. Zboril, *Czechoslov. J. Phys.*, 2005, **55**, 893–911.
- 15 G.-C. Yi, C. Wang and W. Il Park, *Semicond. Sci. Technol.*, 2005, **20**, S22–S34.
- 16 T. González-Carreño, M. P. Morales, M. Gracia and C. J. Serna, *Mater. Lett.*, 1993, **18**, 151–155.
- 17 G. L. Messing, S.-C. Zhang and G. V. Jayanthi, *J. Am. Ceram. Soc.*, 1993, **76**, 2707–2726.
- 18 R. Strobel, A. Baiker and S. E. Pratsinis, *Adv. Powder Technol.*, 2006, **17**, 457–480.

---

## Chapter 4. Evaluation of the electrochemical performances of ZnFe<sub>2</sub>O<sub>4</sub>, ZnO and $\gamma$ -Fe<sub>2</sub>O<sub>3</sub>

---

Selected powders presented in the previous chapter were tested in half cells vs. lithium to evaluate their electrochemical performances. Battery tests as cyclic voltammetry and galvanostatic cyclings are presented for ZnFe<sub>2</sub>O<sub>4</sub> in the first part whereas ZnO and Fe<sub>2</sub>O<sub>3</sub> mixtures performances are detailed in a second part. A deeper understanding of the lithium storage mechanism was made possible by operando X-ray diffraction and <sup>57</sup>Fe Mössbauer measurements.

I. Choice of the electrode formulation and of the electrolyte

The electrochemical performances of the different samples were evaluated vs. metallic lithium by using coin-type half-cells assembled in an argon-filled glove box (see chapter 2).

To choose the proper electrode formulation and electrolyte, several galvanostatic tests (between 0.01 V and 3.0 V at 100 mA.g<sup>-1</sup>) were conducted (in Montpellier and in NTU) by varying the binder, the carbon additives (CB: carbon black and VGCF: vapor-grown carbon fibers) and the electrolyte.

These measurements were realized using the sample ZFO-3 as active material. The different combinations of formulations and electrolytes are summarized in the table below (Table 4.1).

	Active material	Binder	Carbon additives	Solvent	Electrolyte
<b>C1</b>	ZFO-3 (70% wt.)	CMC (12% wt.)	CB (18% wt.)	DI H <sub>2</sub> O	EC PC 3DMC + 1M LiPF <sub>6</sub>
<b>C2</b>	ZFO-3 (70% wt.)	CMC (12% wt.)	CB+VGCF (9% + 9% wt.)	DI H <sub>2</sub> O	EC PC 3DMC + 1M LiPF <sub>6</sub>
<b>C3</b>	ZFO-3 (70% wt.)	CMC (12% wt.)	CB+VGCF (9% + 9% wt.)	DI H <sub>2</sub> O	EC DMC + 1M LiPF <sub>6</sub>

*Table 4.1. Electrode formulations and electrolytes for coin cells preparation*

The influence of VGCF in the electrode formulation was studied by comparing the electrochemical performances of C1 and C2. The charge and discharge capacities, the efficiency, the reversible capacity retention and the cumulative irreversible capacity are presented in the graphs below (Figure 4.1).

## Choice of the electrode formulation and of the electrolyte

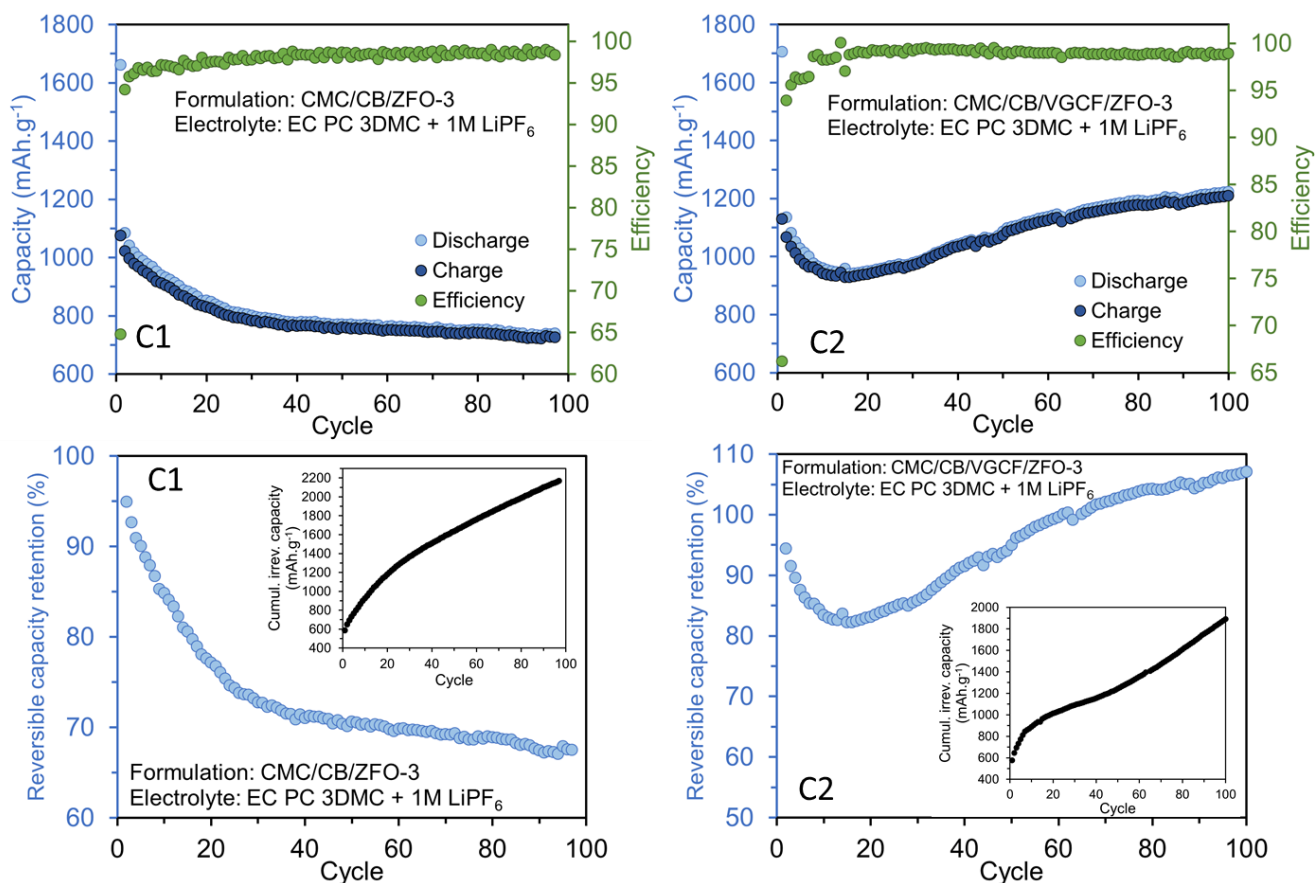


Figure 4.1. Galvanostatic cycling at  $100 \text{ mA.g}^{-1}$  for ZFO-3 using CB (C1) and CB + VGCF (C2) as carbon additives

For the first cycle, the discharge capacity is above the theoretical value ( $1000 \text{ mAh.g}^{-1}$ ) for both samples with a first cycle efficiency around 65%. During the charge/discharge process, the reversible capacity of C1 decreases progressively leading to only 68% of capacity retention after 100 cycles while the cumulative irreversible capacity increases rapidly (more than  $2000 \text{ mAh.g}^{-1}$  after 100 cycles). The cycling behavior is clearly different for C2 sample with a progressive increase of the reversible capacity after 20 cycles. Due to this phenomenon, after 100 cycles, C2 is able to retain more than  $1200 \text{ mAh.g}^{-1}$ . The capacity retention is thus better than for C1 and the cumulative irreversible capacity slightly lower ( $1900 \text{ mAh.g}^{-1}$  after 100 cycles). The addition of VGCF in the C2 formulation may enhance the electronic percolation in the electrode explaining a higher reversible capacity than C1 after 100 cycles.

The comparison between C2 and C3 was then realized to highlight the advantages and drawbacks of two different electrolytes: EC PC 3DMC +  $1 \text{ M LiPF}_6$  and EC DMC +  $1 \text{ M LiPF}_6$  (Figure 4.2).

## Choice of the electrode formulation and of the electrolyte

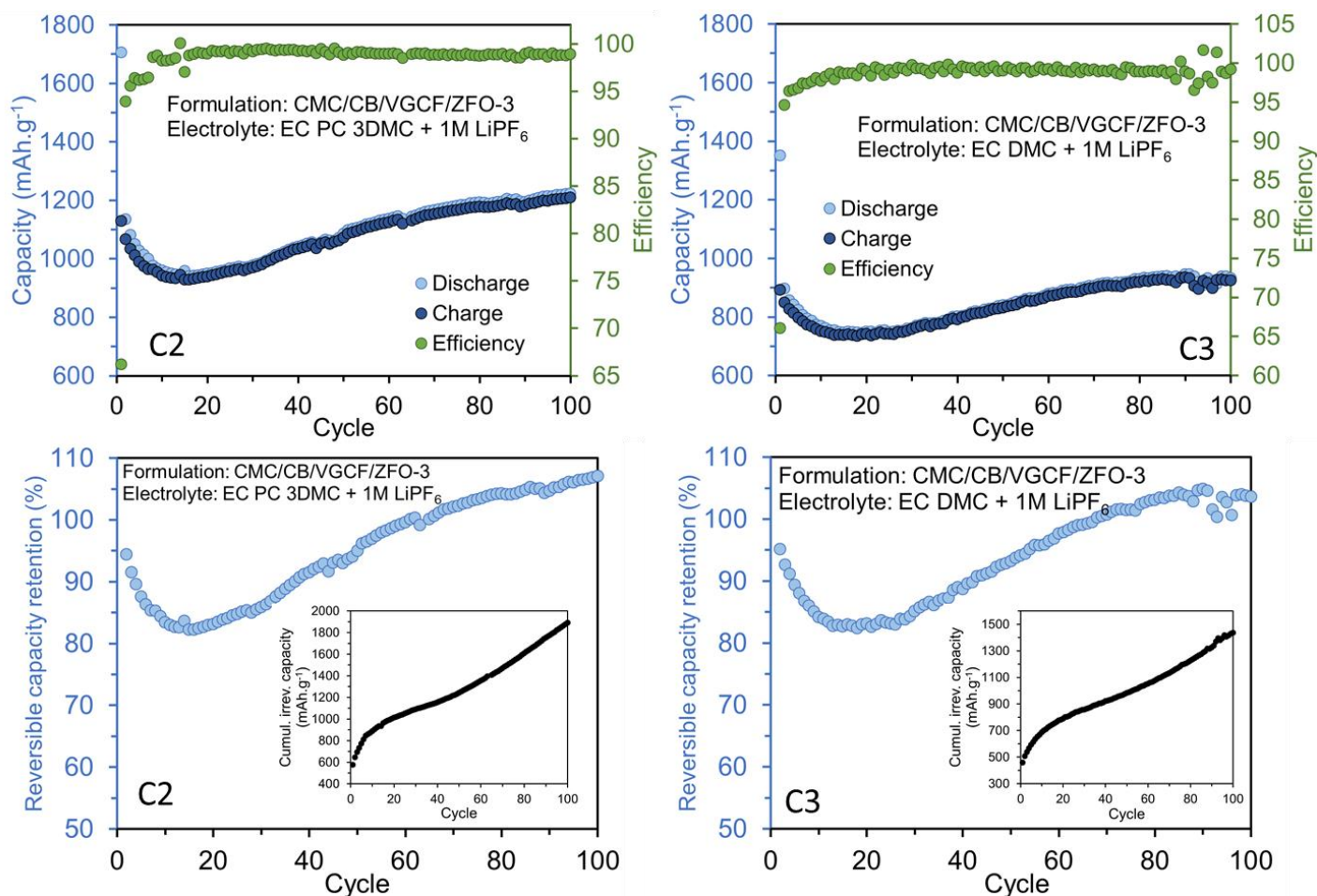


Figure 4.2. Galvanostatic cycling at  $100 \text{ mA.g}^{-1}$  for C2 (with EC PC 3DMC) and C3 (with EC DMC)

For C2 and C3, the cycling behaviors are relatively similar with a decrease of the reversible capacity during the first 20 cycles and then an increase of the reversible capacity to reach more than  $1200 \text{ mAh.g}^{-1}$  for C2 and around  $900 \text{ mAh.g}^{-1}$  for C3. The efficiency is comprised between 99% and 99.5% for both samples after the first 20 cycles. Like the charge and discharge capacities, the capacity retention is increasing for C2 and C3 during cycling leading to more than 100% of capacity retention after 100 cycles. The main difference between C2 and C3 lies in the values of the reversible capacity and cumulative irreversible capacity. During the first cycle, the irreversible capacity is higher for C2 than for C3 and this trend stays for the following cycles leading to a cumulative irreversible capacity of  $1900 \text{ mAh.g}^{-1}$  for C2 and  $1400 \text{ mAh.g}^{-1}$  for C3. The use of PC in the electrolyte for C2 might favor parasitic reactions linked to this irreversible capacity. However, the reversible capacity obtained during cycling is clearly higher with PC than without PC in the electrolyte.

According to the above results, the use of two carbon additives (carbon black and VGCF) may enhance the cyclability of the zinc iron oxides by maintaining a good electronic percolation in the

### Choice of the electrode formulation and of the electrolyte

electrode. Between C2 and C3, the cycling behavior is similar but C2 with EC PC 3DMC + 1M LiPF<sub>6</sub> electrolyte was preferentially chosen to study zinc iron oxides electrochemical performances thanks to a higher reversible capacity during cycling.

Finally, the chosen electrode formulation consists in 70% wt. of active material, 12% wt. of CMC as binder and 18% wt. of carbon additives (9% of carbon black and 9% of VGCF) dissolved in deionized water and EC PC 3DMC + 1M LiPF<sub>6</sub> was used as electrolyte. These electrolyte and electrode formulation were also chosen in respect with previous works realized by Marino *et al.* at the AIME laboratory in Montpellier showing the better performances of some intermetallic-based negative electrodes with this protocol<sup>1,2</sup>.

II. Electrochemical performances of ZnFe<sub>2</sub>O<sub>4</sub> nanopowders

1. Influence of the grain size distribution of ZnFe<sub>2</sub>O<sub>4</sub> nanoparticles

The electrochemical performances of ZFO-1 and ZFO-5 samples were evaluated vs. metallic lithium to observe the influence of the morphology on the battery cycling. The samples correspond to nanopowders with different size distributions: ZFO-1 shows a bimodal size population of particles whereas ZFO-5 only consists in small nanoparticles. The theoretical capacity of ZFO-1 is estimated around 1000 mAh.g<sup>-1</sup> according to the theoretical capacities of ZnFe<sub>2</sub>O<sub>4</sub> (1001 mAh.g<sup>-1</sup>) and γ-Fe<sub>2</sub>O<sub>3</sub> (1007 mAh.g<sup>-1</sup>). For ZFO-5, the theoretical capacity is the one of ZnFe<sub>2</sub>O<sub>4</sub>.

Galvanostatic cyclings for 100 cycles between 0.01 V and 3.0 V at the current density of 100 mA.g<sup>-1</sup> (corresponding to C/10 current rate or 10 hours/discharge) and 1000 mA.g<sup>-1</sup> (1C current rate, 1 hour/discharge) were first carried out for ZFO-1 and ZFO-5 electrodes. These current rates were chosen to ease the comparison with the results in the literature.

The charge and discharge capacities, the coulombic efficiency and the cumulative irreversible capacity for the cycling of ZFO-1 and ZFO-5 at 100 mA.g<sup>-1</sup> are plotted in the graphs below (Figure 4.3).

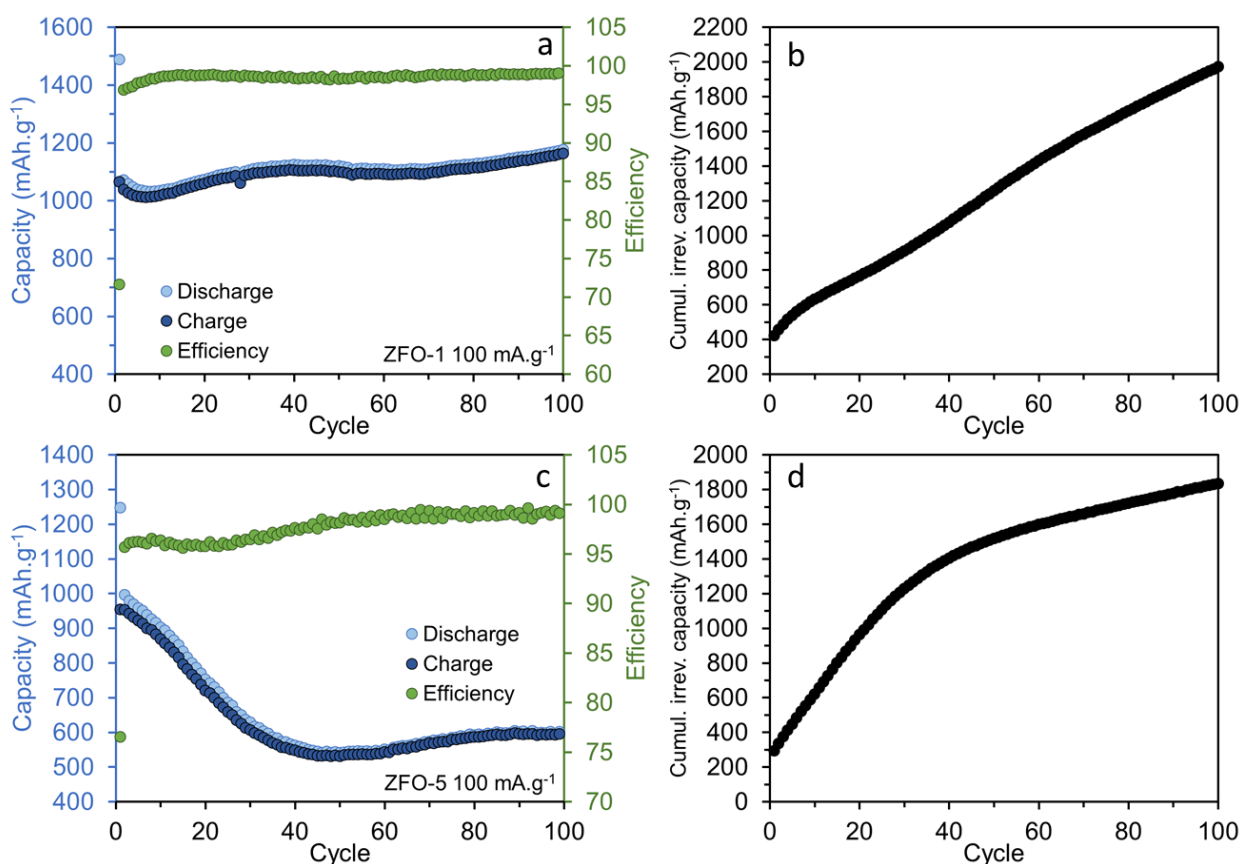


Figure 4.3. Galvanostatic cycling at 100 mA.g<sup>-1</sup> for ZFO-1 and ZFO-5: charge/discharge capacity plots (a, c) and cumulative irreversible capacity plots (b, d)

## Electrochemical performances of ZnFe<sub>2</sub>O<sub>4</sub> nanopowders

For the first cycle at C/10 of ZFO-1, the discharge and charge capacities are 1488 mAh.g<sup>-1</sup> and 1066 mAh.g<sup>-1</sup> respectively, leading to a coulombic efficiency of 71.6%. Similarly, ZFO-5 shows a first coulombic efficiency of 76.5% at the same current rate, with the first lithiation and delithiation capacities of 1247 mAh.g<sup>-1</sup> and 948 mAh.g<sup>-1</sup> respectively. In both case the first discharge capacity is higher than the theoretical value. The additional capacity is generally explained by some parasitic reactions of the electrolyte at low potential that create a solid electrolyte interphase (SEI) as well as a polymeric gel-type layer around the nanoparticles that traps part of the lithium<sup>3</sup>. SEI formation irreversibly traps part of the lithium whereas the polymeric gel-type layer is assumed to be formed reversibly<sup>4</sup>. ZnFe<sub>2</sub>O<sub>4</sub> electrodes suffer from a large capacity loss during the first cycle (ZFO-1: 422 mAh.g<sup>-1</sup> of irreversible capacity, ZFO-5: 299 mAh.g<sup>-1</sup> of irreversible capacity) leading to a low coulombic efficiency which is rather common for transition metal oxides electrodes<sup>5-7</sup>. This irreversible capacity may be attributed to the SEI formation which is enhanced in the case of nanostructured electrodes where active material shows high specific surface<sup>8</sup>.

While the behavior of the two samples is roughly similar during the first cycle, some changes occur for the subsequent cycles. A slow decrease of the reversible capacity is observed for ZFO-1 for the first 7<sup>th</sup> cycles to reach 1012 mAh.g<sup>-1</sup>. This is probably due to the gradual inactivation of a part of the active material or to the formation of a thick SEI leading to additional lithium trapping. Nevertheless, after this slight decrease, the capacity progressively increases to deliver about 1160 mAh.g<sup>-1</sup> at the 100<sup>th</sup> cycle, what is still higher than the theoretical capacity. Despite this increase of reversible capacity, the cumulative irreversible capacity continues to increase and reaches a high value of 1971 mAh.g<sup>-1</sup> at 100 cycles. For ZFO-5, the capacity falls rapidly to 530 mAh.g<sup>-1</sup> during the next 50 cycles before slowly increasing to reach finally 595 mAh.g<sup>-1</sup> after 100 cycles. The cumulative irreversible capacity value of 1833 mAh.g<sup>-1</sup> is reached what is similar to ZFO-1. The coulombic efficiency stabilizes after several cycles for both samples with an average value for the last 50 cycles of 98.8% for ZFO-1 and 98.9% for ZFO-5. The increase in capacity during cycling, sometimes leading to a capacity higher than the theoretical one, is not uncommon for transition metal oxides and has been reported for Fe<sub>2</sub>O<sub>3</sub><sup>9</sup>, Fe<sub>3</sub>O<sub>4</sub><sup>10</sup> and ZnFe<sub>2</sub>O<sub>4</sub><sup>11</sup>. This effect has been attributed in the literature to the reversible reaction of a polymeric gel-type layer formed by the partial decomposition of the electrolyte, kinetically activated by the electrode material at the electrode/electrolyte interface. The formation of this polymeric layer has already been observed for transition metal oxides but also for other conversion materials like NiSb<sub>2</sub><sup>12</sup>. According to Laruelle *et al.*, it seems that this polymeric layer is specific to transition metal compounds as its *in situ* formation is promoted by the presence of highly reactive metallic nanograins at the end of the discharge<sup>13</sup>. The existence of such an active layer accounts for the additional capacity of the electrodes, largely exceeding the theoretical one<sup>14,15</sup>. This reversible reaction, leading to a capacity increase, must be distinguished from the conventional

## Electrochemical performances of ZnFe<sub>2</sub>O<sub>4</sub> nanopowders

irreversible consumption of Li during SEI formation. This additional reversible storage of lithium may also come from a contribution of carbon additives during the charge/discharge process (taking into account that there is 18% of carbon additives in the electrode, an additional reversible contribution up to 60 mAh.g<sup>-1</sup> can be considered)<sup>1</sup>.

To better understand the lithiation process and the differences of performance between ZFO-1 and ZFO-5, the voltage profiles for the 1<sup>st</sup>, 2<sup>nd</sup>, 10<sup>th</sup>, 50<sup>th</sup> and 100<sup>th</sup> cycles were plotted for the two samples with the dQ/dV curves (Figure 4.5).

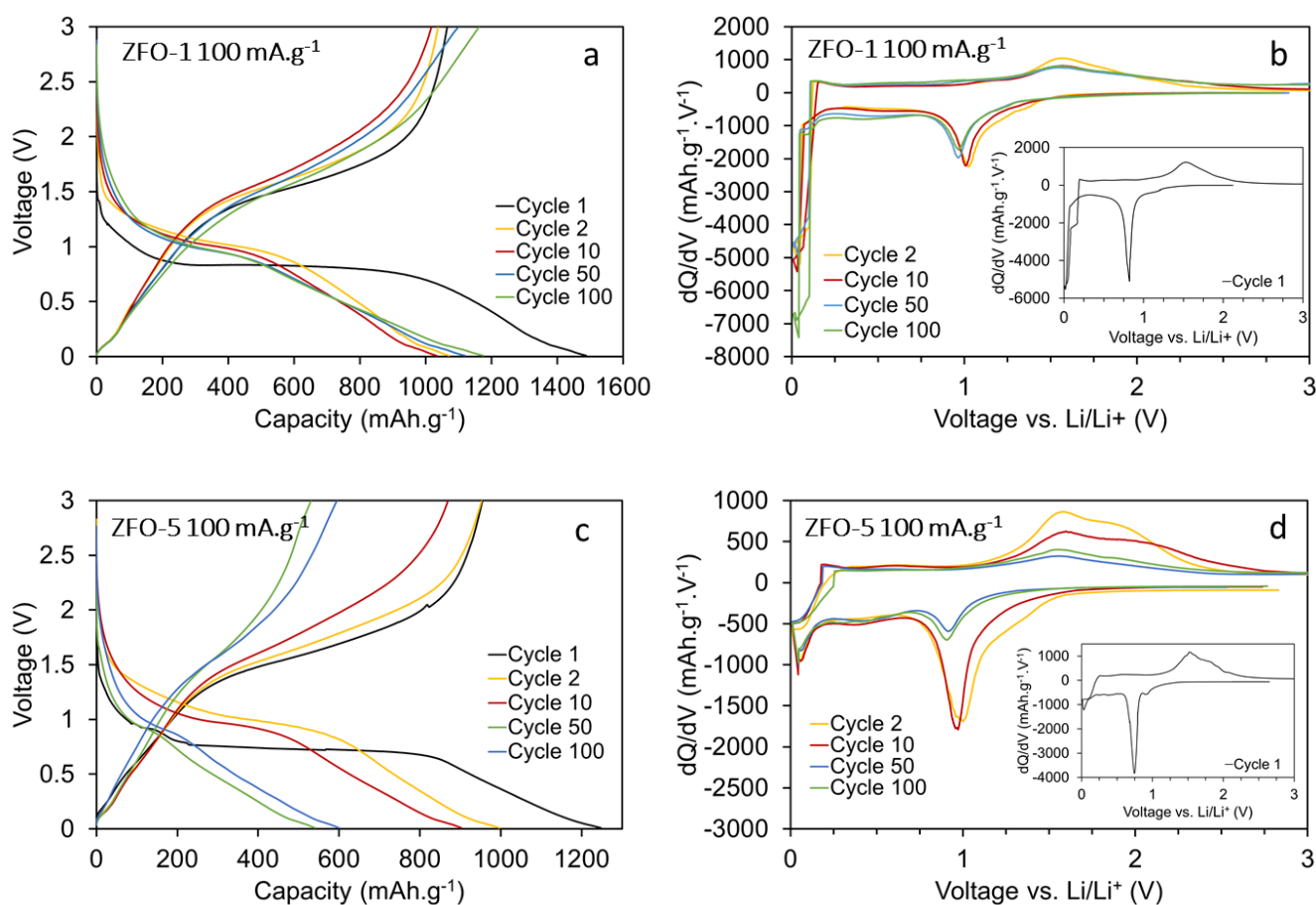


Figure 4.4. Charge/discharge profiles (a, c) and dQ/dV curves (b, d) for ZFO-1 and ZFO-5 galvanostatic cyclings at 100 mA.g<sup>-1</sup> between 0.01 V and 3.0 V

For ZFO-1 and ZFO-5, according to the charge/discharge profiles, the first lithiation starts from OCV (around 2.1V) to a deep discharge at 0.01 V. This first discharge can be divided into three distinct voltage regions. For ZFO-1, at the beginning, a slope can be observed from 2.1 V to 0.8 V that corresponds to a capacity of 220 mAh.g<sup>-1</sup> (~2 mol Li) which is attributed to the lithium intercalation into the ZnFe<sub>2</sub>O<sub>4</sub> crystalline structure<sup>16</sup>. For ZFO-5, the first voltage region is also located between

2.1 V and 0.8 V and corresponds to 230 mAh.g<sup>-1</sup> what is similar to ZFO-1. The second voltage region is a long plateau at 0.8 V for the two samples. The corresponding capacities of 700 mAh.g<sup>-1</sup> for ZFO-1 and 600 mAh.g<sup>-1</sup> for ZFO-5 are equivalent to the consumption of 6.3 mol and 5.4 mol of lithium ions per formula unit of ZnFe<sub>2</sub>O<sub>4</sub>, respectively. This plateau at 0.8 V is ascribed by different authors to the conversion reaction leading to the destruction of the ZnFe<sub>2</sub>O<sub>4</sub> crystalline structure and to the formation of Zn and Fe metallic particles embedded into an amorphous Li<sub>2</sub>O matrix<sup>17,18</sup>. The long plateau is then followed by a sloping curve to the cut-off potential of 0.01 V: for ZFO-1, a capacity of 570 mAh.g<sup>-1</sup> (~ 5.1 mol Li) is obtained whereas for ZFO-5, only 420 mAh.g<sup>-1</sup> (~3.8 mol Li) is stored in the anode material. The capacity obtained between 0.8 V and 0.01 V is generally explained as the formation of the SEI and the polymeric gel-type layer around the metallic particles together with reactions with the electrolyte. However, alloying reaction with Zn<sup>19</sup> and contribution of carbon in the capacity can also occur at these low potentials. In the next cycles, the plateau at 0.8 V shifts towards 1.0 V and becomes shorter. However, for ZFO-1, the plateau still contributes for around 400 mAh.g<sup>-1</sup> of the total capacity after 100 cycles whereas for ZFO-5, it almost disappears, and the major part of the capacity seems to come from reactions below 0.8 V.

Derivative curves were plotted to define more accurately the three distinct regions of the lithiation process. For the first cycle, a main oxidation peak is observed at 0.82 V for ZFO-1 and at 0.74 V for ZFO-5 what is consistent with the charge/discharge profiles. The region from 0.62 V and 1.02 V for ZFO-1 and the region from 0.54 V to 0.94 V for ZFO-5 can be defined as the conversion region (meaning that the major part of the conversion reaction may occur between these voltages). The voltage window from 3.0 V to 1.02 V and from 3.0 V to 0.94 V is attributed to the intercalation region for ZFO-1 and ZFO-5 respectively. The voltage region below the conversion peak is qualified here as an “extra capacity” region: the discharge capacity in this region is generally attributed to parasitic reactions due to electrolyte degradation (SEI formation, polymeric-gel type layer)<sup>20</sup> but also to reactions with carbon (additional capacity), alloying reaction with zinc (to form ZnLi) and the end of the conversion reaction. For the subsequent cycles, these three regions are shifted due to the shift of the conversion peak to lower voltages.

The percentage of discharge capacity with reference to the first discharge capacity is presented in the graphs below for ZFO-1 and ZFO-5. In respect with the definition of the three voltage regions, the discharge capacity contribution of each region is also detailed (Figure 4.5, a, c). The evolution of the polarization during cycling (defined as the potential difference between discharge and charge to 50% of the full capacity) is added below (Figure 4.5, b, d).

## Electrochemical performances of ZnFe<sub>2</sub>O<sub>4</sub> nanopowders

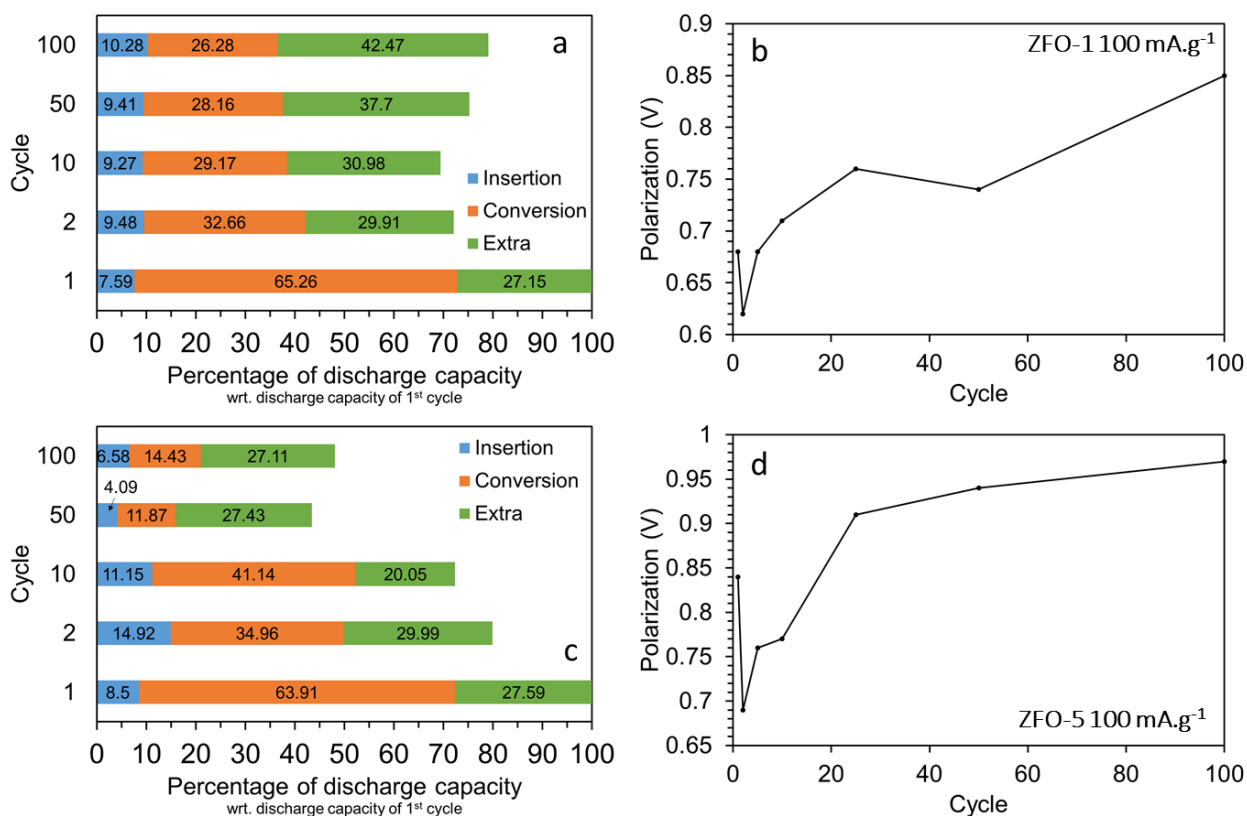


Figure 4.5. Discharge capacity contribution from each region (a, c) and evolution of the polarization (b, d) for ZFO-1 and ZFO-5 cycling at 100 mA.g<sup>-1</sup> between 0.01 V and 3.0 V.

For ZFO-1 and ZFO-5, it is clear that for the first ten cycles, the discharge capacity is decreasing. The contribution of the intercalation region is minor (between 5% and 15% of the total discharge capacity) and the one of the extra capacity region is comprised between 20% and 30%. The capacity drop during the first cycles seems to come from the decrease of the conversion region contribution, especially between the 1<sup>st</sup> and the 2<sup>nd</sup> cycle (from 65% to 33% for ZFO-1 and from 64% to 35% for ZFO-5). An increase of the discharge capacity is then observed for both samples between the 50<sup>th</sup> and 100<sup>th</sup> cycle. This phenomenon seems to be due to an increase of the discharge capacity in the extra capacity region (from 31% to 42% for ZFO-1 and from 20% to 27% in the case of ZFO-5). The extra capacity region contributes for the main part of the discharge capacity. This supports the assumption that the rise of capacity may come from additional reactions that can sometimes progressively counterbalanced the loss of capacity coming from the conversion region. However, it is still difficult to ascribe the increase of capacity to only one specific reaction (polymeric gel-type layer, alloying reaction or carbon contribution). The more drastic capacity drop in the conversion region may be attributed to the rise of the polarization during cycling (Figure 4.5, b, d). As observed in the graph above, for ZFO-1 and ZFO-5, the second cycle polarization is lower than the first one (0.62 V vs. 0.68 V for ZFO-1 and 0.69 V vs. 0.84 V for ZFO-5) but then it is rapidly increasing, reaching 0.85 V and 0.97 V

## Electrochemical performances of ZnFe<sub>2</sub>O<sub>4</sub> nanopowders

at the 100<sup>th</sup> cycle for ZFO-1 and ZFO-5 respectively. Generally, the increase of polarization is related to a less reversible reaction. This rise of the polarization is particularly high for the first cycles and lower between the 50<sup>th</sup> and the 100<sup>th</sup> cycle. This is consistent with the decrease of the discharge capacity at the beginning of the cycling and then the increase of capacity after the 50<sup>th</sup> cycle.

Although the evolution of the polarization is quite similar for ZFO-1 and ZFO-5 at 100 mA.g<sup>-1</sup>, the polarization is higher for ZFO-5. Indeed the polarization starts from 0.68 V for ZFO-1 and 0.84 V for ZFO-5 and after 100 cycles, ZFO-1 shows a polarization of 0.85 V whereas ZFO-5 experiences a higher value of 0.97 V. This is consistent with the better capacity and cyclability observed for ZFO-1 than for ZFO-5.

Similarly, the cyclability of ZFO-1 and ZFO-5 was studied at a higher current rate. The electrodes were cycled at 1000 mA.g<sup>-1</sup> between 0.01 V and 3.0 V (Figure 4.6).

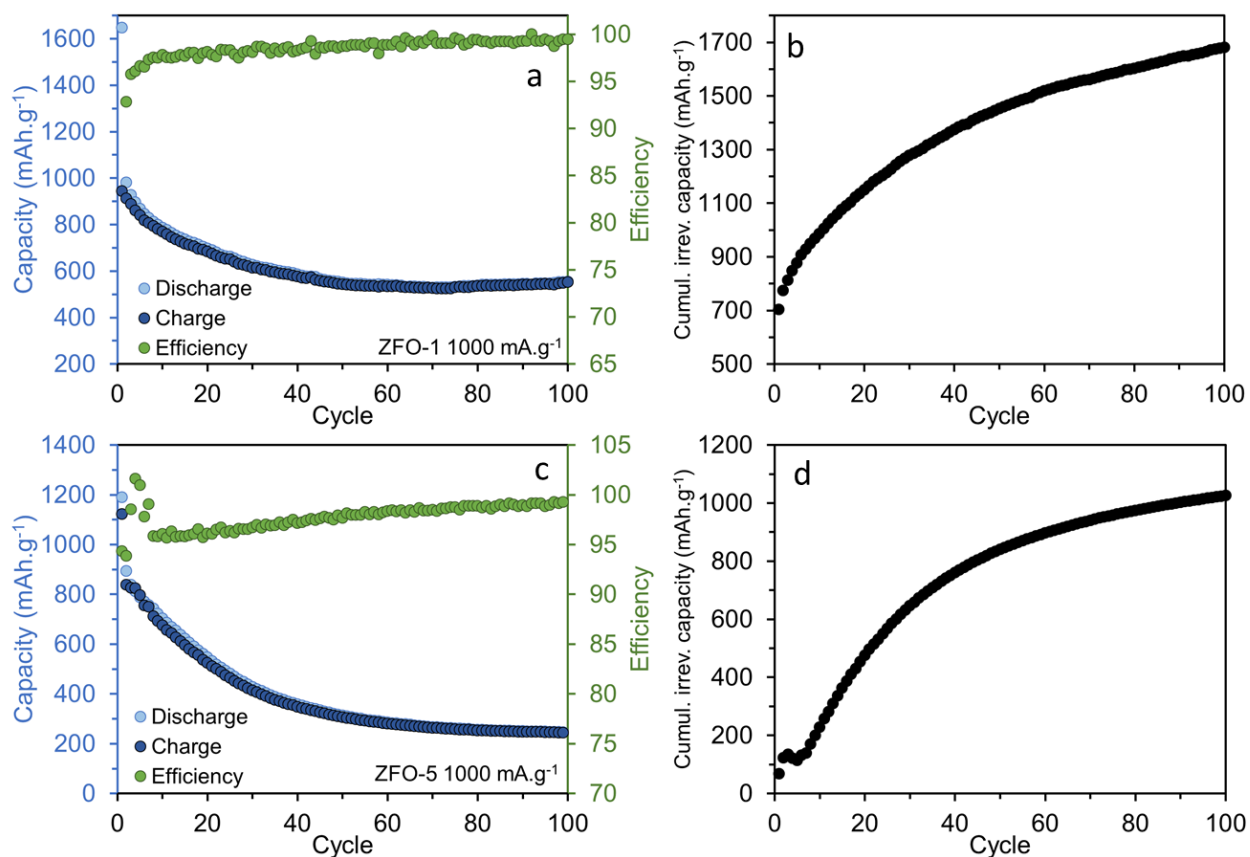


Figure 4.6. Galvanostatic cyclings at 1000 mA.g<sup>-1</sup> for ZFO-1 and ZFO-5: charge/discharge capacity plots (a, c) and cumulative irreversible capacity plots (b, d)

The trend is similar at 1C current rate as at C/10. ZFO-1 and ZFO-5 both show a first lithiation capacity above the theoretical value. Like at C/10, the reversible capacity decreases after the first

## Electrochemical performances of ZnFe<sub>2</sub>O<sub>4</sub> nanopowders

cycle. For ZFO-1, the reversible capacity slowly decreases from the first cycle to be maintained around 550 mAh.g<sup>-1</sup> after 100 cycles. For ZFO-5, the reversible capacity drastically decreases to be maintained at 240 mAh.g<sup>-1</sup> beyond 80 cycles. The coulombic efficiency is relatively stable for ZFO-1 after the first 20 cycles with an average efficiency of 99.8% for the last 50 cycles indicating satisfying efficiency and reversibility of the lithium insertion/extraction in ZnFe<sub>2</sub>O<sub>4</sub>. The cumulative irreversible capacity of ZFO-1 increases during cycling but the rise of the irreversible capacity is particularly important for the first cycles. For ZFO-5, the efficiency increases slowly during cycling to become stable for the last 30 cycles around 98.6% on average. The cumulative irreversible capacity follows a similar trend to ZFO-1 with a rapid increase for the first cycles and a slower increase after 50 cycles.

Contrary to the cycling at 100 mA.g<sup>-1</sup>, no increase of capacity is observed at 1000 mA.g<sup>-1</sup>.

The charge/discharge profiles and the dQ/dV plots shown below reveal the presence of the three regions as for the cyclings at 100 mA.g<sup>-1</sup> (Figure 4.7).

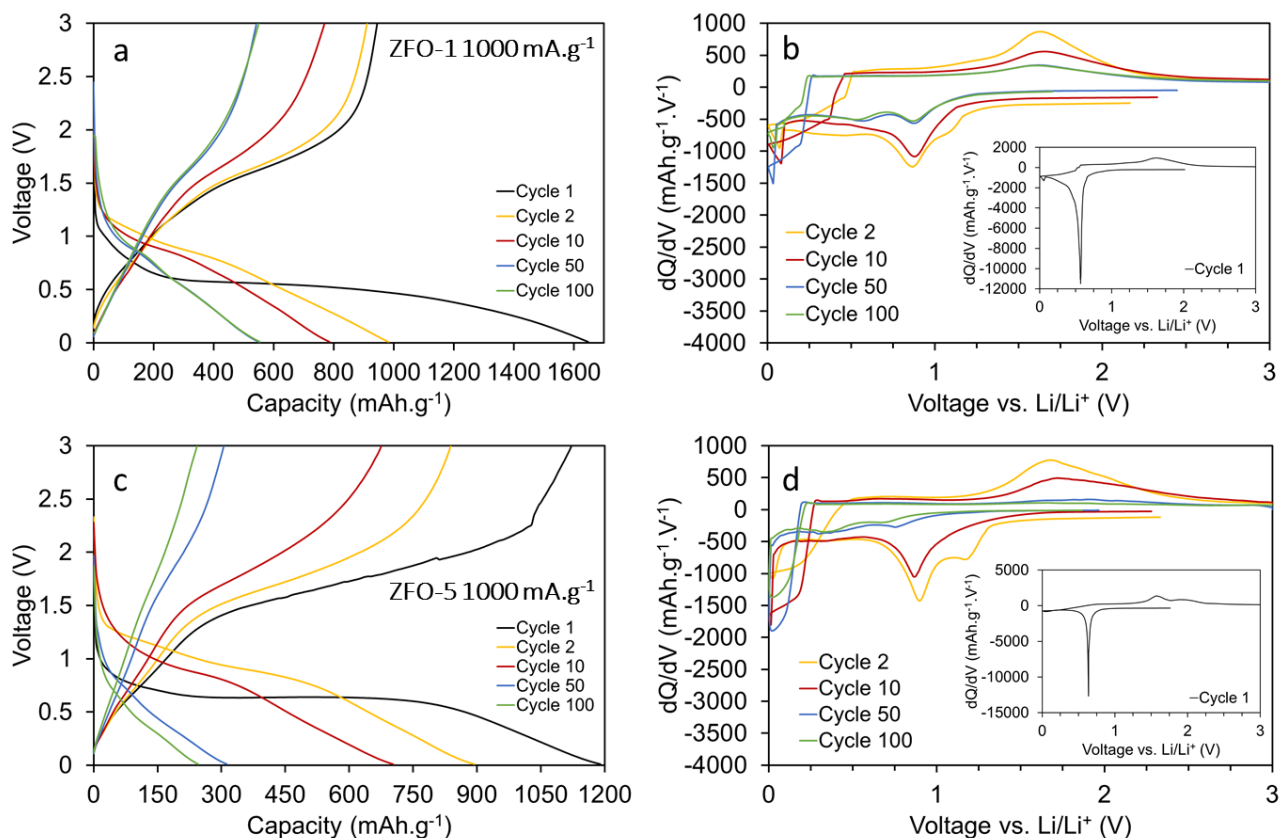


Figure 4.7. Charge/discharge profiles (a, c) and dQ/dV curves (b, d) for ZFO-1 and ZFO-5 galvanostatic cyclings at 100 mA.g<sup>-1</sup> between 0.01 V and 3.0 V

The evolution of the polarization and the evolution of the discharge capacity in the insertion, conversion and extra capacity zones are also shown in Figure 4.8.

## Electrochemical performances of ZnFe<sub>2</sub>O<sub>4</sub> nanopowders

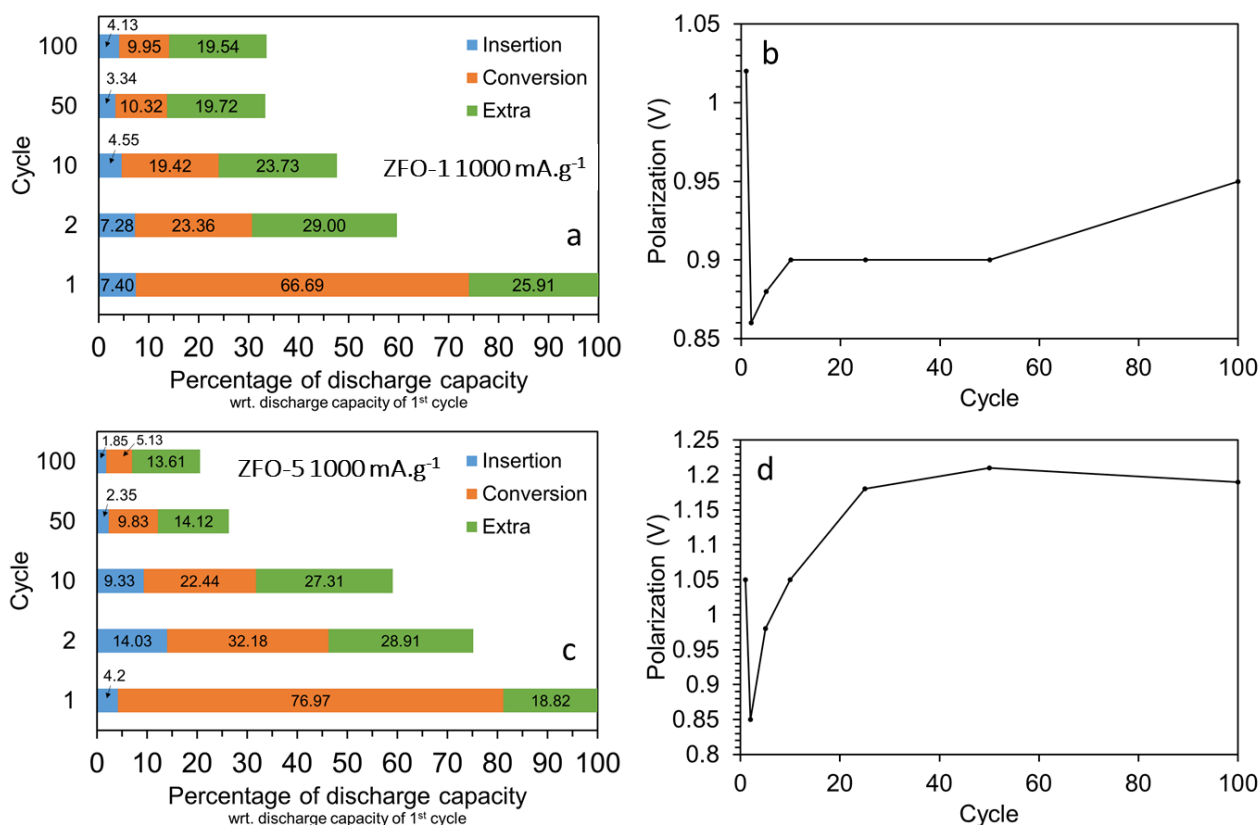


Figure 4.8. Discharge capacity contribution from each region (a, c) and evolution of the polarization (b, d) for ZFO-1 and ZFO-5 cyclings at 1000 mA.g<sup>-1</sup> between 0.01 V and 3.0 V

The percentage of discharge capacity is decreasing progressively for both samples, particularly in the conversion region as at 100 mA.g<sup>-1</sup>. However, in this case, no increase of capacity is observed during cycling which is consistent with the evolution of the discharge capacity shown in Figure 4.6. Contrary to the cyclings at 100 mA.g<sup>-1</sup>, the extra capacity region does not experience any rise of the discharge capacity. The reactions that cause the increase of capacity seem to depend on the current rate.

Concerning the polarization, it is still higher for ZFO-5 than for ZFO-1, consistent with the better performances of ZFO-1. With the higher current rate, the polarization is higher too and instead of 0.85 V and 0.97 V after 100 cycles at 100 mA.g<sup>-1</sup>, the polarization is of 0.94 V for ZFO-1 and 1.19 V for ZFO-5. The poorer results at higher current rate may be attributed to these higher values of polarization.

When compared to capacities recorded at C/10, the ones reported here for 1C are significantly lower, as could be expected. Higher current rates (fast cycling) seems to enhance the polarization effects in the electrode and impedes core diffusion of Li in the particles, leading to low capacity.

## Electrochemical performances of ZnFe<sub>2</sub>O<sub>4</sub> nanopowders

The performances of ZFO-5 are far below those of ZFO-1. Although the behavior of the samples are comparable for the first cycle, ZFO-5 shows a very poor capacity retention with a specific capacity more than twice lower than for ZFO-1 after 100 cycles at C/10 and 1C current rates. The prominent contrast in terms of reversible capacity between the two materials may come from the difference of morphology that influences the formation of the SEI (Figure 4.9).

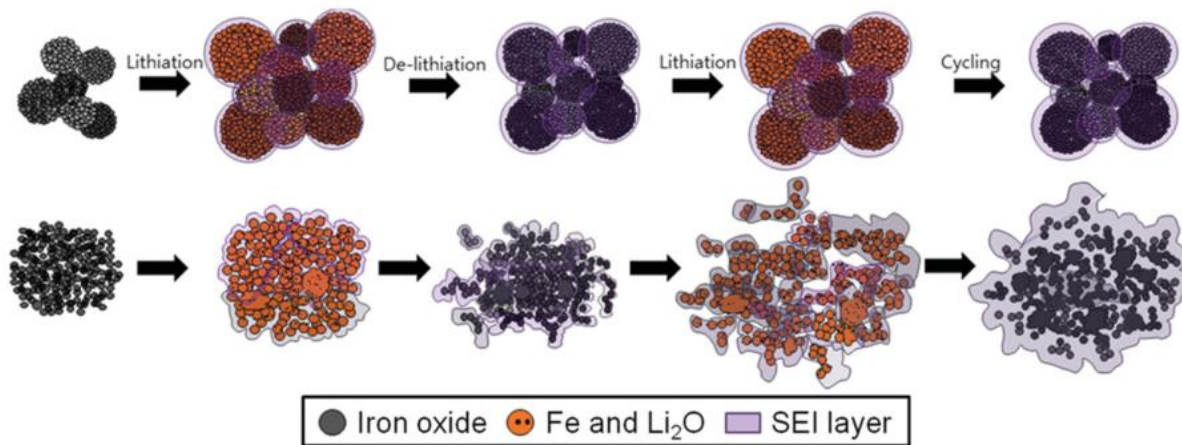


Figure 4.9. Formation of the SEI around iron oxides depending on different particles morphologies<sup>21</sup>

As reported by Yu *et al* in a study concerning iron oxides nanostructures and pictured in Figure 4.9, the formation of SEI in the case of dense agglomerates, which can be compared to the large nanostructured particles in ZFO-1, produces less deleterious effects on capacity retention than for high specific surface structures.

If one considers that the ZFO-1 sample keeps the bimodal size population of particles during cycling, the compact structure may ensure keeping sufficient contact between the particles, while in the case of more isolated nanoparticles the electronic percolation can rapidly be lost for a part of the material. This assumption would explain the higher polarization for the small nanoparticles of ZFO-5 sample. The “disconnected” particles for ZFO-5 may increase the polarization and lead to lower performance. In addition, ZFO-1 may have a lower surface area than ZFO-5 and thus generates relatively few SEI formation in comparison with the fractal-like and highly porous structures obtained with small nanoparticles that may suffer from an excessive and thick SEI layer formation.

Finally, the large nanostructured particles encountered in ZFO-1 sample could constitute a good compromise to benefit from nanostructuring in terms of cycling stability without paying to strong tribute to SEI issues in relation with specific surface. Moreover, the interconnected nature of the nanoparticles agglomerates obtained by laser pyrolysis could preserve electronic percolation upon cycling and lead to improved performances when compared to the literature. Some examples from

## Electrochemical performances of ZnFe<sub>2</sub>O<sub>4</sub> nanopowders

the literature of electrochemical performances obtained for various morphologies of ZnFe<sub>2</sub>O<sub>4</sub> are summarized below (Table 4.2).

	Morphology	1 <sup>st</sup> cycle			Reversible capacity/n <sup>th</sup> cycle	Voltage range	Current rate
		Lithiation	Delithiation	Efficiency			
1	Nanospheres <sup>22</sup>	1215 mAh.g <sup>-1</sup>	851 mAh.g <sup>-1</sup>	70%	500 mAh.g <sup>-1</sup> 50 <sup>th</sup> cycle	0.005-3.0V	50 mA.g <sup>-1</sup>
2	Cubic nanoparticles <sup>23</sup>	1151 mAh.g <sup>-1</sup>	801 mAh.g <sup>-1</sup>	70%	367 mAh.g <sup>-1</sup> 50 <sup>th</sup> cycle	0.01-3.0V	60 mA.g <sup>-1</sup>
3	Agglomerated nanoparticles <sup>16</sup>	1180 mAh.g <sup>-1</sup>	810 mAh.g <sup>-1</sup>	69%	615 mAh.g <sup>-1</sup> 50 <sup>th</sup> cycle	0.005-3.0V	60 mA.g <sup>-1</sup>
4	Hollow spheres <sup>24</sup>	1200 mAh.g <sup>-1</sup>	900 mAh.g <sup>-1</sup>	75%	900 mAh.g <sup>-1</sup> 50 <sup>th</sup> cycle	0.005-3.0V	65 mA.g <sup>-1</sup>
5	Nanorods <sup>25</sup>	1339 mAh.g <sup>-1</sup>	1112 mAh.g <sup>-1</sup>	83%	625 mAh.g <sup>-1</sup> 300 <sup>th</sup> cycle	0.01-3.0V	150 mA.g <sup>-1</sup>
6	Inflorescence spicate architecture <sup>11</sup>	1647 mAh.g <sup>-1</sup>	1221 mAh.g <sup>-1</sup>	74%	1398 mAh.g <sup>-1</sup> 100 <sup>th</sup> cycle	0.01-3.0V	1000 mA.g <sup>-1</sup>

*Table 4.2. Performances of some ZnFe<sub>2</sub>O<sub>4</sub> powders in the literature*

Specific morphologies like hollow spheres (example 4) or nanorods (example 5) are able to keep capacities around 900 mAh.g<sup>-1</sup> at 65 mA.g<sup>-1</sup> and 60 mA.g<sup>-1</sup> respectively but never exceed the theoretical capacity. On the contrary, a very specific morphology consisted in an inflorescence spicate architecture (example 6) is able to retain a capacity higher than the theoretical value after cycling at 1000 mA.g<sup>-1</sup>. For ZFO-1 more than 1100 mAh.g<sup>-1</sup> is still delivered after 100 cycles at 100 mA.g<sup>-1</sup> but such a high value is not observed at 1000 mA.g<sup>-1</sup>. It is however difficult to compare the performances of the different samples in the literature as the cycling conditions and electrode formulation are not rigorously identical.

Generally, the presence of large particles is not desired in lithium-ion batteries as lithium diffusion may be more difficult. However, in our case, the good stability of ZFO-1 compared to most of the examples of the literature could be explained by the interconnected and poorly dense agglomerates obtained through laser pyrolysis that could enhance ion diffusion from the electrolyte homogeneously interpenetrated in the electrode structure, together with insuring efficient electric percolation. Such advantageous distribution of particles was highlighted by BET study of pores distribution for SnO<sub>2</sub> nanoparticles synthesized by laser pyrolysis showing similar agglomeration<sup>26</sup>.

## Electrochemical performances of ZnFe<sub>2</sub>O<sub>4</sub> nanopowders

To observe if the presence of large particles in ZFO-1 can be disadvantageous at high current rates, galvanostatic cyclings at different current densities were conducted. The charge and discharge capacities for 100 cycles at 500 mA.g<sup>-1</sup> (C/2), 2000 mA.g<sup>-1</sup> (2C) and 4000 mA.g<sup>-1</sup> (4C) between 0.01 V and 3.0 V are illustrated below (Figure 4.10). For the cycling at 500 mA.g<sup>-1</sup>, a first cycle at C/90 (11 mA.g<sup>-1</sup>) was performed before the cycles at C/2.

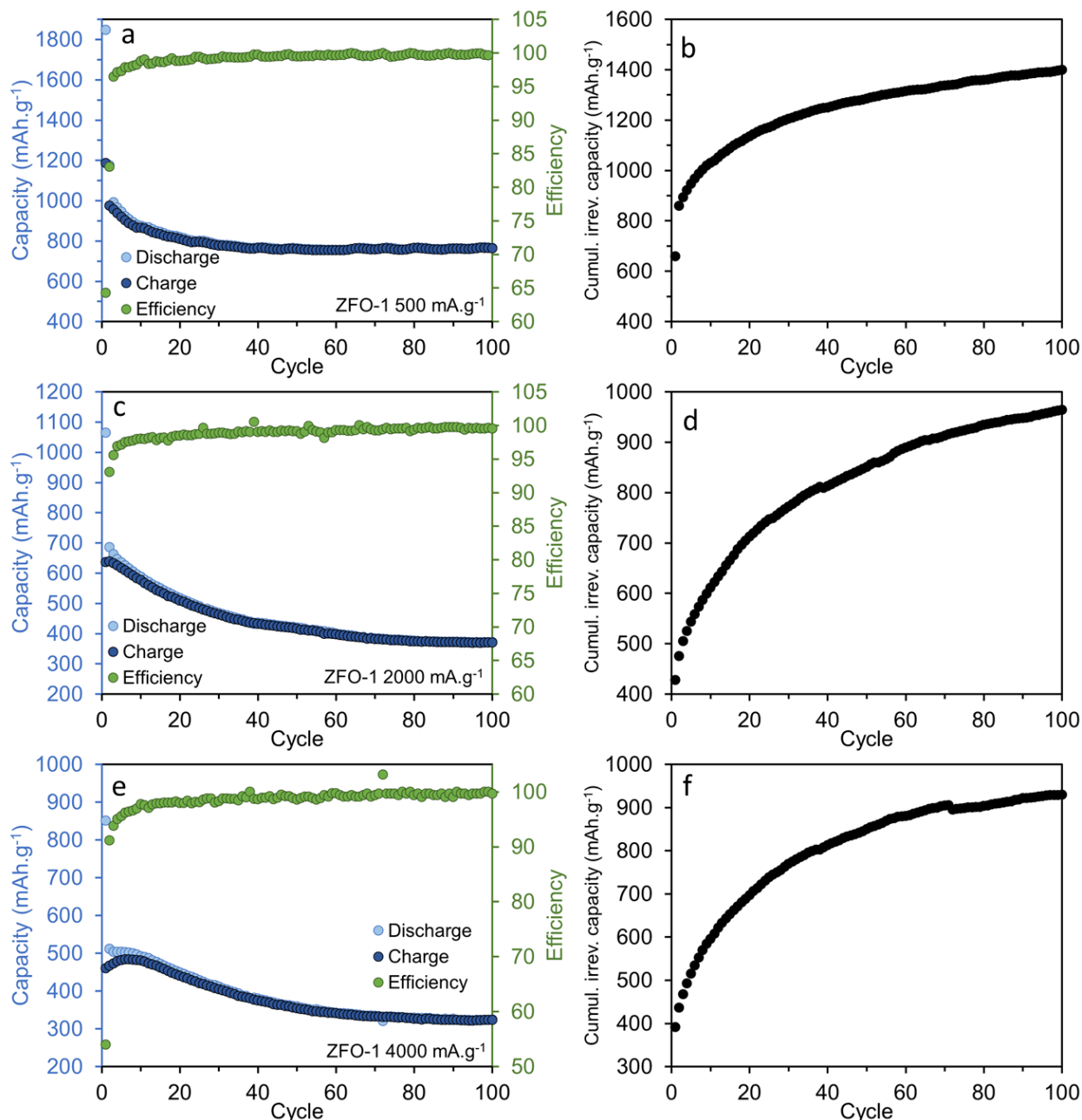


Figure 4.10. Galvanostatic cyclings at 500, 2000 and 4000 mA.g<sup>-1</sup> for ZFO-1: charge/discharge capacity plots (a, c, e) and cumulative irreversible capacity plots (b, d, f)

The first lithiation capacity is higher than the theoretical value for C/90 current rate and 2C current rate (respectively 1847 mAh.g<sup>-1</sup> and 1064 mAh.g<sup>-1</sup>) whereas for the cycling at 4C, only 851 mAh.g<sup>-1</sup> is lithiated for the first cycle. The first delithiation capacities of 1187, 637 and 460 mAh.g<sup>-1</sup> for

## Electrochemical performances of ZnFe<sub>2</sub>O<sub>4</sub> nanopowders

C/90, 2C and 4C respectively are lower than the lithiation value and correspond to a first coulombic efficiency of 64.3%, 59.8% and 54.1% respectively. The first cycle capacities as well as the first coulombic efficiencies are higher for lower current densities. This behavior is confirmed for the subsequent cycles as the reversible capacity obtained after 100 cycles is lower for higher current rates. The specific capacity decreases after the first cycle and is maintained at 760 mA.h.g<sup>-1</sup>, 370 mA.h.g<sup>-1</sup> and 324 mA.h.g<sup>-1</sup> after 100 cycles for cyclings at C/2, 2C and 4C. The coulombic efficiency is relatively stable for the cyclings at C/2 and 2C (respectively 99.7% and 99.4% on average for the last 50 cycles) and increases slowly for the cycling at 4C with an average value after 50 cycles around 99.5%. Unlike the cyclings at C/10, no increase of capacity during cycling is observed here. Anyway, even during fast cyclings, the bimodal size distribution of particles is able to keep a stable capacity for 100 cycles. As at C/10 and 1C, the cumulative irreversible capacity increases very fast for the first 50 cycles for the different current rates and increases slower when the coulombic efficiency becomes relatively stable. The first cycling at C/90 (for the sample cycled at C/2 then) does not seem to have a particular impact on the cycling behavior. The first lithiation capacity is very high but the evolution of the coulombic efficiency is similar to the one for C/10, 1C, 2C and 4C cyclings.

To compare the lithiation process for the cyclings at 500, 2000 and 4000 mA.g<sup>-1</sup> to the cyclings at 100 and 1000 mA.g<sup>-1</sup>, the charge/discharge profiles and the dQ/dV curves were plotted (Figure 4.11).

## Electrochemical performances of ZnFe2O4 nanopowders

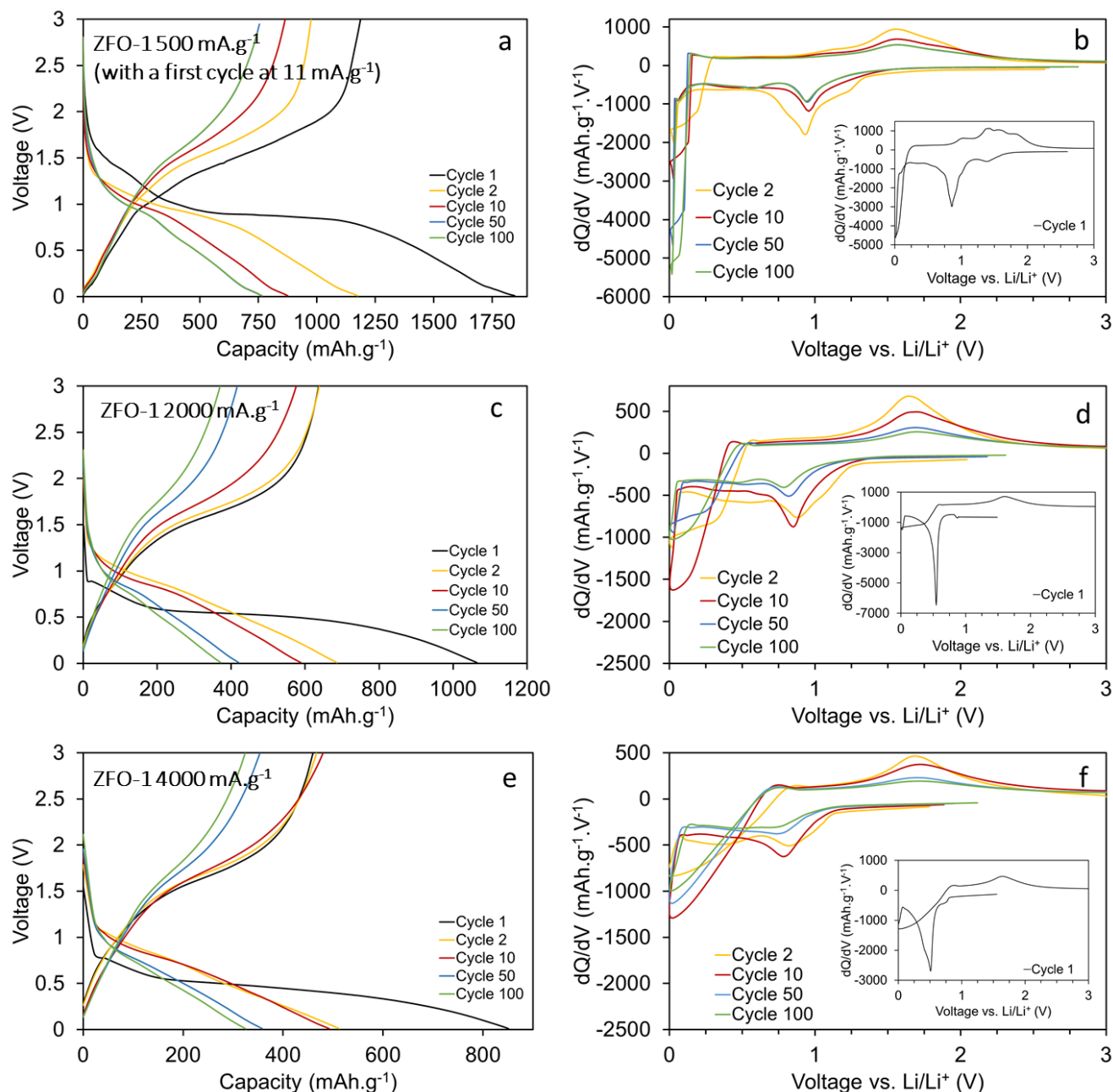


Figure 4.11. Charge/discharge profiles (a, c, e) and  $dQ/dV$  curves (b, d, f) for ZFO-1 galvanostatic cyclings at 500, 2000 and 4000  $\text{mA.g}^{-1}$  between 0.01 V and 3.0 V

The charge/discharge profiles and the derivative curves highlight the presence of the three voltage regions as previously. An intercalation region, a conversion region and an extra capacity region can be defined thanks to the main conversion peak for the lithiation process. What is noticeable is the shift of the conversion peak for the first discharge depending on the current rate. The conversion peak shifts to lower potential for higher current rate. This is particularly observable for the cyclings at 2000 and 4000  $\text{mA.g}^{-1}$  compared with the cycling at 500  $\text{mA.g}^{-1}$ . This shift to the lower voltages at higher current rates also occurs for the next cycles.

## Electrochemical performances of ZnFe2O4 nanopowders

The percentage of discharge capacity and the evolution of the polarization based on the above curves are shown in the figure below (Figure 4.12).

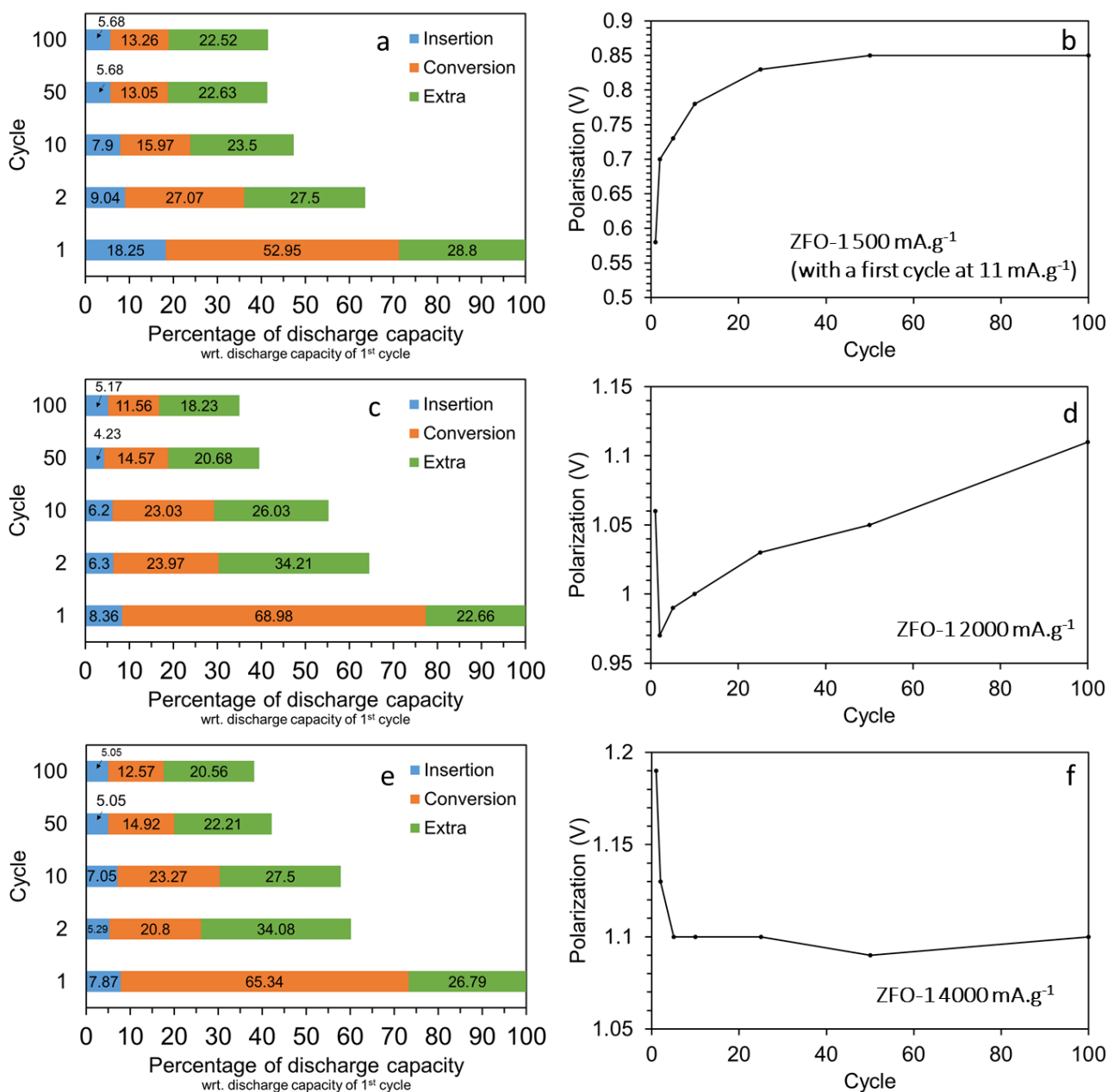


Figure 4.12. Discharge capacity contribution from each region (a, c, e) and evolution of the polarization (b, d, f) for ZFO-1 cyclings at 500, 2000 and 4000 mA.g<sup>-1</sup> between 0.01 V and 3.0 V

For the first discharge capacity and for the three current rates, the conversion region represents the main contribution in capacity with more than 50% of the total lithiated capacity. At the second cycle, the discharge capacity dramatically decreases especially because of the capacity drop in the conversion region. The capacity contribution in this region is twice to three times lower than for the first cycle. This can also be seen on the dQ/dV curves with the decrease of the integrated area in

## Electrochemical performances of ZnFe<sub>2</sub>O<sub>4</sub> nanopowders

the conversion zone. After 50 cycles, it seems that the main part of the capacity is coming from the extra capacity region. It is interesting to observe the evolution of the polarization depending on the current rate. As for C/10 and 1C cyclings, the polarization of the first cycle for 2C and 4C is higher than for the second cycle. For C/2 with the first cycle at C/90, the polarization of the first cycle is lower than for the second one showing that the voltage hysteresis is dependent on the current rate. For C/2, the polarization rises rapidly but reach a stable value after 50 cycles of 0.84 V. At 2C current rate, 1.1 V of polarization is obtained after 100 cycles as for 4C current rate. However, at 4C current rate, the polarization is relatively stable directly after the second cycle.

To understand if the poorer performances at higher current rates is limited by lithium diffusion or by charge transfer at fast rates, the resistance at the 100<sup>th</sup> cycle for C/10, C/2, 1C, 2C and 4C was calculated. The resistance was defined as the ratio of the polarization to the current density. The evolution of the polarization and of the resistance are shown below (Figure 4.13).

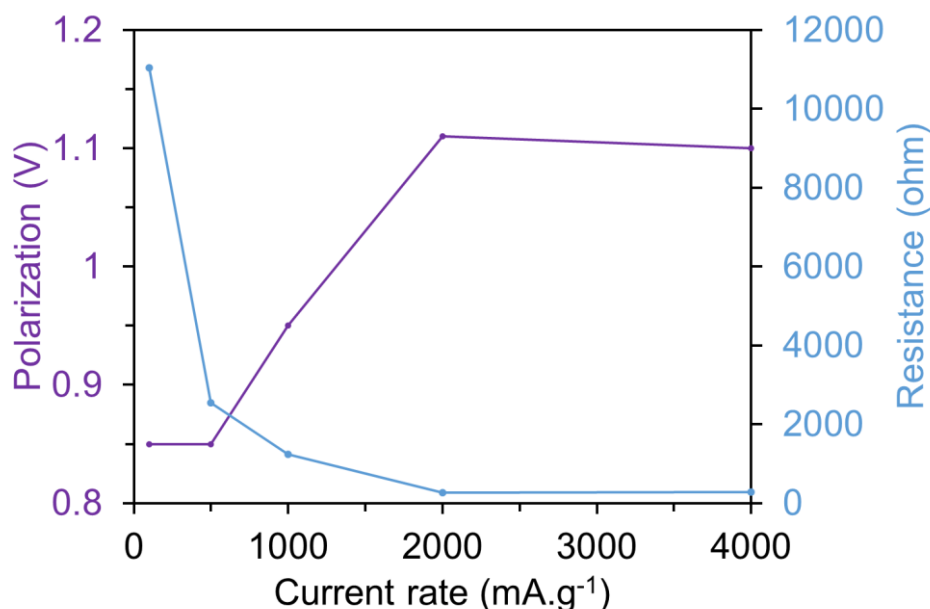


Figure 4.13. Evolution of the polarization and of the resistance at the 100<sup>th</sup> cycle depending on the current rate for ZFO-1

The decrease of the electrode resistance is observed whereas the polarization increases for higher current rates. This suggests that the lithiation process is mainly limited by lithium diffusion into the material rather than charge transfer at fast rates. If charge transfer was limiting, the resistance and the polarization would have followed the same trend<sup>20</sup>. The decrease of capacity with higher current rates may be explained by less reactivity due to limited lithium diffusion into the material that causes the increase of polarization (and the shift of the conversion peak to lower potentials during discharge on the dQ/dV curves).

A study of the rate capability was also performed to demonstrate the stability of the material (Figure 4.14). The current density was increased in several steps after every five cycles from C/5 (200 mA.g<sup>-1</sup>) to 4C (4000 mA.g<sup>-1</sup>) and then decreased to C/5. The capacity values decrease with increasing current rate, as could be expected. The electrode shows a very good cyclability with a reversible capacity varying from 876 mAh.g<sup>-1</sup> to 422 mAh.g<sup>-1</sup>. At the second C/5 current rate, the material recovers a capacity of 756 mAh.g<sup>-1</sup> which is slightly lower than for the first cycles.

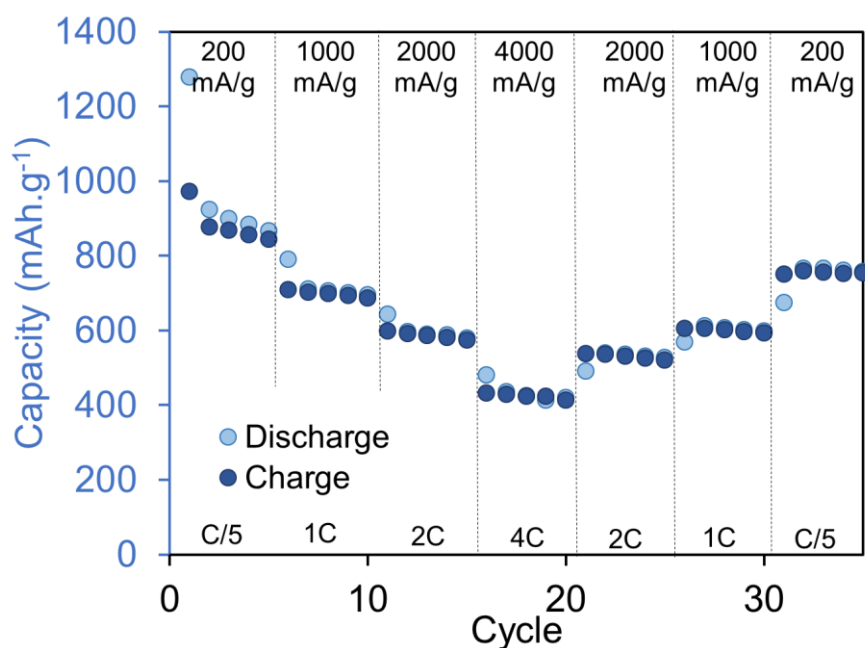


Figure 4.14. Rate capability between 0.01 V and 3.0 V from C/5 to 4C

These results demonstrate that ZnFe<sub>2</sub>O<sub>4</sub> sample with a bimodal size distribution has an enhanced rate capability, stability and capacity at different current densities when compared to the monomodal distributed sample. This difference is assumed to be the consequence of a more stable and less extended SEI formation upon cycling at the surface of the large nanostructured particles.

## 2. Investigation of the lithium storage mechanism

To identify the potential of each electrochemical process during the lithiation and delithiation of the ZnFe<sub>2</sub>O<sub>4</sub> phase, cyclic voltammetry between 0.01 V and 3.0 V was conducted on ZFO-1. CV curves recorded for the five first cycles are shown below (Figure 4.15).

## Electrochemical performances of ZnFe<sub>2</sub>O<sub>4</sub> nanopowders

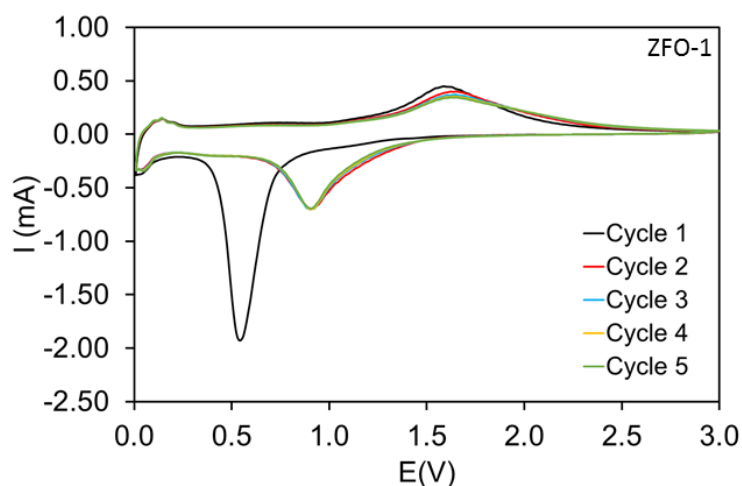


Figure 4.15. Cyclic voltammetry of ZFO-1 for the five first cycles, between 0.01 V and 3.0 V at  $0.1 \text{ mV}\cdot\text{s}^{-1}$  scan rate

During the first lithiation, one sharp cathodic peak appears at 0.55 V which is then shifted and replaced by a smaller peak at 0.94 V for the following cycles. This reduction peak can probably be attributed to the insertion of lithium inside the crystalline structure leading to its amorphization and to the conversion reaction with Zn(II) and Fe(III) which are reduced to their metallic states<sup>27</sup>. The first delithiation curve shows an anodic peak at 1.6 V which may be associated to the oxidation of Zn(0) and Fe(0) to Zn(II) and Fe(III)<sup>28</sup>. The potential shift is characteristic of conversion-type reactions and is related to the replacement of the conversion potential plateau in first discharge by a mostly sloping curve corresponding to the cycling of the *in situ* formed nanomaterial. Another contribution to the drastic changes in voltage between discharge and charge in the first cycle has an origin in the amorphous character of the  $\text{Li}_2\text{O}/\text{M}$  ( $\text{M}=\text{Fe}, \text{Zn}$ ) nanocomposite (see the proposed mechanism below) at the end of the discharge which implies differences in free energy, and, therefore, in reaction equilibrium potential.

The decrease of the integrated area between the first and the second cycle is consistent with the low coulombic efficiency of 71.6% observed at the first cycle. It can also be noted that the characteristic peaks position and the value of the integrated area are almost maintained after the first cycle revealing the excellent capacity retention of ZFO-1.

To obtain more information on the lithiation storage mechanism, operando XRD was conducted on ZFO-1 sample for the first discharge (Figure 4.16). The slow discharge was realized from the OCV to 0.01 V with a current density of  $5.6 \text{ mA}\cdot\text{g}^{-1}$  (theoretically 180 hours for a full lithiation). Diffractograms were acquired every two hours in the  $10^\circ - 44^\circ$  angular range. As no peak appeared during the first lithiation, the peaks shown below are those for which a modification was observed during the first discharge.

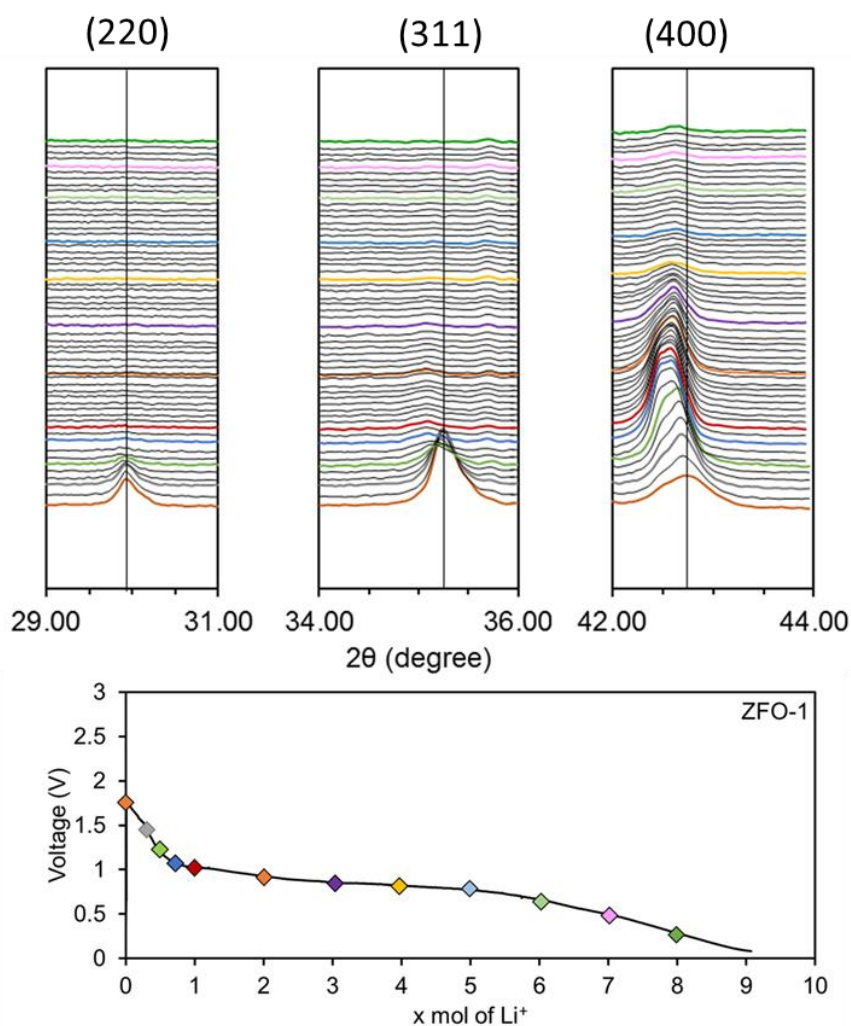


Figure 4.16. Operando X-ray diffraction for the first lithiation of ZFO-1 between 0.01 V and 3.0 V at 5.6 mA.g<sup>-1</sup>

The XRD patterns acquired between the OCV and 1.0 V clearly reveal a shift of the ZnFe<sub>2</sub>O<sub>4</sub> peak from 43.7° to 42.5°. This shift to lower 2θ values indicates an increase of the lattice parameter related to the insertion of lithium into the spinel structure to form a Li<sub>x</sub>ZnFe<sub>2</sub>O<sub>4</sub> phase (x ≈ 1 mol here). No shift can be observed for the two other peaks at 30° and 35.3° though but no explanation is given for this phenomena. With further lithiation, the intensity of the different peaks decreases progressively. This decrease starts around 1.0 V (consistent with the position of the plateau) for the peak at 42.5° and slightly earlier for the two peaks at 30° and 35.3°, it might be a consequence of the progressive destruction of the crystalline structure. After a full discharge, no peak can be observed anymore and in particular, the XRD pattern cannot reveal the presence of any Fe, Zn or LiZn crystalline structure. The absence of any feature on the diffraction pattern of the fully lithiated is relevant with the formation of an amorphous Li<sub>2</sub>O phase with highly dispersed ZnLi and Fe particles as reported in the literature<sup>5,29</sup>. As the active material becomes amorphous after the first lithiation, operando XRD

was not conducted for the reverse charge process and other operando measurements were privileged then.

To investigate the structure and species evolution, operando <sup>57</sup>Fe Mössbauer measurements were then conducted on the first cycle and a half. The data analysis was realized by L. Stievano and M. Sougrati from the Charles Gerhardt Institute in Montpellier, following a procedure detailed in appendix.

The whole set of Mössbauer spectra obtained during the first one and a half cycles are shown, for the inner part, in Figure 4.17. Since the spectrum of the initial material contains a broad magnetic component which extends to large velocities, the first part of the operando spectra was measured using a velocity range extending from -14 to 14 mm/s. However, this broad component definitively disappears after only a few spectra. For this reason, in order to improve the number of experimental points in the region of interest, the velocity range was reduced to the range -4 – +4 mm/s starting from spectrum #14.

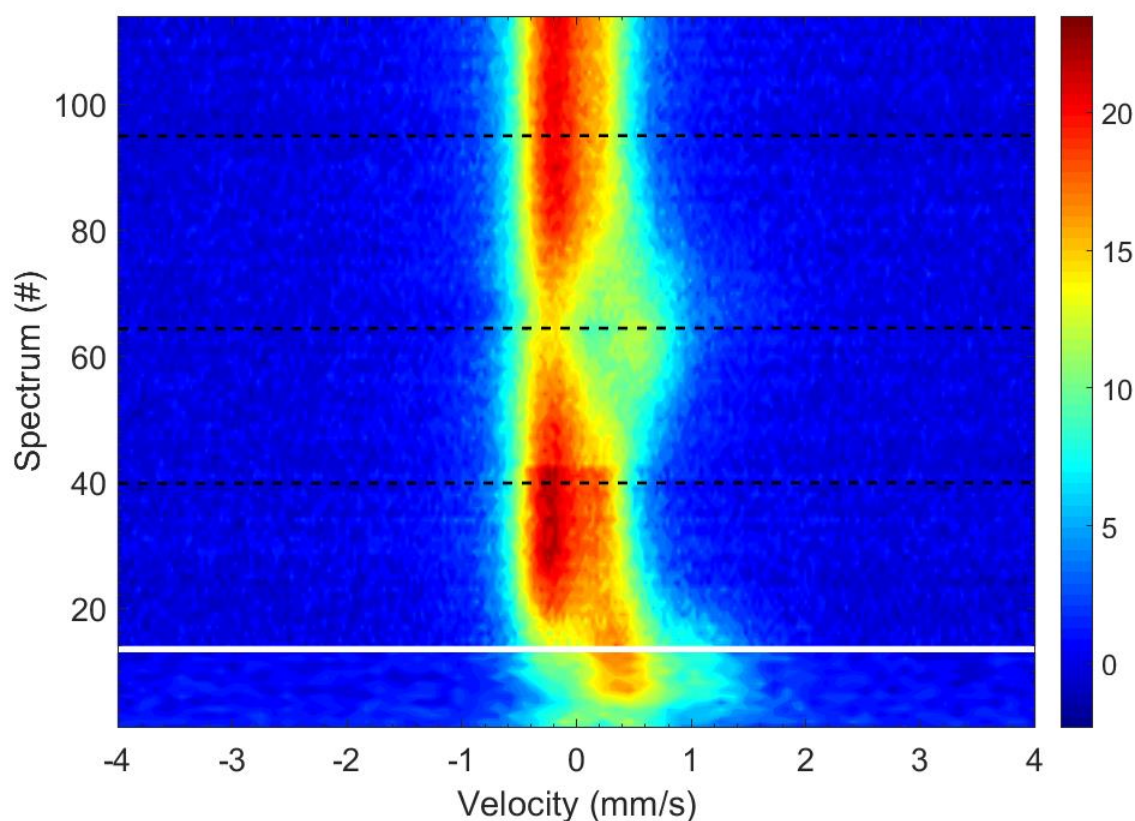


Figure 4.17. Operando <sup>57</sup>Fe Mössbauer spectra measured during the first one and a half cycle (discharge/charge/discharge). The horizontal dotted lines represent the end of the different processes. The step between spectra 13 and 14 corresponds to the reduction of the velocity range from -14 – +14 to -4 – +4 mm/s.

## Electrochemical performances of ZnFe<sub>2</sub>O<sub>4</sub> nanopowders

In Figure 4.18 is shown electrochemical curve corresponding to the whole operando experiment. As clearly shown, the first discharge ends at spectrum #39, and is followed by the first charge between spectra #40 and #65. Unfortunately, due to technical problems, part of the first charge was lost, as indicated by the red portion of the potential curve in Figure 4.18. The second discharge ends at spectrum #95, and is followed by a long relaxation period during which the Mössbauer spectra remain virtually unchanged (Figure 4.17).

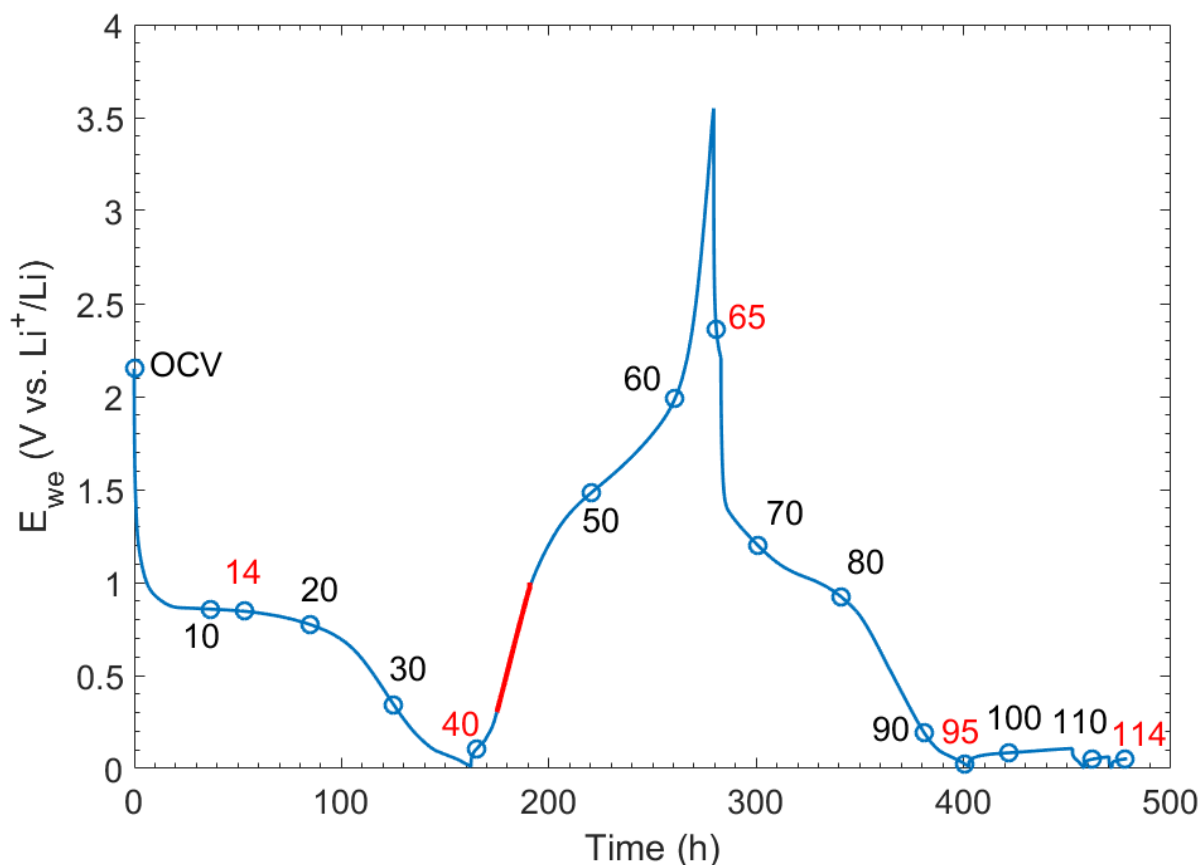


Figure 4.18. Electrochemical signature of the operando cell and corresponding Mössbauer spectra. The red line corresponds to a region where no spectra could be measured due to technical issues (between spectra #42 and #43). The velocity range was reduced starting from spectrum #14.

Due to the two different velocity ranges, the whole series of spectra could not be treated in a single step, but the spectra at the two velocity ranges had to be treated separately. The results of the PCA analysis of the first 13 spectra measured in the large velocity range are summarised in Figure 4.19.

## Electrochemical performances of ZnFe<sub>2</sub>O<sub>4</sub> nanopowders

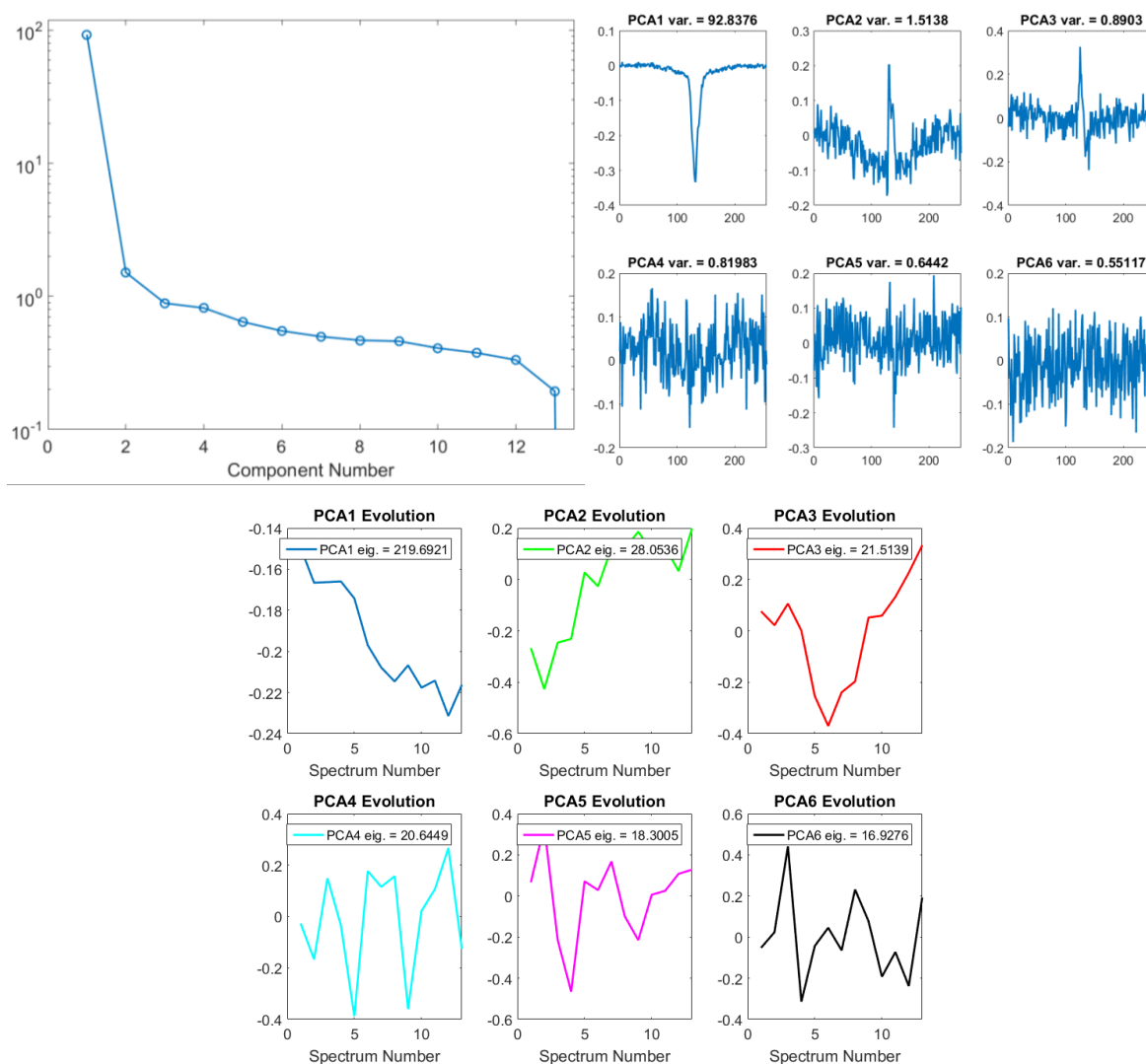


Figure 4.19. Variance plot (top left), principal components (top right) and evolution of the scores (bottom) during the first 13 Mössbauer spectra of the first discharge measured in the velocity range  $-14 - +14$ .

The variance plot suggests that at least two principal components are necessary to reproduce 99% of the total variance of the whole series of spectra, the residual part being supposedly due to experimental noise. However, an inspection of the shape of the principal components and a first observation of the evolution of the scores suggests that a third component may also be significant. The MCR-ALS analysis was thus conducted using either 2 or 3 components, and the analysis with 3 components, with a constraint of unimodality for all of them was tried. The best results were obtained with 3 components, the results are summarised in Figure 4.20.

## Electrochemical performances of ZnFe<sub>2</sub>O<sub>4</sub> nanopowders

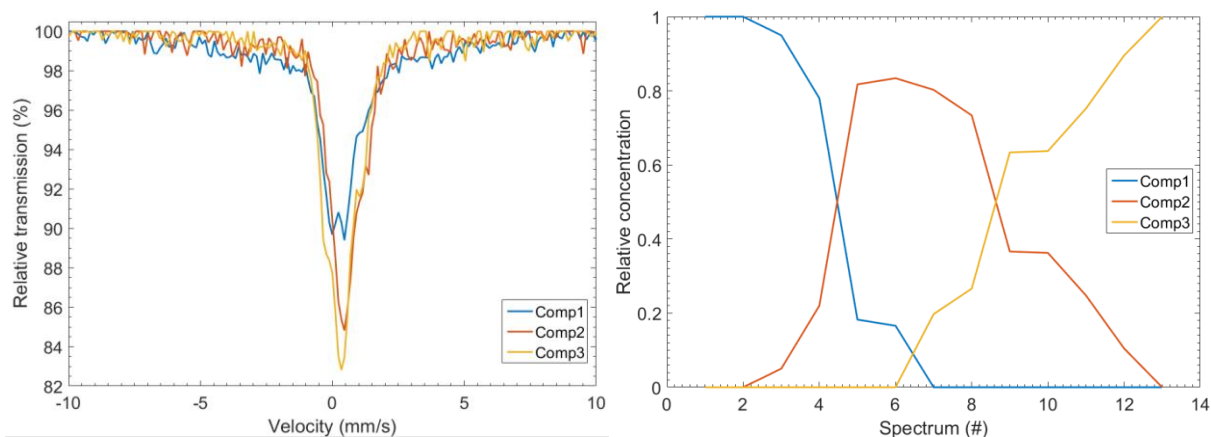


Figure 4.20. MCR-ALS components (left) and their evolution (right) during the first 13 Mössbauer spectra of the first discharge measured in the velocity range -14 – +14 mm/s.

At a first inspection, the first component is practically identical to the spectrum of the pristine composite, showing the broad magnetic component in addition to the intense quadrupole doublet in the middle of the spectrum (see chapter 3 page 98). During the very first part of the discharge (first 7 spectra), the magnetically split component completely disappears and is replaced by an intense asymmetric component pointing at 0.5 mm/s. This second component is then replaced by a third one, which is rather similar but in addition presents a shoulder at negative velocities.

Starting from spectrum 14, the velocity range was reduced and kept constant during the rest of operando experiment. Therefore, all spectra collected during the second part of the first discharge, the first charge and the second discharge could be treated together first using PCA, and the MCR-ALS analysis. The results of the PCA analysis of the 101 spectra measured in the reduced velocity range are summarised in Figure 4.21.

## Electrochemical performances of ZnFe<sub>2</sub>O<sub>4</sub> nanopowders

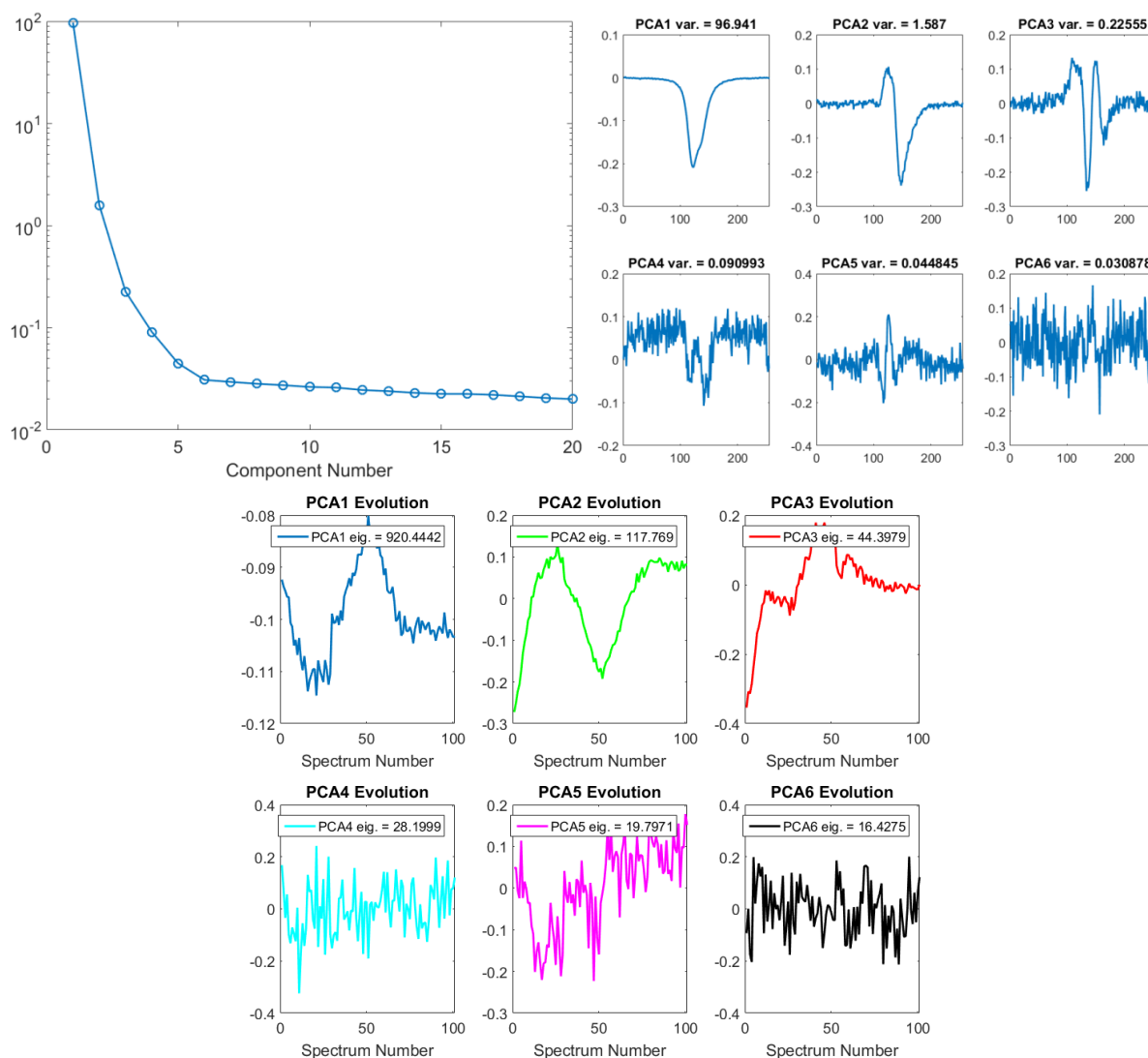


Figure 4.21. Variance plot (top left), principal components (top right) and evolution of the scores (bottom) during the 101 Mössbauer spectra of the operando experiment measured in the velocity range  $-4 - +4$  mm/s.

By looking at the variance plot and at the shapes of the component, there seem to be up to 5 principal components carrying information exceeding the experimental error. However, an inspection of the scores shows that the components 4 and 5 have a very hectic evolution during the experiment, suggesting that they may also represent rather noise than chemical information. Indeed, all tests with MCR using more than 3 components produced only three distinct components, independent of the imposed constrains, while all additional components resembled very strongly to the component representing the spectrum at the end of the discharge processes. For this reason, only the MCR-ALS analysis with 3 components was retained: the best results were obtained with a constraint of unimodality for one of the three components, and the results are summarised in Figure 4.22.

## Electrochemical performances of ZnFe<sub>2</sub>O<sub>4</sub> nanopowders

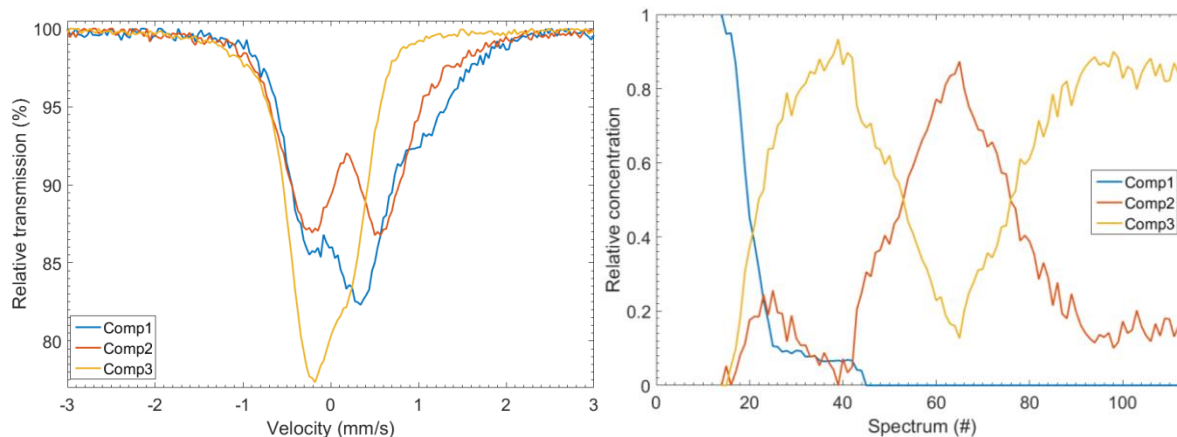


Figure 4.22. MCR-ALS components (left) and their evolution (right) during the collection of the 101 Mössbauer spectra of the operando experiment measured in the velocity range -4 – +4 mm/s.

As clearly visible, the first component is rapidly replaced by component 3, which becomes dominant and reaches its maximum at spectrum #39, corresponding to the end of the discharge. During the charge process, component 3 is replaced by component 2, which on its turn becomes dominant at the end of spectrum 63, *i.e.*, at the end of the charge. The following discharge process results in the replacement of component 2 by component 3.

Summarising, 6 components are thus globally necessary to follow the whole operando experiment, and are represented in Figure 4.23 together with their evolution.

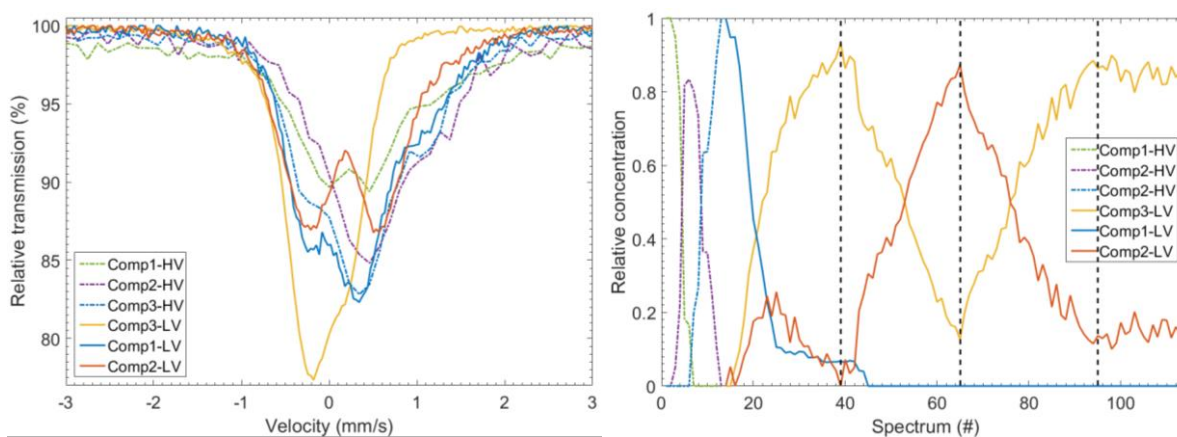


Figure 4.23. MCR-ALS components (left) and their evolution (right) during the whole operando Mössbauer experiment.

At a first inspection, the following observations can be made:

- 5 components, 3 in the high velocity range and 2 in the low velocity range are necessary for the first discharge
- 2 components are necessary for understanding the first charge and the second discharge.

- The last component in the high velocity range is quite similar to the first one measured in the low velocity range. An increase of the shoulder at low velocities is compensated by a decrease of the signal at high velocities.

These components can then be treated as normal Mössbauer spectra, in order to help us to understand the chemical state of the iron through the different electrochemical processes.

The first component, shown in Figure 4.24, is similar to the spectrum of the pristine ZnFe<sub>2</sub>O<sub>4</sub>/Fe<sub>2</sub>O<sub>3</sub> composite material, and is in fact fitted in a similar way, *i.e.*, a broad magnetic field distribution accounting for 45% of the total resonance area plus two additional doublets, one of them representing of zinc ferrite ZnFe<sub>2</sub>O<sub>4</sub> (41% of the total resonance area). The slight increase of the shoulder at high velocities compared to the spectrum of the pristine material, correspond to an increase of the intensity of the second doublet, characterised by a quadrupole splitting  $\Delta = 1.15$  mm/s and an isomer shift  $\delta = 0.90$  mm/s. Such isomer shift is quite small to represent divalent iron compounds, but also definitely too high to represent trivalent iron species. Intermediate iron oxidation states are commonly observed in spinels, e.g., in magnetite (Fe<sub>3</sub>O<sub>4</sub>), where adjacent divalent and trivalent iron sites undergo fast electron hopping processes, resulting in an average oxidation state of +2.5<sup>30</sup>. On the other hand, species with similar isomer shifts are currently observed in non-stoichiometric iron oxides containing both divalent and trivalent iron centres such as wüstite<sup>31,32</sup> or during its reduction with lithium<sup>33</sup>. In our case, this component may represent either Fe<sup>2+</sup> or Fe<sup>2.5+</sup> iron species.

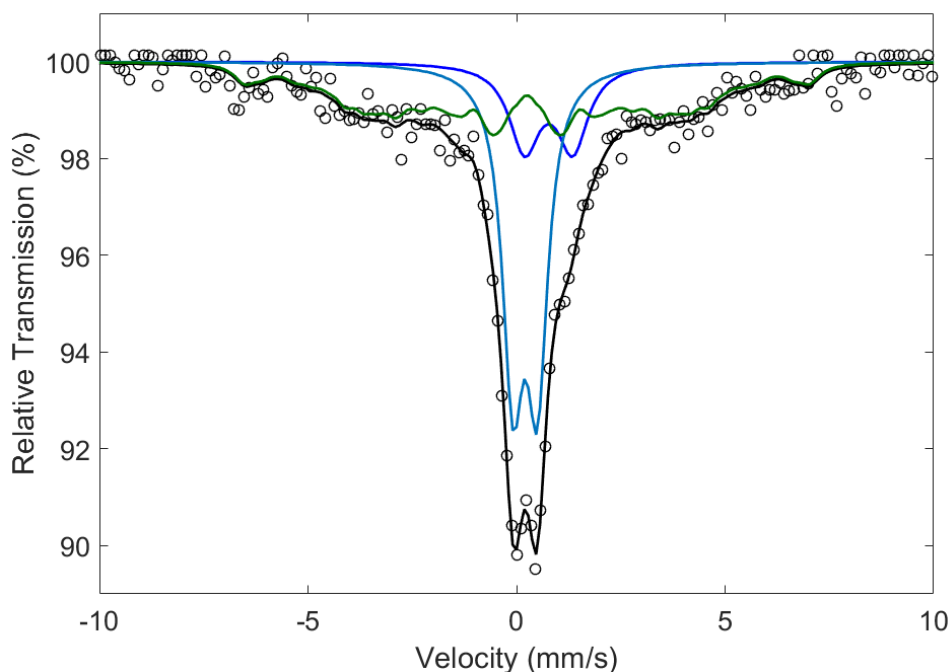


Figure 4.24. Fitting of the first component obtained by the MCR-ALS analysis of the first 13 Mössbauer spectra of the first discharge measured in the velocity range -14 – +14 mm/s.

The second and third components found in the analysis of the high velocity range and the first and third one of the low velocity range spectra, shown in Figure 4.25, are relatively similar and can be fitted together with the same number of quadrupole doublets. The hyperfine parameters resulting from the common fitting of these four spectra is also reported in Table 4.3.

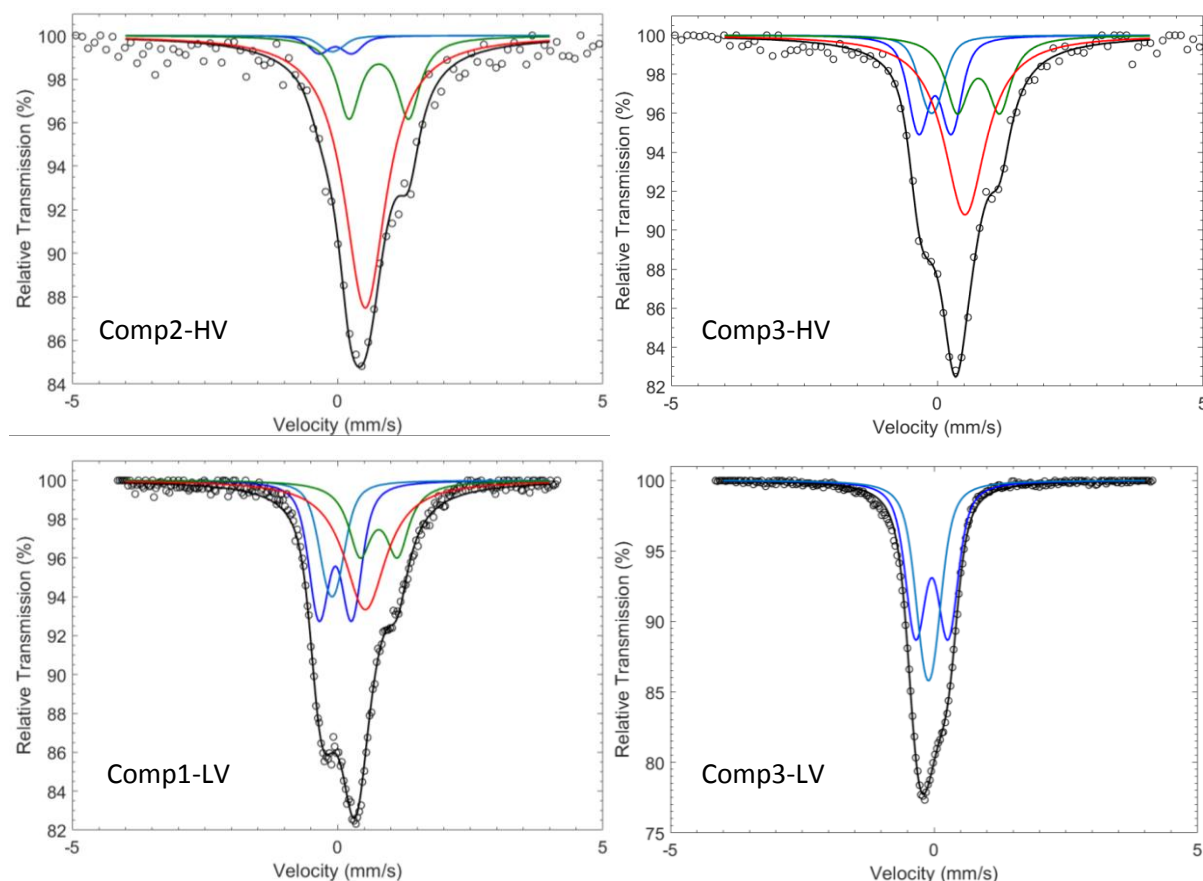


Figure 4.25. Fitting of the second (left) and the third (right) component obtained by the MCR-ALS analysis of the Mössbauer spectra measured in the velocity range -14 – +14 mm/s (top), and of the first (left) and third (right) component obtained by the MCR-ALS analysis of the spectra measured in the velocity range -4 – +4 mm/s (bottom).

Four quadrupole doublets are necessary to fit these four components:

- The first doublet (in green in Figure 4.25) is similar to the doublet with ill-defined isomer shift described above for the first component in the high velocity range.
- This doublet is accompanied by an additional one (in red in Figure 4.25) with almost no quadrupole splitting and an isomer shift practically identical to that of Fe<sup>2.5+</sup> in magnetite. However, differently from bulk magnetite, no magnetically splitting is observed, in line with the superparamagnetic nature of this species, probably related to the small size of the magnetic domains (< 5 nm)<sup>34,35</sup>.

## Electrochemical performances of ZnFe<sub>2</sub>O<sub>4</sub> nanopowders

- The two additional doublets (both in blue in Figure 4.25) are the only ones contained in the spectrum of the second component measured in the low velocity range, and can be attributed to zerovalent iron metal nanosized particles. In fact, superparamagnetic iron metal usually shows this typical asymmetric shape usually fitted with two components, both centred at about  $\delta = 0$  mm/s<sup>36-41</sup>.

On-going from the first to the last component, a gradual decrease of the first two doublets is observed, with the first doublet at lower isomer shift decreasing more rapidly, together with the concomitant increase of the two doublets representing iron metal nanoparticles. The latter species is the dominant one at the end of the discharge.

Parameters	Doublet 1	Doublet 2	Doublet 3	Doublet 4
$\Delta$ (mm/s)	1.12-0.70	0.00	0.62(3)	0.19(5)
$\delta$ (mm/s)	0.88(3)	0.63(3)	0.06(1)	0.00(1)
$\Gamma$ (mm/s)	0.5(1)	0.96(9)	0.28(3)	0.28(3)
$\sigma_{\text{GAUSS}}$ (mm/s)	-	-	0.12(2)	0.12(2)
Resonance area (%)				
Comp2-HV	23(7)	71(9)	4(3)	2(2)
Comp3-HV	21(8)	48(9)	21(8)	10(8)
Comp1-LV	20(6)	35(8)	30(7)	15(7)
Comp3-LV	0	0	57(4)	43(4)

*Table 4.3. Hyperfine parameters obtained by the fitting of the second and third component obtained by the MCR-ALS analysis of the Mössbauer spectra measured in the velocity range -14 – +14 mm/s, and of the first and third component obtained by the MCR-ALS analysis of the spectra measured in the velocity range -4 – +4 mm/s.*

Finally, the remaining component is the second one measured in the low velocity range, shown in Figure 4.26.

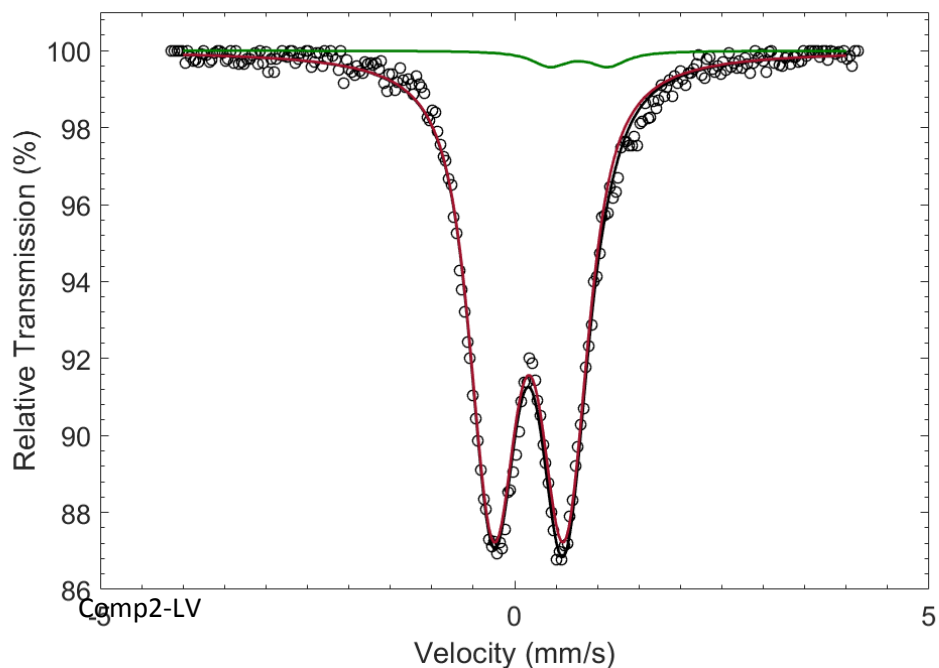


Figure 4.26. Fitting of the second component obtained by the MCR-ALS analysis of the Mössbauer spectra measured in the velocity range  $-4 - +4$  mm/s.

This spectrum is dominated by a dominant broad quadrupole doublet characterised by  $\delta = 0.28$  mm/s and  $\Delta = 0.88$  mm/s, typical of nanosized trivalent iron oxides. It is very interesting to observe that, while during the first discharge several intermediate species with different, sometimes mixed valence states are observed, during the following charge and discharge only zerovalent and trivalent iron seem to form.

Using the composition of the different components in terms of different quadrupole doublets, and following the evolution of their respective concentration during cycling, one can reconstruct the evolution of the average oxidation state of the iron during cycling. These results over are summarised in Figure 4.27. In this case, it was assumed that the component centred at 0.88 mm/s represents Fe<sup>+2</sup>, whereas the component at  $\delta = 0.63$  mm/s corresponds to Fe<sup>+2.5</sup>.

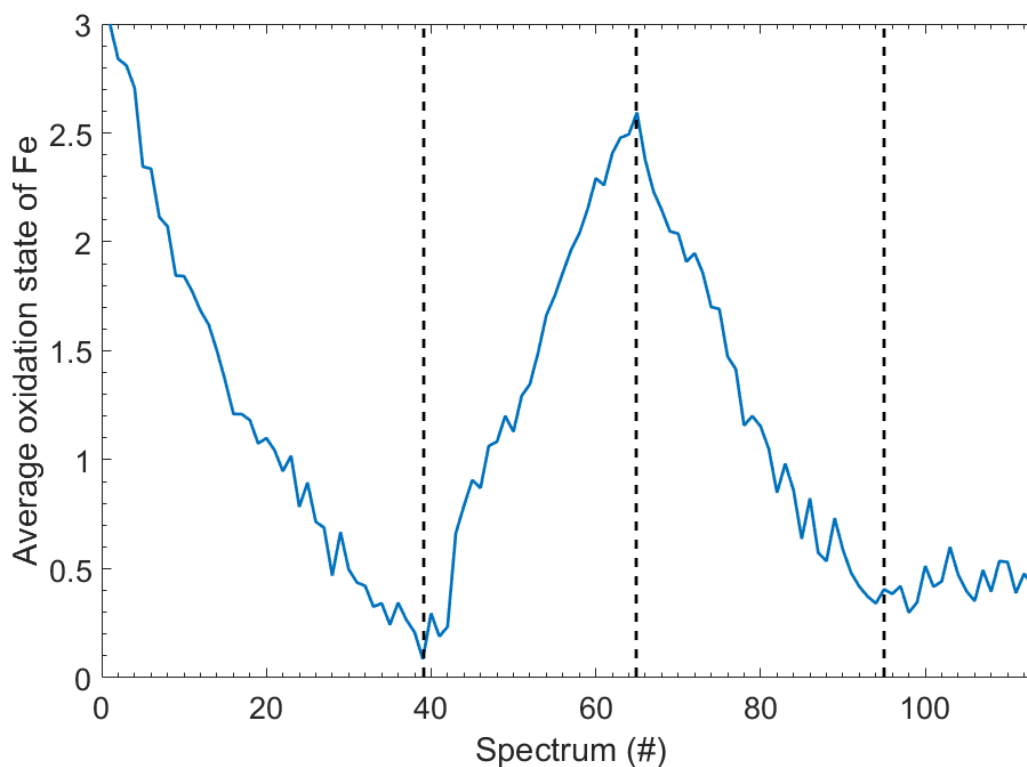


Figure 4.27. Average oxidation state of the iron during cycling obtained from the weighted relative resonance areas of the MCR-ALS components.

From these results, it is clear that the oxidation state of the iron varies in a non-linear way during the first discharge, but a more rapidly decreasing slope is observed during the first part of the first discharge, corresponding to a more rapid decrease of the oxidation state, followed by a slower reduction rate during the second part. This different reduction rate might be related to the simultaneous reduction of the Zn during the second part of the first discharge. A similar trend is observed also during the following charge and discharge processes, even though that is not easy to observe during the first charge due to a technical problem that stopped the acquisition of the Mössbauer spectra at the beginning of the first charge process (between spectra 42 and 43).

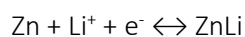
Based on the aforementioned characterizations results and on assumptions made by different authors in the literature<sup>42,43</sup>, the lithium storage mechanism for ZnFe<sub>2</sub>O<sub>4</sub> can be proposed as follows. The first cycle can be decomposed in three distinct reactions:

- intercalation of lithium into the crystalline structure (up to 1 lithium per formula unit), consistent with the XRD results.
- destruction of this crystalline structure during the first discharge (also confirmed by operando XRD) and conversion reaction to form Zn(0) and Fe(0) particles embedded in an amorphous Li<sub>2</sub>O matrix. The formation of metallic iron is confirmed by the operando Mössbauer study.

## Electrochemical performances of ZnFe<sub>2</sub>O<sub>4</sub> nanopowders

However, no evidence of Zn particles formation neither Li<sub>2</sub>O formation is given by the previous results.

- alloying reaction between Zn and Li to form ZnLi: this is only an assumption based on literature as no evidence of ZnLi particles was given by XRD.



Further studies have to be conducted, in particular to confirm or not the reduction of Zn(II) to Zn(0) and the alloying reaction with lithium. Operando XAS measurements are planned to investigate deeper the storage mechanism for ZnFe<sub>2</sub>O<sub>4</sub>.

Thus, after the first cycle, the initial ZnFe<sub>2</sub>O<sub>4</sub> structure is not recovered but replaced by separated phases of ZnO and Fe<sub>2</sub>O<sub>3</sub>. As already evocated, It becomes then interesting to evaluate the electrochemical performances of a ZnO/Fe<sub>2</sub>O<sub>3</sub> mixture (50% at. for each phase) as starting material and study its lithium storage mechanism to compare it with the one of ZnFe<sub>2</sub>O<sub>4</sub>.

### III. Electrochemical performances of ZnO and Fe<sub>2</sub>O<sub>3</sub>

#### 1. Electrochemical performances of ZnO, Fe<sub>2</sub>O<sub>3</sub> and ZnO/Fe<sub>2</sub>O<sub>3</sub> mixture

The electrochemical performances of the transition metal oxides ZnO and Fe<sub>2</sub>O<sub>3</sub> (ZnOx-2 and FeOx-3 samples) were evaluated as well as the performances of a mixture of 50% at. ZnO and 50% at. Fe<sub>2</sub>O<sub>3</sub> (ZnO/Fe<sub>2</sub>O<sub>3</sub>) using the same starting samples. The ZnO/Fe<sub>2</sub>O<sub>3</sub> electrode was directly prepared by ball-milling the two nanopowders with the binder and the carbon additives. The lithium storage mechanisms for ZnO/Fe<sub>2</sub>O<sub>3</sub> mixture were then investigated and compared to the ones of ZnFe<sub>2</sub>O<sub>4</sub> to highlight any particular interest of this ternary phase. Taking into account the morphology of the two binary oxides samples used for this study, the presented results have to be compared to ZFO-5 sample for the ternary phase (monomodal size distribution).

ZnO, Fe<sub>2</sub>O<sub>3</sub> and ZnO/Fe<sub>2</sub>O<sub>3</sub> were cycled in a galvanostatic mode at 100 mA.g<sup>-1</sup> current rate between 0.01 V and 3.0V for 100 cycles (Figure 4.28).

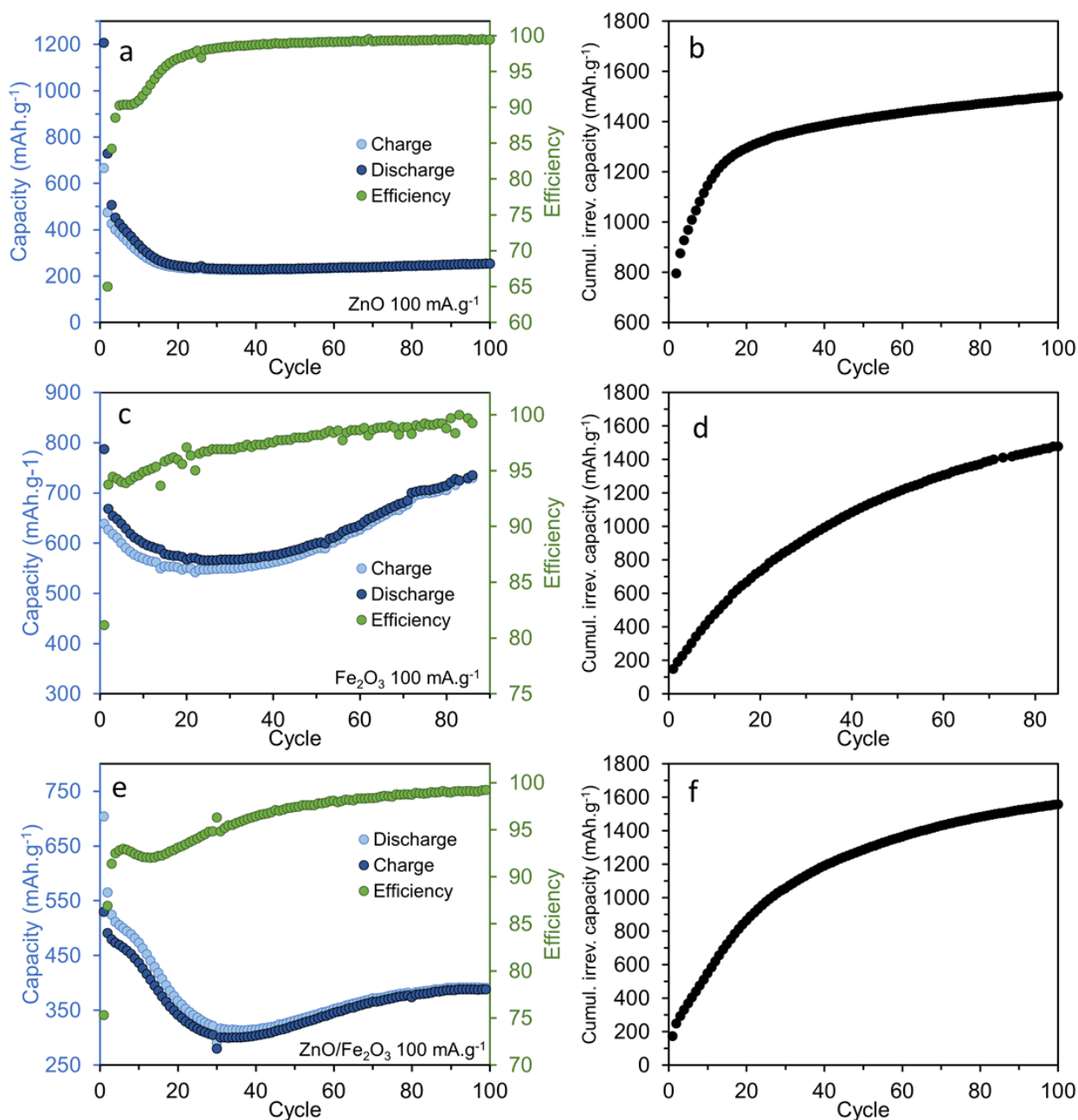


Figure 4.28. Galvanostatic cyclings at  $100 \text{ mA.g}^{-1}$  for ZnO,  $\text{Fe}_2\text{O}_3$  and ZnO/ $\text{Fe}_2\text{O}_3$  mixture: charge/discharge capacity plots (a, c, e) and cumulative irreversible capacity plots (b, d, f)

For ZnO,  $1206 \text{ mAh.g}^{-1}$  is stored during the first lithiation. The first delithiation capacity of  $666 \text{ mAh.g}^{-1}$  leads to a first coulombic efficiency of 55.2% for this material. As for  $\text{ZnFe}_2\text{O}_4$ , the difference of capacities between the first lithiation and the first delithiation may come from the SEI formation. In the case of  $\text{Fe}_2\text{O}_3$ , the first discharge capacity is around  $800 \text{ mAh.g}^{-1}$  and the first coulombic efficiency of only 81% can also be attributed to the SEI formation. After the first cycle, both ZnO and  $\text{Fe}_2\text{O}_3$  show decrease in the reversible capacity for 20 to 30 cycles and a fast increase of the cumulative irreversible capacity. The delithiation capacity is then stabilized for ZnO and a charge

capacity of 252 mAh.g<sup>-1</sup> is maintained after 100 cycles. The behavior is different for Fe<sub>2</sub>O<sub>3</sub> with an increase in capacity from the 20<sup>th</sup> to the 90<sup>th</sup> cycle, similarly to ZnFe<sub>2</sub>O<sub>4</sub>. The reversible capacity reaches a value of 730 mAh.g<sup>-1</sup> after 90 cycles. This increase in capacity during cycling is also observed in the ZnO/Fe<sub>2</sub>O<sub>3</sub> mixture. For ZnO/Fe<sub>2</sub>O<sub>3</sub>, a first lithiation capacity of 704 mAh.g<sup>-1</sup> is reached whereas only 530 mAh.g<sup>-1</sup> is obtained after the first delithiation leading to a coulombic efficiency of 75.3% for the first cycle. As for ZnO and Fe<sub>2</sub>O<sub>3</sub>, the capacity drops drastically to reach 280 mAh.g<sup>-1</sup> after 30 cycles leading to a cumulative irreversible capacity above 1000 mAh.g<sup>-1</sup> before 50 cycles. However, the reversible capacity increases then to 390 mAh.g<sup>-1</sup> after 100 cycles and the irreversible capacity for each cycle becomes lower. As for ZnFe<sub>2</sub>O<sub>4</sub> and Fe<sub>2</sub>O<sub>3</sub>, the reversible capacity increases after several cycles. As this improvement of the reversible capacity is not observed with ZnO, it is assumed that this phenomenon may be favored by the presence of iron in the material. Considering that this increase of capacity is due to the formation of a reversible polymeric gel-type layer, one possible explanation is that this polymeric layer is preferentially formed around certain metal species than others. However, the mechanism for the formation of this polymeric film remains unclear.

The performances of ZnO/Fe<sub>2</sub>O<sub>3</sub> can be compared to the performance of ZFO-5 at 100 mA.g<sup>-1</sup> (Figure 4.3). The behavior during the cycling is very similar for the two materials with the decrease of capacity for the first cycles and then an increase of capacity. However, the reversible capacity for ZFO-5 after 100 cycles is higher than the one of ZnO/Fe<sub>2</sub>O<sub>3</sub> (595 mAh.g<sup>-1</sup> vs. 390 mAh.g<sup>-1</sup>, respectively).

To understand the contrast in terms of performances between ZnO/Fe<sub>2</sub>O<sub>3</sub> and ZFO-5, the charge/discharge profiles, the dQ/dV curves and the polarization for ZnO, Fe<sub>2</sub>O<sub>3</sub> and the mixture of these two oxides were studied.

The charge/discharge profiles for ZnO are shown in Figure 4.29 (a). Derivative curves were calculated and plotted between 0.01 V and 3.0 V (b) and between 0.01 V and 1.1 V (c) to observe the relative position of the 50<sup>th</sup> and 100<sup>th</sup> cycle curves. The evolution of the polarization is also shown (d).

## Electrochemical performances of ZnO and Fe<sub>2</sub>O<sub>3</sub>

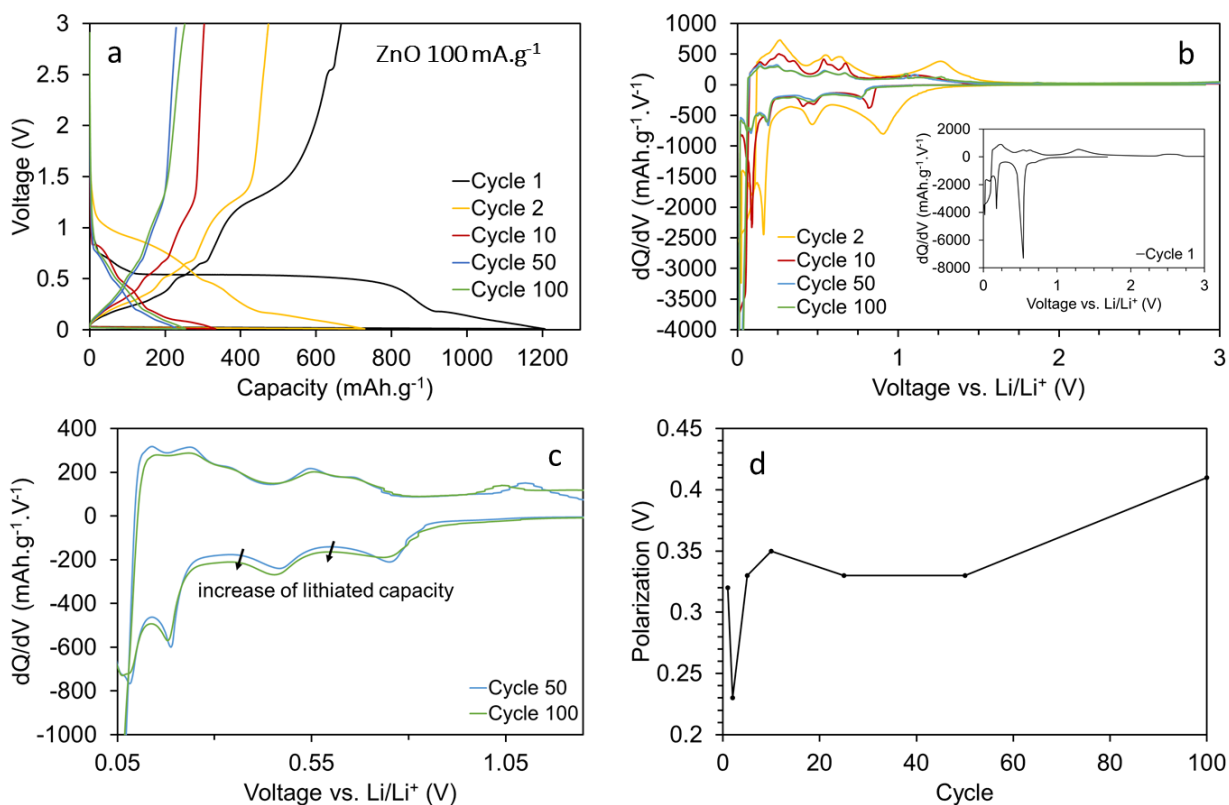


Figure 4.29. Charge/discharge profiles (a), dQ/dV curves (b, c) and polarization (d) for ZnO cycled at 100 mA.g<sup>-1</sup>

For ZnO, a very short plateau is observed at 0.73 V and then a short slope to 0.54 V, corresponding to a stored capacity of 150 mAh.g<sup>-1</sup>. A long plateau is then observed at 0.54 V which may be related to the conversion reaction between lithium and ZnO leading to the reduction of Zn(II) to Zn(0). The plateau contributes for 750 mAh.g<sup>-1</sup> of the total capacity. A very short plateau is then observed at 0.18 V and corresponds to less than 100 mAh.g<sup>-1</sup> what may be attributed to the alloying reaction between Zn metallic particles and lithium to form a ZnLi phase<sup>19,44</sup>. The corresponding derivative curves are shown in Figure 4.29b. The two main reduction peak may be attributed to the conversion then alloying reaction as explained for the charge/discharge profiles. These peaks are then shifted to higher voltages. The integrated area is decreasing along cycling but a very low increase of the capacity is observed between the 50<sup>th</sup> and the 100<sup>th</sup> cycle. By magnifying the scale of the dQ/dV plots for these two cycles, it is observed that the discharge curve for cycle 100 is below the one for cycle 50, meaning that the lithiated capacity is increasing in this area. The slight increase of capacity for ZnO may be related to parasitic reactions occurring at low voltages. The polarization (Figure 4.29d) shows the same trend as ZFO-1 and ZFO-5 samples with a decrease of the voltage hysteresis between the first and second cycle, followed by a rapid increase of the polarization until the 50<sup>th</sup> cycle and finally a low increase of the polarization between the 50<sup>th</sup> and the 100<sup>th</sup> cycle.

Similar curves were also plotted for Fe<sub>2</sub>O<sub>3</sub> electrode (Figure 4.30). However, for this sample, the dQ/dV curves were very noisy even after smoothing for the first cycles. Only the 50<sup>th</sup> and the 70<sup>th</sup> cycles are shown below.

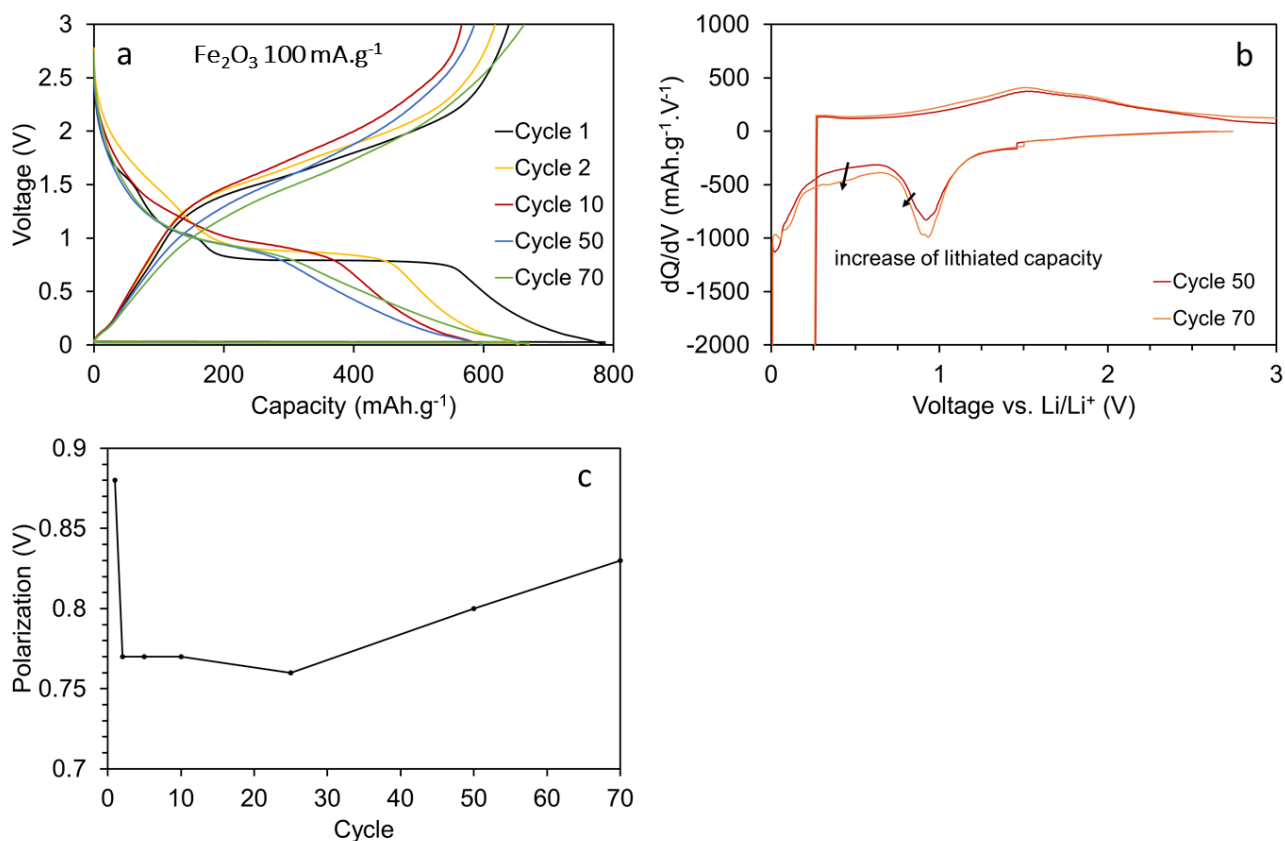


Figure 4.30. Charge/discharge profiles (a), dQ/dV curves (b) and polarization (c) for Fe<sub>2</sub>O<sub>3</sub> cycled at 100 mA.g<sup>-1</sup>

For Fe<sub>2</sub>O<sub>3</sub>, two short plateaus are observed at 1.57 V and 1.03 V which may correspond to the progressive insertion of 1.2 mol of lithium into the crystalline structure (~200 mAh.g<sup>-1</sup>). At 0.76 V, the main plateau of 400 mAh.g<sup>-1</sup> may be attributed to the reduction of Fe<sub>2</sub>O<sub>3</sub> to form metallic iron and Li<sub>2</sub>O during the conversion reaction. The remaining capacity of 200 mAh.g<sup>-1</sup> between 0.74 V and 0.01 V is likely due to the decomposition of the electrolyte forming SEI that traps part of the lithium ions<sup>45</sup>. Three regions can also be defined with the derivative curves, similarly to ZFO-1 and ZFO-5 with the main peak corresponding to the conversion reaction. The increase of lithiated capacity for Fe<sub>2</sub>O<sub>3</sub> seems to mainly come from the extra capacity region. The evolution of the polarization during cycling for Fe<sub>2</sub>O<sub>3</sub> is slightly different from the one for ZFO-1 and ZFO-5; in particular, after the first cycle with 0.88 V of polarization, the voltage hysteresis does not increase rapidly and the obtained value after 70 cycles (0.83 V) is still lower than the one of the first cycle.

To compare the performances of ZFO-5 with the ZnO/Fe<sub>2</sub>O<sub>3</sub> mixture, the charge/discharge profiles, derivative curves and polarization are shown below.

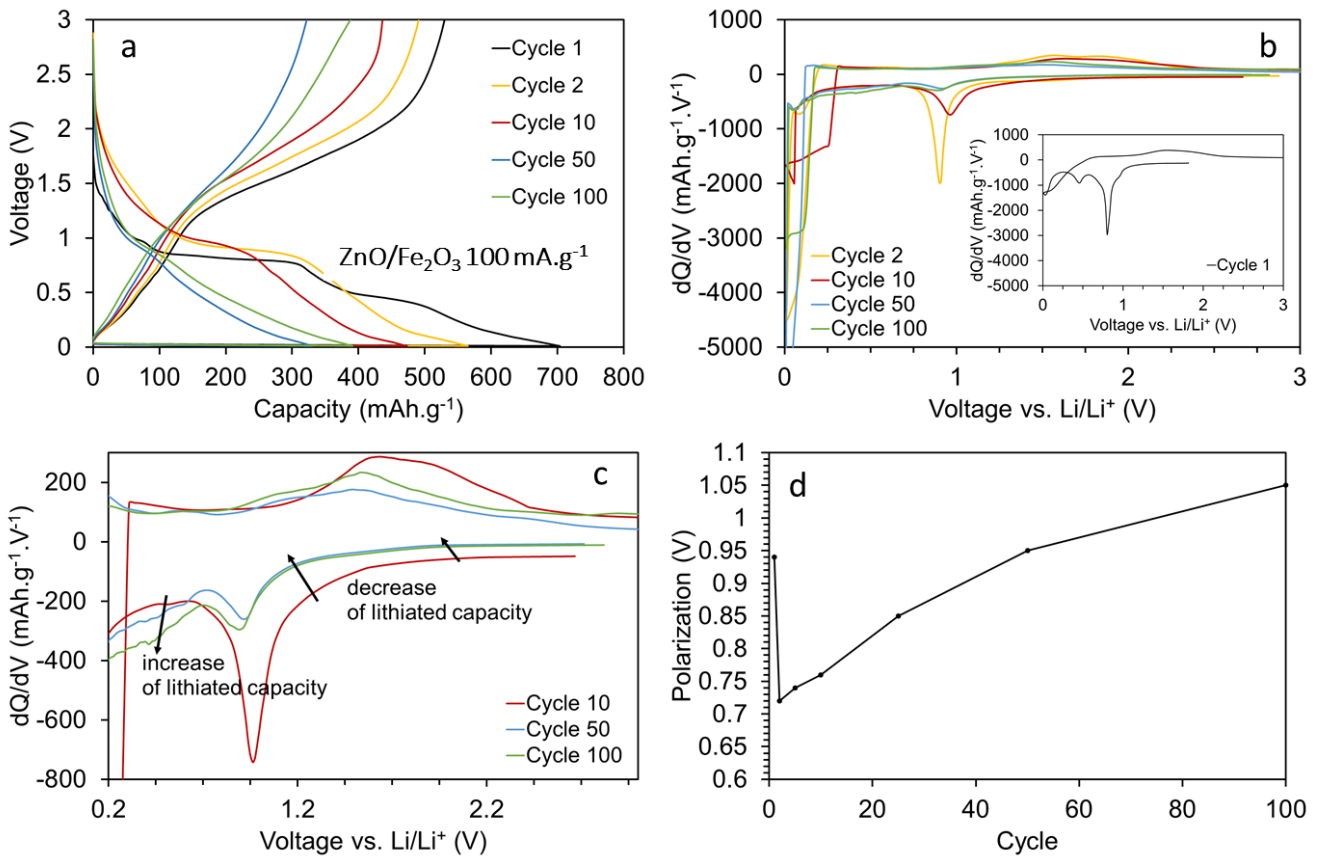


Figure 4.31. Charge/discharge profiles (a), dQ/dV curves (b, c) and polarization (d) for ZnO/Fe<sub>2</sub>O<sub>3</sub> cycled at 100 mA.g<sup>-1</sup>

The charge and discharge curves and the derivative curves of the mixture ZnO/Fe<sub>2</sub>O<sub>3</sub> show different steps that can be separately observed in the curves recorded for ZnO and Fe<sub>2</sub>O<sub>3</sub>. For ZnO/Fe<sub>2</sub>O<sub>3</sub>, the short plateau at 1.0 V and the slope before 0.8 V contributes for 100 mAh.g<sup>-1</sup> of the total capacity (~ 0.9 mol of Li). On the contrary of the ternary ZnFe<sub>2</sub>O<sub>4</sub> where only one plateau at 0.8 V could be distinguished, two long plateaus can then be observed for the mixture at two different potentials: a first plateau at 0.8 V and a second one at 0.5 V. According to the charge/discharge curves for ZnO and Fe<sub>2</sub>O<sub>3</sub>, the plateau at 0.8 V can be attributed to the conversion reaction with the iron oxide to form metallic iron whereas the plateau at 0.5 V may reveal the reduction of Zn(II) to Zn(0). The remaining 200 mAh.g<sup>-1</sup> below 0.5 V may come from the alloying reaction between Zn and Li and from the SEI formation. The integrated area of the dQ/dV curves experiences a fast decrease for the first cycles (coherent with the decrease of the reversible capacity). The mixture shows a rise of the capacity after 40 cycles according to Figure 4.28e. On Figure 4.31c, the decrease and increase regions are determined thanks to the relative positions of the curves. During the lithiation process, a decrease of the discharge capacity is observed during cycling in the voltage region above the conversion peak

and in the one including the conversion peak. An increase of the capacity is observed in the low voltage region below 0.7 V between the 10<sup>th</sup> and the 100<sup>th</sup> cycle. The increase of the discharge capacity in the low voltage region during cycling may finally counterbalanced the loss of capacity in the conversion region and explain the increase of discharge capacity after 40 cycles. However, even with the rise of capacity, ZnO/Fe<sub>2</sub>O<sub>3</sub> shows poorer performance compared to the ZnFe<sub>2</sub>O<sub>4</sub> oxide with a similar morphology (ZFO-5, small nanoparticles). Another important difference between ZnO/Fe<sub>2</sub>O<sub>3</sub> and ZnFe<sub>2</sub>O<sub>4</sub> is the polarization values during cycling. The mixture shows a polarization of 1.05 V after 100 cycles whereas for ZFO-5, the polarization value is 0.97 V at the 100<sup>th</sup> cycle, suggesting a poor reversibility of the lithium insertion/extraction into the mixture compared to ZFO-5.

## 2. Understanding of the lithium storage mechanism

Cyclic voltamograms were then carried out for ZnO, Fe<sub>2</sub>O<sub>3</sub> and ZnO/Fe<sub>2</sub>O<sub>3</sub> at a scan rate of 0.01 mV.s<sup>-1</sup> between 0.01 V and 3.0 V. The five first cycles are illustrated below (Figure 4.32).

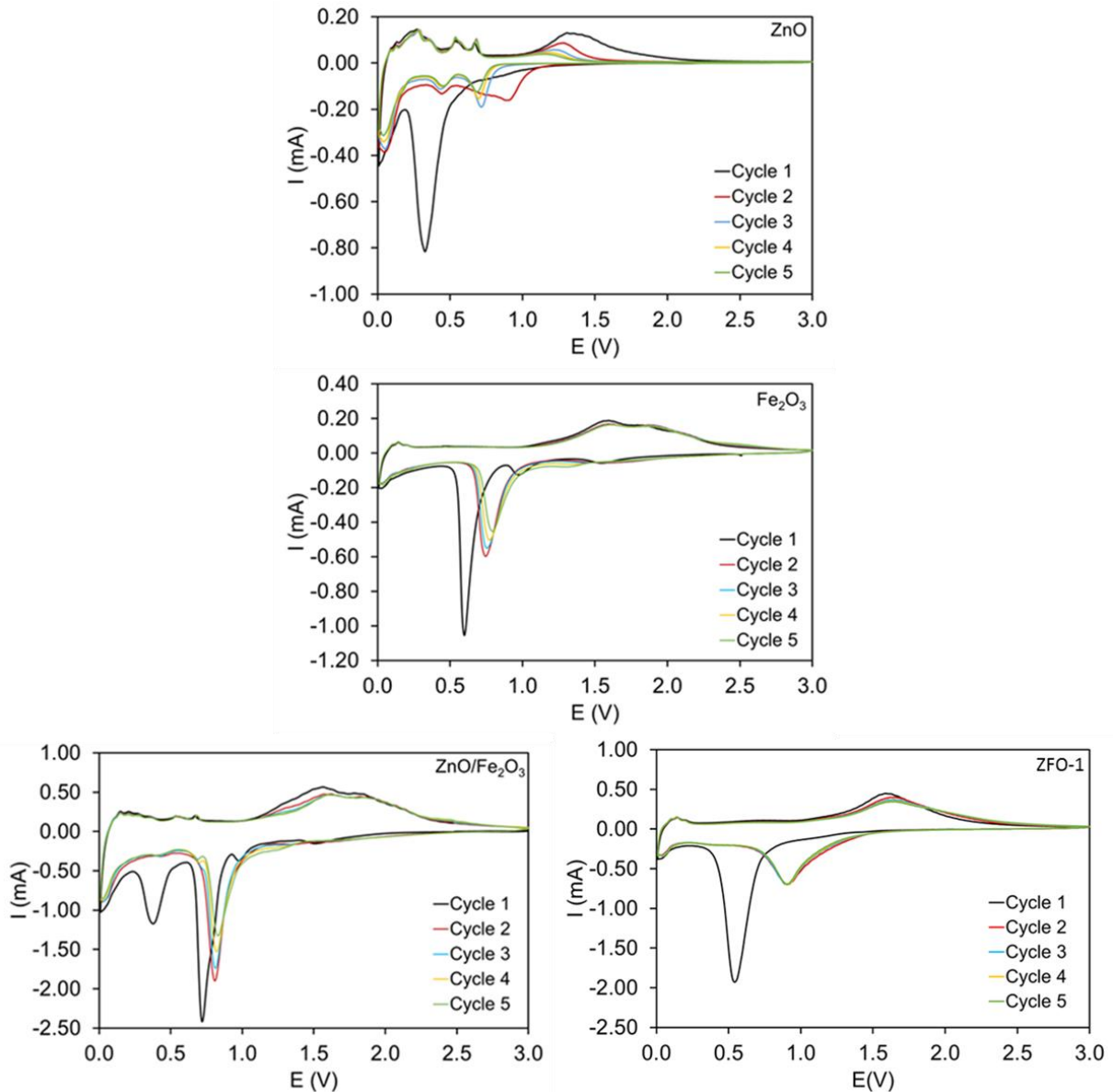


Figure 4.32. Cyclic voltamograms for ZnO, Fe<sub>2</sub>O<sub>3</sub>, ZnO/Fe<sub>2</sub>O<sub>3</sub> and ZnFe<sub>2</sub>O<sub>4</sub> (ZFO-1) at a scan rate of 0.01 mV.s<sup>-1</sup>

For ZnO, the first cathodic scan only shows one strong peak at 0.33V. This peak may contain the reduction of ZnO to Zn as well as the formation of the ZnLi alloy and eventually the growth of the SEI layer. During the delithiation process, several small peaks can be observed between 0.3V and 0.7V and are ascribed to the multistep dealloying process of the ZnLi alloy. The large peak at 1.37 V corresponds to the oxidation of Zn to form ZnO. The different anodic peaks match well with the

charge profiles shown in Figure 4.31. For the second cycle, two cathodic peaks can be noticed, located at 0.45 V and 0.91 V which progressively shift to lower potentials in the subsequent cycles. These two peaks can be attributed to the reduction of ZnO and to the alloying reaction. The shift may be due to the polarization during the storage process. During the delithiation, the small peaks keep their location at low potentials whereas the main peak is shifted towards lower potential, going from 1.37V to 1.25V. This behavior is in good agreement with the charge/discharge profiles of ZnO observed above, with the shifting of the plateau to a slightly higher potential during lithiation and lower potential during delithiation.

For Fe<sub>2</sub>O<sub>3</sub>, one main peak is observed at 0.6V which may correspond to the plateau at 0.8V on the charge/discharge profiles and thus may be attributed to the conversion reaction (Fe(III) to Fe(0)). Two small peaks at 0.98V and 1.56V are also observed on the CV curves and may be due to the progressive insertion of lithium into the Fe<sub>2</sub>O<sub>3</sub> crystalline structure, which is consistent with the two short plateaus at 1.03V and 1.57V on the discharge profile. For the anodic process, several peaks between 1.5 V and 2.0 V can be related to the oxidation of metallic iron to recover Fe<sub>2</sub>O<sub>3</sub>.

For ZnO/Fe<sub>2</sub>O<sub>3</sub>, the first lithiation presents four distinct cathodic peaks. The two first peaks at 1.6V and 0.95V are consistent with those on the cyclic voltamogram presented for Fe<sub>2</sub>O<sub>3</sub> and can correspond to the insertion of lithium into the crystalline structure of Fe<sub>2</sub>O<sub>3</sub>. The large peak at 0.7V is similar to the conversion peak for Fe<sub>2</sub>O<sub>3</sub> whereas the other large peak at a lower potential of 0.4 V seems similar to the one reported for ZnO. The location of these peaks are consistent with the different voltage plateaus on the charge/discharge profiles for ZnO, Fe<sub>2</sub>O<sub>3</sub> and ZnO/Fe<sub>2</sub>O<sub>3</sub>. The mechanism that can be assumed for the mixture is that the first reaction occurs with the iron phase. The lithiation of the iron phase is realized first with the insertion of lithium into the material followed by the destruction of the crystalline structure to form Fe and Li<sub>2</sub>O thanks to the conversion reaction. After the reaction with the iron oxide, lithium may react with zinc oxide to form Zn metallic particles. On the charge process, the different small peaks at low potential may be related to the progressive dealloying of ZnLi followed by the oxidation of Zn to ZnO first and then Fe to Fe<sub>2</sub>O<sub>3</sub>. This multi-step dealloying reaction cannot be seen on the CV curves for ZnFe<sub>2</sub>O<sub>4</sub>. Moreover, during the subsequent charges, two main peaks are observed for the mixture between 1.6 and 1.8 V whereas it is not the case for ZnFe<sub>2</sub>O<sub>4</sub>, where only one peak centered at 1.6 V is present. This may indicate that, even if ZnFe<sub>2</sub>O<sub>4</sub> forms ZnO and Fe<sub>2</sub>O<sub>3</sub> after the first cycle, the storage mechanism may be different from a simple mixture of ZnO and Fe<sub>2</sub>O<sub>3</sub>.

The different CV curves for ZnO, Fe<sub>2</sub>O<sub>3</sub> and ZnO/Fe<sub>2</sub>O<sub>3</sub> show a decrease of their integrated area coinciding with the large irreversibility observed during galvanostatic cyclings.

To obtain more information on the lithium storage mechanism for ZnO/Fe<sub>2</sub>O<sub>3</sub>, operando X-ray diffraction measurements were conducted for the first lithiation (Figure 4.33). The lithiation was conducted between the OCV and 0.01 V with a low current rate of 8.3 mA.g<sup>-1</sup> (120 h for a full discharge). A diffractogram was acquired every two hours.

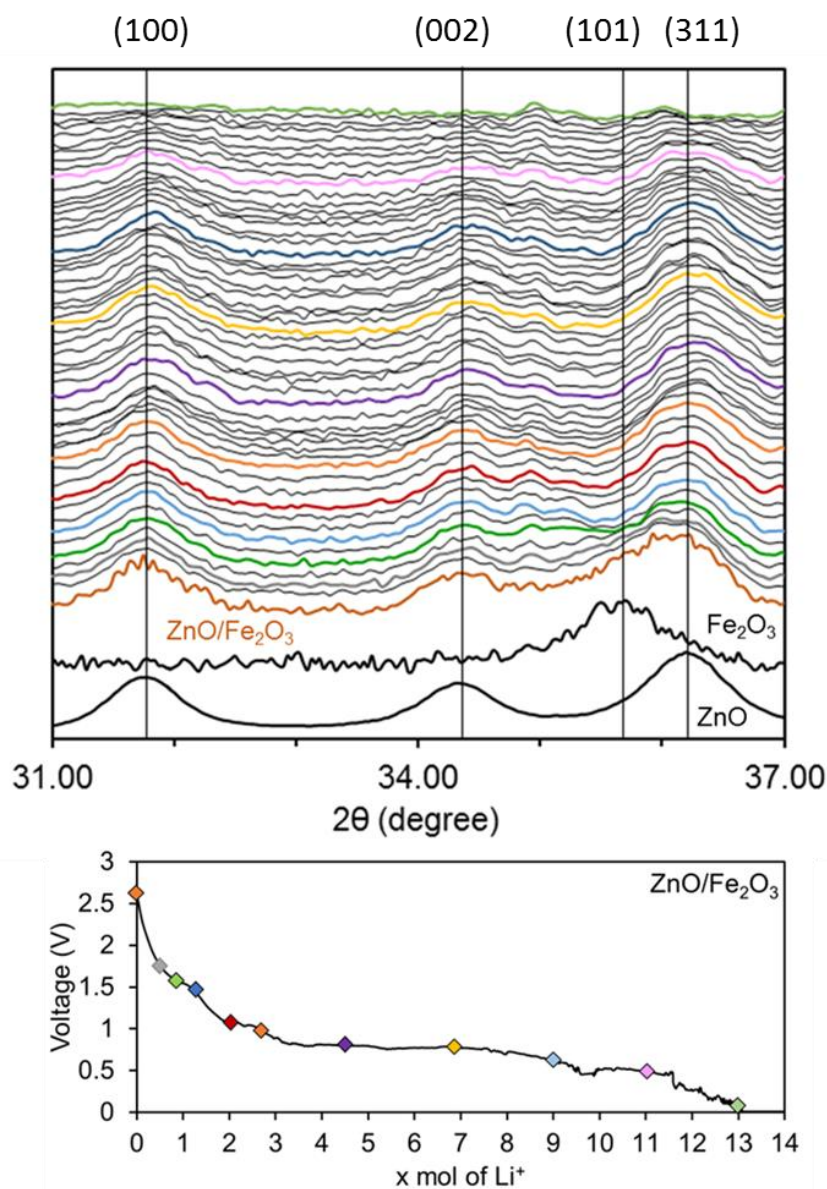


Figure 4.33. Operando XRD during the first lithiation of ZnO/Fe<sub>2</sub>O<sub>3</sub> between 0.01 V and 3.0 V

The diffractograms for ZnO and for Fe<sub>2</sub>O<sub>3</sub> are reminded on the figure 4.33. The signal is only reported between 31° and 37° as the most visible peaks of ZnO and Fe<sub>2</sub>O<sub>3</sub> are located in this angular range. No apparition of peaks can be related outside this window during the first lithiation indicating that no new crystalline phase was formed.

The first peak that seems to disappear during the lithiation process is the iron phase peak around 35.7° whose intensity decreases progressively until complete vanishing of the peak, from the OCV to the voltage plateau around 0.8V. Before 0.8V, no modification for the ZnO phase is noticeable. Once the iron oxide peak totally disappears after the 0.8V plateau, the ZnO peaks start to decrease in intensity, especially on the small plateau at 0.5V. The ZnO peaks disappear totally at the end of the discharge and no crystalline structure can be observed anymore. It is assumed that the deep lithiation conducts to the amorphization of the material. As for the different ZnFe<sub>2</sub>O<sub>4</sub> samples, no peak for Zn, Fe or ZnLi particles can be found on the XRD patterns what can be due to the formation of an amorphous Li<sub>2</sub>O phase with highly dispersed ZnLi and Fe particles.

From the CV curves and the operando XRD measurements, it can be assumed that the first lithiation for ZnO/Fe<sub>2</sub>O<sub>3</sub> is divided into several steps. It seems that the lithium reacts with the iron oxide first by an intercalation process followed by a conversion process leading to the formation of metallic iron nanoparticles. The reaction between lithium and zinc only occurs in a second step with the reduction of ZnO to Zn and then the formation of the ZnLi alloy. CV measurements indicate that during the reverse charge process, oxidation of zinc occurs first prior to the oxidation of iron. However, as the active material becomes amorphous after the first lithiation, XRD measurements cannot confirm this assumption. Future studies by operando <sup>57</sup>Fe Mössbauer may give further information on the lithiation and delithiation mechanisms for the ZnO/Fe<sub>2</sub>O<sub>3</sub> mixture.

This study shows that several differences can be noticed between ZnFe<sub>2</sub>O<sub>4</sub> based samples and ZnO/Fe<sub>2</sub>O<sub>3</sub> mixtures during the lithium storage process. In particular, for ZnFe<sub>2</sub>O<sub>4</sub>, a single plateau is observed during the first lithiation instead of two plateaus for ZnO/Fe<sub>2</sub>O<sub>3</sub>. As suggested by Cabana *et al*, the occurrence of mixed states at the Fermi level may lead to a simultaneous reduction reaction for ZnFe<sub>2</sub>O<sub>4</sub><sup>46</sup>. The difference of mechanism for the first lithiation is not very surprising as the two materials are different. However, the comparison of the CV curves for the next cycles reveals differences in the storage mechanisms whereas both samples may correspond to ZnO and Fe<sub>2</sub>O<sub>3</sub>. Further operando studies (in particular, <sup>57</sup>Fe Mössbauer and X-ray Absorption Spectroscopy) are needed to be able to conclude about the lithiation and delithiation processes involved in both ZnFe<sub>2</sub>O<sub>4</sub> and ZnO/Fe<sub>2</sub>O<sub>3</sub> and highlight interest, if any, of the ternary oxide.

#### IV. Intermediate conclusion

The evaluation of ZFO-1 and ZFO-5 performance showed the importance of the size distribution to optimize the battery cycling. In particular, conversion materials like  $\text{ZnFe}_2\text{O}_4$  generally suffer from a large voltage hysteresis. The use of a bimodal size population of particles seems to be more efficient to limit the polarization and this may be due to a better contact during cycling between the ZFO-1 particles whereas for ZFO-5, a thick SEI formation may isolate particles. This limits the lithium diffusion in the active material and makes the lithiation process more difficult. However, even if ZFO-1 shows higher specific capacity than ZFO-5, it also shows a high irreversible capacity which will be an issue for a full battery with a cathode for which the lithium amount will be limited.

A better understanding of the lithium storage process was obtained thanks to operando measurements on  $\text{ZnFe}_2\text{O}_4$  and  $\text{ZnO}/\text{Fe}_2\text{O}_3$ . Operando XRD and Mössbauer acquisitions strengthen the hypothesis of an intercalation then conversion process but no evidence of the alloying process can be pointed out here due to the formation of an amorphous phase after the first discharge. However, the origin of the increase of capacity during cycling still has to be studied.

This chapter also compared the performances of  $\text{ZnFe}_2\text{O}_4$  with a mixture of  $\text{ZnO}$  and  $\text{Fe}_2\text{O}_3$ . The zinc iron oxide shows a higher reversible capacity. This may be due to the voltage hysteresis which is lower for  $\text{ZnFe}_2\text{O}_4$  than for the mixture, suggesting a better reversibility of the reaction. However, further operando studies need to be conducted to understand the better performances of  $\text{ZnFe}_2\text{O}_4$ .

References

- 1 C. Marino, *PhD thesis. Marino, Cyril. Optimisation de nouvelles électrodes négatives énergétiques pour batteries lithium-ion : caractérisation des interfaces électrode/électrolyte. (Université de Montpellier 2)*, 2012.
- 2 V. Sivasankaran, C. Marino, M. Chamas, P. Soudan, D. Guyomard, J. C. Jumas, P. E. Lippens, L. Monconduit and B. Lestriez, *J. Mater. Chem.*, 2011, **21**, 5076–5082.
- 3 E. Peled, *J. Electrochem. Soc.*, 1979, **126**, 2047–2051.
- 4 K. Mani, D. Pliszka, C. H. Sow and S. Ramakrishna, *ACS Appl. Mater. Interfaces*, 2013, **5**, 9957–9963.
- 5 P. F. Teh, Y. Sharma, S. S. Pramana and M. Srinivasan, *J. Mater. Chem.*, 2011, **21**, 14999.
- 6 X. Yao, J. Kong, X. Tang, D. Zhou, C. Zhao, R. Zhou and X. Lu, *RSC Adv.*, 2014, **4**, 27488.
- 7 S. H. Choi and Y. C. Kang, *Int. J. Electrochem. Sci.*, 2013, **8**, 6281–6290.
- 8 Y.-G. Guo, J.-S. Hu and L.-J. Wan, *Adv. Mater.*, 2008, **20**, 2287–2878.
- 9 Z. Wang, D. Luan, M. Srinivasan, H. Yong and X. W. (David) Lou, *Energy Environ. Sci.*, 2012, **5**, 5252–5256.
- 10 J. Xu and Y. Zhu, *ACS Appl. Mater. Interfaces*, 2012, **4**, 4752–4757.
- 11 X. Hou, X. Wang, L. Yao, S. Hu, Y. Wu and X. Liu, *New J. Chem.*, 2015, **39**, 1943–1952.
- 12 C. Marino, B. Fraisse, M. Womes, C. Villevieille, L. Monconduit and L. Stievano, *J. Phys. Chem. C*, 2014, **118**, 27772–27780.
- 13 S. Laruelle, S. Grugeon, P. Poizot, M. Dollé, L. Dupont and J.-M. Tarascon, *J. Electrochem. Soc.*, 2002, **149**, A627–A634.
- 14 G. Zhou, D. W. Wang, F. Li, L. Zhang, N. Li, Z. S. Wu, L. Wen, G. Q. Lu and H. M. Cheng, *Chem. Mater.*, 2010, **22**, 5306–5313.
- 15 S. J. Rezvani, R. Gunnella, A. Witkowska, F. Mueller, M. Pasqualini, F. Nobili, S. Passerini and A. Di Cicco, *ACS Appl. Mater. Interfaces*, 2017, **9**, 4570–4576.
- 16 Y. Sharma, N. Sharma, G. V. S. Rao and B. V. R. Chowdari, *Electrochim. Acta*, 2008, **53**, 2380–2385.
- 17 A. K. Rai, S. Kim, J. Gim, M. H. Alfaruqi, V. Mathew and J. Kim, *RSC Adv.*, 2014, **4**, 47087–47095.

- 18 J. M. Won, S. H. Choi, Y. J. Hong, Y. N. Ko and Y. C. Kang, *Sci. Rep.*, 2014, **4**, 1–5.
- 19 X. Guo, X. Lu, X. Fang, Y. Mao, Z. Wang, L. Chen, X. Xu, H. Yang and Y. Liu, *Electrochem. commun.*, 2010, **12**, 847–850.
- 20 J. Tang, C. E. Zavala Lugo, S. F. Acuña Guzmán, G. Daniel, V. G. Kessler, G. A. Seisenbaeva and V. G. Pol, *J. Mater. Chem. A*, 2016, **4**, 18107–18115.
- 21 S.-H. Yu, S. H. Lee, D. J. Lee, Y.-E. Sung and T. Hyeon, *Small*, 2015, 1–27.
- 22 H. Xu, X. Chen, L. Chen, L. Li, L. Xu, J. Yang and Y. Qian, *Int. J. Electrochem. Sci.*, 2012, **7**, 7976–7983.
- 23 X.-B. Zhong, B. Jin, Z.-Z. Yang, C. Wang and H.-Y. Wang, *RSC Adv.*, 2014, **4**, 55173–55178.
- 24 X. Guo, X. Lu, X. Fang, Y. Mao, Z. Wang, L. Chen, X. Xu, H. Yang and Y. Liu, *Electrochem. commun.*, 2010, **12**, 847–850.
- 25 L. Yao, X. Hou, S. Hu, J. Wang, M. Li, C. Su, M. O. Tade, Z. Shao and X. Liu, *J. Power Sources*, 2014, **258**, 305–313.
- 26 L. P. Wang, Y. Leconte, Z. Feng, C. Wei, Y. Zhao, Q. Ma, W. Xu, S. Bourrioux, P. Azais, M. Srinivasan and Z. J. Xu, *Adv. Mater.*, 2017, **29**, 1–12.
- 27 Y. Ding, Y. Yang and H. Shao, *Electrochim. Acta*, 2011, **56**, 9433–9438.
- 28 N. Wang, H. Xu, L. Chen, X. Gu, J. Yang and Y. Qian, *J. Power Sources*, 2014, **247**, 163–169.
- 29 D. Bresser, E. Paillard, R. Kloepsch, S. Krueger, M. Fiedler, R. Schmitz, D. Baither, M. Winter and S. Passerini, *Adv. Energy Mater.*, 2013, **3**, 513–523.
- 30 E. Murad, in *Iron in Soils and Clay Minerals*, eds. J. W. Stucki, B. A. Goodman and U. Schwertmann, Springer Netherlands, Dordrecht, 1988, pp. 309–350.
- 31 D. J. Elias and J. W. Linnett, *Trans. Faraday Soc.*, 1969, **65**, 2673–2677.
- 32 N. N. Greenwood and T. C. Gibb, *Mössbauer spectroscopy*, Chapman and Hall Ltd, London, UK, 1971.
- 33 L. Aldon and J.-C. Jumas, *Solid State Sci.*, 2012, **14**, 354–361.
- 34 L. Stievano and F. E. Wagner, in *Characterization of Solid Materials and Heterogeneous Catalysts*, eds. M. Che and J. C. Védrine, Wiley-VCH Verlag GmbH & Co. KGaA, Weinheim, Germany, 1st edn., 2012, pp. 407–452.

- 35 J. W. 'Hans' Niemantsverdriet, A. M. van der Kraan, W. N. Delgass and M. A. Vannice, *J. Phys. Chem.*, 1985, **89**, 67–72.
- 36 J. L. Tirado, P. Lavela, C. Pérez Vicente, B. León and C. Vidal-Abarca, *Hyperfine Interact.*, 2012, **207**, 53–59.
- 37 C. Vidal-Abarca, P. Lavela and J. L. Tirado, *J. Phys. Chem. C*, 2010, **114**, 12828–12832.
- 38 A. Darwiche, M. Toiron, M. T. Sougrati, B. Fraisse, L. Stievano and L. Monconduit, *J. Power Sources*, 2015, **280**, 588–592.
- 39 M. Chamas, P. Lippens, J. Jumas, K. Boukerma, R. Dedryvère, D. Gonbeau, J. Hassoun, S. Panero and B. Scrosati, *J. Power Sources*, 2011, **196**, 7011–7015.
- 40 F. Bødker, I. Chorkendorff and S. Mørup, *Z. Phys. D*, 1997, **40**, 152–154.
- 41 J.-C. Jumas, M. Womes, R. Alcántara, P. Lavela and J. L. Tirado, *Hyperfine Interact.*, 2008, **183**, 1–5.
- 42 C. Yuan, H. Bin Wu, Y. Xie and X. W. D. Lou, *Angew. Chem. Int. Ed. Engl.*, 2014, **53**, 1488–1504.
- 43 L. Yao, X. Hou, S. Hu, X. Tang, X. Liu and Q. Ru, *J. Alloys Compd.*, 2014, **585**, 398–403.
- 44 X. H. Huang, X. H. Xia, Y. F. Yuan and F. Zhou, *Electrochim. Acta*, 2011, **56**, 4960–4965.
- 45 M. V Reddy, T. Yu, C. H. Sow, Z. X. Shen, C. T. Lim, G. V Subba Rao and B. V. R. Chowdari, *Adv. Funct. Mater.*, 2007, **17**, 2792–2799.
- 46 J. Cabana, L. Monconduit, D. Larcher and M. R. Palacín, *Adv. Mater.*, 2010, **22**, E170--92.

---

### Conclusions and recommendations for future works

---

The study of  $\text{ZnFe}_2\text{O}_4$  nanoparticles synthesized by laser pyrolysis as anode material for lithium-ion battery was addressed during my 3-years PhD work and presented in this manuscript. The objective was to determine on one hand how nanostructuration could enhance the behaviour of this high capacity material in terms of cycling stability. On the other hand, a comparison was required between the Li storage mechanisms in the ternary oxide and in the mixture of the two binary oxides reported to be formed after the first cycle, in order to highlight the potential interest of  $\text{ZnFe}_2\text{O}_4$ .

As detailed in the document, laser pyrolysis allowed the one step synthesis of  $\text{ZnFe}_2\text{O}_4$ ,  $\text{ZnO}$  and  $\text{Fe}_2\text{O}_3$  nanopowders from cheap and convenient precursors dissolved in water or ethanol. In particular, it was demonstrated that the choice of some experimental parameters has a strong influence on the structure of the obtained products. Indeed, the use of iron nitrate as Fe precursor was found to foster the synthesis of an unexpected bimodal size distribution of particles for zinc iron oxides and iron oxides whereas with chlorides or acetylacetonates precursors, a more conventional monomodal size distribution of small nanoparticles (around 10 nm) was obtained. Low melting point of iron nitrates was assumed to modify the aerosol droplet decomposition mechanisms and subsequently the growth of the particles, leading to this bimodal distribution.

The addition of air in the reaction also plays a key role on the produced phase. Indeed, when this combustion based process is activated, secondary phases were identified in addition to  $\text{ZnFe}_2\text{O}_4$ . This effect was assumed to be a consequence of the higher reaction temperature that can be achieved with a combustion flame, which promotes the decomposition of the ternary oxide which is not stable at high temperature. As reported in the literature, this leads to a loss of oxygen in the medium and to the formation of binary and suboxide phases.

The electrochemical performances of zinc iron oxides were studied for the two different morphologies. It was observed that the bimodal size population shows enhanced performances during galvanostatic cyclings at C/10 and 1C when compared to the monomodal size population. The cyclings were reported to be more stable and the specific capacity after 100 cycles reached a value up to  $1160 \text{ mAh.g}^{-1}$  at C/10. Such a capacity is among the best performances in the literature for this material, in particular when compared to larger grained material. This demonstrates the interest of using a finer microstructure. Nevertheless, the smallest nanoparticles retain only  $595 \text{ mAh.g}^{-1}$  at the same current rate. This improvement in cycling performance for bimodal size distribution was attributed to the specific morphology that may limit the SEI formation during cycling due to an

## Conclusions and recommendations for future works

assumed smaller surface area. The larger particles size of few hundreds nanometers could be a good compromise between the benefits of size reduction in terms of structure stability, and its drawback in terms of available surface for electrolyte degradation. Moreover, the interconnected nature of the nanoparticles agglomerates obtained by laser pyrolysis could preserve electronic percolation upon cycling and lead to improved performances when compared to the literature.

As reported in the bibliography, the storage mechanism was found to involve the destruction of  $\text{ZnFe}_2\text{O}_4$  starting phase after the first cycle and the formation of  $\text{ZnO}$  and  $\text{Fe}_2\text{O}_3$  phases instead. A mixture of these two binary oxides, previously prepared by laser pyrolysis too, was also cycled at C/10 to be compared to the ternary phase. The performance of the mixture was found to be significantly lower than the one of the ternary phase, with a capacity of only  $390 \text{ mAh.g}^{-1}$  after 100 cycles.

To investigate the differences, if any, in the lithium storage mechanism for  $\text{ZnFe}_2\text{O}_4$  and for the mixture of  $\text{ZnO}$  and  $\text{Fe}_2\text{O}_3$ , operando measurements were conducted. Particularly, operando XRD was realized for both samples for the first lithiation. For  $\text{ZnFe}_2\text{O}_4$ , the lithiation of the material consists in several steps: first, the insertion of lithium into the crystalline structure, up to 1 mol of  $\text{Li}^+$  per formula unit, then, the conversion reaction occurs around 0.8 V leading to the amorphization of the material. No evidence of the alloying reaction  $\text{ZnLi}$  was clearly highlighted. As no more information can be provided by XRD after the first lithiation,  $^{57}\text{Fe}$  Mössbauer measurements were conducted for the first cycle and a half by ICGM laboratory (Montpellier, France). The results gave information about the iron oxidation state during the first discharge, the first charge, and the second discharge. It is clear that the lithiation process conducts to the formation of iron nanoparticles and the delithiation process to the formation of  $\text{Fe}^{3+}$ . The first lithiation though shows intermediate oxidation states for iron whereas it is not the case for the first delithiation and the second lithiation.

For the  $\text{ZnO}/\text{Fe}_2\text{O}_3$  mixture, operando XRD was conducted and highlighted differences with  $\text{ZnFe}_2\text{O}_4$  during the first lithiation. In particular, it seems that the reaction with iron and zinc do not happen simultaneously. The lithiation starts with the reduction of the iron oxide first, which is followed by the reduction of the zinc oxide. Here again, XRD cannot give evidence of any iron, zinc or  $\text{ZnLi}$  phases due to the amorphization of the material.

It has been observed that  $\text{ZnFe}_2\text{O}_4$  is able to retain a higher specific capacity during cycling than the mixture of  $\text{ZnO}$  and  $\text{Fe}_2\text{O}_3$  and this may be due to a difference of polarization during cycling. Indeed, during cycling at  $100 \text{ mA.g}^{-1}$ , the polarization is higher for the mixture than for the ternary oxide.

The different results detailed in this thesis show the interest of  $\text{ZnFe}_2\text{O}_4$  nanoparticles as anode material thanks to their high specific capacity during cycling, good stability and capacity retention. However, further studies have to be done before considering the substitution of graphite by

## Conclusions and recommendations for future works

mixed-transition metal oxides in commercial batteries. Moreover, the use of such a high potential anode would be possible only with new cathodes materials with a higher working voltage too to ensure a high energy density. In the same way, new electrolytes have to be found that will be stable at high potentials.

From the synthesis point of view, it was shown that the control of the phase purity for these ternary oxide phases was difficult to achieve. Additional work on laser pyrolysis, especially with lower laser power, should be pursued in order to decrease the reaction temperature and preserve the ternary structure. A specific study should also be devoted to the aerosol evolution during the reaction in order to validate the assumed mechanisms that govern the reaction with nitrates or with other precursors. In a more general aspect, experimental development remains to be done on the laser assisted combustion reaction aiming at a better control and understanding of the process.

From the electrochemical point of view, the use of operando characterizations helped in the understanding of the mechanisms involved in the lithium storage. However, to obtain more information, in particular on the zinc oxidation state during cycling and for the ZnO/Fe<sub>2</sub>O<sub>3</sub> mixture, Mössbauer analyses were conducted for the mixture as they were recently performed for ZnFe<sub>2</sub>O<sub>4</sub>. Operando X-ray absorption spectroscopy (XAS) measurements were realized in synchrotron SOLEIL using ROCK beamline on the ternary oxide as well as on the mixture of binary oxides for one cycle and a half at Fe and Zn edges. The very large amount of data is still under study and could not be presented in this manuscript.

To conclude with this fundamental research approach, it would also be interesting to work on other mixed-transition metal oxides to investigate the effect of the counter-ion (Co, Mn) on the electrochemical performances and working voltage.

SEI related issues were also pointed out in this work, with the expected irreversible Li consumption during the first cycle but also with a more specific increase of the capacity during cycling also observed by other groups in the literature and ascribed to the degradation of the electrolyte into a material able to store Li reversibly. It is then mandatory to understand these phenomena in order to control them and provide a more stable SEI. Such stabilization could be expected thanks to carbon coating on the oxide surface, together with other performance improvements as detailed in chapter 1. This study, that opens a new pathway for the pursuit of this research work, was already initiated in the last months. As reported in chapter 3, zinc iron oxide nanopowders with large amount of free carbon were synthesized by laser pyrolysis, showing a continuous coating of the particles by a carbon based material. Preliminary studies were conducted to evaluate the performances of ZnFe<sub>2</sub>O<sub>4</sub> with different

## Conclusions and recommendations for future works

ratio of carbon (controlled by post annealing), at 100 and 1000 mA.g<sup>-1</sup> (Figure 5.1). The active material was ZFO-5 (monomodal size distribution) which was annealed at different temperatures between 300°C and 400°C to remove part of the carbon and observe the effect of the carbon ratio on the material performance.

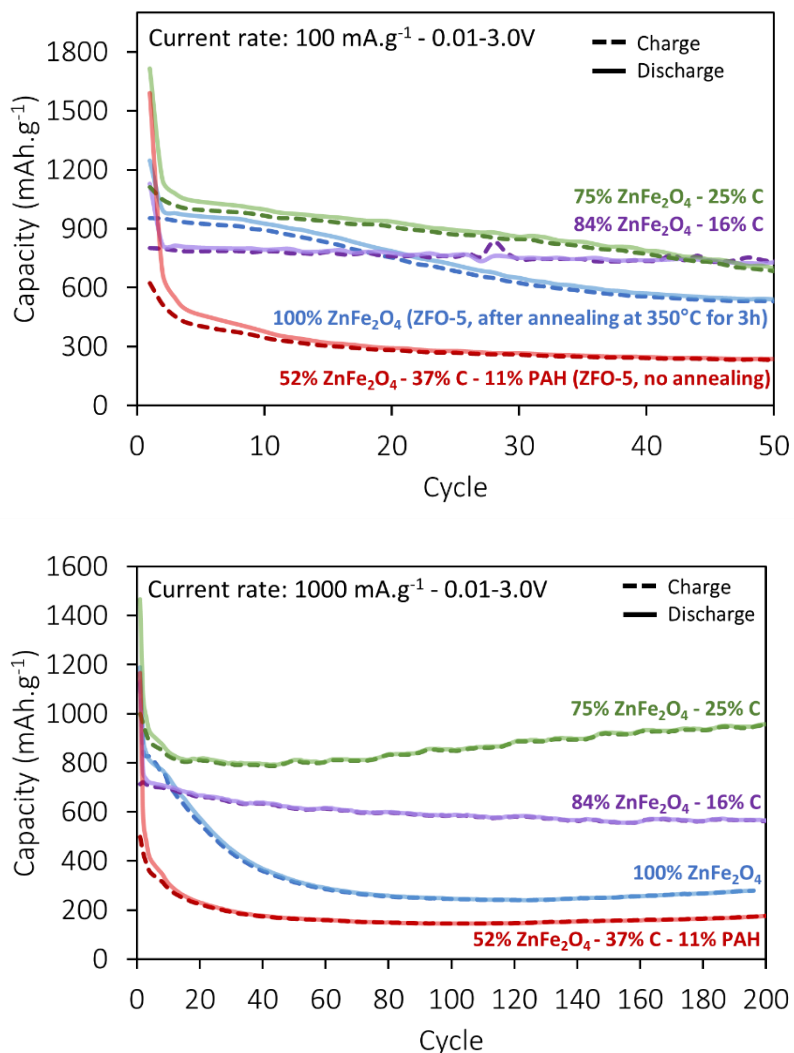


Figure 5.1. Cycling of ZnFe<sub>2</sub>O<sub>4</sub>/C with different carbon ratios at 100 and 1000 mA.g<sup>-1</sup>

The first results show differences between the different materials. The increase of carbon amount in the nanopowder normally decreases the theoretical capacity (ZnFe<sub>2</sub>O<sub>4</sub>: 1001 mAh.g<sup>-1</sup> and C: 372 mAh.g<sup>-1</sup> if graphite, less if any other disordered carbon). Nevertheless, according to the galvanostatic curves, a low amount of carbon is better than no carbon addition (violet curve vs blue curve) with a higher capacity and a better stability. These very preliminary results encourage the pursuit of this research orientation that will go through the direct control by laser pyrolysis of the thickness of the carbon coating on the ZnFe<sub>2</sub>O<sub>4</sub> particles.

## Conclusions and recommendations for future works

The other interesting route concerning SEI is to study more specifically the degradation of the electrolyte and the formation of the interphase that appears to contribute to the global capacity of the electrode in these conversion materials.

On a longer time scale, some general issues remain to be addressed if such oxides turned to be employed for commercial devices. On charge/discharge profiles, a large voltage hysteresis is observed for the different materials, keeping them far from industrial application as it penalizes the battery efficiency. This phenomena is not well understood yet and further studies on this topic should be realized to investigate its origin. Moreover, the reported coulombic efficiencies values would also impedes the use of this material in battery configuration where the amount of Li is limited. A work on the stabilization of the SEI is thus once again mandatory.

For such high potential materials at the anode, it must also be reminded that corresponding high capacity cathode materials, as well as electrolytes able to withstand these working conditions, remain to be developed and are currently the subject of intense research work.



---

## Appendix

---

### PCA and MCR-ALS analysis for operando Mössbauer acquisitions

The  $^{57}\text{Fe}$  Mössbauer spectra corresponding to the first complete cycle plus the second discharge were globally analysed using a statistical method based on Principal Component Analysis (PCA)<sup>1</sup>. PCA is a factor analysis, i.e., a multivariate technique for reducing matrices of data to their lowest dimensionality by the use of an orthogonal factor space: in such methods, the analysed matrix corresponds to the experimental spectra, and each spectrum is considered as an n-dimensions vector with n corresponding to the number of points within each XAS spectrum. The first principal component has the largest initial variance, i.e., alone it takes into account as much as possible the whole set of data. The following principal components are built orthogonal to the first one, and allow the reproduction of the experimental spectra with the highest possible variance via adapted linear combinations of them. This supposes that the group of analysed spectra is intrinsically bilinear, which means that all spectra can be expressed as linear combinations of an orthogonal basis set of uncorrelated spectra. This basis set, which has a lower dimensionality than the number of original spectra, is thus obtained from the calculation. In the different linear combinations which are built to reconstruct each experimental spectrum, the multiplication factors of the principal components are usually called scores. More precisely, it is used here to determine the number of independent components contributing to the whole series of collected spectra during electrochemical cycling.

However, principal components are just orthogonal mathematical functions and cannot be used nor treated as real spectra. Their number, determined by PCA, can nevertheless be used as the basis for other available methodologies to reconstruct the real spectral components which are necessary for interpreting the whole multiset of collected spectra, as well to follow as their evolution. In this case, one of the most known methodologies, Multivariate Curve Resolution-Alternating Least Squares (MCR-ALS) analysis is used<sup>2,3</sup>. A detailed description of this method from a theoretical point of view is given by Tauler et al., who also proposed it for the analysis of *in situ* spectroscopic data<sup>4,5</sup>. The intrinsic limits of this method and of its application are discussed by Ruckebusch *et al.*<sup>6</sup>. The application of MCR-ALS to the whole set of Mössbauer spectra was performed with the following constraints: (i) non-negativity of the concentration and of the transmission values of the components, (ii) unimodality for a certain number of components and (iii) closure (sum of the components equal or lower than 100 % of the total intensity). The analysis resulted in the reconstruction of six spectral components, which were then analysed as normal Mössbauer spectra.

## References

- 1 D. L. Massart, B. G. M. Vandeginste, L. M. C. Buydens, S. De Jong, P. J. Lewi and J. Smeyers-Verbeke, *Handbook of Chemometrics and Qualimetrics: Part A*, Elsevier B.V., Amsterdam, 1st Editio., 1997.
- 2 J. Jaumot, A. de Juan and R. Tauler, *Chemom. Intell. Lab.*, 2015, **140**, 1–12.
- 3 J. Jaumot, R. Gargallo, A. de Juan and R. Tauler, *Chemom. Intell. Lab.*, 2005, **76**, 101–110.
- 4 A. de Juan, J. Jaumot and R. Tauler, *Anal. Methods*, 2014, **6**, 4964.
- 5 R. Tauler, *Chemom. Intell. Lab.*, 1995, **30**, 133–146.
- 6 C. Ruckebusch and L. Blanchet, *Anal. Chim. Acta*, 2013, **765**, 28–36.